

AD-A279 130

WL-TR-92-2032



(2)

INFLUENCE OF FATIGUE CRACK CLOSURE ON THE GROWTH RATE OF SURFACE FLAWS

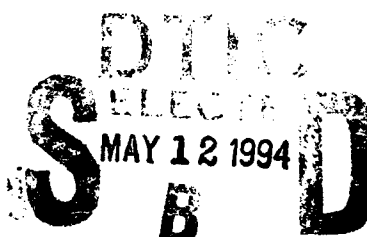


William A. Troba

Turbine Branch
Turbine Engine Division

February 1994

Final Report for Period September 1982 - May 1988



Approved for Public Release; distribution is unlimited.



Aero Propulsion & Power Directorate
Wright Laboratory
Air Force Materiel Command
Wright-Patterson AFB, OH 45433-7251

94 5 10 009

NOTICE

When Government drawings, specifications, or other data are used for any purpose other than in connection with a definitely Government-related procurement, the United States Government incurs no responsibility or any obligation whatsoever. The fact that the government may have formulated or in any way supplied the said drawings, specifications, or other data, is not to be regarded by implication, or otherwise in any manner construed, as licensing the holder, or any other person or corporation; or as conveying any rights or permission to manufacture, use, or sell any patented invention that may in any way be related thereto.

The report is releasable to the National Technical Information Service (NTIS). At NTIS, it will be available to the general public, including foreign nations.

This technical report has been reviewed and is approved for publication.



WILLIAM A. TROHA
Chief, Turbines Branch
Turbine Engine Division
Aero Propulsion & Power Directorate



THOMAS J. SIMS
Chief
Turbine Engine Division
Aero Propulsion & Power Directorate

If your address has changed, if you wish to be removed from our mailing list, or if the addressee is no longer employed by your organization please notify WL/POTC, WPAFB OH 45433-7251 to help us maintain a current mailing list.

Copies of this report should not be returned unless return is required by security considerations, contractual obligations, or notice on a specific document.

Unclassified

SECURITY CLASSIFICATION OF THIS PAGE

REPORT DOCUMENTATION PAGE

Form Approved
OMB No. 0704-0188

1a. REPORT SECURITY CLASSIFICATION Unclassified		1b. RESTRICTIVE MARKINGS	
2a. SECURITY CLASSIFICATION AUTHORITY		3. DISTRIBUTION/AVAILABILITY OF REPORT Approved for Public Release; distribution is unlimited	
2b. DECLASSIFICATION/DOWNGRADING SCHEDULE		4. PERFORMING ORGANIZATION REPORT NUMBER(S)	
5. MONITORING ORGANIZATION REPORT NUMBER(S)		6a. NAME OF PERFORMING ORGANIZATION Wright Laboratories Aero Propulsion & Power Dir.	
6b. OFFICE SYMBOL (If applicable) WL/POTT		7a. NAME OF MONITORING ORGANIZATION	
6c. ADDRESS (City, State, and ZIP Code) WL/POTT Wright-Patterson AFB OH 45433-7251		7b. ADDRESS (City, State, and ZIP Code)	
8a. NAME OF FUNDING/SPONSORING ORGANIZATION		8b. OFFICE SYMBOL (If applicable)	
8c. ADDRESS (City, State, and ZIP Code)		9. PROCUREMENT INSTRUMENT IDENTIFICATION NUMBER	
		10. SOURCE OF FUNDING NUMBERS	
		PROGRAM ELEMENT NO. 62203F	PROJECT NO. 3066
		TASK NO. 06	WORK UNIT ACCESSION NO. 14
11. TITLE (Include Security Classification) Influence of Fatigue Crack Closure on the Growth Rate of Surface Flaws			
12. PERSONAL AUTHOR(S) William A. Troha			
13a. TYPE OF REPORT Final	13b. TIME COVERED FROM Sep 82 TO May 88	14. DATE OF REPORT (Year, Month, Day) May 92	15. PAGE COUNT 335
16. SUPPLEMENTARY NOTATION			
17. COSATI CODES		18. SUBJECT TERMS (Continue on reverse if necessary and identify by block number)	
FIELD	GROUP	SUB-GROUP	
19. ABSTRACT (Continue on reverse if necessary and identify by block number)			
<p>Inconsistent experimental results of fatigue crack closure studies over the past 15 years have caused recent investigators to conclude that the fundamental phenomena controlling the crack driving mechanisms are not understood. A major contributor to this misunderstanding is an inadequate understanding of the complex three-dimensional nature of closure. This is true for two-dimensional thru-the-thickness cracks as well as for three-dimensional part-thru surface cracks.</p> <p>To assess the three-dimensional influences of fatigue crack closure on the growth rate of surface flaws, an experimental investigation was conducted using a rectangular plate of polymethylmethacrylate (PMMA) material loaded in four-point bending. The use of transparent PMMA material and a Newton optical interferometer system with a laser light source provided the capability to simultaneously measure three-</p>			
20. DISTRIBUTION/AVAILABILITY OF ABSTRACT <input checked="" type="checkbox"/> UNCLASSIFIED/UNLIMITED <input type="checkbox"/> SAME AS RPT. <input type="checkbox"/> DTIC USERS		21. ABSTRACT SECURITY CLASSIFICATION Unclassified	
22a. NAME OF RESPONSIBLE INDIVIDUAL William A. Troha		22b. TELEPHONE (Include Area Code) 513-255-2744	22c. OFFICE SYMBOL WL/POTT

BLOCK 19 (CONTINUED)

dimensional crack opening displacement (COD) profiles and closure loads (P_{c1}). Experimental results are presented for a constant load test, a variable block loading test, and two constant stress intensity factor tests controlled along the crack free-surface and into the specimen thickness.

The formation of a "void" area internal to the crack surfaces was found to be a major factor in defining three crack types which directly influenced COD, P_{c1} and fatigue crack growth. The three experimentally determined crack types and three distinct closure loads are used to establish corresponding definitions of effective stress intensity factor (ΔK_{eff}). In the closure load region, current prediction models are hypothesized to underestimate K along most of the crack tip boundary due to the different crack types. The crack P_{c1} , P_{c1}/P_{max} and fatigue crack growth rate (FCGR) data are presented as a function of crack length.

FCGR data are compared using applied ΔK and several definitions of ΔK_{eff} . Selection from several effective load ranges definitions for calculating ΔK_{eff} is based on the best correlation of FCGR data. The use of ΔK_{eff} for predicting fatigue cycles was found to be of superior accuracy over applied ΔK .

COD predictions for surface cracks using the weight function approach were found to underestimate displacement amplitude and to not adequately model profile distributions away from the crack tip.

Accession For	
NTIS GRA&I	<input checked="" type="checkbox"/>
DTIC TAB	<input type="checkbox"/>
Unannounced	<input type="checkbox"/>
Justification	
By _____	
Distribution/ _____	
Availability Codes	
Dist	Avail and/or Special
R'	

ACKNOWLEDGMENT

This research was initiated under the USAF Long-Term Full-Time Training Program, and represents partial fulfillment of a Doctoral degree at Purdue University. The research was conducted under the direction of Professor A. F. Grant at Purdue University, and Dr. Ted Nicholas at the Materials Behavior Branch, Materials Directorate, Wright Laboratory, Wright Patterson Air Force Base, Ohio. Although not all inclusive, I would like to recognize the following individuals who offered exceptional guidance, support, encouragement, advise and understanding during the years needed to complete this research.

To Professor A. F. Grandt, Jr., my Ph.D. advisor and research committee chairman, for his expert guidance and endless suggestions during the selection and development of this research. To my committee advisors: Professors C. T. Sun, B. M. Hillberry and M. D. Bowman for their many helpful suggestions.

To Professor Henry Yang (former committee member and Head of the Aeronautics and Astronautics Engineering School at Purdue, and current Dean of Engineering) for taking the time and having the interest to encourage me to stay at Purdue and finish my Ph.D. His interest and support, as he has provided to students over the years, were the deciding factors in my decision to continue "one more semester."

To Dr. Ted Nicholas, my mentor at the AF Materials Directorate during my research at WPAFB. For his exceptional guidance, technical insight and sharing of in-depth knowledge of fracture mechanics. For always taking the time to listen, and endless discussions concerning the observed phenomena. For being receptive to new ideas and providing essential stimuli to this investigation -- as he has provided that extra spark of enthusiasm to all investigators who have been fortunate to work with him.

To the talented group of scientists, engineers, technicians, secretaries and support personnel at the Materials Behavior Branch. Thanks to Dr. Jack Henderson, who headed the Branch during the time of my research, for his support and for making the work in his area such a rewarding experience. Thanks to Mr. Bob Tate for setting-up the laser interferometry system, Mr. Steve Russ for assisting in reducing portions of the experimental data, and to the many others too numerous to mention.

To my colleagues at the Air Force Aero Propulsion and Power Directorate of Wright Laboratory who assisted me by providing encouragement and valuable time. To Col. Jack Mattingly who provided inspirational leadership to myself and all Branch personnel. To Col. George Strand for encouragement and extending the opportunity to continue my technical education. To Diane Henn for being Diane, pulling us together. To Arlene Keller for her pleasant and energetic support in keeping the Branch functioning.

And last, but certainly not least, I dedicate this effort to my family and parents. To my mother who is always available to help no matter what the occasion or circumstance. To my father who encouraged me to continue my education. And especially to my children who endured me being away to accomplish this effort: Todd -- who was the mature man-of-the-house while I was away at school; Kris -- who always provides a pleasant smile and a warm disposition; and Shaye -- a charming daughter who is blossoming into a lovely young lady.

TABLE OF CONTENTS

LIST OF FIGURES	iv
LIST OF TABLES.....	xi
LIST OF SYMBOLS AND ABBREVIATION.....	xiii
I. INTRODUCTION.....	1
II. BACKGROUND.....	3
Fatigue Crack Growth and Closure.....	3
Surface Cracks	4
Closure Models	6
Plasticity-Induced Closure	7
Oxide-Induced Closure	15
Roughness-Induced Closure.....	15
Viscous Fluid-Induced Closure	17
Phase Transformation-Induced Closure.....	17
Crack Opening Displacement Measurements	18
Closure Observations.....	18
Closure Problem Areas.....	24
III. PROBLEM STATEMENT	27
Objective	27
Approach.....	28
Experimental Data Generation	31
Experimental Data Reduction	31
Experimental Data Analysis.....	32
IV. EXPERIMENTAL PROCEDURES.....	34
Test Procedures and Equipment.....	34
Newton Interferometry System	34
Digitizing Crack Displacement Profiles	43
X-Y Traveling Microscope	46
Fatigue Machine	46
Load History Selection	47
Plasticity Considerations.....	47
Isolating Plasticity Effects	50

Specimen Material Selection	59
Material Selection.....	60
Polymer Characteristics	63
Relaxation of PMMA	64
Specimen Preparation.....	68
Specimen Size	68
Specimen Annealing.....	70
Specimen Polishing	70
Crack Initiation Site.....	71
Precracking Procedures	72
Minimizing Precracking Influences	75
V. CRACK OPENING DISPLACEMENT AND CLOSURE LOAD MEASUREMENTS.....	77
Crack Opening Displacement (COD) Profiles	77
Typical COD Profiles.....	78
COD Profiles with Applied Load.....	85
COD Variation with Crack Size.....	89
COD Variation with Load History	97
Crack Compliance	103
Closure/Openning Loads	106
Closure Load Definitions.....	108
Closure Load Variations with Crack Size	113
Closure Load Variations with Load History.....	115
VI. EFFECTIVE STRESS INTENSITY FACTOR DEFINITIONS	130
Effective Stress Intensity Factor for a Type I Crack	132
Effective Stress Intensity Factor for a Type II Cracks.....	135
Effective Stress Intensity Factor for a Type III Crack.....	141
Closure Load Considerations.....	145
VII. EFFECTIVE STRESS INTENSITY FACTOR CORRELATION WITH FATIGUE CRACK GROWTH RATES	149
Closure Load Stress Intensity Factor	149
Effective Stress Intensity Factor Correlation	157
Fatigue Crack Growth Predictions.....	168
VIII. CRACK OPENING DISPLACEMENT PREDICTIONS USING WEIGHT FUNCTIONS.....	176
COD Predictions Versus Measurements	180
Displacement Profile Model Modifications	184
IX. SUMMARY, CONCLUSIONS AND RECOMMENDATIONS.....	185
Summary and Conclusions	185
Recommendations	189
LIST OF REFERENCES.....	191

APPENDICES.....	197
Appendix A	
Constant ΔK_a Test Data.....	197
Appendix B	
Constant ΔK_d Test Data.....	202
Appendix C	
Constant Load Test Data.....	208
Appendix D	
Block Loading Test Data	211
Appendix E	
Precracking Load Cycle Determination.....	215

LIST OF FIGURES

Figure		Page
2.1	Surface flawed fatigue crack specimen loaded in bending.....	5
2.2	Schematic illustration of the various mechanisms of fatigue crack closure (Ref. 4).....	8
2.3	Plastic wake and residual stresses developed on a growing fatigue crack during a constant amplitude cyclic load control test (Ref. 3).....	9
2.4	Shape of Plastic zone at the tip of a thru-thickness crack (Ref. 10)	9
2.5	Schematic of applied and effective stress intensity (ΔK_{eff}) load ranges (Ref. 3).....	11
2.6	Definition of closure stress intensity level using load versus displacement (P-V), or Load versus offset displacement (P - ΔV), plots. P_l represents the minimum load where the displacement is linear, and P_{cl} the tangents of two intersections on the P - V plot (Ref. 3).....	13
2.7	Effect of load ratio (R) on fatigue crack growth rate da/dN (a) without closure and (b) with closure load influences (Ref. 3)	14
2.8	Variation in fatigue crack propagation rate with (a) nominal ΔK and (b) effective stress intensity ΔK_{eff} range values for a 0.17% C steel. Data points represent short cracks emanating from notches as compared to long crack da/dN data represented by the solid line (Ref. 4).....	16
2.9	Schematic of the Newton interferometry method for generating fringe patterns from crack opening displacements (Ref. 19).....	19
2.10	Comparison of surface and center fatigue crack opening displacement profiles at various tensile loads for a thru-thickness crack in a PMMA specimen (Ref. 19).....	21
2.11	Schematic of the closure contact areas of thru-thickness crack opening displacement patterns using fractographic measurements in metals (Ref. 21).....	22

Figure		Page
3.1	Surface crack schematic showing locations A, B, C and D reference points, and angle ϕ	29
3.2	Block diagram of the experimental test and data analysis.....	30
4.1	Experimental arrangement of the MTS electro-hydraulic controller, load frame with the specimen in a four-point bending fixture, and the laser powered interferometry system.....	35
4.2	Newton interferometry arrangement using a laser light source which reflects off the surface crack as shown (a) schematically and (b) pictorially with the laser, reflecting mirrors, beam splitter, bellows and 35mm camera mounted on an adjustable baseplate.....	37
4.3	Surface crack schematic of a void formation internal to the crack surface.....	39
4.4	Interferometry fringe pattern photos showing various stages of crack opening displacement at various applied loads levels: (a) zero load, (b) 1/2 of the fully-open load, (c) 3/4 of the fully-open load, and (d) fully-open load	41
4.5	Experimental setup for digitizing the fringe order using a photo enlarger and digitizing board	44
4.6	Surface flaw crack opening displacement pattern for half the crack displacement along the $\phi = 90$ degree line for various loads in the closure load region	45
4.7	Actual load shedding pattern, and constant stress intensity factor calculated at the crack tip free-surface (ΔK_d , $\phi=0$ degrees), to maintain a constant plastic zone wake.....	51
4.8	Schematic of the plasticity induced wake and residual plastic zone developed from a growing fatigue crack during a constant stress intensity factor cyclic load test in a thru-thickness specimen.....	52
4.9	Actual load shedding pattern, and constant stress intensity factor calculated at the crack tip internal to the specimen thickness (ΔK_a , $\phi=90$ degrees), to maintain a constant plastic zone wake.....	54

Figure		Page
4.10	Actual applied constant load, and variable stress intensity factor calculated at the crack tip free-surface (ΔK_d , $\phi=0$ degrees), to generate a continually increasing plastic zone wake.....	55
4.11	Schematic representation of continually increasing plastic wake generated by growing a fatigue crack during a constant amplitude cyclic load control test (Ref. 3).....	56
4.12	Actual block loading pattern, and resulting stress intensity factor calculated at the crack tip free-surface (ΔK_d) to generate large plastic-zone wakes.....	57
4.13	Fatigue crack growth rate curves for several engineering polymers; curves for polymethylmethacrylate (PMMA), low density polyethylene (LDPE), acrylonitrile-butadiene-styrene resin (ABS), polycarbonate (PC), and nylon 66 (Ref. 32)	61
4.14	Fatigue crack growth rate curve for PMMA (Ref. 19).....	62
4.15	Interference fringe order traces showing relaxation effects immediately after test cycling (solid contours lines), and after 15 minutes hold time (dotted lines) for (a) high aspect ratio crack ($a=0.12$, $c=0.14$), at 17% of the maximum applied load, and (b) a low aspect ratio crack crack ($a=0.19$, $c=0.30$) at zero load	66
4.16	Photograph of the PMMA specimen before testing. Note the polished end and crack initiation site located in the specimen center	69
4.17	Cross-section schematic of the symmetrical crack initiation site showing the cutting tool radius of curvature	73
5.1	Surface crack schematic showing a void formation internal to the crack surface.....	79
5.2	Schematic of the crack opening displacement patterns under zero load for the three crack types - type I, II & III	80
5.3	Cross-section schematic of the crack opening displacement pattern under zero load for the three crack types between location A & B ($\phi=90$ & 0 degrees, respectively)	82

Figure		Page
5.4	Schematic of the crack opening displacement patterns as load is applied to a type II crack from zero load at (a) to a load level where the crack is completely open at (e)	86
5.5	Interference photograph of the crack surface displacement at (a) near zero load showing the internal void formation for a type III crack (Ref. Figure 5.4b), and (b) for a fully-open crack in the closure load region showing the minimum displacement at location C, $\phi=12$ to 15 degrees (Ref. Figure 5.4d)	88
5.6	Surface flaw crack opening displacement pattern for half the crack displacement for various loads in the closure load region of the constant ΔK_d eff test($\phi=90$ degrees)	90
5.7	Schematics of the COD pattern for defining the "void" displacement δ , Δ_1 and Δ_2 distances from the crack tip	92
5.8	Location of the void maximum displacement for various crack sizes under zero load	94
5.9	Changes in void maximum displacement for two crack sizes and at several applied moments	96
5.10	Measured crack aspect ratio (a/c) versus a/t size of four tests. The circle identifies a common crack size used to compare COD and closure loads	101
5.11	Void maximum displacement pattern at several load levels for three load histories at a common crack size. Numbers in parentheses represent applied moments	102
5.12	Load versus displacement comparison of the four load histories (constant ΔK_d , ΔK_a & load) at a common crack size	104
5.13	Load versus displacement plot to compare the COD patterns measured at various distances from the crack tip along the $\phi=90$ degree line	105
5.14	Load versus displacement plot at the crack face (location B, $\phi=90$ degrees) as a function of crack size	107

Figure		Page
5.15	Typical crack opening displacement fringe pattern with applied load. The three closure/opening loads are defined as aPop, bPop, and cPop at locations A, B and C.....	109
5.16	COD profiles along line AB ($\phi=90$ degrees) at various loads to correlate closure loads with opening patterns.....	110
5.17	Schematic COD profiles between locations A & B ($\phi=90$ degrees) for the three crack types at zero load, and the three closure load levels (aPop, bPop & cPop)	112
5.18	Closure load (aPop, bPop & cPop) variation with crack size (a/t) from the constant ΔK_d test	114
5.19	Closure to maximum load ratios plotted as a function of crack size (a/t) (a/t) from the constant ΔK_d test	116
5.20	Closure load (aPop, bPop & cPop) as function of crack size (a/t) from the constant ΔK_a test	117
5.21	Closure load (aPop, bPop & cPop) as function of crack size (a/t) from the constant load test	118
5.22	Closure load (aPop, bPop & cPop) as function of crack size (a/t) from the block loading test	119
5.23	Comparison of the c P_{Op} closure loads for all four tests as a function of crack size (a/t)	120
5.24	Comparison of the b P_{Op} closure load for all four tests as a function of crack size (a/t)	121
5.25	Comparison of the aPop closure load for all four tests as a function of crack size (a/t)	122
5.26	Comparison of the c P_{Op}/P_{max} closure ratio as a function of crack size	123
5.27	Comparison of the b P_{Op}/P_{max} closure ratio as a function of crack size	124
5.28	Comparison of the a P_{Op}/P_{max} closure ratio as a function of crack size	125

Figure		Page
6.1	Schematic representation of K as a function of applied load for a type I crack at location A or C	134
6.2	Schematic of load versus displacement at the crack free-surface to relate closure load regions (1,2,3) from Figure 6.1 for a type I crack	136
6.3	Schematic representation of K as a function of applied load for a type II crack at location A ($\phi=90$ degrees). Three potential ΔK_a eff definitions are represented	137
6.4	Schematic of load versus displacement at the crack free-surface to relate closure load regions (1,2,3,4) to Figure 6.3 for a type II crack	140
6.5	Schematic representation of K as a function of applied load at location C ($\phi=12$ degrees) for three crack types	142
6.6	Schematic representation of K as a function of applied load for a type III crack at location A ($\phi=90$ degrees). Three potential ΔK_a eff definitions are represented	143
7.1	Stress intensity factors at the crack tip free-surface ($\phi=0$ degrees) due to the cPop closure load level as a function of crack size (a/t) for all tests	152
7.2	Stress intensity factors at the crack tip free-surface ($\phi=0$ degrees) due to the bPop closure load level as a function of crack size (a/t) for all tests	153
7.3	Stress intensity factors into the specimen thickness at the crack tip ($\phi=90$ degrees) due to the cPop closure load level as a function of crack size (a/t)	154
7.4	Stress intensity factors into the specimen thickness at the crack tip ($\phi=90$ degrees) due to the bPop closure load level as a function of crack size (a/t)	155
7.5	Crack growth rate at location A (da/dN) due to the nominal applied load ($K_{max} - K_{min}$) for all four test cycles.....	158
7.6	Crack growth rate at location C (dc/dN) due to the nominal applied load ($K_{max} - K_{min}$) for all four test cycles	159

Figure		Page
7.7	Crack growth rate at locations A (da/dN) and C (dc/dN) due to the nominal load ($K_{max} - K_{min}$) for all four test cycles	160
7.8	Crack growth rate at location A (da/dN) due to the effective load ($\Delta K^b_{a cl}$) for all four test cycles	161
7.9	Crack growth rate at location A (da/dN) due to the effective load ($\Delta K^c_{a cl}$) for all four test cycles	162
7.10	Crack growth rate at location C (dc/dN) due to the effective load ($\Delta K^b_{c cl}$) for all four test cycles	163
7.11	Crack growth rate at location C (dc/dN) due to the effective load ($\Delta K^c_{c cl}$) for all four test cycles	164
7.12	Crack growth rate at location A (da/dN) and C (dc/dN) due to the effective load (ΔK^b_{cl}) for all four test cycles.....	165
7.13	Crack growth rate at location A (da/dN) and C (dc/dN) due to the effective load (ΔK^c_{cl}) for all four test cycles.....	166
7.14	Comparisons of predicted and experimental crack growth patterns for the constant ΔK_d test	173
8.1	Comparison of experimental and analytical predictions of crack opening displacement profiles at three load levels. The crack tip into the specimen depth is at $r/a=0$, and the crack free-surface at $r/a=1$	181
8.2	Comparison of experimental and analytical predictions on a load-displacement plot for the same crack size as Figure 8.1	183

LIST OF TABLES

Table		Page
2.1	Summary of closure ratio and closure parameters (U) values	24
5.1	Crack Size when Transition Occurs Between Crack Types I and II, and Crack Types II and III.....	83
5.2	Range of Measured Crack Size for the Three Crack Types	84
5.3	Constant ΔK_d Test Effects on the Void Maximum Displacement Location with <u>Zero Load</u>	91
5.4	Void Maximum Displacement Location for a Constant ΔK_d Test Effects with an <u>Applied Load</u>	95
5.5	Void Maximum Displacement Location for a Constant ΔK_a Test Effects with an <u>Applied Load</u>	98
5.6	Void Maximum Displacement Location for a Constant Load Test with an <u>Applied Load</u>	99
5.7	Void Maximum Displacement Location for a Block Loading Test with an <u>Applied Load</u>	100
5.8	Closure Load Values at a Common Crack Size ($a=0.14$, $c= 0.20$)	129
6.1	Hypothesized Closure Load and K-Solution Needs to Define ΔK_{eff} at Crack Tip <u>Location A</u>	146
6.2	Hypothesized Closure Load and K-Solution Needs to Define ΔK_{eff} at Crack Tip <u>Location C</u>	146
7.1	Closure Stress Intensity Factor (K_{cl}) Variables Used to Evaluate Several ΔK_{eff} definitions.....	150
7.2	Polynomial Coefficients for $K_c^c cl$ as a Function of a/t (Figure 7.1).....	156
7.3	Polynomial Coefficients for $K_c^b cl$ as a Function of a/t (Figure 7.2)	156
7.4	Polynomial Coefficients for $K_a^c cl$ as a Function of a/t (Figure 7.3).....	156

Table		Page
7.5	Polynomial Coefficients for $K^b_{a/c}$ as a Function of a/t (Figure 7.4)	157
7.6	Comparison of fatigue crack growth predictions using a "Round Robin" experimental data set and the Newman-Raju K-solutions.....	170
7.7	Comparison of Experimental and Predicted Fatigue Crack Growth Patterns and Cycles Using Uncorrected and Corrected Paris Law Constants	172
7.8	Comparison of Experimental and Predicted FCG Using an Assumed Constant P_{cl}/P_{max} Value for Surface Flaws	174

LIST OF SYMBOLS AND ABBREVIATION

a	Depth of surface crack (in)
a/c	Crack aspect ratio
aP_{op}	Crack closure/opening load at location A (lbs)
aP_{op}/P_{max}	Closure load ratio for aP_{op}
bP_{op}	Crack closure/opening load at location B (lbs)
bP_{op}/P_{max}	Closure load ratio for bP_{op}
c	Half-length of the surface crack free-surface (in)
cP_{op}	Crack closure/opening load at location C (lbs)
cP_{op}/P_{max}	Closure load ratio for cP_{op}
d	Half the distance between crack surfaces (in)
da/dN	Fatigue crack growth rate in the 'a' direction (in/cycle)
dc/dN	Fatigue crack growth rate in the 'c' direction (in/cycle)
K	Stress intensity factor for mode I crack (psi $\sqrt{\pi}$ in)
K_0	Stress intensity factor at $f = 0$ degrees
K_{90}	Stress intensity factor at $f = 90$ degrees
K_a	Stress intensity factor at crack tip location A (ref. figure 3.1)
K_c	Stress intensity factor at crack tip location C (ref. figure 3.1)
K_{cl}	Crack closure stress intensity factor (psi $\sqrt{\pi}$ in)
$K_{a cl}^b$	Closure load K at crack tip location A due to bP_{op}
$K_{a cl}^c$	Closure load K at crack tip location A due to cP_{op}
$K_{c cl}^b$	Closure load K at crack tip location C due to bP_{op}
$K_{c cl}^c$	Closure load K at crack tip location C due to cP_{op}

K_d	Stress intensity factor at crack tip location D (ref. figure 3.1)
ΔK_{eff}	Effective stress intensity factor $K_{max} - K_{cl}$ (psi $\sqrt{\pi}$ in)
$\Delta K_{a\ eff}^b$	ΔK_{eff} at crack tip location A due to bPop
$\Delta K_{a\ eff}^c$	ΔK_{eff} at crack tip location A due to cPop
$\Delta K_{c\ eff}^b$	ΔK_{eff} at crack tip location C due to bPop
$\Delta K_{c\ eff}^c$	ΔK_{eff} at crack tip location C due to cPop
K_{max}	Maximum value of K reached during fatigue cycling (psi $\sqrt{\pi}$ in)
K_{min}	Minimum value of K reached during fatigue cycling (psi $\sqrt{\pi}$ in)
ΔK	Range in stress intensity factor during fatigue cycling -- $K_{max} - K_{min}$ (psi $\sqrt{\pi}$ in)
K_{op}	Crack opening stress intensity factor (psi $\sqrt{\pi}$ in)
M	Nominal applied bending moment (in-lbs)
N	Number of fatigue cycles
h	Fringe order numbers: 1,2,3,....
P_{cl}	Nominal applied closure load (lbs)
P_{max}	Maximum applied load during fatigue cycling (lbs)
P_{min}	Minimum applied load during fatigue cycling (lbs)
PMMA	Polymethylmethacrylate polymer
R	Stress ratio (P_{min} / P_{max})
r_p	Plastic zone size
t	Specimen thickness (in)

tP_{op}	Nominal transition load which defines elastic opening displacement
U	Closure parameter $(K_{max} - K_{cl})/(K_{max} - K_{min})$
U_a	Closure parameter where K_{cl} is a function of aP_{op}
U_b	Closure parameter where K_{cl} is a function of bP_{op}
U_c	Closure parameter where K_{cl} is a function of cP_{op}
ν	Poisson's ratio
λ	Laser light source wave length (\AA) of the Newton interferometry fringe order measurement system
f	Angle of rotation from the crack free-surface about the crack middle point (not elliptical angle) -- ref. figure 3.1
s_{ys}	Material yield strength (psi)
s_{max}	Maximum applied stress (psi)

I. INTRODUCTION

The phenomena of fatigue crack closure was originally investigated by Elber (1) in the early 1970's. His discovery that the crack remains closed during the initial portion of the load cycle led to the definition of an "effective" load range, as opposed to the applied load range, for predicting fatigue crack growth behavior. In effect, the applied load range is reduced by the closure load level, thus defining an effective stress intensity factor range. Elber later utilized this closure information to develop representative models for predicting fatigue crack growth. According to Paris (2), understanding of this observation has the potential for contributing significant insight into explaining observed crack growth behavior. This statement by Paris places significant emphasis on conducting a thorough and complete investigation into all aspects of closure.

With an increased understanding of the closure phenomena, it has become evident that a consistent set of definitions of terms such as, closure load level, crack opening displacement profiles and the inherent effective stress intensity factor has not been established because of the complex nature of closure. This is a major problem area which has caused inconsistencies in generating experimental data and evaluation of results. Several technical reviews on closure, such as those by Banerjee (3), and Suresh and Ritchie (4), have identified the need to establish a cohesive closure data base utilizing a consistent set of definitions.

The selection of surface flaws (part-thru-cracks) for this investigation of closure effects on fatigue crack growth rate was based on its occurrence in many engineering applications. Although a common crack type, the amount of crack closure information available on surface flaws in comparison to thru-thickness cracks is relatively small. This is due to the three-dimensional complexities of surface flaw crack opening displacement (COD) patterns, the difficulty of measuring COD experimentally, and the lack of usable stress intensity factor solutions around the crack boundary.

The three-dimensional aspects of closure in surface flaws impose major measurement restrictions in metals since only the crack face is directly visible. Typical closure and fatigue crack growth (FCG) measurement techniques used in the past have not provided real-time information, but required data to be analyzed at the end of a test (such as with heat tinting and crack replication) or utilized analytical representations of crack opening displacements (such with compliance gauges). The use of a transparent material in this investigation solves many of these problems.

II. BACKGROUND

The following sections present a background review of prior experimental and analytical investigations of closure, surface flaws, and the use of closure for predicting fatigue crack growth.

Fatigue Crack Growth and Closure

The fracture mechanics concept of plasticity-induced fatigue crack closure was originally introduced by W. Elber (1) some 20 years ago. In essence, Elber found that cracks do not open elastically under applied load, but are held closed by some mechanism which he termed crack closure. He determined that the closure load of an aluminum panel with a cracked hole could be as much as 50% of the applied loading amplitude, leaving this range of the load cycle ineffective for growing the crack. The closure concept initially gained widespread popularity in the fracture mechanics community because of its potential to predict fatigue crack retardation. After years of research, interest in the closure concept began to waver in the late 70's because of a lack of progress in sorting out the many variables.

The importance of closure for predicting fatigue crack growth has gained renewed enthusiasm in recent years as a result of new findings. This rekindling of interest has come about because of a better understanding of the implications of closure and because of an expansion of theoretical closure models. As was stated by Paris (2), closure is "the most central question still to be resolved" in the area of fatigue crack growth. This is a strong statement coming from a scientist who has made significant contributions to validate the use of the stress intensity factor (K) in crack growth analysis. In reference to closure, Paris describes it as "simply good luck" that the usefulness of K was not eliminated because the

closure phenomena had been overlooked. In a recent paper by Paris, "Twenty Years of Reflection on Questions involving Fatigue Crack Growth," he concluded:

It seems that crack closure reappears as a key factor and that methods must be found to analyze it or a new fundamental way of avoiding it in analysis needs to be formulated. It is viewed by this author as raising the most central question still to be resolved. It seems difficult to avoid concluding that crack closure is a key physical phenomenon in the fatigue cracking process.

The relationship for fatigue crack growth (FCG) rate was given by Paris as:

$$da/dN = C (\Delta K)^n \quad (2.1)$$

and modified by Elber to include the closure parameter U (discussed later), such that:

$$da/dN = C (U \Delta K)^n \quad (2.2)$$

$$= C (\Delta K_{eff})^n \quad (2.3)$$

where C and n are material constants, and ΔK the cyclic change in stress intensity factor.

Surface Cracks

A great deal of fracture mechanics technology is based on experimental evidence using two-dimensional through-the-thickness crack specimens and stress intensity factor solutions. Although surface cracks (Figure 2.1) represent the most common natural defect shape for crack initiation and propagation, analytical modeling complexities have caused investigators to work with the more manageable thru-crack configuration. The complexities of modeling surface crack stress intensities arise from its three-dimensional characteristics,

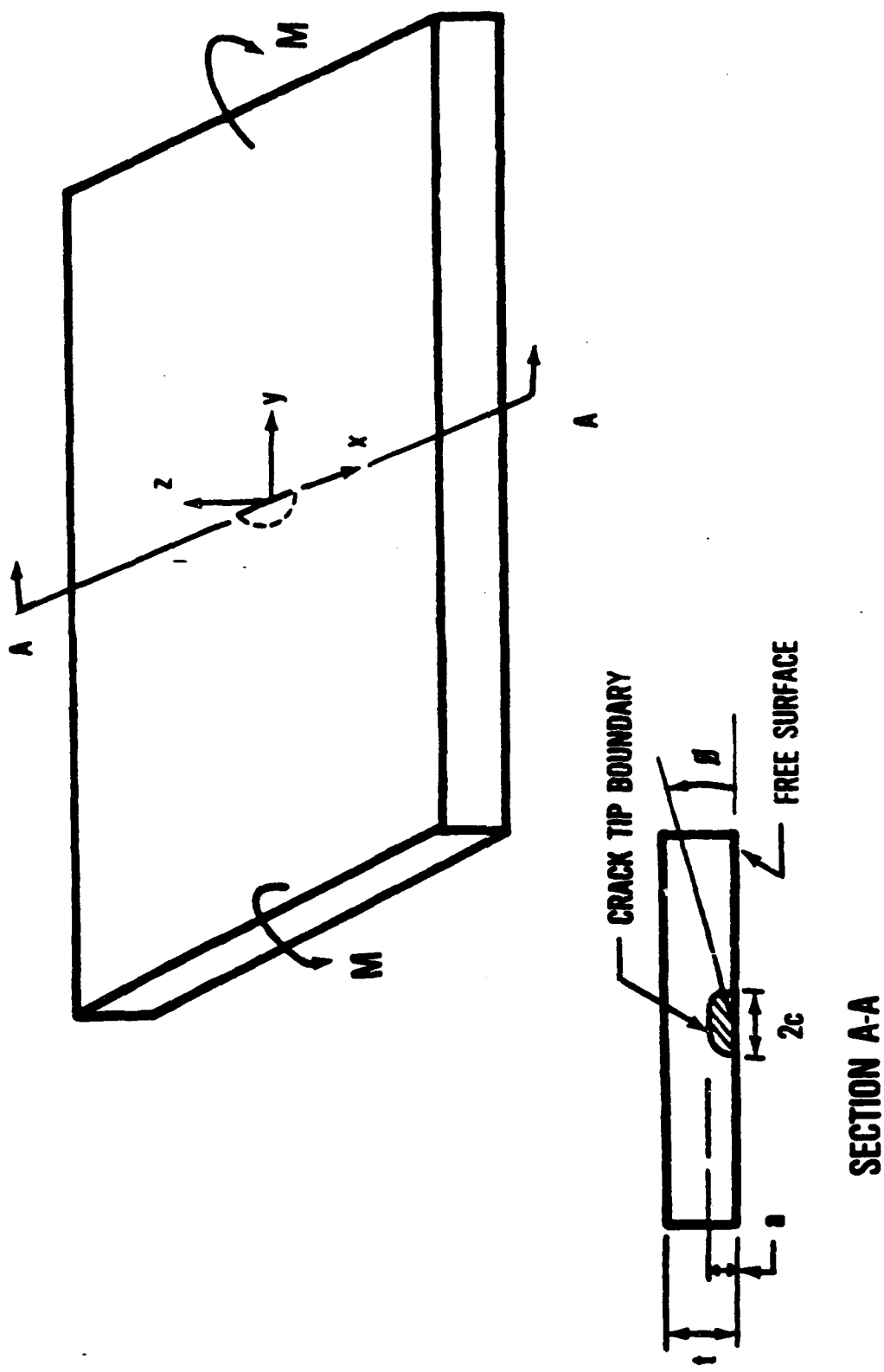


Figure 2.1 Surface flawed fatigue crack specimen loaded in bending

such as constantly changing stress field and stress intensity factor around the crack tip perimeter, changing crack aspect ratio (a/c) during crack growth, and a lack of available closed-form stress intensity factor solutions.

The lack of a useful surface flaw stress intensity factor solution has been a major reason for the scarcity of experimental fatigue crack growth data. In recent years, this condition has improved with the introduction of stress intensity factor solutions for surface flaws in cracked plates. One of the more popular solutions was presented by Newman and Raju (5), who utilized finite element calculations to develop empirical relationships for numerous crack configurations. These correlation's were developed for both tension and bending -- using parameters such as crack depth (a) and length (c), plate thickness (t) and width (b), and angular location around the crack perimeter (ϕ).

Orange's (6) report to the ASTM Task Group E24.01.05 on "Part-Through Crack Testing" also identified a general lack of experimental data on surface flaws. His conclusions were based on a survey questionnaire of the major aircraft companies, NASA, and the Atomic Energy Commission. In a November 1984 telephone conversation, he reiterated that besides the introduction of stress intensity factor solutions, little had been accomplished since 1975 to change his original recommendations.

Closure Models

The physical representation of closure is based on five fundamental models: the original plasticity-induced closure model, and four recent models which have developed from microscopic descriptions of crack surfaces. These five closure models constituted a growing awareness of closure complexities, and provide a brief insight as to why the fracture mechanics community has struggled to quantify closure relationships to crack growth. The four recent models have been shown to be of particular importance in the near-threshold

region, and are identified as oxide-induced, roughness-induced, viscous fluid-induced and phase transformations-induced. Each model type is represented schematically in Figure 2.2 and briefly described in the following paragraphs.

Plasticity-Induced Closure

The Elber plasticity-induced closure model (Figure 2.2a) is characterized by the development of a plastic zone around the crack tip, and subsequent growth of the fatigue crack thru this plastic zone. This zone is described as a residual "wake" of plastically deformed material around the crack face (Figure 2.3) which produces the crack closure effect. The approximate size of the plastic zone at the crack tip was originally modeled by Irwin (7) as circular, and later by Dugdale (8) as a narrow strip. The plastic zone radius (r_p) was represented by Irwin for plane stress as:

$$r_p = [K / \sigma_{ys}]^2 / 2\pi \quad (2.4)$$

and for plane strain as:

$$r_p = [K / \sigma_{ys}]^2 / 6\pi \quad (2.5)$$

where K is the mode I stress intensity factor and σ_{ys} the material yield strength.

When a three-dimensional stress field is modeled by using the Tresca or von Mises relationships, the crack tip plastic zone is more complex than a circular or narrow strip, forming a kidney shape. Banks and Garlick (9) present a detailed discussion of three-dimensional plastic zones for both plane stress and plane strain in isotropic and anisotropic materials. Since K is a direct function of stress, Figure 2.4 reflects the general shape of a

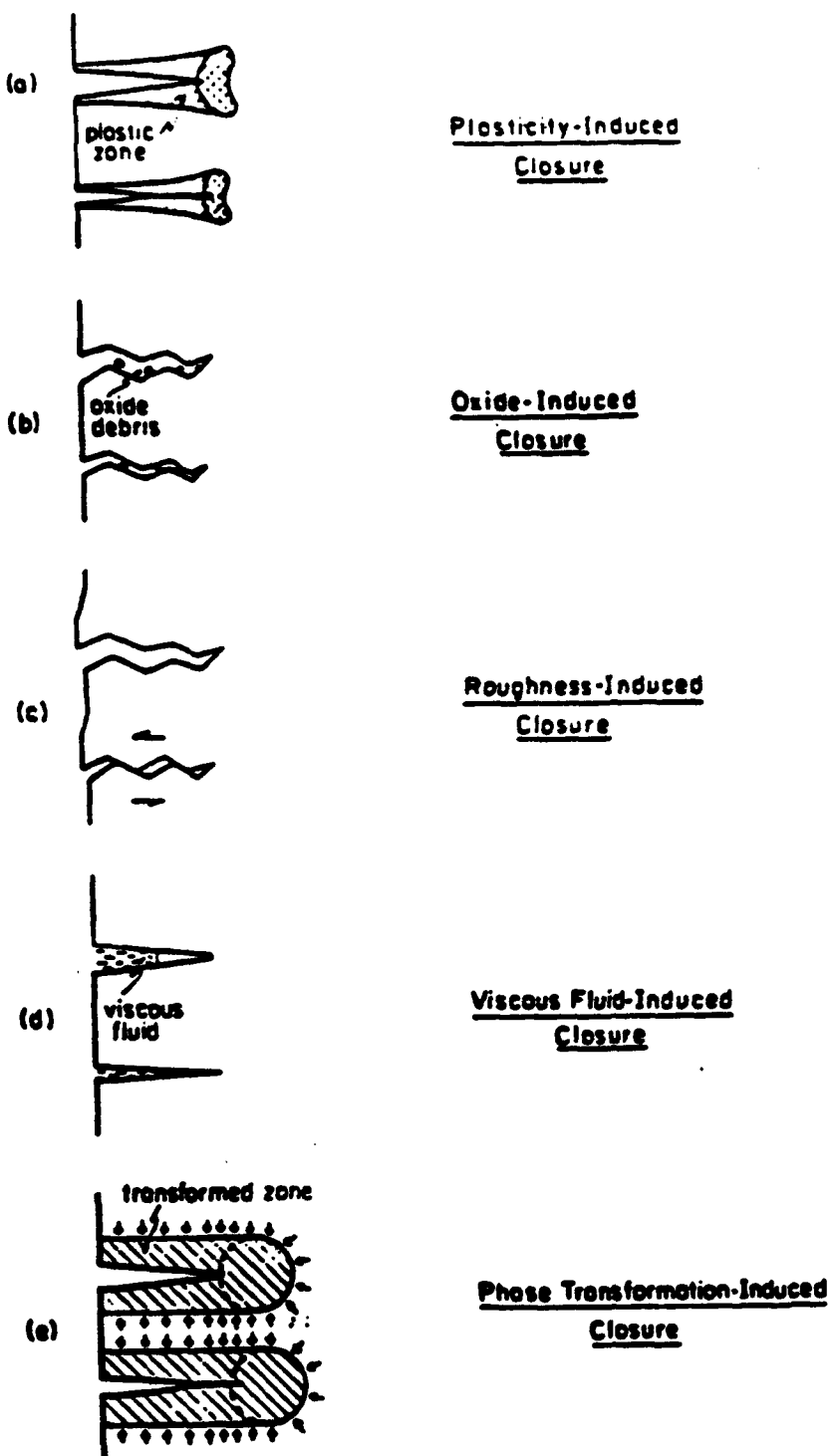


Figure 2.2 Schematic illustration of the various mechanisms of fatigue crack closure (Ref. 4)

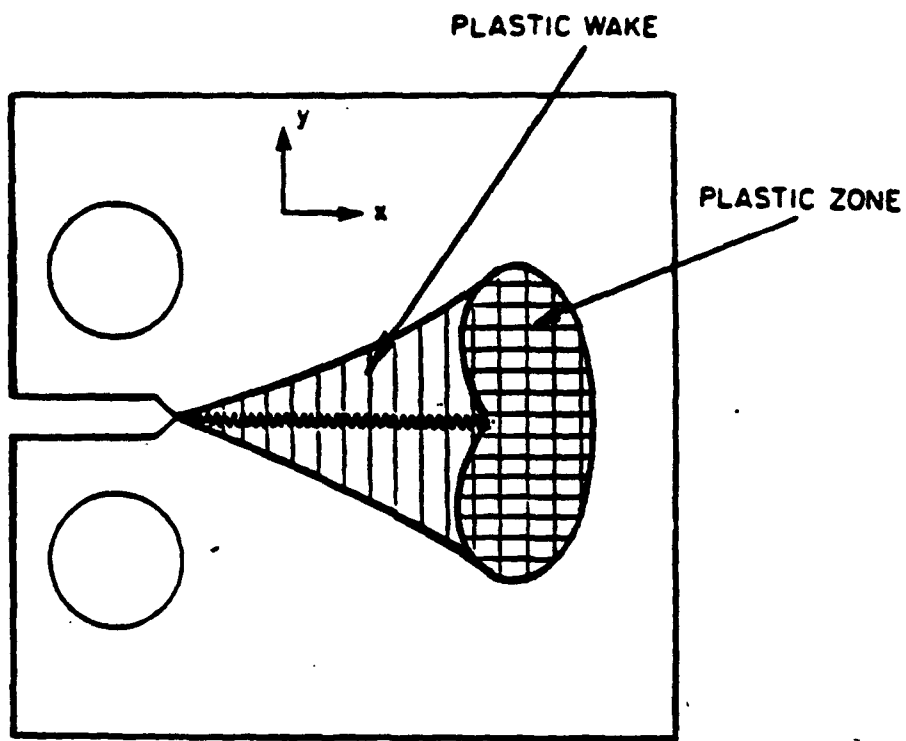


Figure 2.3 Plastic wake and residual stresses developed on a growing fatigue crack during a constant amplitude cyclic load control test (Ref. 3)

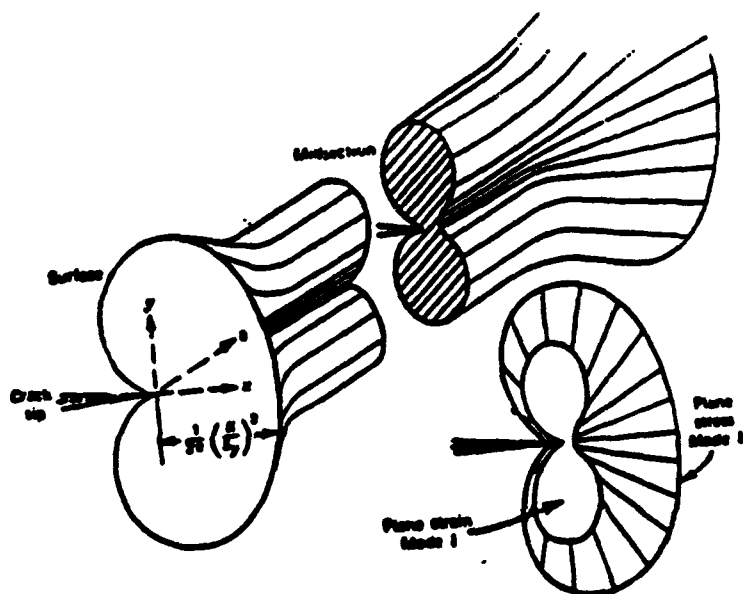


Figure 2.4 Shape of Plastic zone at the tip of a thru-thickness crack (Ref. 10)

thru-the-thickness yield surface where the most yielding occurs at the free surface (plane stress, $\sigma_z = 0$), while a smaller yield zone is present at the middle of the specimen (plane strain, $\epsilon_z = 0$).

As an expansion to his original closure model, Elber (11) presented an analytical relationship to account for mean stress (quantified by the stress ratio, R) influence on closure loads in aluminum. This approach led Elber to define an effective stress intensity factor (ΔK_{eff}) which is related to fatigue crack growth rate (da/dN) by an effective stress intensity factor closure parameter (U) and the applied cyclic stress intensity factor (ΔK) such that:

$$da/dN = C(U \Delta K)^n = C(\Delta K_{eff})^n \quad (2.6)$$

where:

$$\Delta K_{eff} = U \Delta K = K_{max} - K_{cl} \quad (2.7)$$

and C and n are empirical material constants determined from the Paris da/dN versus ΔK fatigue crack growth curve. The effective stress intensity factor closure parameter is defined as:

$$U = \frac{K_{max} - K_{cl}}{K_{max} - K_{min}} = \frac{K_{max} - K_{cl}}{\Delta K} \quad (2.8)$$

Here K_{max} , K_{min} and K_{cl} or K_{op} (Figure 2.5) are the maximum, minimum and closure stress intensity factors, respectively. In effect, if K_{cl} is larger than K_{min} , the usable ΔK for growing the crack is reduced, thus reducing the fatigue crack growth rate.

The terms opening and closure stress intensity factor (K_{op} or K_{cl} , respectively) are often used interchangeably in the literature, although there are important differences between

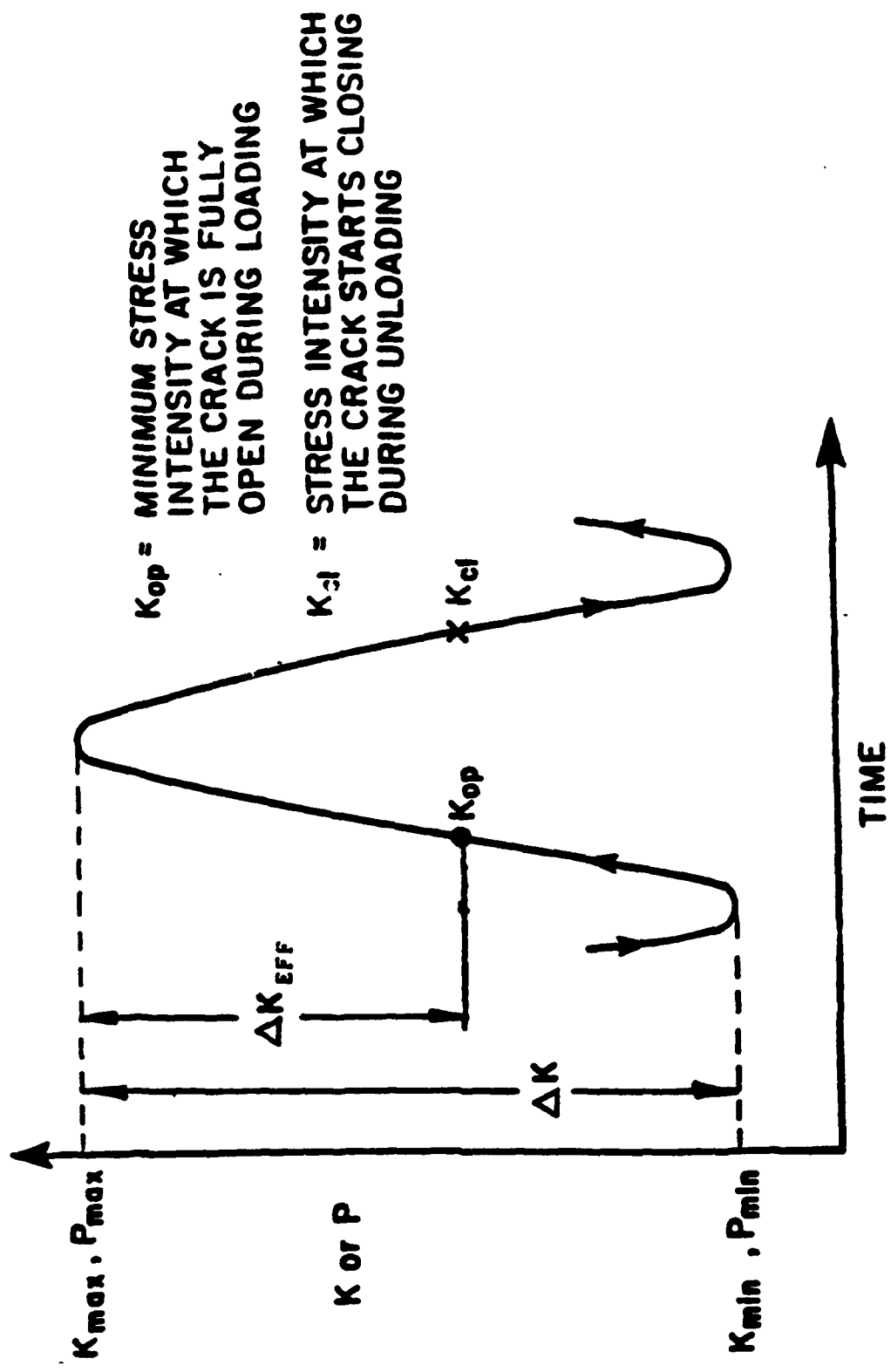


Figure 2.5 Schematic of applied and effective stress intensity (ΔK_{eff}) load ranges (Ref. 3)

the two. K_{op} is used to define closure when load is applied to the specimen (increased loading) whereas K_{cl} is used when the specimen is unloaded (decreased loading). Although the closure stress intensity factor (K_{cl}) and opening stress intensity factor (K_{op}) have different definitions, they have been reported to be approximately equal (3). As a general guideline, most researchers agree that the opening load should be used to determine ΔK_{eff} for fatigue crack growth calculations instead of the closure load. This is based on the crack tip opening (versus closing) being a primary driving mechanism for fatigue crack growth. All values reported in this investigation are opening loads, unless specifically stated to be a "closure" load for comparison purposes. Otherwise, the term closure and opening load may be used interchangeably.

For 2024-T3 aluminum, Elber determined that U was related to the stress ratio R (where $R = P_{min}/P_{max}$) as:

$$U = 0.5 + 0.4R \quad (2.9)$$

for $-0.1 < R < 0.7$. Since its original introduction, the coefficients of this formulation for aluminum have changed, but the general approach for modeling the effective stress intensity factor is being used today.

The generally-agreed-upon experimental definition of closure can be seen in Figure 2.6, where applied load is plotted against crack opening displacement (V) or offset displacement (ΔV). The load versus displacement measurement is typically generated using a clip gauge attached to the crack face, or more recently by using an optical interferometry system (12, 13, 14). The offset displacement definition of closure is considered more sensitive to data deviations with experimenters using the interferometry systems (15). The effective load range associated with equation 2.7 is defined by $(P_{max} - P_{cl})$ or $(P_{max} - P_l)$.

Two examples of the usefulness of crack closure can be seen by reviewing Figures 2.7a and 2.7b. Figure 2.7a shows the direct relationship of stress ratio (R) to fatigue crack

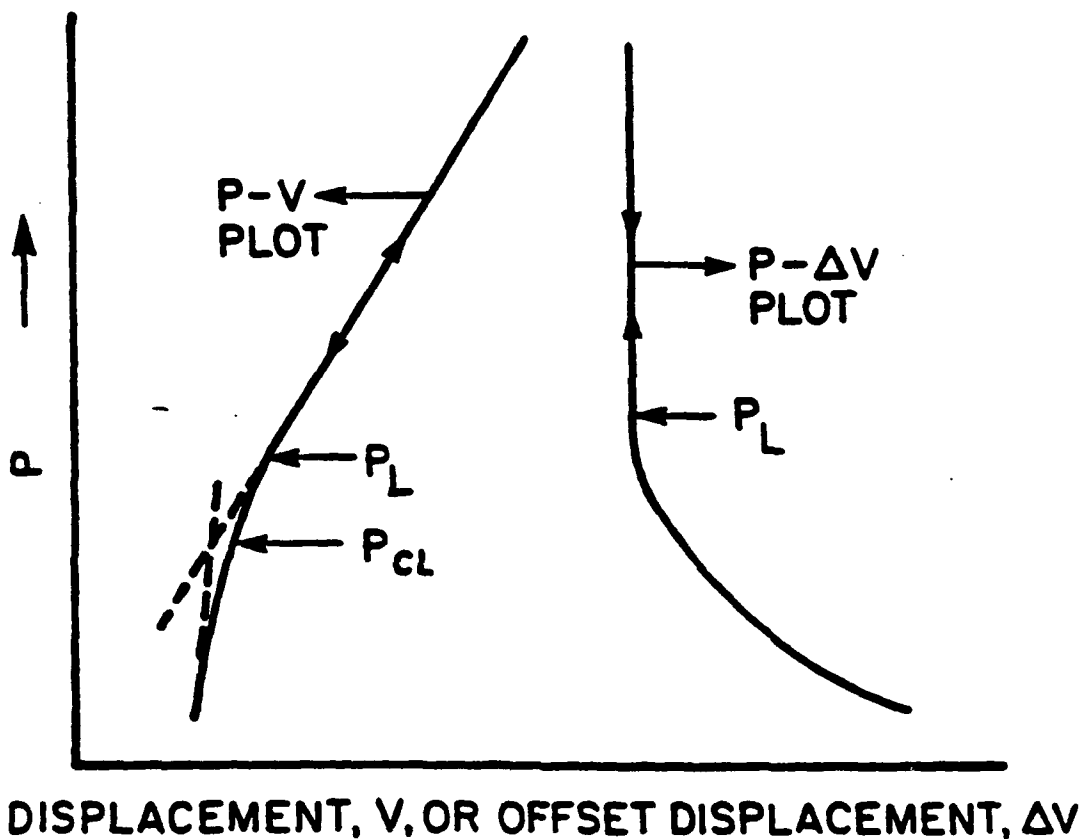


Figure 2.6 Definition of closure stress intensity level using load versus displacement (P - V) or Load versus offset displacement (P - ΔV) plots. P_l represents the minimum load where the plots are linear, and P_{cl} the load where the two tangents on the P - V plot intersect (ref. 3)

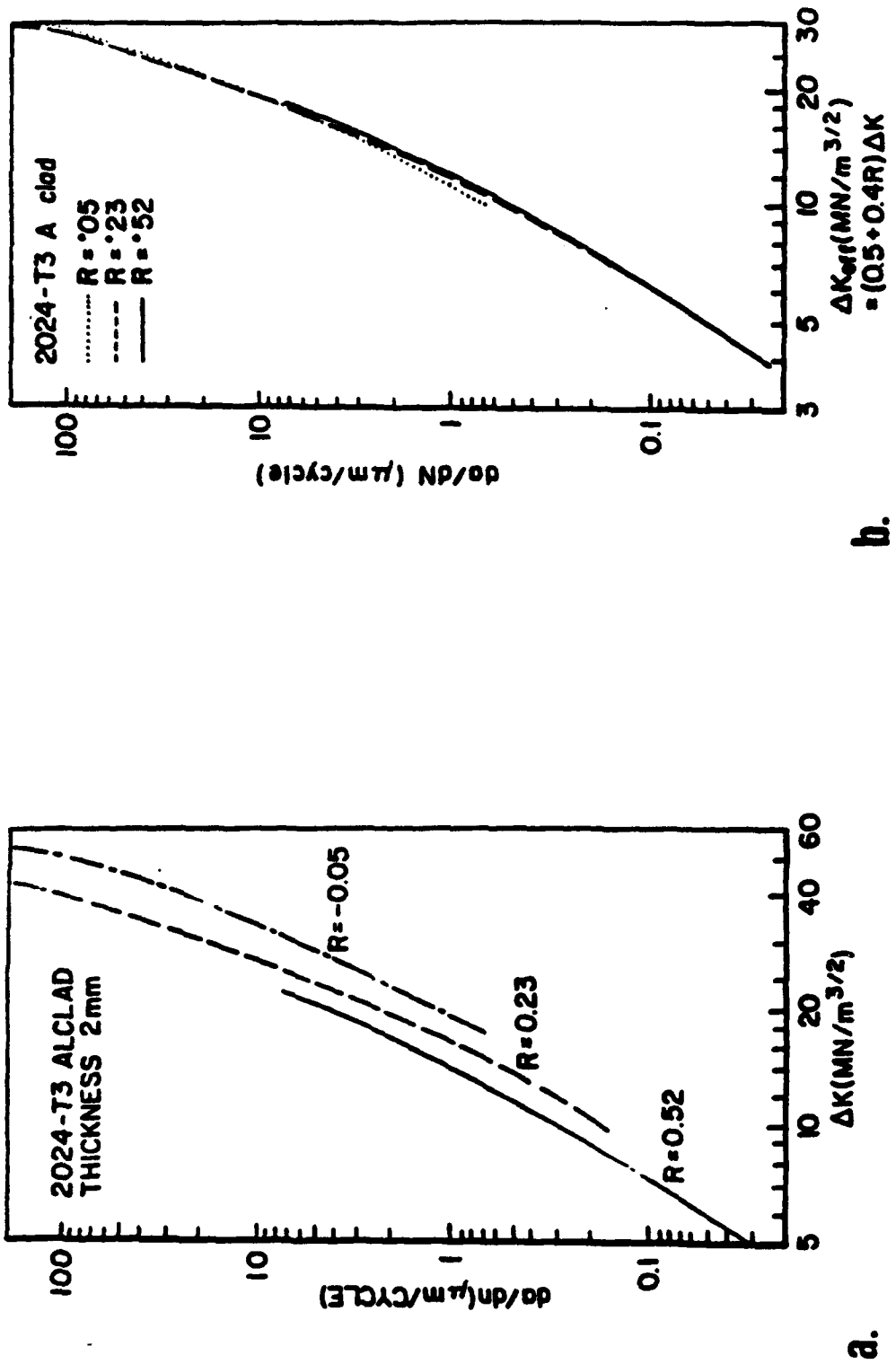


Figure 2.7 Effect of load ratio (R) on fatigue crack growth rate da/dN (a) without closure and (b) with closure load influences (Ref. 3)

growth rate (FCGR) - as R increases, FCGR increases. By utilizing closure stress intensity factor (K_{Cl}) to calculate an effective stress intensity factor (ΔK_{eff}), instead of an applied ΔK used in Figure 2.7a, the data collapse around one FCGR curve (Figure 2.7b). Similar effects are seen in Figure 2.8 where comparisons are made between ΔK and ΔK_{eff} for notched steel specimens in the near-threshold region for short and long cracks. These examples are an indication that closure is a fundamental mechanism for controlling FCGR, that effective stress intensity factor normalizes the FCGR data, and that applied ΔK does not totally reflect the crack growth driving mechanism.

Oxide-Induced Closure

The oxide-induced closure mechanism (Figure 2.2b) arises when oxide deposits collect on the crack internal surfaces and wedge the crack open during unloading. This mechanism has also been used to describe the influence of a moist environment on fatigue crack growth rate (FCGR). The model is particularly useful in the near-threshold region where closure stress intensity factor (K_{Cl}) levels are comparable to the minimum stress intensity factor (K_{min}) levels.

Roughness-Induced Closure

The roughness-induced closure mechanism (Figure 2.2c) arises when the crack fracture surface asperity is of a comparable size to crack opening displacement (COD) levels. This mechanism can also be present when significant mode II displacement exists. Like oxide-induced closure, there is a wedging action which keeps the crack surfaces apart during

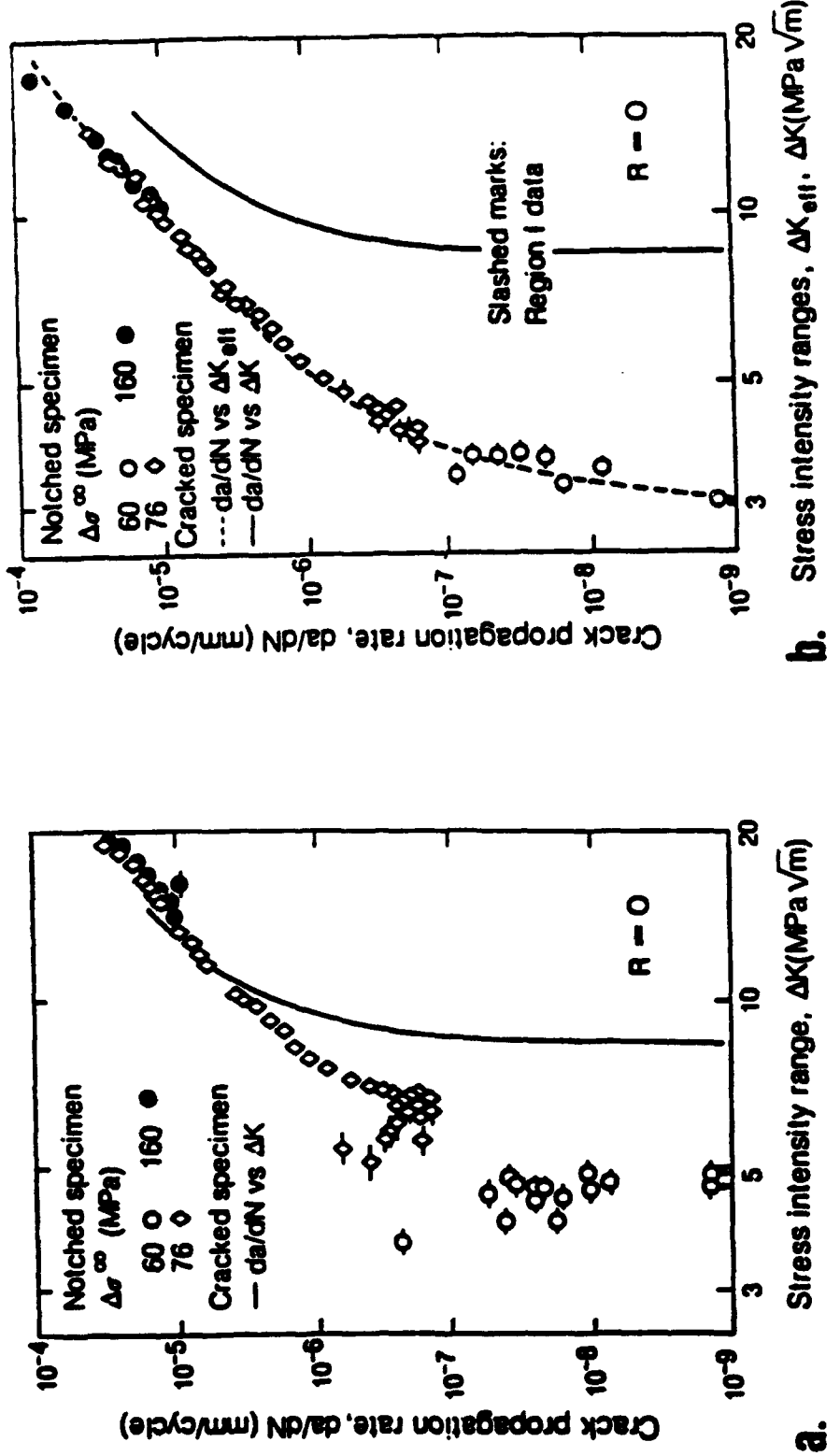


Figure 2.8 Variation in fatigue crack propagation rate with (a) nominal ΔK and (b) effective stress intensity ΔK_{eff} range values for a 0.17% C steel. Data points represent short cracks emanating from notches as compared to long crack da/dN data represented by the solid line (ref. 4)

unloading, causing K_{Cl} to be greater than K^{\min} . Again, this characteristic is dominant in the near-threshold stress intensity factor region. The process effectively lowers ΔK and thus reduces FCGR.

Viscous Fluid-Induced Closure

The presence of a viscous fluid (Figure 2.2d) in the crack can produce a wedging effect due to hydrodynamic pressure when the crack opens and closes. This effect accelerates the fatigue crack growth rate in the near-threshold region, but not in the higher K regions where an oxide-induced mechanisms (caused by the moist environment) dominate the closure loads effect.

Phase Transformation-Induced Closure

Materials which undergo a stress/strain induced phase transformation during cyclic loading produce a closure mechanism similar to plasticity-induced closure (Figure 2.2e). The crack tip plastic zone produces a metallurgical phase transformation which forces the yielded material into a compression state to compensate for the unchanged elastic material. As the crack grows through this transformation zone, it experiences a closure load effect which reduces the nominal stress intensity factor range. Although little experimental data are available, increased temperature is expected to enhance phase-transformation-induced closure.

Crack Opening Displacement Measurements

The use of Newton interferometric measurement techniques for defining crack opening displacement (COD) patterns in a transparent polymer specimen provides a unique experimental capability. The technique employs the principle of interfering light paths reflecting off two surfaces which are typically separated by an air gap (Figure 2.9). Packman (16) described this interferometry technique and its usefulness for measuring stress intensity factors, fracture of materials and stress corrosion. He used the term crack opening interferometry (COI) for measuring crack opening displacements (COD) in order to distinguish it from other experimental techniques such as clip gauges, strain gauges, etc. The COI technique is particularly useful for crack opening measurements since it can distinguish very small displacements (to within a fraction of a wavelength). By counting the number of fringe patterns (η) and knowing the light source wavelength (λ), the air gap thickness produced by COI can be calculated as (17):

$$COI = 2d = (2\eta - 1) \lambda / 4 \quad (2.10)$$

for the destructive fringes (dark lines) with a normal incidence light source (where $\eta = 1, 2, \dots$). This technique has been successfully applied in a number of investigations, and will be discussed in more detail in the body of this report.

Closure Observations

An investigation by Fleck, Smith and Smith (18) used a crack mounted displacement gauge and back face strain gauges to measure surface crack opening displacements on

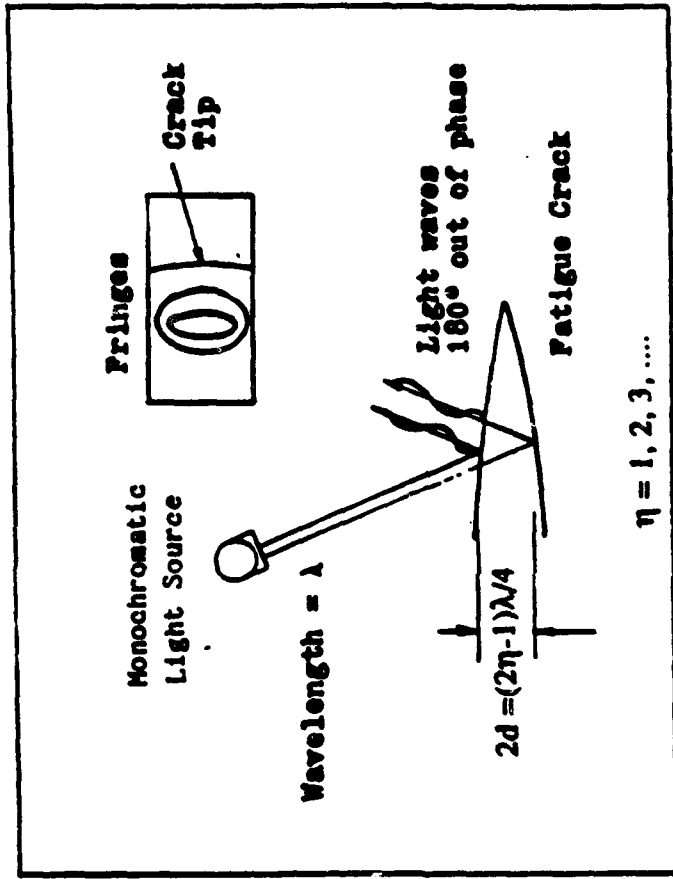


Figure 2.9 Schematic of the Newton interferometry method for generating fringe patterns from crack opening displacement (Ref. 19)

compact tension specimen of BS4360 B50 steel (24% elongation, 55 ksi yield strength). A new "push-rod gauge" was developed to measure crack internal surface displacements in the specimen plane strain region. The investigators found the push-rod gauge to be accurate, and concluded "that a greater degree of crack closure occurs at the surface than the bulk plane strain regions of the specimen." The closure parameter U , defined as $(K_{max} - K_{cl})/(K_{max} - K_{min})$, was calculated to be 0.85 in the plane strain region, and 0.75 at the plane stress region for the surface crack.

Pitoniak (19) used PMMA and a monochromatic light source to measure crack opening displacements of thru-the-thickness cracks in compact tension specimens. His crack opening displacement (Figure 2.10) measurements revealed that at zero load the thru-crack was closed at the specimen surface (plane stress regions), but was always open in the crack center (plane strain regions). That is, at zero load the COD plots show the crack internal surface to be open approximately 1.3E-4 inches (3.3E-3 mm) at the max displacement point, while closed at the crack face.

Further interpretation made here of the closure load measurements in the Pitoniak report reveal that approximately 17% of the maximum applied load (P_{op}/P_{max}) is required to open the internal crack tip plane strain region, 30% to open the crack face middle and 47% to open the crack tip plane stress region at the crack face (compared to 50% for 2024 aluminum). It is also noted that the point of maximum displacement is located approximately 30% of the crack length from the crack tip. These findings are significant since they not only show an internal displacement under zero load, but also because the measured closure load ratios (P_{op}/P_{max}) are similar in magnitude to those seen in metals even though the plastic zone size is considered to be small.

The COD pattern observations by Pitoniak, et al., (20) using PMMA material were later observed by Pelloux, Faral and McGee (21) using fractographic analysis in metals. These findings are shown in Figure 2.11, where the mid-crack tip region (plane strain region) is shown to be open under zero load while closed at the specimen free-surface (plane stress

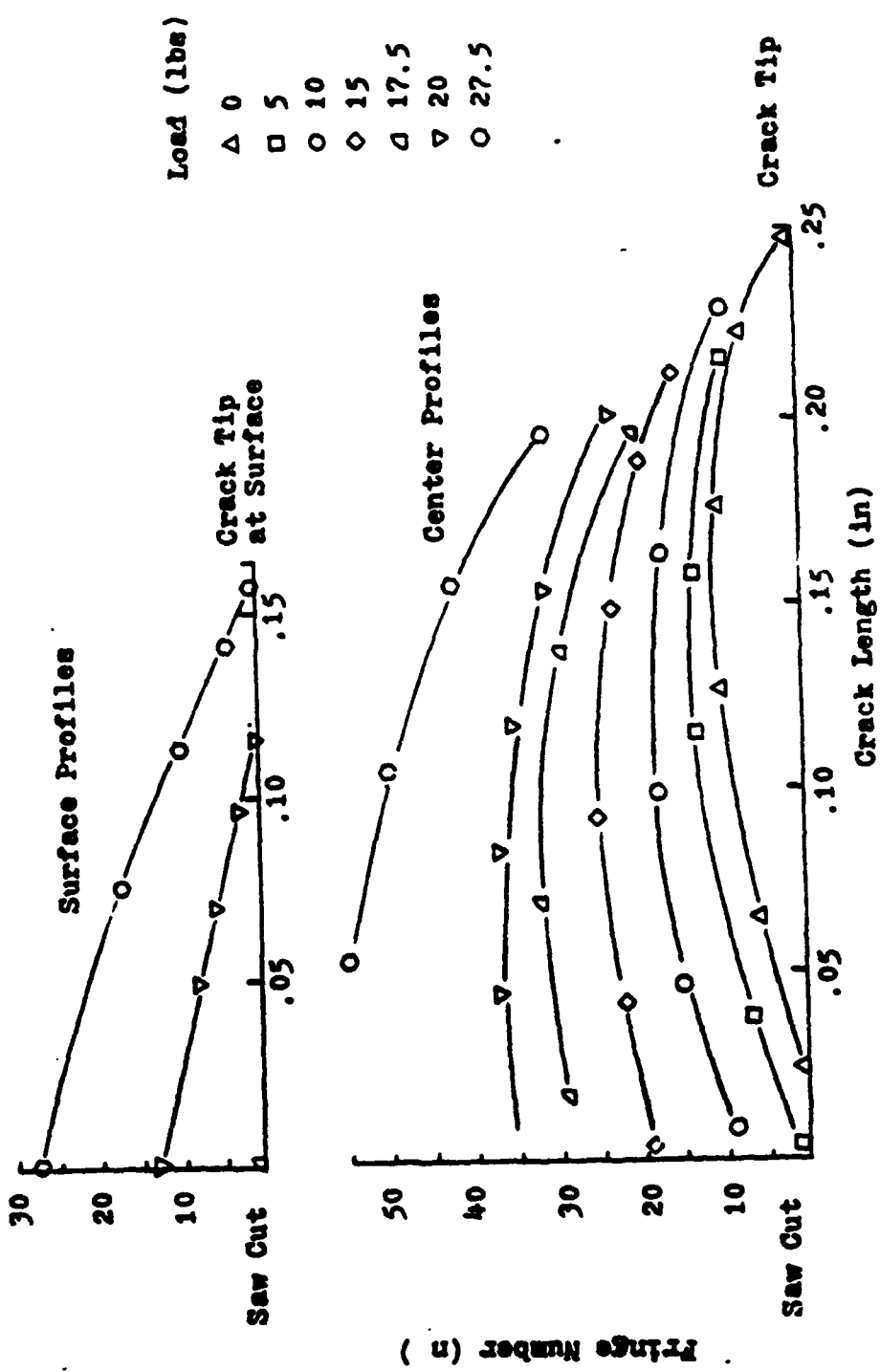


Figure 2.10 Comparison of surface and center fatigue crack opening displacement profiles at various tensile loads for a thru-thickness crack in a PMMA specimen (Ref. 19)

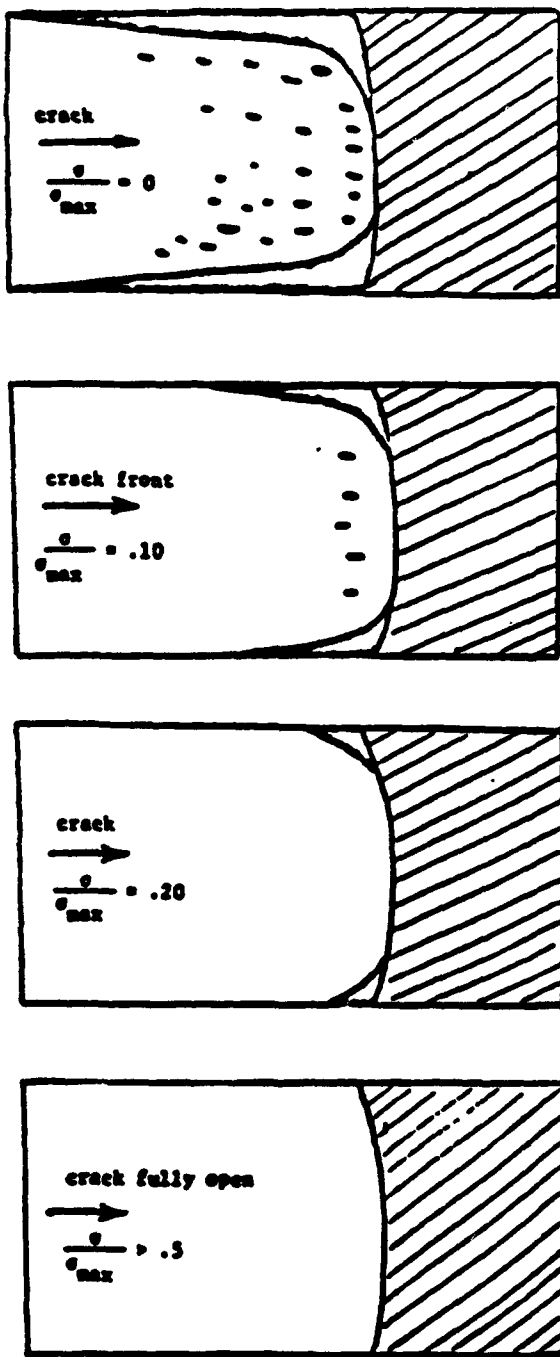


Figure 2.11 Schematic of the closure contact areas of thru-thickness crack opening displacement patterns using fractographic measurements in metals (Ref. 21)

region). With load application, the crack opens outward from the internal crack surface toward the crack free surface. For the crack surface to be fully open required an applied to maximum load ratio greater than 0.5 for 2124-T351 aluminum alloy.

Analytical results of Newman (22) showed the closure ratio (K_c/K_{max}) to be in the range of 0.25 to 0.35 for plane strain, and 0.5 to 0.6 for plane stress. Analysis by Fleck (23), using an elastic-perfectly plastic two-dimensional finite element analysis developed by Newman (24), determined that closure load behavior is insensitive to material property changes of σ_{ys}/E and ν (where σ_{ys} is the yield stress, E is Young's modulus and ν Poisson's ratio). When closure ratio was plotted against $\Delta a/(K_{max}/\sigma_{ys})^2$ at the plane stress and plane strain regions of the crack, definite closure load trend differences were noted. The plane strain region showed a decreasing closure ratio with increasing load ratio (σ_{max}/σ_{ys}). However, the plane stress region showed little difference for various load ratios. The closure ratio levels calculated by Fleck were similar to those calculated by Newman.

Fleck found that the closure parameter (U) values for thru-crack measurements were similar to those for surface flaws (0.84 for plane strain and 0.74 for plane stress). These values compare quite favorably with the PMMA measurements of approximately 0.83 and 0.70 for the plane strain and plane stress regions, respectively, reported by Pitoniak, et al., (18). Ray and Grandt report similar results for thru-thickness compact tension specimens (25) and surface flaws (26).

Again, it is of interest to note that although the plastic zone size for PMMA is reported to be small, the closure parameter (U) is of the same relative magnitude as values reported for a ductile steel (Fleck, Ref. 18), 2024 aluminum (Elber, Ref. 11) and for analysis (Ref. 22). These results are summarized in Table 2.1.

Table 2.1 Summary of Closure Ratio and Closure Parameter (U) Values

<u>Thru-Crack Specimens</u>	<u>K_{c1}/K_{max}</u>	<u>U</u>
Elber -- 2024 Aluminum	0.50	0.50
Fleck -- Mild Steel	0.27	0.74
Newman -- Analytical	0.50-0.60	0.50-0.40
Pitoniak -- PMMA	0.47	0.53
Ray/Grandt -- PMMA	0.38	0.69

Part-thru Surface Cracks

Fleck -- Mild Steel	0.25	0.76
Ray/Grandt -- PMMA	0.18-0.30	0.91-0.78

Closure Problem Areas

Detailed literature reviews of closure research have identified important questions concerning the state-of-the-art in understanding and using closure relationships to predict fatigue crack growth (FCG). In general, these reviews have identified the need for more fundamental research into this area.

Banerjee (3) makes the following observations in his review of crack closure:

1. Even though the use of an effective stress intensity factor (ΔK_{eff}) has normalized fatigue crack growth rate data over a wide range of K_{max} , K_{min} and R values, the actual closure mechanisms are not well understood.
2. The dependence of closure stress intensity factor (K_{c1}) on K_{max} , K_{min} and R for constant amplitude load test is not clearly established. As an example,

K_{cl} has been observed to increase, remain constant or even decrease with increased K_{max} .

3. Effects of cyclic load history on closure have not been established. This includes the effects of precracking, variable amplitude loading, frequency changes, etc.
4. Even though crack stress intensity varies along the crack perimeter (and is thus different at the interior and at the exterior of the crack - reference Figure 2.4), the influences of plane stress and plane strain conditions are not clearly defined, well understood or typically accounted for in the literature.
5. There is little distinction in the literature concerning free-surface and mid-thickness closure behaviors. The lack of a consistent definition has led to confusion about the actual crack tip stress intensity.
6. The extent of closure and residual displacement produced by closure is rarely reported.
7. Plasticity induced closure depends on the formation of plastic zones and inelastic deformations in the vicinity of the crack tip.
8. The fundamental closure models (plasticity versus asperity, oxide-induced, etc.) reflect observed phenomena in separate stress intensity factor (K) regions - plasticity in the high K region, asperity and oxide in the low K regions.
9. Asperity and oxide induced closure operate only in the near threshold region.

Conclusions by Surech and Ritchie (4) follow the same general theme. Their observations are summarized here:

1. Understanding the role of closure is essential to understanding the behavior of short cracks, variable amplitude loading, single overloads and block loading above and below the threshold..

2. Crack length is critical to evaluate closure because of wake effect - effect of load history on the wake/closure relationship.

III. PROBLEM STATEMENT

A great deal of activity has gone into understanding crack closure and opening displacement characteristics since Elber's initial description of the closure phenomenon. Most of these investigations have used thru-crack specimens because of the availability of stress intensity factor solutions and the relative ease of making closure measurements. In comparison, relatively few closure investigations have been conducted with surface cracks.

The inability to measure three-dimensional crack opening displacements in metals has been the major deterrent in conducting surface flaw investigations. The fundamental data required to address the influence of plane stress and plane strain effects on closure are also lacking for the same reasons.

Many of the three-dimensional measurement difficulties associated with metals can be resolved by using an optically transparent polymer to measure surface flaw crack growth. By employing interferometry techniques to accurately measure internal crack opening displacement (COD) under various opening loads, the influence of crack closure on fatigue crack growth can be established. The key to this effort is being able to directly measure three-dimensional COD, closure and crack growth simultaneously using Newton interferometry techniques in a transparent polymer.

Objective

The objective of the current research is to determine the influence of closure on the fatigue crack growth of surface flaws loaded in cyclic bending in a transparent polymethylmethacrylate (PMMA) material.

Approach

An experimental investigation was conducted to determine the influence of fatigue crack closure on the growth of surface flaws. The investigation was undertaken to broaden the understanding of surface flaw crack opening displacement (COD), closure loads and growth rate characteristics. The approach is made possible by combining a unique interferometric measurement capability with a transparent polymethylmethacrylate (PMMA) polymer which exhibits fatigue crack growth properties which are represented with conventional fracture mechanics analysis procedures. The transparent polymer material provided the ability to evaluate three-dimensional crack opening displacement (COD) characteristics of surface flaws. Optical interferometry measurements, using a helium-neon laser light source for the first time, were used to define the crack opening displacement profiles and crack opening loads. The fatigue tests were conducted on rectangular plate specimens (Ref. Figure 2.1) loaded in four-point bending.

To evaluate plasticity effects on closure, four different load histories were tested: (1) constant stress intensity factor along the crack surface (ΔK_d), (2) constant stress intensity factor into the crack depth (ΔK_a), (3) constant load and (4) constant amplitude blocks loading where subscripts "a" and "d" identify crack tip boundary locations A and D, respectively (Figure 3.1). COD and closure measurements were made for various crack lengths and aspect ratios.

The investigation was organized into six tasks (Figure 3.2): data generation (tasks 1-4), data reduction (task 5) and data analysis (task 6). A description of these tasks is presented below. The approach for tasks 1-4 is presented in Section IV, experimental results are presented in Section V, and data analysis in Sections VI through VIII.

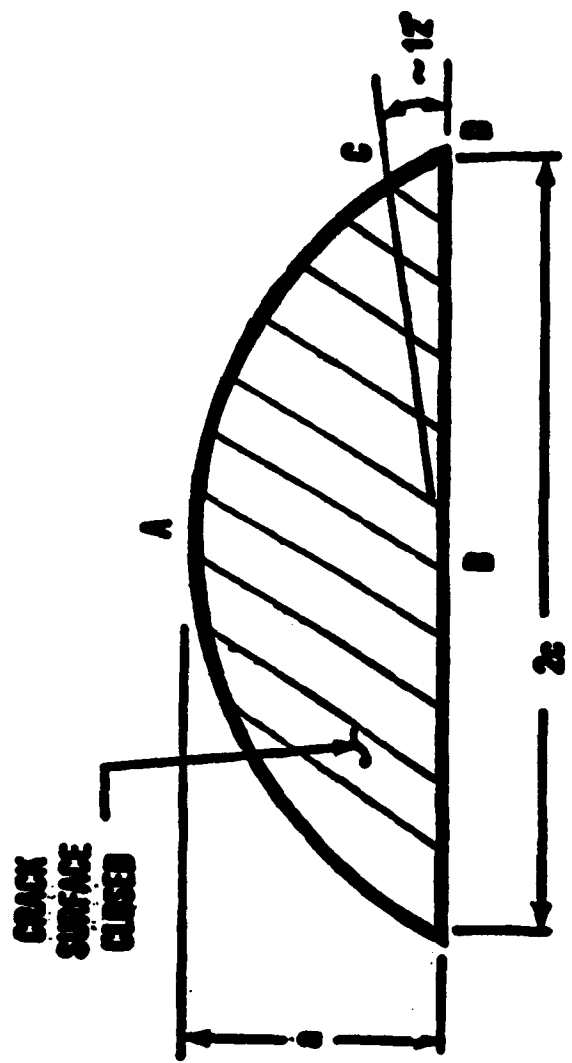


Figure 3.1 Surface crack schematic showing locations A,B,C and D
reference points, and angle ϕ

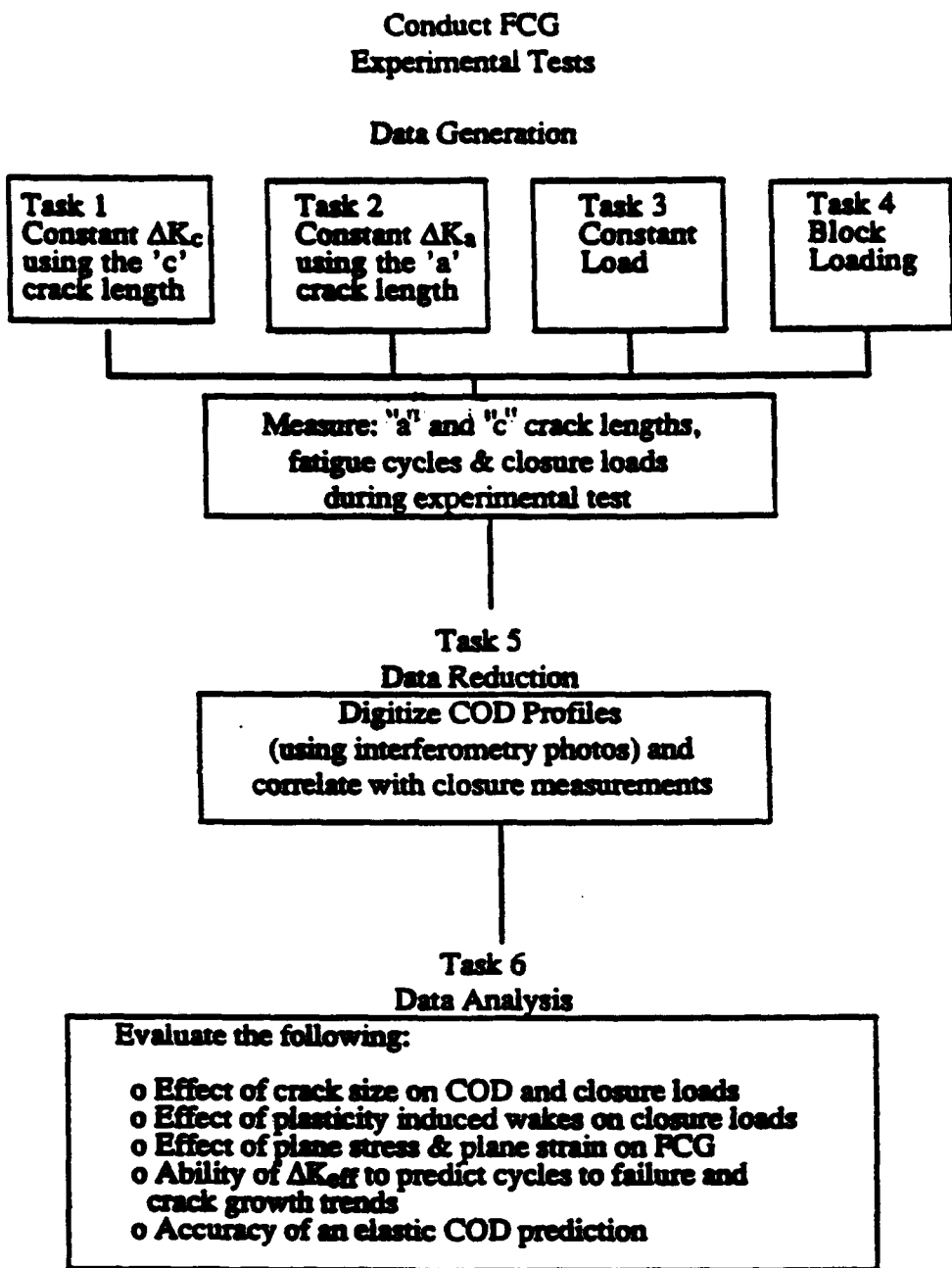


Figure 3.2 Block diagram of the experimental test and data analysis

Experimental Data Generation

The objective of tasks 1-4 is to generate closure load (K_{Cl}), crack opening displacement (COD) and fatigue crack growth rate (da/dN and dc/dN) data for surface flaws in a polymethylmethacrylate (PMMA) specimen subjected to cyclic four-point bending loads. The specimen were loaded with a four-point bending fixture mounted on an MTS closed loop, electro-hydraulic, fatigue machine. Four loading histories were generated to isolate plasticity induced closure load effects -- two low level constant stress intensity factor (ΔK) tests, a variable ΔK test (constant load), and a block loading test. An x-y traveling microscope was used to track the crack growth in the "a" and "c" directions. Photographs of the crack interference fringe patterns were taken as load was applied from zero to a level greater than the closure loads. Fringe pattern photos were taken at "c" crack length intervals of approximately 0.05 in (1.23 mm) for crack sizes which ranged between 0.02 and 0.60 inch. Additional measurements of "a" and "c" crack lengths and closure loads were taken when unexpected occurrences were noted during the experiment.

Experimental Data Reduction

The objective of task 5 is to organize the experimental data from tasks 1-4 into a cohesive set of crack opening displacement (COD) and closure load definitions. Because of the diversity of information required to address the closure question, experimental data reduction was evaluated from several perspectives: the effect of crack opening displacement (COD) formation on closure loads, the ability to quantify COD and closure loads, the effect of the four load histories on closure, and the influence of COD and closure in defining ΔK_{eff} . These evaluations are covered in Chapters V and VI.

Experimental Data Analysis

The object of task 6 is to use the experimental data to evaluate fatigue crack growth (FCG) and COD prediction procedures. This is accomplished by the following data reduction and analysis steps:

- A. Categorize and evaluate crack opening displacement (COD) and closure loads as a function of crack size.
- B. Evaluate the influence of COD and plasticity induced wakes on closure loads. Measure closure loads from constant stress intensity factor tests (tasks 1 & 2) and compared to those from a constant load test (tasks 3). Determine if closure load differences are attributable to load history and/or plasticity induced wake patterns.
- C. Compare the influence of plane stress and plane strain on COD and closure using results from tasks 1 & 2. Since the constant stress intensity factor tests is conducted by maintaining the same K value at the crack tip locations A and D ($\phi = 0$ and 90 degrees in Figure 2.1, respectively), relative differences in measured closure and COD are emphasized.
- D. Compare fatigue crack growth rate analysis using applied ΔK and ΔK_{eff} . Compare predicted and experimental FCG data (da/dN & dc/dN). Use the Newman-Raju (5) stress intensity factor solutions.
- E. Evaluate the ability of ΔK_{eff} to normalize FCG rate predictions using measured and an assumed closure loads. Analysis of all tasks provided insight into how closure loads influence fatigue crack growth. Utilize Paris Law material constants from available literature sources when applicable.

F. Compare predictions of elastic crack opening displacement (COD) amplitudes to measured COD amplitudes.

IV. EXPERIMENTAL PROCEDURES

This section covers the experimental procedures used in this investigation. Included are discussions of the test equipment, loading histories, material selection, and preparation of the specimens for fatigue testing.

Test Procedures and Equipment

Development of the Newton interferometry system for mapping crack surface displacement profiles was a major part of this investigation, and is an original experimental setup. This technique provided a precision method for measuring closure loads and crack opening displacement (COD) patterns. This detailed information, in combination with a carefully selected test matrix, provided a unique data set for understanding the influences of the closure mechanism or fatigue crack growth of surface flaws. A photograph of the experimental arrangement (MTS electro-hydraulic controller, load frame with the specimen mounted in a four-point bending fixture and the laser interferometry system) is presented in Figure 4.1.

Newton Interferometry System

A laser interferometer system was used to record optical interference fringe patterns under various applied loads during fatigue cycling of the specimen. The Newton interferometer system combines a 10-milliwatt helium-neon laser monochromatic light source ($\lambda = 6328 \text{ \AA}$), a reflecting mirror, beam splitter and 35mm camera mounted to a three-way adjustable base plate. The laser monochromatic light source was used instead of a

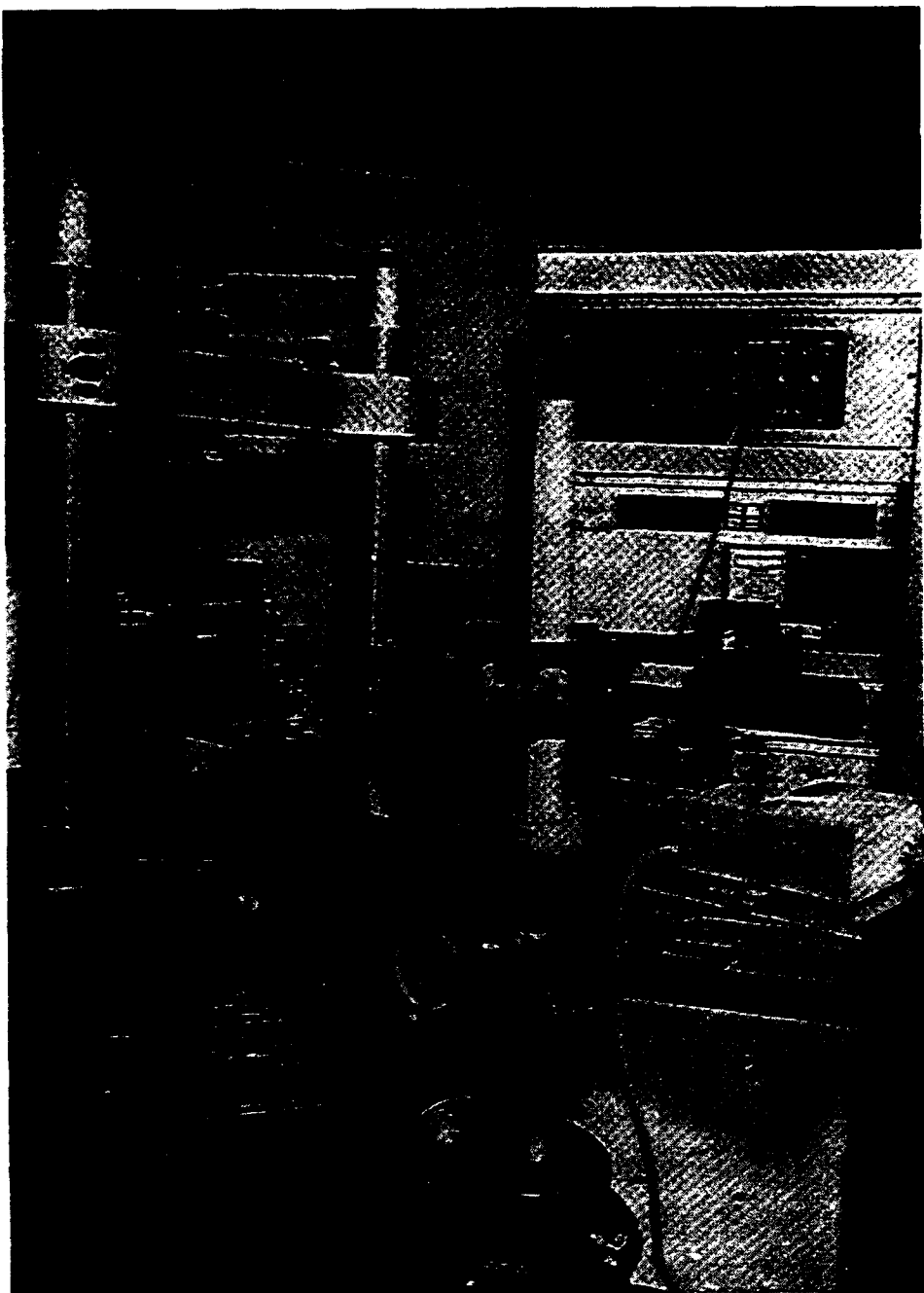


Figure 4.1 Experimental arrangement fo the MTS electro-hydraulic controller, load frame with the specimen in a four-point bending fixture, and the laser powered interferometry system.

sodium arc light source ($\lambda = 5890 \text{ \AA}$), as proposed by Packman (16), to increase the light intensity reflecting from the crack surface. A schematic and photograph of the laser interferometry system are presented in Figures 4.2a and b, respectively. Light from the laser is reflected 90 degrees at the mirror, split into two beams at the partial-mirror beam-splitter where one beam passes into the specimen and reflects off the two crack surfaces. The two reflected rays from the crack surfaces destructively interfere, due to a 180° waveshift off the crack back surface, forming fringe patterns. The rays then pass back through the beam splitter, thru a bellows and into the 35-mm camera. The beam splitter is used to minimize the angle between the light source and the light reflecting back to the camera, providing a direct line of sight between the crack surface and the camera.

Since the fringe patterns represent contour lines of constant crack surface displacement, the interferometry system, with the transparent PMMA material, provides the unique capability to measure very small displacements over the complete crack interior surface (16,20,25). By counting the interference fringe orders as the crack opens under an applied load, displacement changes of $6.22\text{E-}6 \text{ in.}$ ($1.58\text{E-}4 \text{ mm}$) can be resolved between zero displacement and the first fringe order formation. As an example, fringe order #2 in the schematic diagram of Figure 4.3 represents a constant displacement between the two crack surfaces of $1.87\text{E-}5 \text{ in.}$ ($4.75\text{E-}4 \text{ mm}$) in accordance with the optical relationship for total crack opening displacement given by eq. 4.1 (17):

$$d = (2\eta - 1) \lambda / 8 \quad (4.1)$$

Here λ is the wave length of light, and d is half of the total crack surface separation for fringe order of $\eta = 1, 2, 3, \dots$. The zero order fringe defines the location where the crack surfaces are closed. The maximum displacement point occurs within the second fringe order contour line (in this example), and is known to be less than the displacement corresponding to a third fringe order or $3.11\text{E-}5 \text{ in.}$ ($7.91\text{E-}4 \text{ mm}$). This topographical information can be

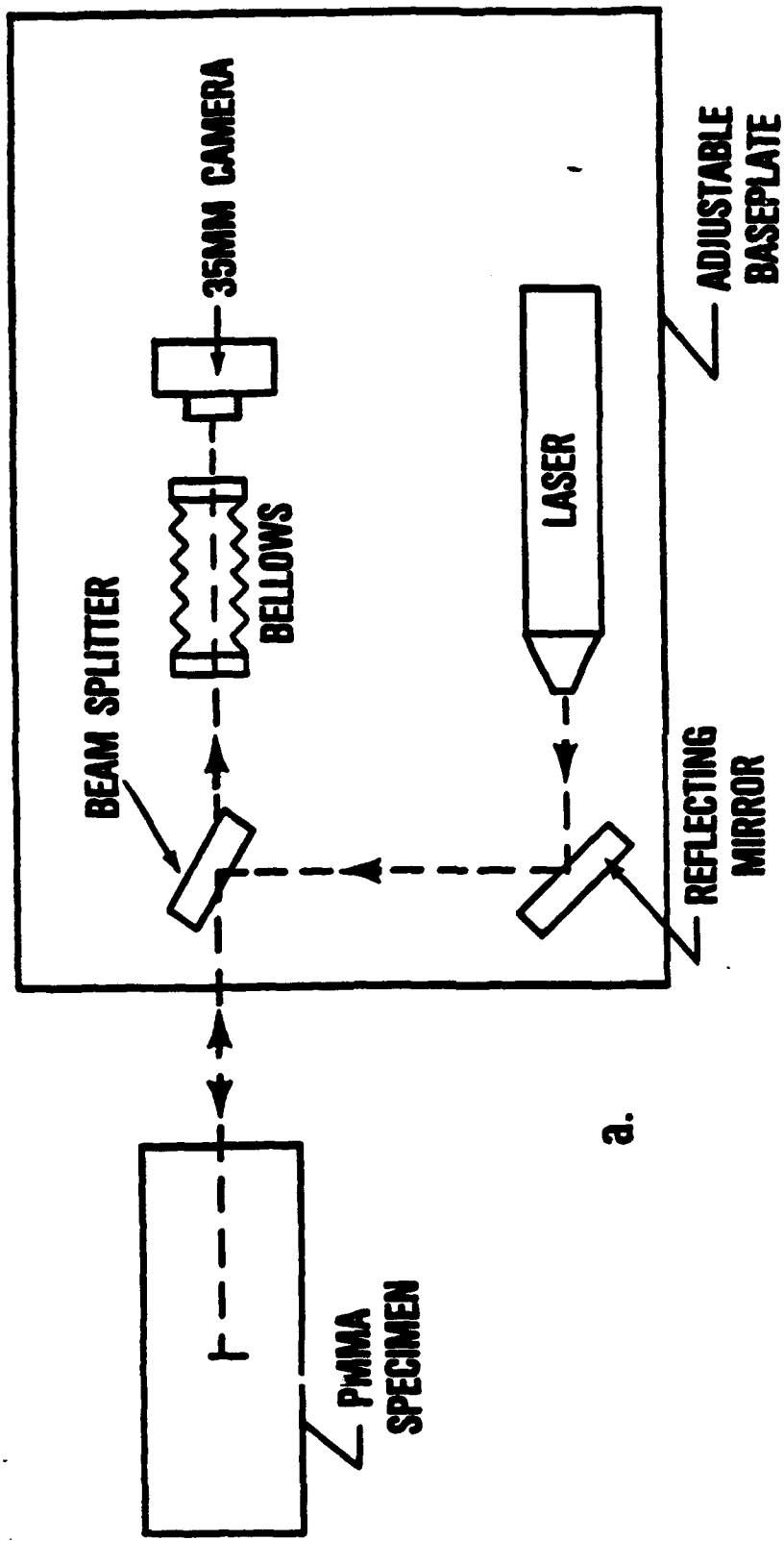


Figure 4.2 Newton interferometry arrangement using a laser light source which reflects off the surface crack as shown (a) schematically and (b) pictorially with the laser, reflecting mirror, beam splitter, bellows and 35mm camera mounted on an adjustable baseplate.



Figure 4.2 (Continued)

b

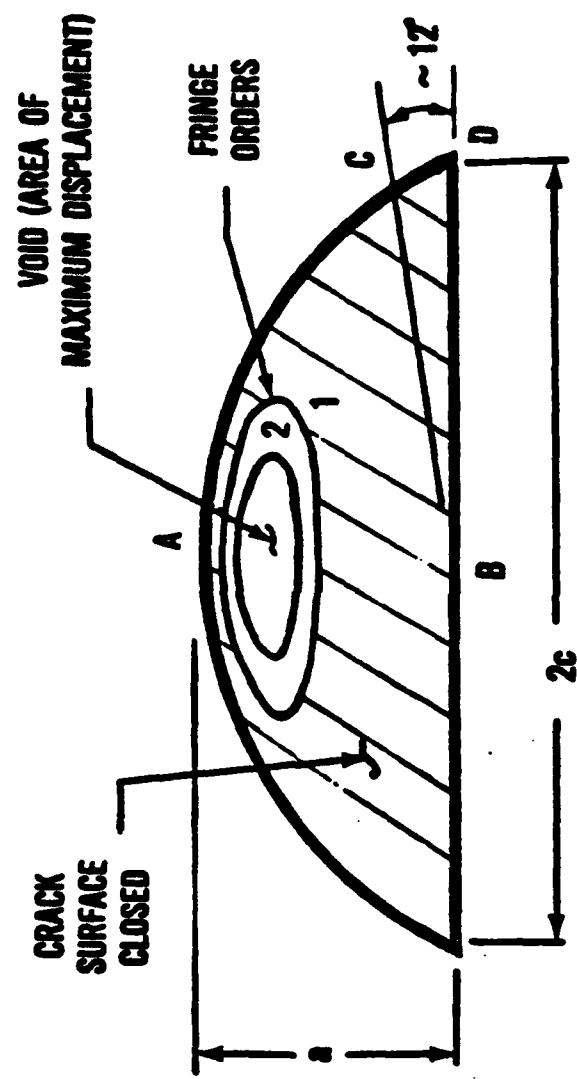


Figure 4.3 Surface crack schematic of a void formation internal to the crack surface.

used to define COD profiles, as well as identify profile trends with applied load and changes with crack size.

Example fringe patterns produced by the laser interferometry system are shown in Figures 4.4a through 4.4d using a test specimen with a 0.187 inch long surface crack (2c). The photos show relative crack opening displacement as load is increased from zero (4.4a) to half of the fully-open load (4.4b), 3/4 of the fully-open load (4.4c), and at a load level when the crack is fully-open (4.4d). As can be seen in Figure 4.4a, the crack surfaces and crack tip (location A) are open (fringe order #1) with no applied load to the specimen. Note the four crack boundary locations A, B, C and D, the crack free-surface length (2c) and depth (a). As a bending moment is applied, the crack surfaces open toward the crack free-surface (Figures 4.4b and 4.4c), and are completely open in Figure 4.4d. The crack free-surface and reflection from the PMMA specimen are shown in Figure 4.4d. The crack maximum measured height at the fully-open load level is shown in this figure by the 13th fringe order to have a total displacement between crack surfaces of 1.6E-4 in. (3.19E-4 mm). The plane stress/strain constraint effect is shown by location C being the last portion of the crack surfaces to fully-open (Ref. Figure 4.3).

The sequence of fringe order photographs shown in Figure 4.4 are an example set obtained at four different loadings. During the experimental tests, interferometry and crack size photos were taken at approximately 0.050 in (1.27 mm) increments of crack size along the specimen free-surface (2c). At each of these crack lengths, 10 to 15 photos were taken of the interference fringe patterns as load was applied to the specimen. Analysis of this data for all load histories is presented in Chapter V.

Visual observations of optical interference fringe orders were used to determine closure/opening load levels. Opening and closure loads are used interchangeably here since less than 5% difference in load level was measured to achieve the same displacement when the load was increased on the specimen (opening) or reduced (closure). However,

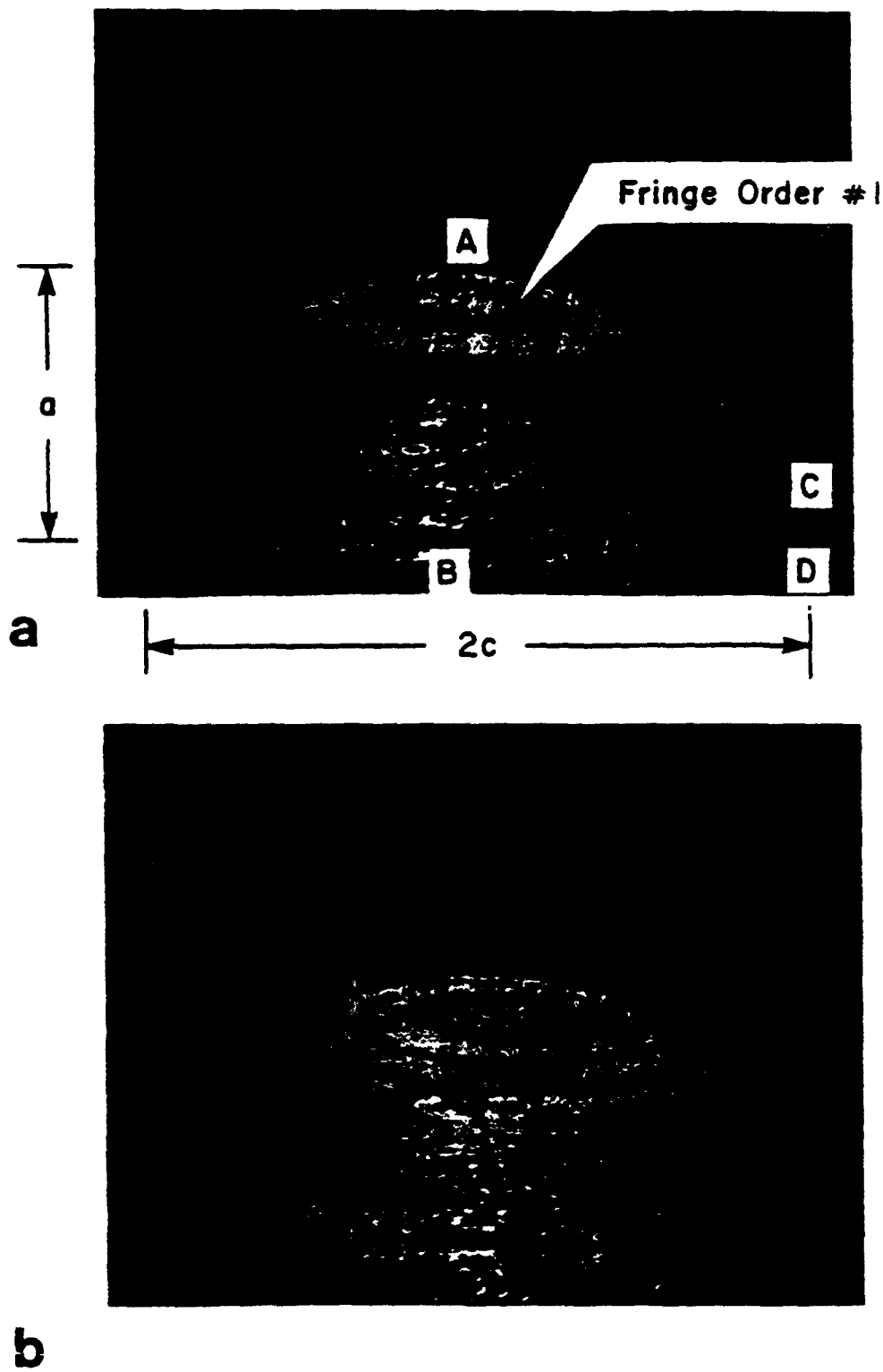
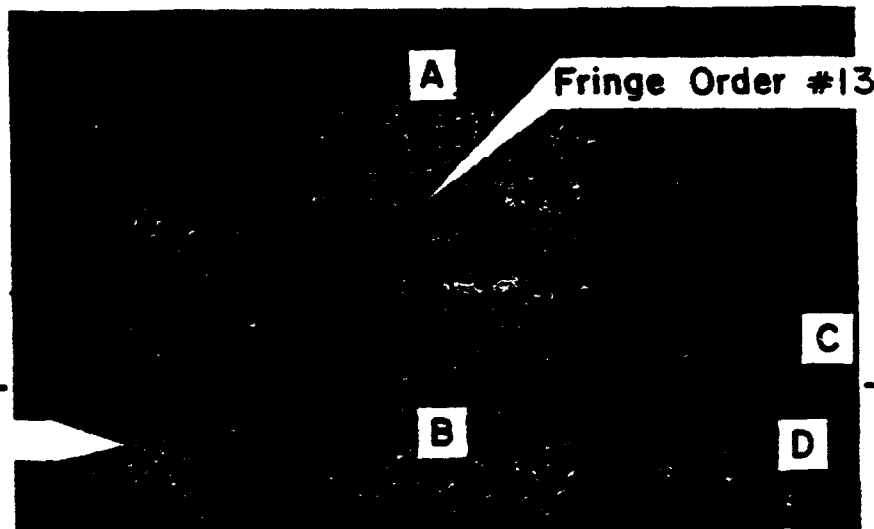


Figure 4.4 Interferometry fringe pattern photos showing various stages of crack opening displacement at various applied loads levels: (a) zero load, (b) 1/2 of the fully-open load, (c) 3/4 of the fully-open load, and (d) fully-open load



C



d

Figure 4.4 (Continued)

measurement values presented in this report are all crack opening loads except where comparisons of opening and closure load are identified in the text.

Digitizing Crack Displacement Profiles

Accurate digital measurement of the interference fringe orders was accomplished by using a 20 inch x 20 inch digitizing plate, a photo negative enlarger (Figure 4.5), and the 35mm negatives generated from the laser interferometer system. The 35mm negatives were inserted into the enlarger to expand the fringe order photos on the digitizing plate. The digitizing plate was connected to a Techtronics terminal with a self-contained magnetic tape for storing the digitized data. A software program written for the Techtronics computer was used to store and analyze the fringe order numbers and x-y digital displacement data. This information was then used to construct a three-dimensional contour map of the COD patterns.

A sample set of digitized COD profiles for zero and various applied loads is shown in Figure 4.6. The discrete data points are connected by straight lines to show the profile at an applied load. Digitizing the fringe orders followed a procedure of initially locating the crack maximum depth "a" to define location A (Figure 4.3). Fringe orders were then located relative to the crack tip (location A) and digitized along a line between locations A and B. Figure 4.6 presents half of the full crack opening displacement (COD) profile for various loads -- with displacement plotted along the ordinate, and distance from the crack tip location A on the abscissa. Loads from zero to levels above the non linear closure load region are presented. A detailed discussion of these patterns is covered in Chapter V.

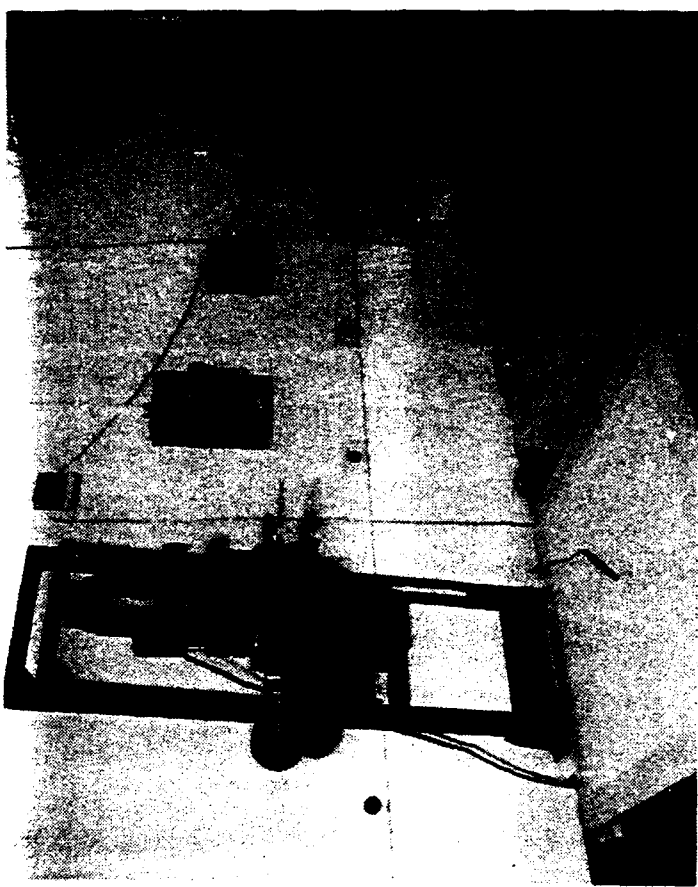


Figure 4.5 Experimental setup for digitizing the fringe order using a photo enlarger and digitizing board

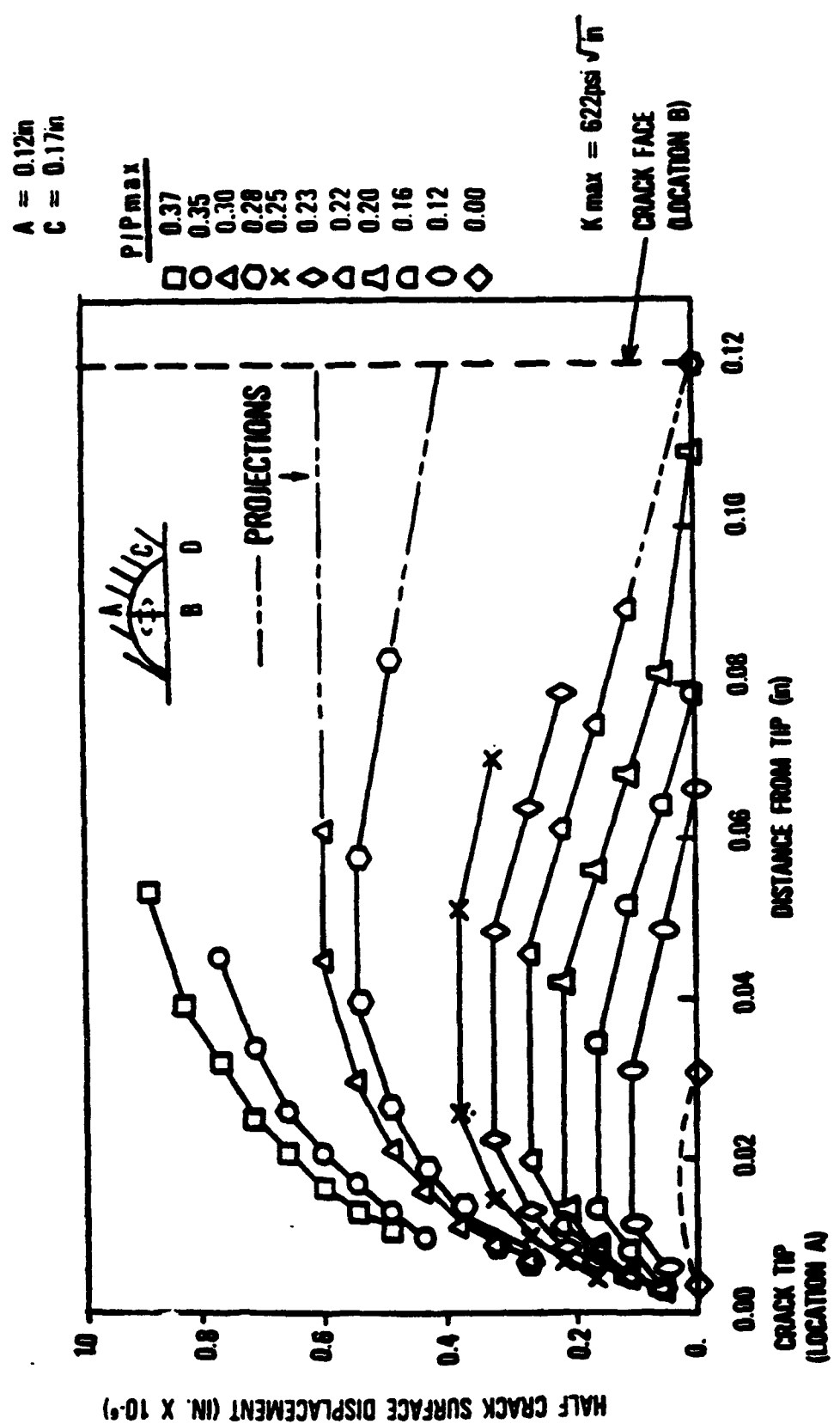


Figure 4.6 Surface flaw crack opening displacement pattern for half crack tip at location A for the crack displacement along the $\theta=90^\circ$ degree line for various loads in the closure load region

X-Y Traveling Microscope

An x-y directional traveling microscope was used to measure the "a" and "c" crack dimensions (Figure 4.3) during fatigue testing. The microscope had a 10 X magnification factor with a 4.5 in (114.3 mm) focal length for viewing the crack through the specimen. The microscope was mounted to the load frame and measurement accuracy calibrated with known reference marks on the specimen. Frequent recalibration checks were conducted to maintain accurate and consistent crack length measurements. The accuracy for measuring the 2c surface crack length (Figure 4.3) was estimated to be 0.001 inch, and into the specimen depth to be 0.002 inch. These differences are attributed to the traveling microscope scale markings, and linear travel distance per revolution of the traveling mechanism. It was assumed that the readings could be missed by ± 2 marks.

The microscope was calibrated by comparing actual measurements to known reference marks on the specimen. The reference marks were placed in the crack plane and the microscope aligned on the fatigue machine to remove parallax error. Measurements were then validated by expanding photographic negatives of the known reference marks and crack. It is estimated that over 1700 individual crack measurements ("a", "c" and closure load) were made using the x-y traveling microscope. These measured values of crack lengths and closure load (along with applied load levels and calculated ΔK , K_{max} , plastic zone sizes and closure stress intensity factor ratios) are included in the appendix.

Fatigue Machine

The experiments were performed on a closed loop MTS fatigue machine with a 5620 pounds. (25 kN) load cell and four-point bending fixture (Figure 4.1). The MTS load cell was calibrated for four load setting ranges. Range 1 was 100 % of the 5,620 pounds (25 kN)

capacity, range 2 was 50%, range 3 was 20%, and range 4 was 10% of maximum capacity. Load range 3 was used during precracking, while load range 2 was used for most of the fatigue testing. Load range 4 was used exclusively for measuring closure load amplitudes. This setting represented a measurement sensitivity of 562 pounds (2.5 kN) at 10 volts, or 56.2 pounds (0.25 kN) per volt. The fatigue fixture exposed the specimen to a bending moment (M , in-lb) of 0.8125 times the applied load P (lb). That is, $M = (3.25/4.0) P = 0.8125 P$ in-lb. ($M = 0.0206 P$ Newton-m, for P in Newtons).

Load History Selection

Four experimental load histories were selected to evaluate the effect of plastic zone patterns on plasticity induced closure. The four plastic zone patterns were generated by fatiguing the specimen to four different load histories: (1) a constant stress intensity factor along the crack surface $\Delta K_d = \text{constant}$ at location D, Figure 4.3); (2) constant stress intensity factor into the specimen depth ($\Delta K_a = \text{constant}$ at location A); (3) a constant cyclic load applied to the specimen and, (4) a variable block loading. The stress ratio (R) was maintained throughout the test at 0.035 to be as close to zero as possible while maintaining a positive load on the bending specimen. These four load histories were briefly described in Section III as task 1-4.

Plasticity Considerations

The four load histories were selected to emphasize plastic zone size differences at locations A and D (predominant plane strain and stress regions, respectively) on the crack

boundary (Figure 4.3) by controlling ΔK_a and ΔK_d . These considerations can be seen by reviewing the stress intensity factor (K) equation for a surface flaw in bending (5). That is:

$$\begin{aligned} K &= \sigma \sqrt{(\pi a/Q)} H f(a,c,\phi) \\ &= 6M/bt^2 \sqrt{(\pi a/Q)} H f(a,c,\phi) \end{aligned} \quad (4.2)$$

where M is the bending moment, b and t are the specimen width and thickness, respectively, "a" is the crack depth into the specimen thickness, "c" is the half surface crack length, Q is the elliptical correction factor, H is the correction term for bending, and $f(a,c,\phi)$ is the functional Boundary Correction Factor -- where "a" is a function of a/c at a given angle ϕ on the crack boundary (Figure 4.3). Removing the constants:

$$K \propto M \sqrt{(a/Q)} f(a,c,\phi) \quad (4.3)$$

showing that K can be defined by controlling M and measuring the "a" and "c" crack lengths -- note that Q is a function of a/c . Thus, by either controlling or measuring these three variables (a, c and M), an experimental approach can be established to investigate how closure load and crack opening displacements vary with K .

The influence of plane stress and strain ($\phi = 0$ and 90 degrees, respectively, Figure 4.3) constraints on plastic zone size was also evaluated as part of the test matrix requirements. This is typically accounted for by a plastic constraint factor (pcf) which is defined as (27):

$$pcf = \sigma_{max} / \sigma_{ys} \quad (4.4)$$

where σ_{max} is the maximum applied stress and σ_{ys} is the material yield stress. By utilizing the Von Mises yield criteria and an assumed Poissons ratio of 1/3 for metal, a pcf value of

3.0 was calculated for plane strain to account for internal yielding constraints, and 1 for plane stress. Since the internal crack surfaces are not in a purely plane strain condition, as calculated by this approach, Irwin (28) used an average pcf value of 1.68 instead of 3 as an effective yield stress, such that the plastic zone radius (r_p) is defined as:

$$\begin{aligned} r_p &= (K/1.68 \sigma_{ys})^2 / 2\pi \\ &= (K/\sigma_{ys})^2 / 6\pi \end{aligned} \quad (4.5)$$

Experimentally, effective values of pcf (29) have been found to vary between 1.5 and 2.0 for metals. Using the Irwin relationships for plastic zone size the following definitions can be established for plane stress (equations 2.4 and 2.5) where r_0 is defined at $\phi = 0$ degrees as (Figure 4.3):

$$r_0 = (K_0/\sigma_{ys})^2 / 2\pi \quad (4.6)$$

and plane strain where r_{90} is defined at $\phi = 90$ degrees, as:

$$r_{90} = (K_{90}/\sigma_{ys})^2 / 6\pi \quad (4.7)$$

If ΔK is then maintained at a constant level at two locations ($\phi = 0$ and 90 degrees) during separate tests, such that K_0 for one test is replaced with K_{90} for another test, it follows that:

$$r_0 = 3 r_{90} \quad (4.8)$$

Therefore, by maintaining a constant plastic zone size at $\phi = 0$ and 90 degrees, such that $r_0 = r_{90}$, it follows that:

$$K_{90} = \sqrt{3} K_0 \quad (4.9)$$

These differences between plane stress and plane strain plastic zone size are utilized in the constant ΔK_d and ΔK_a tests (tasks 1 and 2) to emphasize the relative influence of plastic zone size and/or K level on closure loads. Plastic zone size was not measured experimentally, but was calculated using equations 2.4 and 2.5. The results of these tests are discussed in Chapter V, in the "Closure/Opening Loads" section.

Isolating Plasticity Effects

Four load histories were selected to isolate specific plastic zone influences on closure loads at crack tip boundary locations A and D. Although plasticity effects cannot be isolated for all areas around the crack tip boundary, relative effects of dominant influences can be evaluated at specific locations using distinctive test cycles. The four cyclic load histories selected to experimentally emphasize relative effects of plastic zone differences on closure and fatigue crack growth are defined in tasks 1-4.

Task 1: A constant ΔK_d load history test was conducted to produce a constant plastic zone size along the crack tip free-surface (location D, $\phi = 0$ degrees, Figure 4.3) by load shedding as the crack size increased. The sinusoidal bending load-shed history produced a constant ΔK_d along the crack face shown in Figure 4.7. A schematic of the plastic zone size is theoretically represented by Figure 4.8. A constant stress intensity factor (ΔK_d) of 600 $\text{psi}^{1/2}$ ($659 \text{ KPa}^{1/2}$) was maintained in this test.

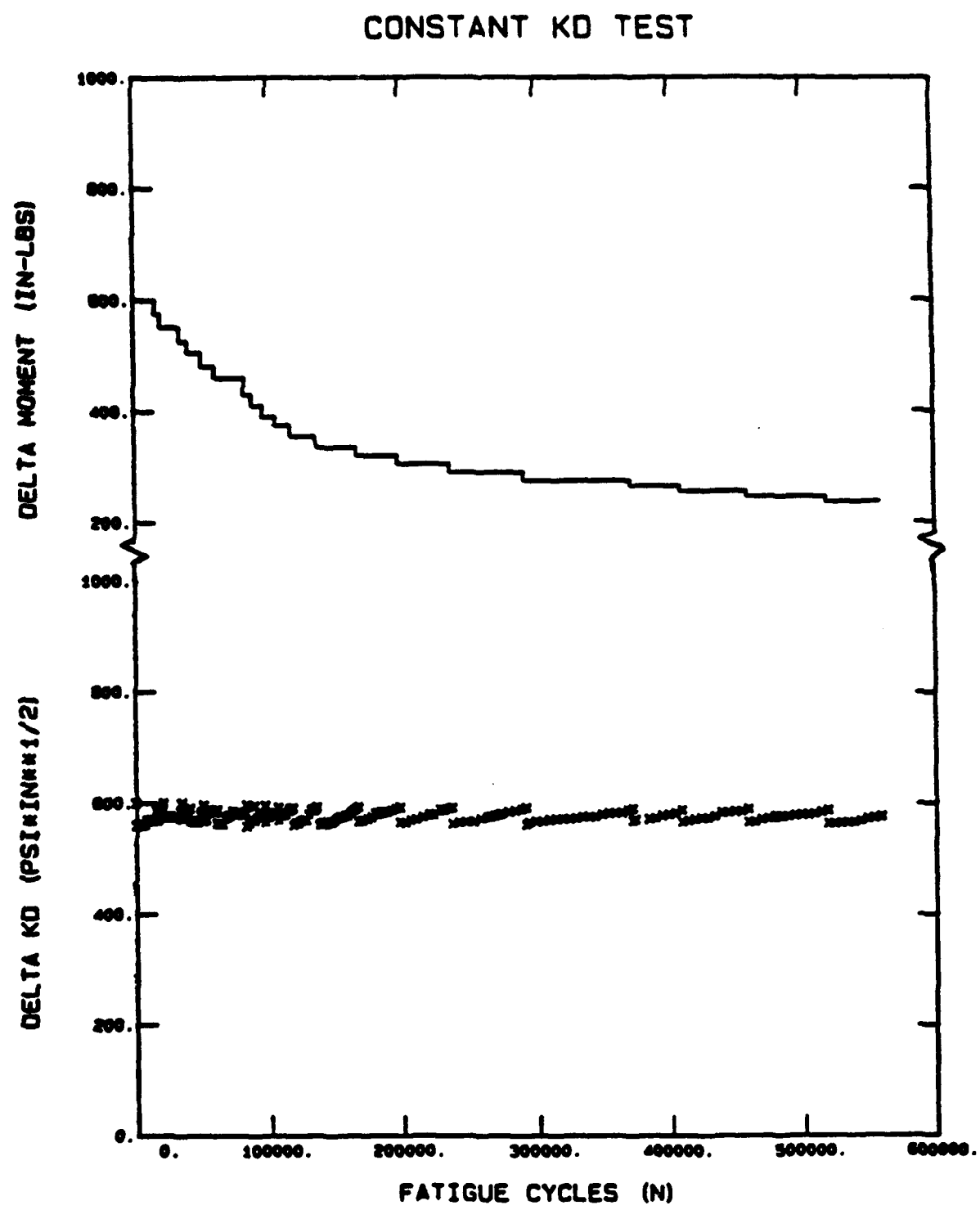


Figure 4.7 Actual load shedding pattern, and constant stress intensity factor calculated at the crack tip free-surface (ΔK_d , $\phi=0$ degrees), to maintain a constant plastic zone wake.

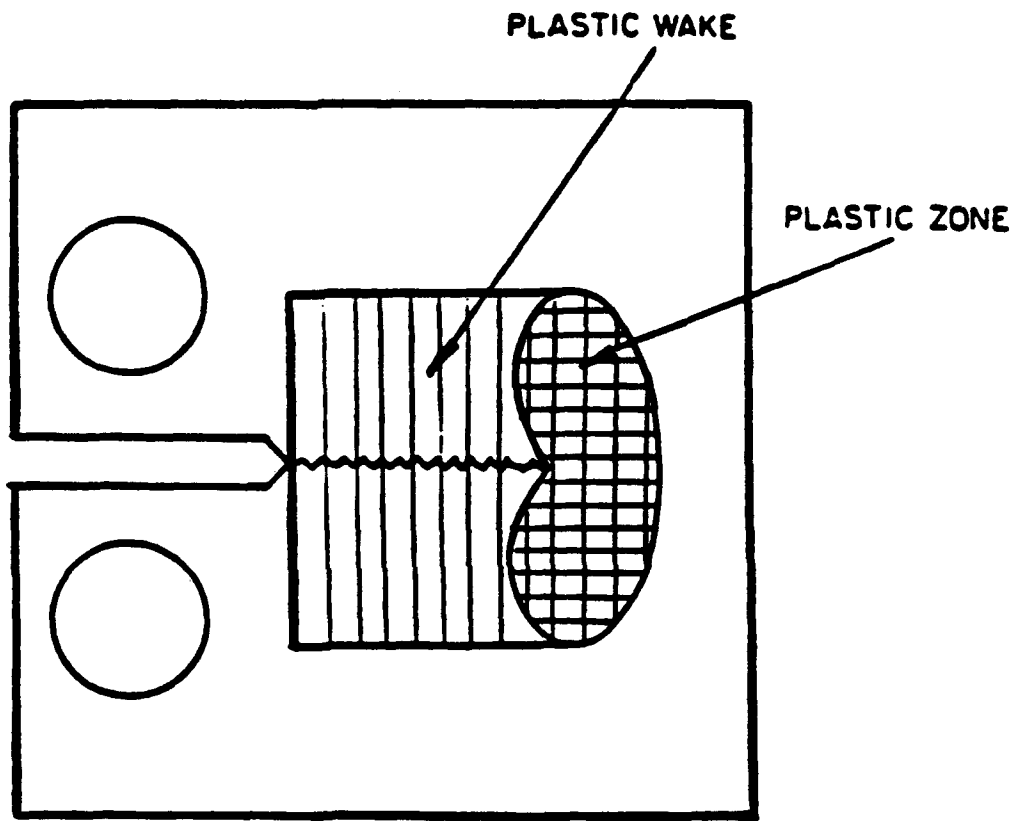


Figure 4.8 Schematic of the plasticity induced wake and residual plastic zone developed from a growing fatigue crack during a constant stress intensity factor cyclic load test in a thru-thickness specimen

Task 2: A constant ΔK_a load history test was conducted to produce a constant plastic zone size into the specimen thickness (location A, $\phi = 90$ degrees, Figure 4.3) by load shedding as the crack size increased during cyclic loading. The sinusoidal bending load-shed history produced the ΔK_a levels shown in Figure 4.9. Representation of the theoretical plastic zone is depicted by Figure 4.8. A constant ΔK_a of $600 \text{ psi}^{1/2} \text{in}^{1/2}$ ($659 \text{ KPa}^{1/2} \text{M}^{1/2}$) was maintained into the crack depth in order to make direct comparisons with data generated in task 1 (as discussed in the previous section, "Plasticity Considerations").

Task 3: A constant amplitude sinusoidal bending load test was conducted to produce a continually increasing plastic zone size along the crack tip boundary. The load history produced the ΔK_d levels shown in Figure 4.10. The continually increasing plastic zone size resulting from crack growth under a constant load, which produces a continually increasing ΔK , is schematically depicted in Figure 4.11.

Task 4: A block loading test (Figure 4.12) was conducted using constant moment segments to evaluate the effects of large plastic zones on closure and fatigue crack growth. Each block loading segment was maintained at a constant bending moment until predetermined ΔK_d levels were reached. The initial block loading segment used a $\Delta M = 644 \text{ in-lb}$, or a ΔK_d level which increased from 608 to $657 \text{ psi}^{1/2} \text{in}^{1/2}$ (40% to 44% of a published reference fracture toughness value of $1500 \text{ psi}^{1/2} \text{in}^{1/2}$, Ref. 27). The load was then increased 20% to a ΔK_d of 790 (53% of K_{1C}), and the specimen fatigued until a ΔK_d value of 996 (66% of K_{1C}) was reached. The load was then decreased 20% to the original starting load level of $\Delta M = 644 \text{ in-lb}$, or $\Delta K_d = 830$ (55% of K_{1C}). Testing continued at this load level until a ΔK_d of 1191 (80% of K_{1C}) was achieved. The final block loading segment was accomplished by reducing the load level 50% to the initial baseline ΔK_d level ($608 \text{ psi}^{1/2} \text{in}^{1/2}$), and testing continued until a large crack size ($a \approx 0.5$, or approximately half through the specimen thickness) was reached ($\Delta K_d = 836$). The intent of this cyclic block

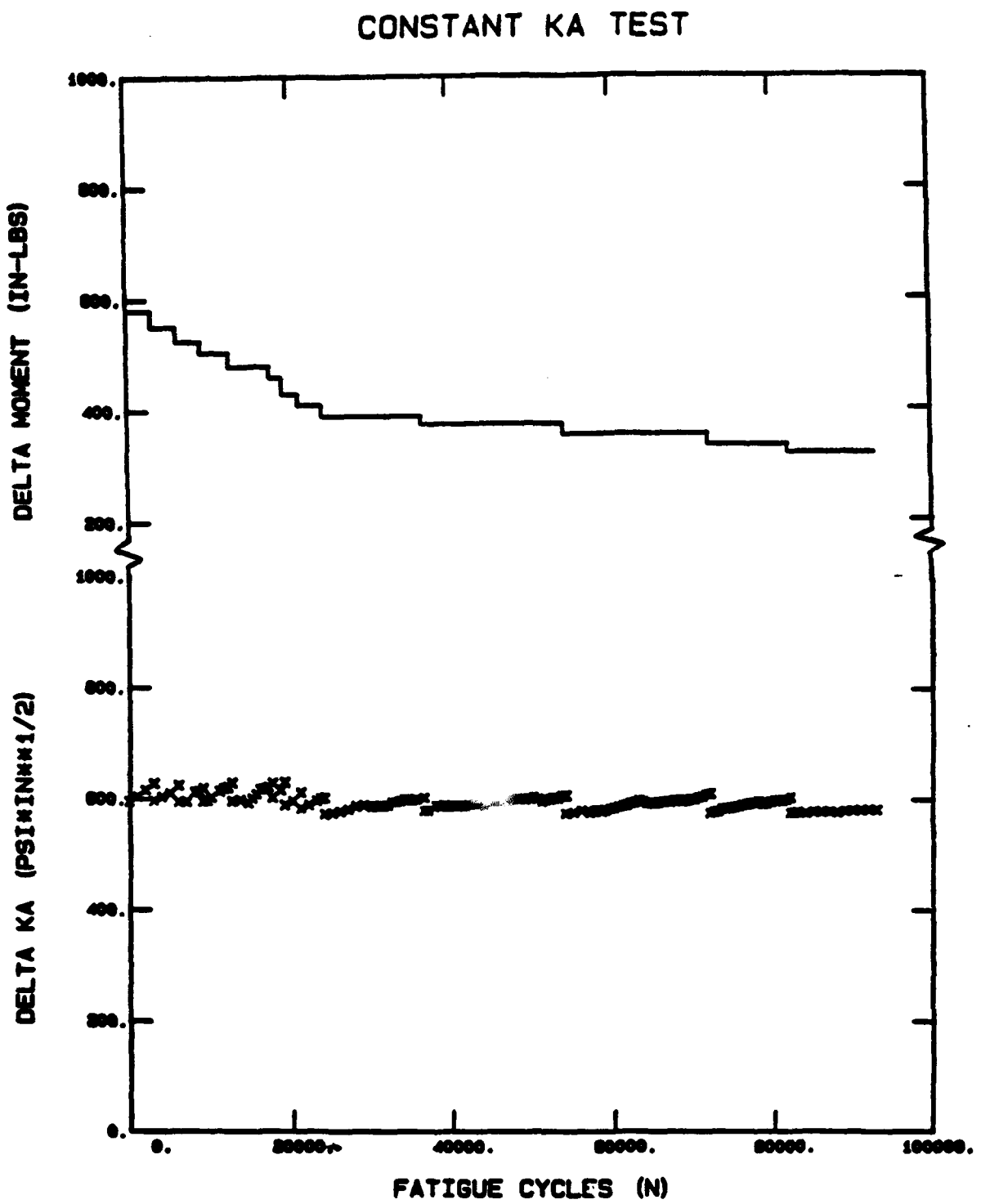


Figure 4.9 Actual load shedding pattern, and constant stress intensity factor calculated at the crack tip internal to the specimen thickness (ΔK_A , $\phi=90$ degrees), to maintain a constant plastic zone wake.

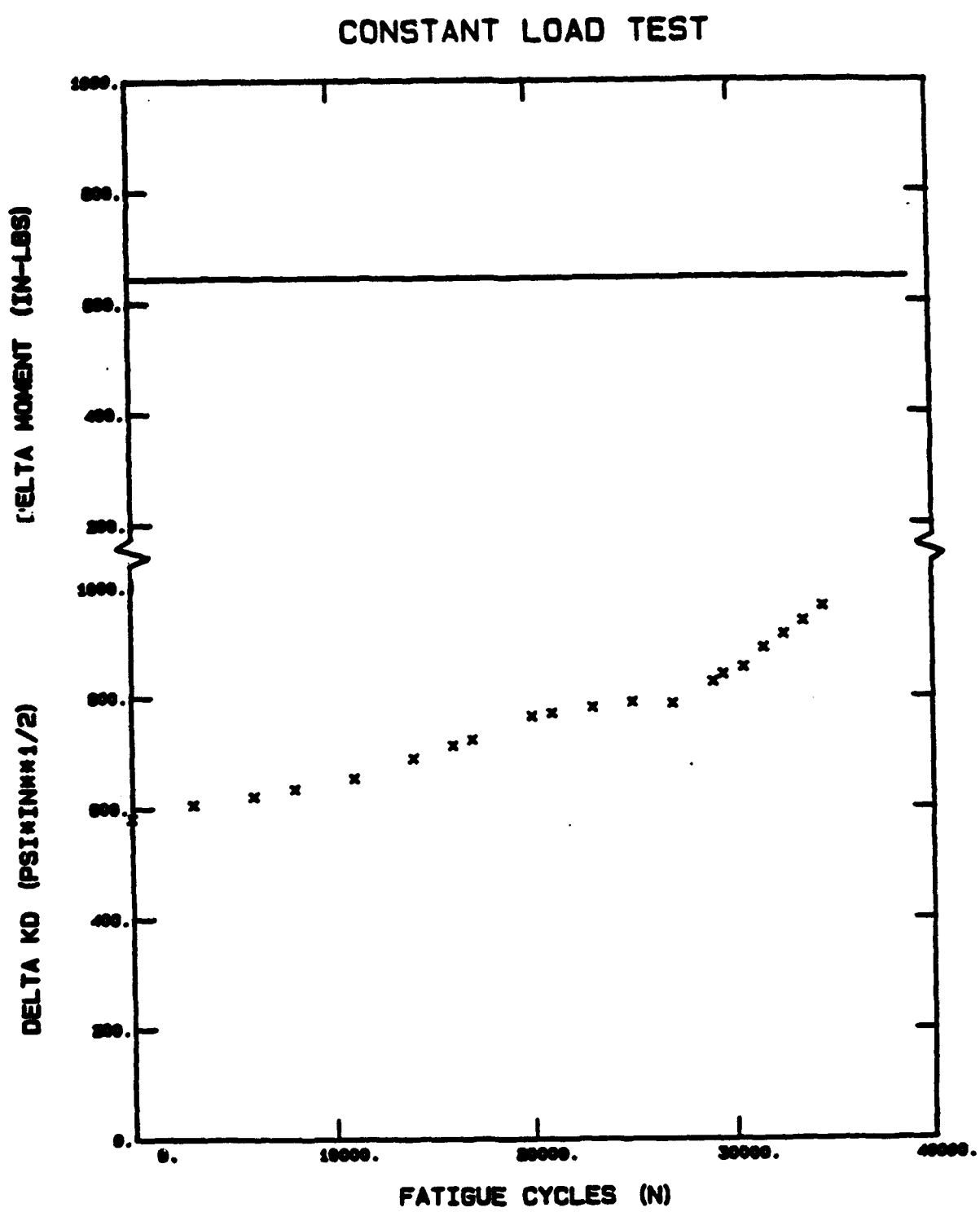


Figure 4.10 Actual applied constant load, and variable stress intensity factor calculated at the crack tip free-surface (ΔK_d , $\phi=0$ degrees), to generate a continually increasing plastic zone wake.

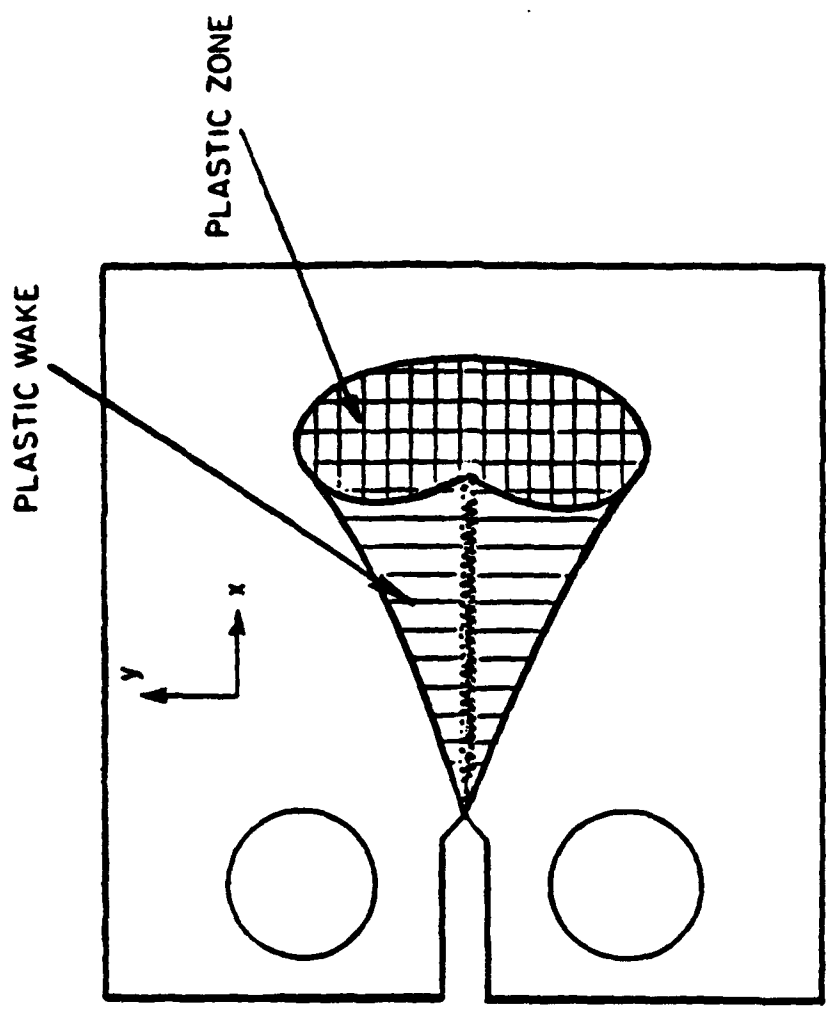


Figure 4.11 Schematic representation of continually increasing plastic wake generated by growing a fatigue crack during a constant amplitude cyclic load control test (ref. 3)

BLOCK LOADING TEST

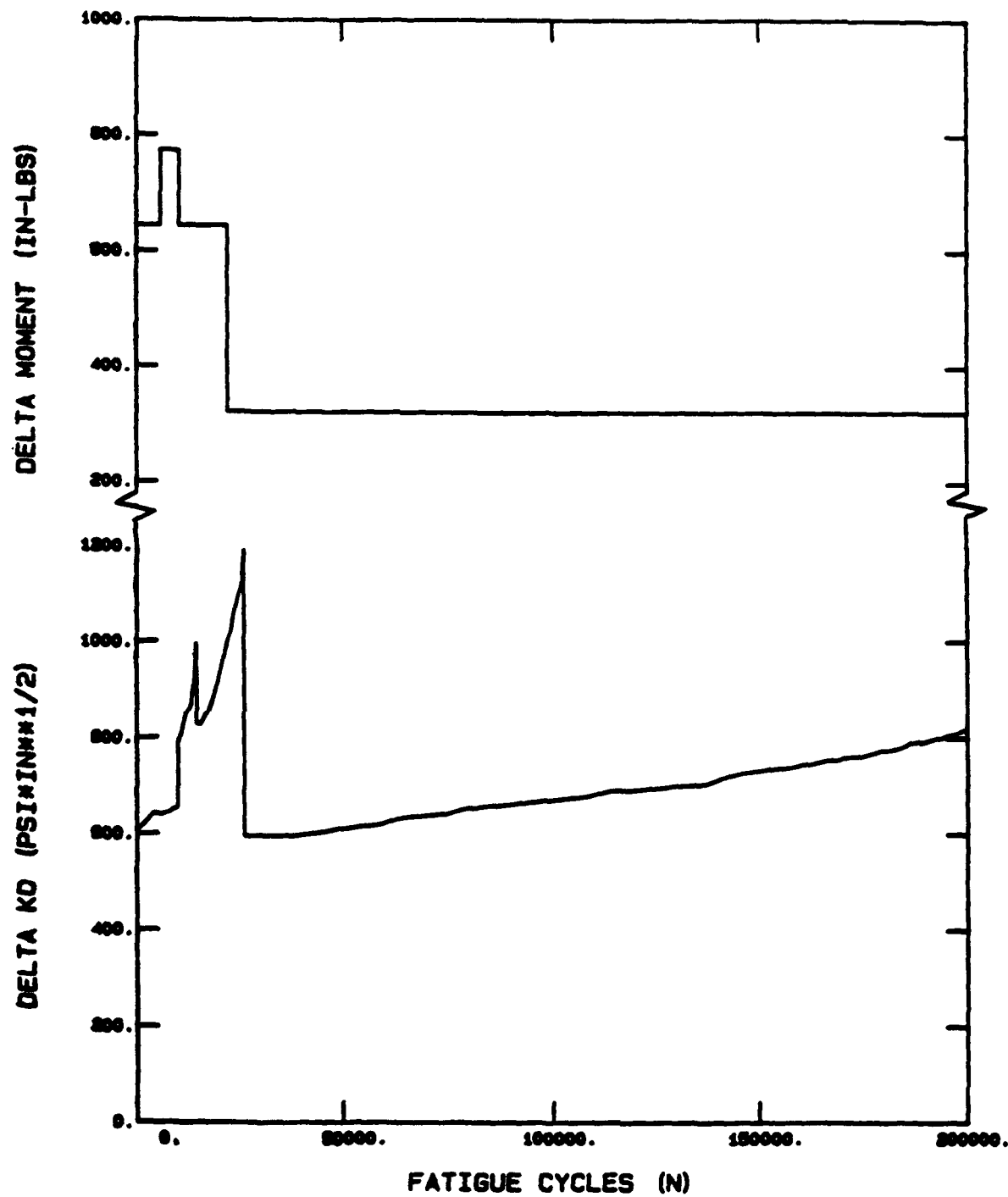


Figure 4.12 Actual block loading pattern, and resulting stress intensity factor calculated at the crack tip free-surface (ΔK_d), to generate large plastic-zone wakes

loading pattern was to grow the crack through two large plastic zones. The crack was grown at least 20 plastic zone diameters past the initial crack tip location before changing the load level.

All four tests used the same precracking procedures to establish a consistent baseline starting ΔK of 600 $\text{psi} \cdot \text{in}^{1/2}$. The two constant stress intensity factor tests were maintained at locations A and D (tasks 1 and 2) to within $\pm 3.7\%$ ($\pm 22 \text{ psi} \cdot \text{in}^{1/2}$ or $\pm 24 \text{ KPa} \cdot \text{M}^{1/2}$) by regularly measuring the "a" and "c" crack dimensions and calculating K levels at those crack sizes. Once a level less than 620 $\text{psi} \cdot \text{in}^{1/2}$ ($680 \text{ KPa} \cdot \text{M}^{1/2}$) was reached, the load was reduced to achieve a level which was greater than 580 $\text{psi} \cdot \text{in}^{1/2}$ ($637 \text{ KPa} \cdot \text{M}^{1/2}$) and the fatigue cycling continued.

Tasks 1 and 2 were selected to emphasize the relative differences between the larger plane stress and smaller plane strain plastic zone at locations A and D on the crack boundary. That is, controlling ΔK_d along the crack free-surface (task 1) to emphasize the plane stress ($\sigma_z=0$) influences. Likewise, controlling ΔK_a into the crack depth (task 2) to emphasize the plane strain ($\epsilon_z=0$) influences on closure relative to task 1.

Comparison of closure load differences due to a constant plastic zone wake pattern and a continually increasing wake pattern (Figures 4.8 and 4.11, respectively) is accomplished by comparing results from task 3 with tasks 1 and 2.

The block loading test (task 4) was conducted to compare relative effects of large plastic zone wakes on closure loads. That is, will the closure load levels for cracks which grow through large plastic zones be significantly different from those generated by the constant ΔK tests?

The four load histories provided a unique set of data for evaluating the influence of plastic zone size on the mechanisms of closure. These test results (task 1-4) are then used to make comparisons between the individual and combined influences of crack opening

displacement (COD) and closure loads on fatigue crack growth characteristics, as discussed in Chapters V and VII.

Specimen Material Selection

To meet the research objectives of measuring surface flaw internal crack opening displacements (COD) and closure loads simultaneously, it was desirable to use a transparent material whose crack growth properties are described using conventional fracture mechanics. This was accomplished by selecting polymethylmethacrylate (PMMA), a polymer which has been used extensively over the past 15 years for fracture mechanics investigations (16,18,20,25,30,31). Although PMMA has been found to be a very good polymer for conducting fatigue crack growth investigations, it is also important to recognize that PMMA is viscoelastic, and that its crack growth characteristics can change under certain test conditions. For this reason, a great deal of attention was paid to controlling and evaluating the influence of variables which can change the polymer crack growth characteristics during the fatigue test (such as test frequency, environmental temperature, viscoelastic relaxation, etc.).

One of the more comprehensive reviews of polymers was conducted by Hertzberg and Manson (32). Their reviews identified the major test variables (test frequency, temperature, etc.) which need to be considered when conducting fatigue crack growth investigation with polymer materials. These variables have undergone a thorough review for this research, and essential variables controlled during the test. The following sections discuss these variables, and address both the positive and negative aspects of using PMMA material for this investigation.

Material Selection

Polymethylmethacrylate (PMMA) is a transparent polymer which has been used in numerous fracture mechanics investigations (16,18,20,25,31,32). A review of polymers by Hertzberg, Manson and Wu (33) found that PMMA, polycarbonate (PC), acrylonitrile-butadiene-styrene (ABS) resin, polyethylene (LDPE) and nylon 66 are a few of the more widely used polymers which follow the familiar fracture mechanics power function relationship between fatigue crack growth rate and stress intensity factor (Figure 4.13).

The positive aspects of using the transparent PMMA as a model material for crack closure studies are summarized by their capability to:

Exhibit conventional fatigue crack growth properties described by fracture mechanics; power law relationship of da/dN versus ΔK , Figure 4.14.

Provide the opportunity to measure three-dimensional crack closure, crack opening displacement (COD) and crack growth patterns (a and c) simultaneously since it is a transparent material (not directly available with metals).

Exhibit closure load ratios (closure load to maximum applied load) which are in the same range as reported for ductile and brittle metals, as well as analytical predictions (Table 2.1).

The limitations of PMMA as a model material for studying fatigue crack growth are also important to the success of this investigation. The primary variables which need to be controlled and/or evaluated during experimental fatigue crack growth testing are:

- Test frequency
- Environmental temperature and humidity
- Viscoelastic relaxation with time

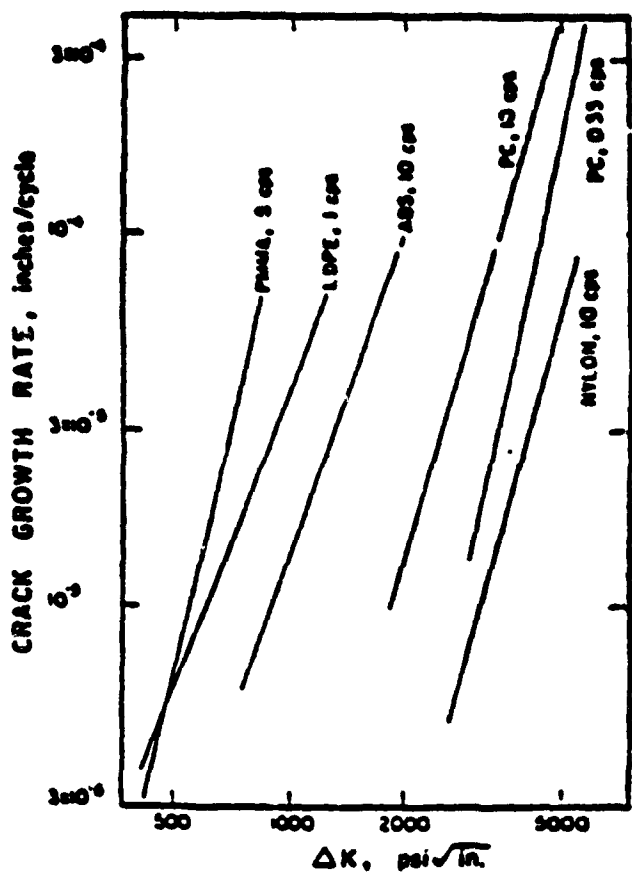


Figure 4.13 Fatigue crack growth rate curves for several engineering polymers; curves for polymethylmethacrylate (PMMA), low density polyethylene (LDPE), acrylonitrile-butadiene-styrene resin (ABS), polycarbonate (PC), and nylon 66 (Ref. 32)

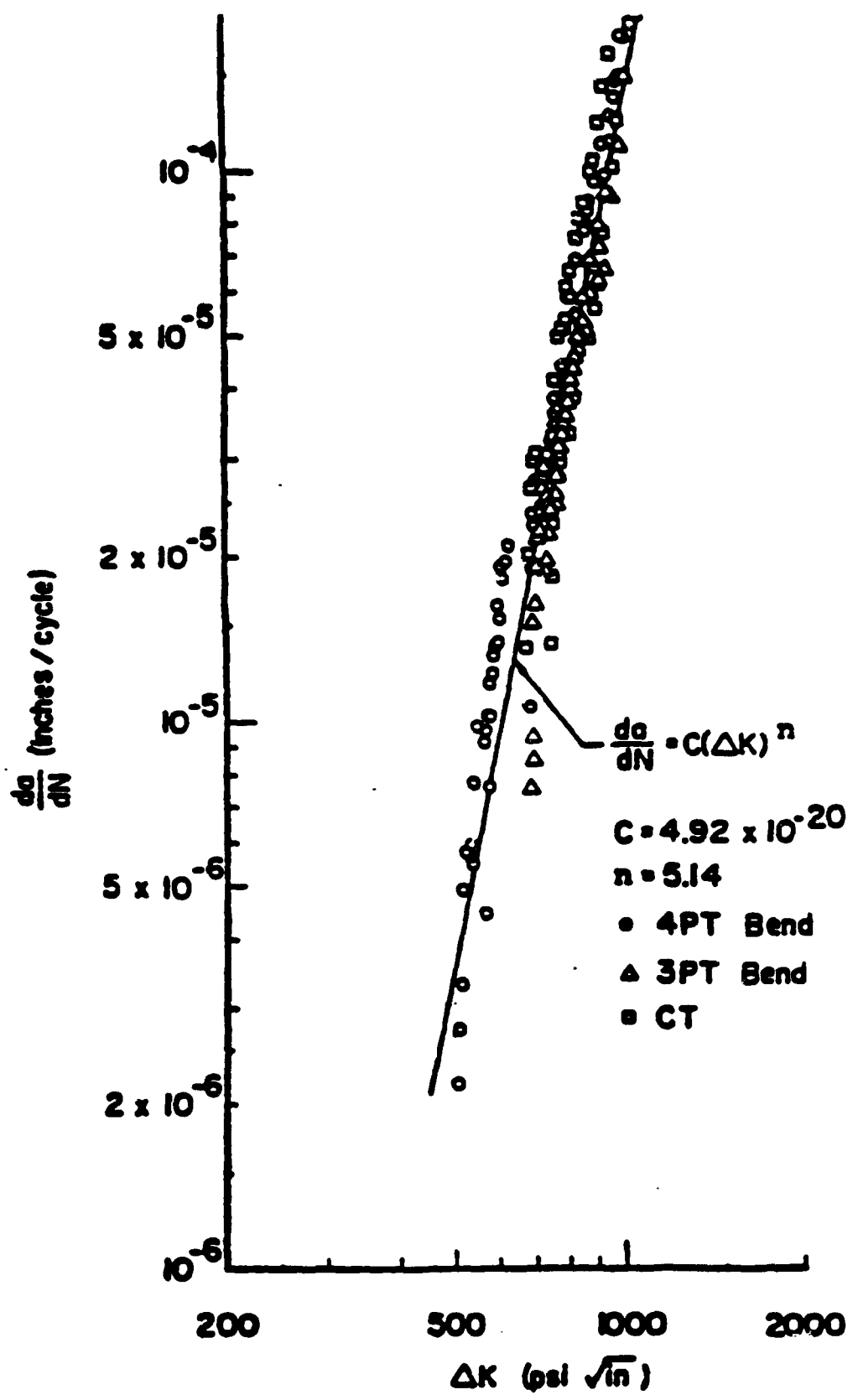


Figure 4.14 Fatigue crack growth rate curve for PMMA (ref. 19)

Each of these variables, and their relationship to this investigation, are discussed in the following sections.

Polymer Characteristics

As with metals, PMMA fatigue crack growth rates are dependent upon frequency, loading wave form, environment and temperature. Of the six categories reviewed by Hertzberg and Manson (32) (molecular characteristics, chemical changes, homogeneous and inhomogeneous changes, transition phenomena and thermal heating), the effect of local thermal heating due to test frequency is the area which requires the greatest control for the present investigation. The other variables were controlled by using the same material batch and annealing procedures for all the tests, as well as conducting the tests at room temperature.

Experimenters have shown that a test frequency above approximately 10 Hz can have a significant effect on PMMA crack growth rates. Atermo and Ostberg (34) showed that higher test frequencies cause excessive heat build-up at the crack tip. It is hypothesized that above 10 Hz, the conductivity of a polymer is not sufficient to dissipate heat away from the crack tip. This results in a local crack tip heat build-up which causes the local crack tip region to reach a "glass phase" state. In this "glass phase," polymers will absorb moisture and exhibit different fatigue crack growth characteristics. It was observed by Hertzberg and Manson that:

"...although heat transfer from the plastic zone to its cooler surrounding environment might limit the rate of crack-tip heating, fatigue testing at high frequencies should nevertheless produce a finite temperature rise at the crack tip. To wit, Atermo and Ostberg [79] recorded a maximum increase in crack-tip temperature of up to 20 degrees K in fatigue testing of PVC, PMMA, and

PC at 11 Hz. With a significant increase in temperature, yielding processes in the material surrounding the crack tip should be enhanced and lead to an increase in the crack-tip radius. This greater radius of curvature at the crack tip should result in a lower effective ΔK . As the effective ΔK decreases, the fatigue crack growth rate is expected to decrease accordingly."

The potential for absorption of moisture at the crack tip was also controlled during the fatigue test. Although effects of humidity are only known to occur when the polymer reaches its "glass phase" temperature (a condition prevented by testing at a low frequency), precautionary measures were taken by sealing the specimen surface around the crack free-surface with a desiccate material.

Relaxation of PMMA

Thru-thickness Cracks. Pitoniak, et al. (20) reported that PMMA crack opening displacement (COD) profiles tend to relax (change in crack internal surface displacement) under zero load. He observed that by allowing the specimen to relax for 1, 15 and 180 minutes after fatiguing the specimen, the internal COD magnitude would decrease. Utilizing information provided in the report, this displacement was calculated to be approximately 2.49E-5 in (6.3E-4 mm), or an 18% change in the total displacement under zero load between 1 minute. and 180 minutes Half of this relaxation was noted to occur within the first 15 minutes. These observations initiated a similiar investigation in this experiment of surface flaws. Results of this effort are discussed in the next section.

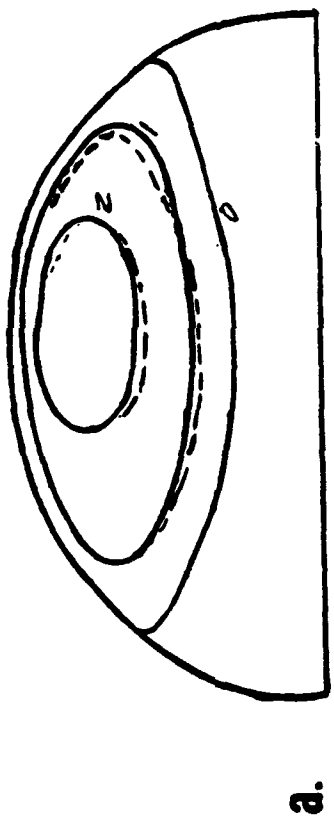
Surface Cracks. An extensive evaluation of surface crack relaxation in PMMA was conducted during this investigation. The need for the evaluation was based on prior findings for thru-thickness compact tension tests discussed above. The surface crack evaluation was accomplished by measuring crack relaxation at various crack sizes as the specimen was

fatigued. The review included the recording of crack displacement changes, as measured using the laser interferometry system, after various relaxation hold times at zero load (no external load on the specimen) and with loads above the closure load levels.

Example tracings of enlarged 35mm photographic negatives showing COD profile patterns before and after the relaxation hold times are presented in Figures 4.15a and b for two crack sizes. The figures are enlarged to emphasize the differences, but are proportional to each other. The solid fringe order contour lines were recorded immediately after testing, and the dotted lines 15 minutes later. Figure 4.15a presents the smaller crack size ($a = 0.12$, $c = 0.14$) under an applied load of 17% of the maximum fatigue load. No changes were noted under zero load for this crack size. Figure 4.15b presents the larger crack size ($a = 0.19$, $c = 0.30$) under zero load. Note the larger number of fringe orders, representing a larger internal displacement, but only minor differences due to the relaxation hold time.

An evaluation of the load needed to return a crack to its original displacement after a 20-minute-relaxation time was conducted for one crack size ($a = 0.079$ in and $c = 0.097$ in). This restoring bending moment was found to be 0.65 in-lb (0.0734 N-m) -- that is, the moment needed to compensate for the relaxation effect. This is 0.11% of the maximum bending moment applied to the specimen during fatigue testing.

Repeatability of the loading and unloading measurement process was also calibrated during the tests. Upon loading a specimen with a crack size of $a = 0.074$ in (1.88 mm) and $c = 0.097$ in (2.46 mm), the first fringe was formed at a load level of 47 in-lb (4.8 N-m), and the crack free-surface initially opened at 67 in-lb (7.6 N-m). Continuing to increase the load level above the COD elastic region (approximately 152 in-lb or 17.2 N-m) and then unloading the specimen, the first fringe order formation occurred at 38 in-lb (4.3 N-m). Continuing to unload the specimen to zero and then reloading, the first fringe order was formed at 41 in-lb (4.6 N-m) -- compared to 42 in-lb during initial loading. This repeatability was demonstrated approximately 20 minutes after the initial load cycle. These measurements represent a repeatability of approximately 2% for an "opening" load

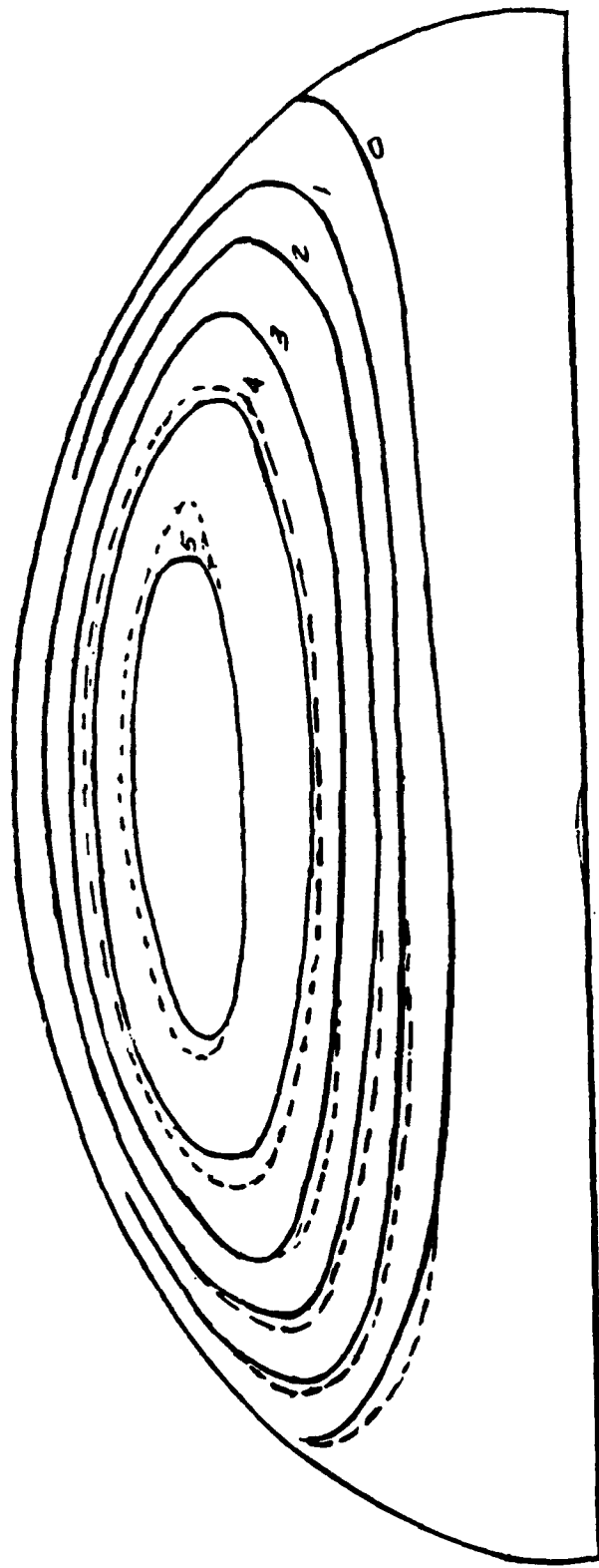


a.

Figure 4.15 Interference fringe order traces showing relaxation effects immediately after test cycling (solid contours lines), and after 15 minutes of hold time (dotted lines) for (a) high aspect ratio crack ($a=0.12$, $c=0.14$), at an applied load of 17% of the maximum, and (b) a low aspect ratio crack crack ($a=0.19$, $c=0.30$), at zero load

b.

Figure 4.15 (Continued)



measurement process, and approximately 10% difference between measurements when "loading" versus "unloading" for this crack size.

In general, the variability of opening load measurements was about 2% for smaller crack sizes -- where the opening load levels were greater than 40 in-lb (4.5 N-m). For larger crack sizes (where the moment required to open the crack was 25 in-lb instead of 40 in-lb) the variability increased from 2% to approximate 10%.

Specimen Preparation

A great deal of care was taken to develop a repeatable crack initiation site and precracking load cycle procedure. This effort was undertaken to minimize precracking effects on the fatigue crack growth experimental results. Primary consideration was given to repeatability of the procedures from specimen to specimen. Other important specimen preparation procedures discussed in this section include annealing and end polishing.

Specimen Size

The experimental tests used a 0.75 x 3 x 7 inches (19.1 x 76.2 x 177.8 mm) specimen with a part-thru crack on one face (Figure 2.1 and 4.16). The specimen size was selected after reviewing recommendations from two primary sources. Jolles, McGowan and Smith (36) indicated that a plate specimen with a width of two and a half times the crack length (2c) experienced the same stress intensity as those for plates of infinite width. Anderson (6) suggested that the width be two and a half times the crack length and the specimen length be two times the width. For this experimental investigation, the selection of a maximum crack length of 1.20 in (30.5 mm) met both of these specimen size criteria.

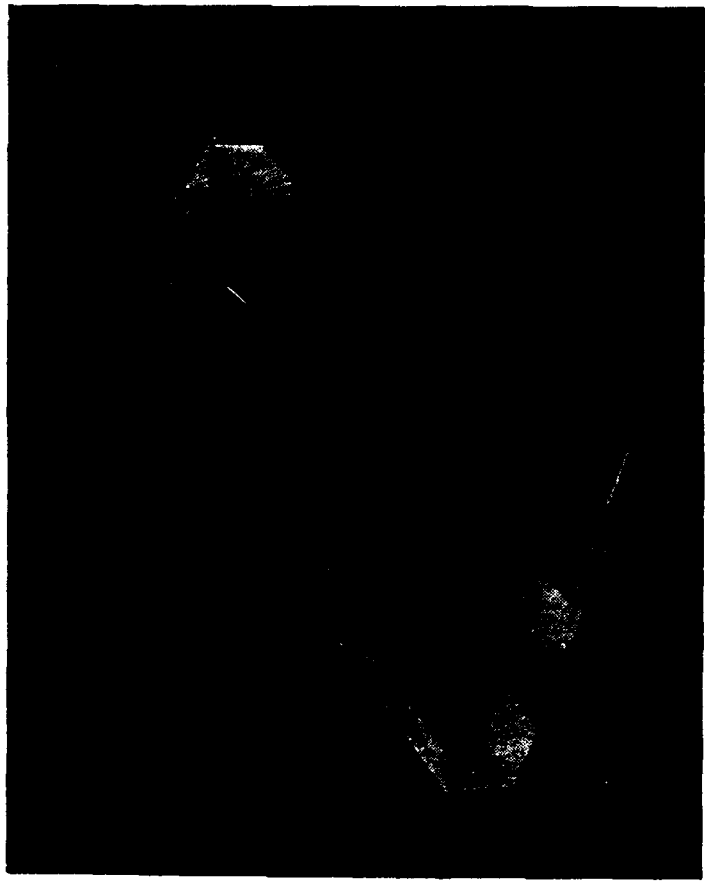


Figure 4.16 Photograph of the PMMA specimen before testing. Note the polished end and crack initiation site located in the specimen center

Specimen Annealing

The specimen annealing process followed those used by Perez (37) to minimize potential residual stress developed in the specimen during machining. The PMMA specimen was annealed at 100 degrees centigrade for 24 hours prior to precracking. The cool down cycle was performed at a rate of approximately 3.5 degrees C per hour until the oven reached 50 degrees C. The specimen was then allowed to cool down to room temperature with the oven door closed. Total cooling time was approximately 48 hours.

Specimen Polishing

In order to utilize the laser interferometry system for measuring interference patterns, it was necessary to have a flat transparent finish on one end of the PMMA specimen. The end polishing procedures developed at the Air Force Wright-Patterson Materials Directorate (38) are as follows:

1. Select the end with the smoothest surface before beginning. Grind that end of the sample with an 8 in diameter polisher at 350 rpm using an 8-in PSA silicon carbide 600-grit disc. This operation should continue until the surface is relatively smooth.
2. Wash the specimen in soap and warm water to remove all residue; flush with methanol and blow dry with hot air.
3. Polish the specimen on an 8 inch diameter polisher using 8 inch PSA nylon cloth, 3-micron diamond paste and oil lubricant. Polish at 350 rpm until surface deformations from the 600-grit polishing operation are completely removed.

4. Clean the specimen as in step #2.
5. Polish the specimen on an 8 inch diameter polisher with an 8 inch PSA micro cloth using 0.06-micron colloidal silicon suspension at 200 rpm until the surface is smooth and transparent.
6. Clean the specimen as in step #2.

Crack Initiation Site

The development of an accurate and repeatable crack initiation site was an important part of the precracking process. It was initially decided that a material removal approach would be used to eliminate buildup of excess material experienced by an indent procedure. Several material removal procedures were considered: (1) feeding the specimen into a rotating foil, (2) scribing a straight line on the specimen with a knife edge, and (3) scribing a mark with a rotating knife edge. The rotating knife edge was selected because it best represented a surface crack shape, and was the most uniform and repeatable crack initiation method.

The crack initiation site procedure was developed to control the cut length and depth dimensions. This was accomplished by using a lathe, with the PMMA specimen mounted on the traversing bed and a knife-edge cutting tool mounted to the lathe rotating head. After mounting the specimen on the lathe, the bed was traversed to the knife-edge which was brazed to a circular rod. The knife-edge was located next to the specimen mid-surface using a thin shim, then rotated away from the specimen and the lathe table (with the specimen) traversed toward the cutter to set the initiation site depth. The knife-edge cutter was then rotated into the specimen, nicking the PMMA material. This procedure scribed a consistent

crack initiation site of 0.005 inch (0.13 mm) deep by 0.060 inch (1.5 mm) long into the specimen surface (Figure 4.17). The knife-edge radius of curvature was 0.0925 inch. All specimens were scribed at the same time to ensure consistency of the crack initiation site (Figure 4.16). Figure 4.17 also identifies an "initial crack" site (dotted lines) where the real crack growth began versus the scribed initiation site generated by the knife-edge cutting tool (solid line). This "initial crack" location and subsequent growth pattern were typical for all tests. With fatigue cycling, the "initial crack" encompassed the initiation site during precracking, and grew to at least 1.5 times the crack initiation site length along the free-surface, and 8 times the initiation site depth into the specimen (as discussed in the next section).

Precracking Procedures

The precracking load shed procedures followed ASTM standard practices for a thru-thickness crack, plus additional criteria established for this investigation of surface flaw. The load level was kept below 80% of the material yield strength, and typically ran below 30% of yield after precracking. The load shedding cycle was established to meet the plastic zone size (or stress intensity factor levels) requirements. This was accomplished by measuring "a" and "c" crack lengths with the traveling microscope, and calculating stress intensity factors (K) using the Newman-Raju (5) solutions to determine when the load should be reduced. The load shedding procedure maintained a constant stress ratio of $R = 0.035$. This ratio was selected to be close to zero while maintaining a positive load on the specimen throughout the test.

A concentrated effort was initiated to define a precracking load cycle which combined both the ASTM standards (39) and additional criteria established for this tests (items 2-4 below). Since there were no ASTM precracking standards for surface flaws, the

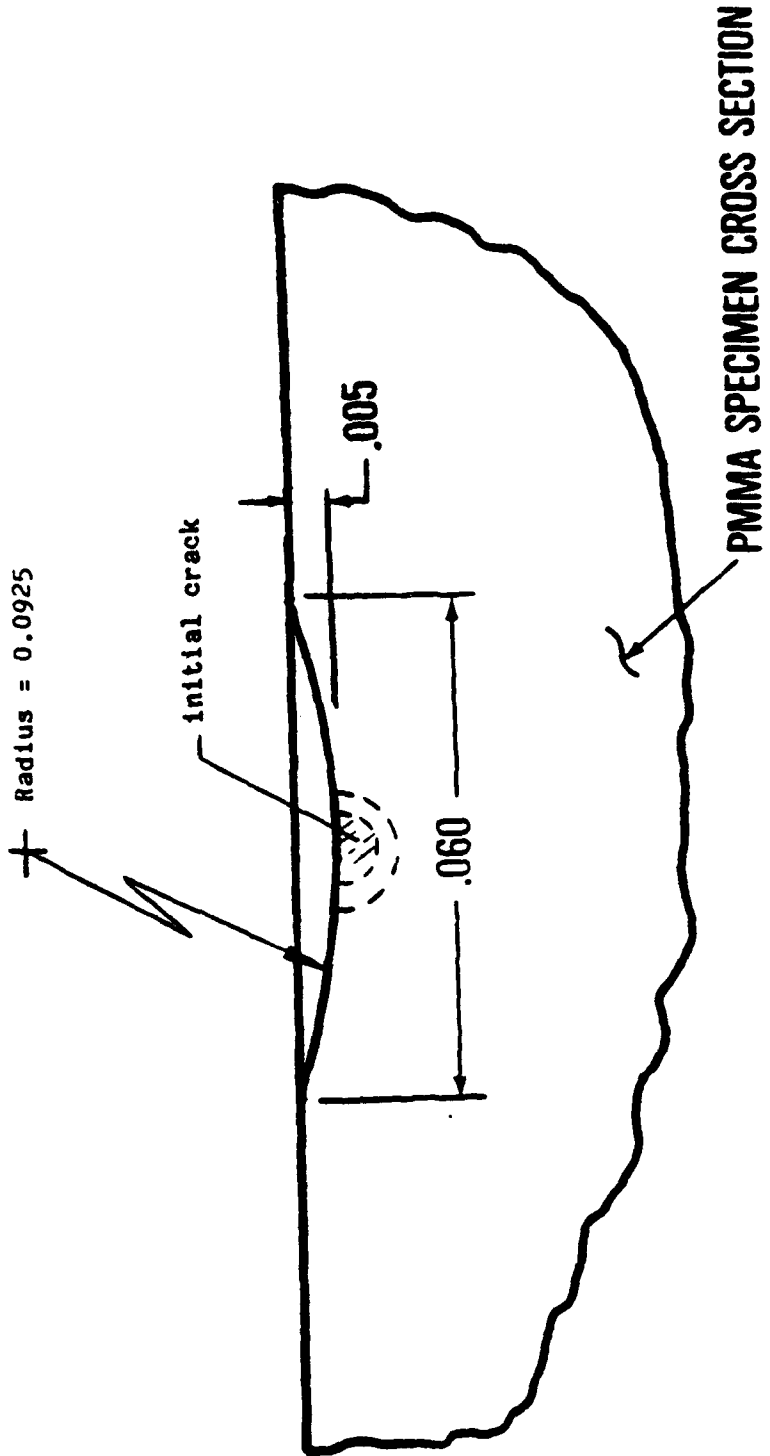


Figure 4.17 Cross-section schematic of the symmetrical crack initiation site showing the cutting tool radius of curvature

standards and the intent of the ASTM thru-crack standards were followed. This was accomplished by writing an iterative computer code to: (1) meet ASTM thru-crack standards, (2) initiate all experimental tests at the same crack tip plastic zone size along the crack surface, (3) ensure the crack size before the fatigue crack growth analysis began (after precracking) was sufficiently large to encompass the crack initiation site, and to be accurately recorded by the laser interferometry photographic system and the traveling microscope, and (4) ensure the plastic zone size was decreased after each load shedding step. In effect, the iterative computer code defined a precracking load shed cycle while maintaining ASTM and other criteria for this investigation of surface flaws.

The ASTM load shedding criteria states that the load shedding level shall be less than 20% of the maximum applied load, and the crack should grow at least 3 times the prior plastic zone diameter. Additional criteria established under this investigation of surface flaws were the minimum to maximum load level (R) be maintained at 0.035, the maximum load level would not exceed 80% of the material yield strength, a crack length "c" would be greater than 0.010 inch (0.25 mm) before the first load shedding occurred to produce an accurate crack length measurement, the load levels were not above the critical stress intensity factor nor below the threshold stress intensity levels, and that the plastic zone size was decreasing from the prior step to the end of the next load shed step.

To meet the above criteria, an assumed value of crack aspect ratio was required for the iterative computational analysis. From experimental tests with PMMA, and experiments by Corn (40) and Mahmoud and Hosseini (41) using various metals, the a/c ratio was found to initially increase from a value less than 1.0 to a value greater than 1.0, and then to decrease below 1.0. For small surface cracks, an a/c value of 1.0 was found to be typical. A sensitivity study of a/c effects on K , using the Newman-Raju stress intensity factor calculations, established that aspect ratios in the range of $0.82 < a/c < 1.0$ only changed the K solutions a small amount. This information, plus additional calculations discussed in the Appendix computer section, led to the selection of 0.85 as an average value of crack aspect

ratio for the precracking load analysis. The value of a/c equal to the initiation site dimensions ($0.005/0.03 = 0.17$) was not realistic since the "initial crack" always started on the scribed initiation site surface (Figure 4.17) and propagated in a semicircular pattern as described in the last section.

The crack growth analysis in this report only uses measurements taken after precracking; although all precracking and crack growth experimental data are presented in Appendix A through D. Per ASTM standard E647 (39), the crack growth data begin when the crack has grown more than three times the plastic zone diameter of the prior load level. This criteria resulted in the fatigue crack size after precracking being at least 1.5 times the crack initiation site size along the surface length, and 8 times the initiation site size into the specimen depth.

Minimizing Precracking Influences

In addition to utilizing identical specimen annealing, crack initiation site and precracking load shedding procedures on each specimen, the final data set was reviewed to ensure the crack free-surface length had grown at least three times the plastic zone diameter after the last precracking load shedding step. This procedure was followed to ensure the experimental crack growth data used in the analysis followed ASTM precracking standards.

For example, the final precracking load shed surface stress intensity factor (ΔK_d) was 600 psi*in^{1/2} (659 KPa*M^{1/2}). For the constant ΔK_d data set (task 1) after precracking, the crack length $c = 0.0365$ inch (0.93 mm), and the plastic zone diameter is 8.73E-3 inch (0.07 mm). Then, for the crack growth data to be used in the analysis, the crack length was

required to be 3 times the plastic zone diameter, or:

$$c = 0.0365 + 3. * (0.0087) \quad (4.10)$$

$$= 0.0452 \quad (4.11)$$

Therefore, all data which had a "c" crack length less than 0.045 inch (1.15 mm) is defined as precracking data, and not used in the fatigue crack growth analysis. This same approach was followed for all fatigue crack growth data sets.

V. CRACK OPENING DISPLACEMENT AND CLOSURE LOAD MEASUREMENTS

The geometric crack opening displacement (COD) patterns and the closure load measurements generated from the experimental tests for surface flaws in bending are presented in this chapter. Because of the complex nature of fatigue crack closure, a number of new definitions were established to describe and organize the experimental data. Three new categories of COD and three definitions of closure load were identified. To differentiate between these effects, the chapter is divided into two major sections -- the first describing the geometric COD patterns which related to the whole crack, and the second describing the closure load measurements needed to define effective stress intensity factor (ΔK_{eff}). The implications of these results for defining ΔK_{eff} are discussed in Chapter VI, and their influence on predicting fatigue crack growth in Chapter VII. Comparisons between predicted and experimental COD data are presented in Chapter VII.

Crack Opening Displacement (COD) Profiles

The experimental investigation of surface flaws in bending has identified three primary crack opening displacement (COD) patterns defined here as types I, II and III. The uniqueness of these COD types is embodied in the crack surface displacement profile patterns under zero load, and during load application. Besides the pure geometric differences between the crack types, each has a direct impact on crack closure/opening load level and crack tip stress intensity factor; and thus, the definition of effective stress intensity factor.

A description of the COD patterns as they apply to crack size, applied load, and fatigue load history is presented in this section. Crack size is found to be a primary factor in organizing COD profile pattern data as will be described in the following sections.

Typical COD Profiles

The experimental investigation identified three primary crack types which were observed to be consistent for all tests. Each crack type is unique because of its influence on crack tip stress intensity factor (K) at various crack tip boundary locations. The crack tip locations identified in Figure 5.1 will be referred to extensively throughout this report. Location A defines the maximum crack depth location, location B the midpoint of the crack free-surface, location C is approximately 12 degrees from the crack tip free-surface, and location D is located at the crack tip free-surface. The angle δ identifies points along the crack perimeter, and is measured from the crack free-surface with respect to line AB (not the elliptical angle). The crack is assumed to be symmetrical about line AB. The fringe order lines (constant displacement contours) shown in the Figure are described in Section IV, "Newton Interference System."

The three crack types are schematically shown in Figure 5.2 for a zero applied load. The Figure is divided into two parts to describe the differences between "crack geometry" and observed "fringes" patterns. The cross-hatched area illustrates that the two mating crack surfaces are closed (in contact). The clear area (not cross-hatched) illustrates that the crack surfaces are separated, and is referred to in this report as a geometric "void." The dotted "fringe order" lines represent contours of constant crack opening displacement (COD) patterns.

The terminology "void" will be used in the remainder of the report to describe a displacement hump which is internal to the crack mating surfaces. This internal void

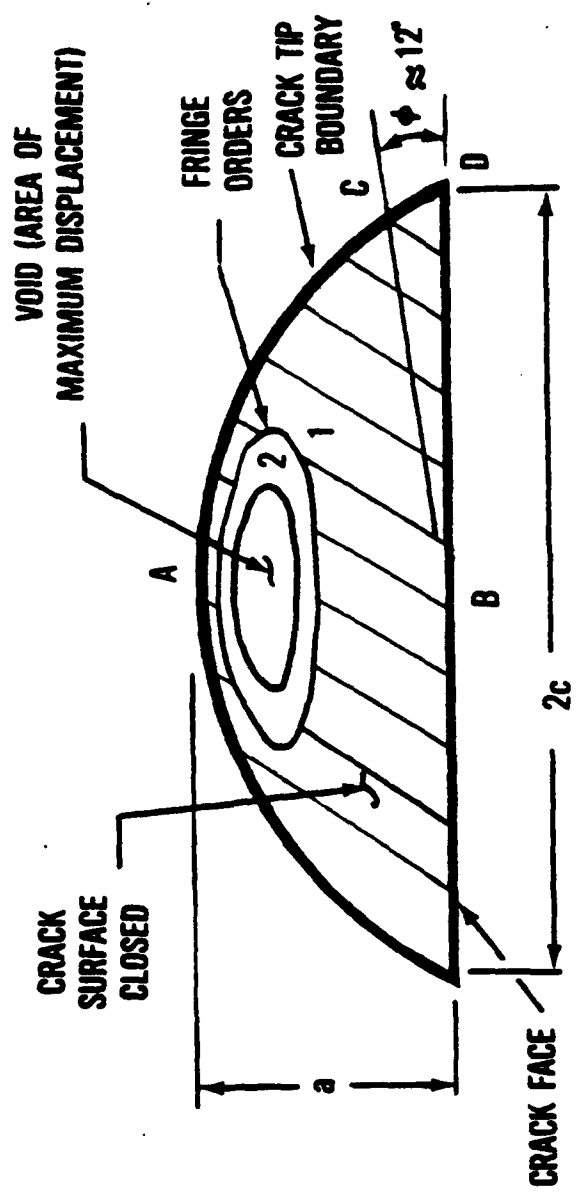


Figure 5.1 Surface crack schematic showing a void formation internal to the crack surface.

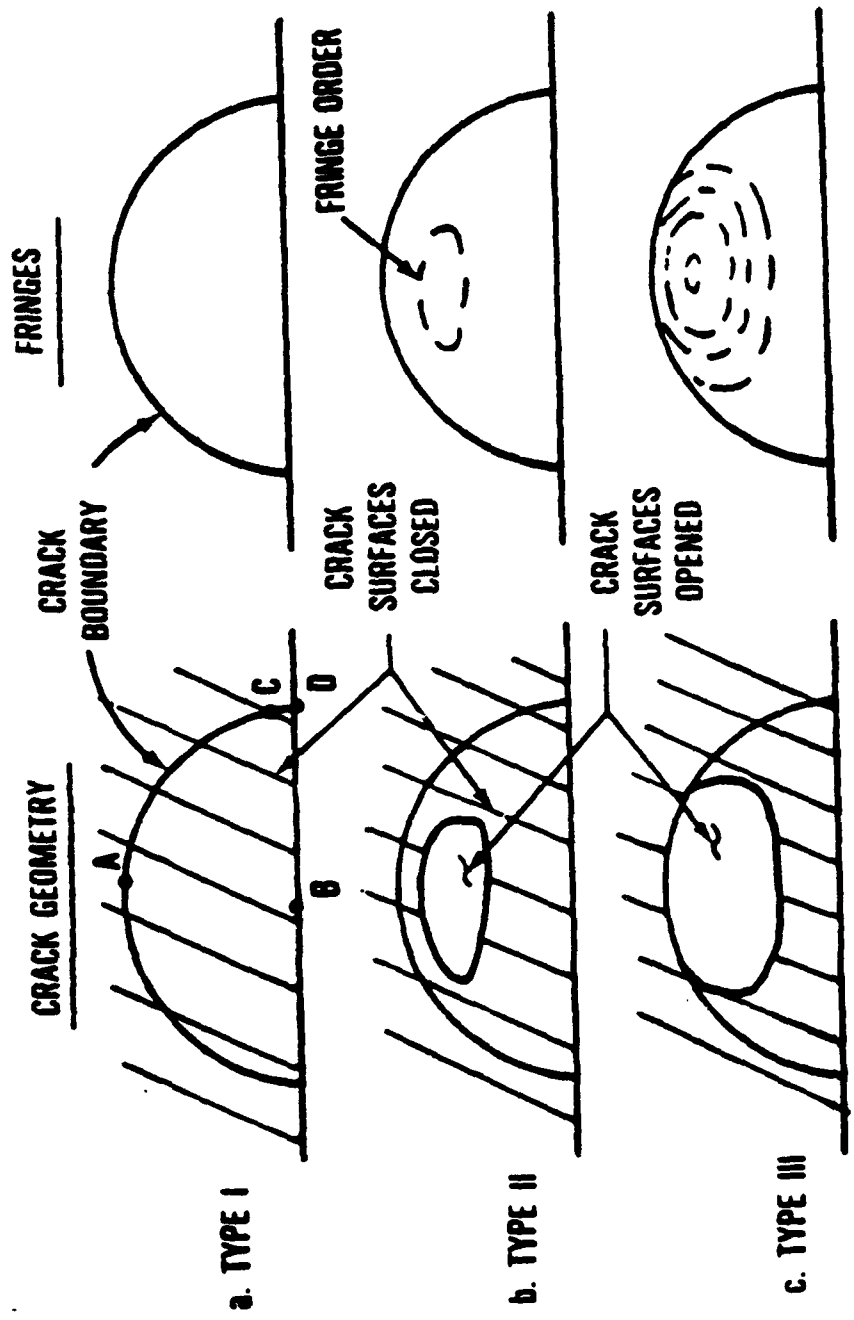


Figure 5.2 Schematic of the crack opening displacement patterns under zero load for the three crack types - type I, II & III

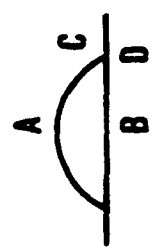
displacement is always open once formed even under zero load. The void formation is depicted in Figure 5.1 by the fringe orders, and shown by interference photos in Figure 4.3a-d.

A type I crack (Figure 5.2a) is defined as the crack geometry where the two mating surfaces are fully closed under zero load. This crack type is typically modeled as an elastic COD pattern. The type I crack was observed for smaller cracks having an a/t value less than 0.095 in this investigation.

As the crack grew in size due to fatigue cycling, a type II crack was formed (Figure 5.2b). This change in crack geometry occurs when the crack internal surfaces separate and form a displacement "void" close to the crack tip at location A. The pattern is distinguished by the interference fringe order contours under zero load. The uniqueness of a type II crack is that under zero load the crack tip boundary is fully closed, while there is an internal nonzero displacement void area separating the two crack surfaces. If the void displacement is too small to be detected by a fringe pattern (the void maximum displacement is less than 6.2E-6 inches), the crack initially opens at this location when load is applied (as shown by the fringe order formation). In this investigation, the formation of a type II crack ranged in size from an a/t of 0.068 to 0.095.

As the crack continues to grow due to fatigue cycling, the void size increases in area and height. This void growth forces the crack tip at location A to separate and remain open even under zero applied load. This opening of the crack tip defines a type III crack (Figure 5.2c). In this investigation, a type III crack was formed when the a/t range was between 0.139 and 0.189 for all tests.

Another means of visualizing the three void types is by slicing the crack between locations A and B ($\phi = 90$ degrees, Figure 5.1) as schematically depicted in Figure 5.3. For a type I crack (Figure 5.3a), the crack mating surfaces are completely closed under zero load. With increased crack growth, a type II crack develops when the crack surfaces separate (forming an internal void area) while the crack tip boundary remains closed (Figure 5.3b).



a. TYPE I

—
A (CRACK TIP)
B (CRACK FREE-SURFACE)

b. TYPE II



c. TYPE III

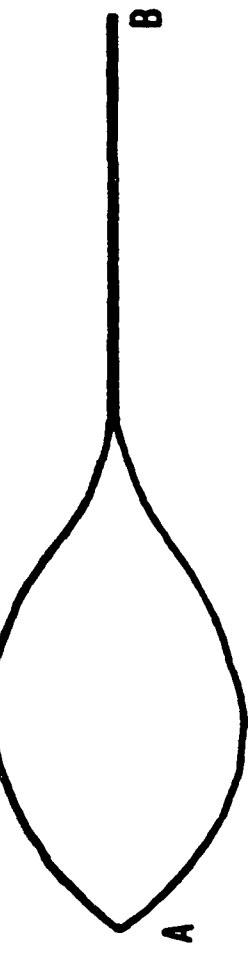


Figure 5.3 Cross-section schematic of the crack opening displacement pattern under zero load for the three crack types between location A & B ($\theta=90^\circ$ & 0° degrees, respectively)

As the crack continues to grow, a type III crack is formed when the void size is sufficiently large to open the crack tip at location A (Figure 5.3c).

The percent of crack tip boundary AD which is open for a type III crack at zero load depends on the crack size. For example, the crack tip boundary between locations A and D is open 17% for a newly formed type III crack ($a/t = 0.156$ and $a/c = 0.652$ from the constant ΔK_d test). When the crack reached the size of $a/t = 0.180$ and $a/c = 0.677$, 30% of the AD boundary is open. With continued fatigue cycling, 65% of the AD boundary is open for a crack size of $a/t = 0.260$ and $a/c = 0.650$. This opening of the crack tip boundary between locations A and D results from an increase in void surface area and internal displacement with crack growth.

Table 5.1 lists the measured crack lengths when transition occurred between crack types I and II, and type II and III cracks. The crack transition size was found to correlate most favorably with a/t . Table 5.2 presents the measured range in crack size for the three crack types. These ranges do not include precracking measurements which show higher a/c values for the smaller crack sizes (Appendix E for a complete data set).

Table 5.1: Crack Size when Transition Occurs Between a Crack Types I and II, and Crack Types II and III.

<u>Transition to</u>	<u>a</u>	<u>c</u>	<u>a/c</u>	<u>a/t</u>
Type II Crack				
Constant ΔK_d	0.051	0.058	0.872	0.068
Constant ΔK_a	0.060	0.075	0.840	0.084
Constant Load	0.071	0.084	0.845	0.095
Block Load	0.052	0.075	0.693	0.069
Type III Crack				
Constant ΔK_d	0.117	0.180	0.652	0.156
Constant ΔK_a	0.127	0.153	0.833	0.169
Constant Load	0.104	0.149	0.698	0.139
Block Load	0.142	0.202	0.705	0.189

Table 5.2: Range of Measured Crack Sizes for the Three Crack Types

	<u>a</u>	<u>c</u>	<u>a/c</u>
- Type I Crack			
Constant ΔK_d	0.043-0.048	0.045-0.056	0.94-0.84
Constant ΔK_a	0.034-0.055	0.038-0.062	0.88-0.71
Constant Load	0.040-0.063	0.043-0.074	0.97-0.85
Block Load	0.049-0.050	0.065-0.071	0.75-0.71
- Type II Crack			
Constant ΔK_d	0.050-0.116	0.058-0.174	0.87-0.67
Constant ΔK_a	0.063-0.127	0.075-0.148	0.85-0.81
Constant Load	0.071-0.098	0.084-0.138	0.84-0.69
Block Load	0.052-0.135	0.075-0.193	0.70-0.64
- Type III Crack			
Constant ΔK_d	0.117-0.325	0.180-0.650	0.65-0.50
Constant ΔK_a	0.127-0.292	0.152-0.651	0.83-0.45
Constant Load	0.104-0.343	0.149-0.826	0.67-0.42
Block Load	0.142-0.357	0.202-0.651	0.71-0.55

A general trend in crack aspect ratio (a/c) is noted in Table 5.2, where a/c for a type I crack is higher than a type II, and a/c for a type II crack is higher than a type III. Although it can be reasoned that this trend is caused by the stress being larger at the crack free-surface than at the depth position due to the bending, this is not the only consideration. First, the stress intensity factor into the crack depth (K_a , location A) can be greater than at the crack free-surface (K_d , location D) for small cracks (depending on the crack a/t and a/c growth pattern). For the constant ΔK_d and block loading tests, ΔK_a was larger than ΔK_d during precracking when a/t was less than 0.040 and 0.061, respectively. Second, even though the

crack initiation sight a/c was 0.17 (which would promote crack growth along the free-surface if stress were the major factor), the crack did not grow along this boundary, but initiated a new site such that a/c was approximately 1.0 (that is, semicircular, ref. Figure 4.17), and then decreased with crack growth.

This crack growth pattern (where a/c is initially equal to or greater than one and then decreases with crack growth) has been demonstrated both analytically (5) and experimentally (40,42) in metals for both bending and tension. The difficulty of growing cracks to desired a/c values in metals was also described by Fleck, et al. (18) when he attempted to force a crack a/c by different initiation site shapes. He stated that "By employing two different shapes of slot we hoped to investigate the effect of crack shape on closure response. Unfortunately, the fatigue cracks quickly grew to similar a/c ratios, precluding a study of crack shape effects."

COD Profiles with Applied Load

The change in COD patterns as load is applied to a surface crack is a direct function of crack type (Figure 5.2). For a type I crack (whose surfaces are fully closed under zero load, Figure 5.2a), the COD pattern is classical in that it begins to open at the crack free-surface (location B), and continues opening symmetrically toward the crack tip boundary. Although the complete crack tip boundary A to D opens at nearly the same load level, location A was observed to open just prior to location D. The elastic opening pattern with applied load forms a fringe pattern schematically illustrated in Figure 5.4e.

The COD patterns during load application for crack types II and III are quite different from a type I crack as shown in Figure 5.4. Note that Figure 5.4 is organized into "crack geometry" and "fringes" groupings (similar to Figure 5.2). The changes between Figures 5.4a and 5.4e are caused by increasing the applied load. Beginning with a type II crack

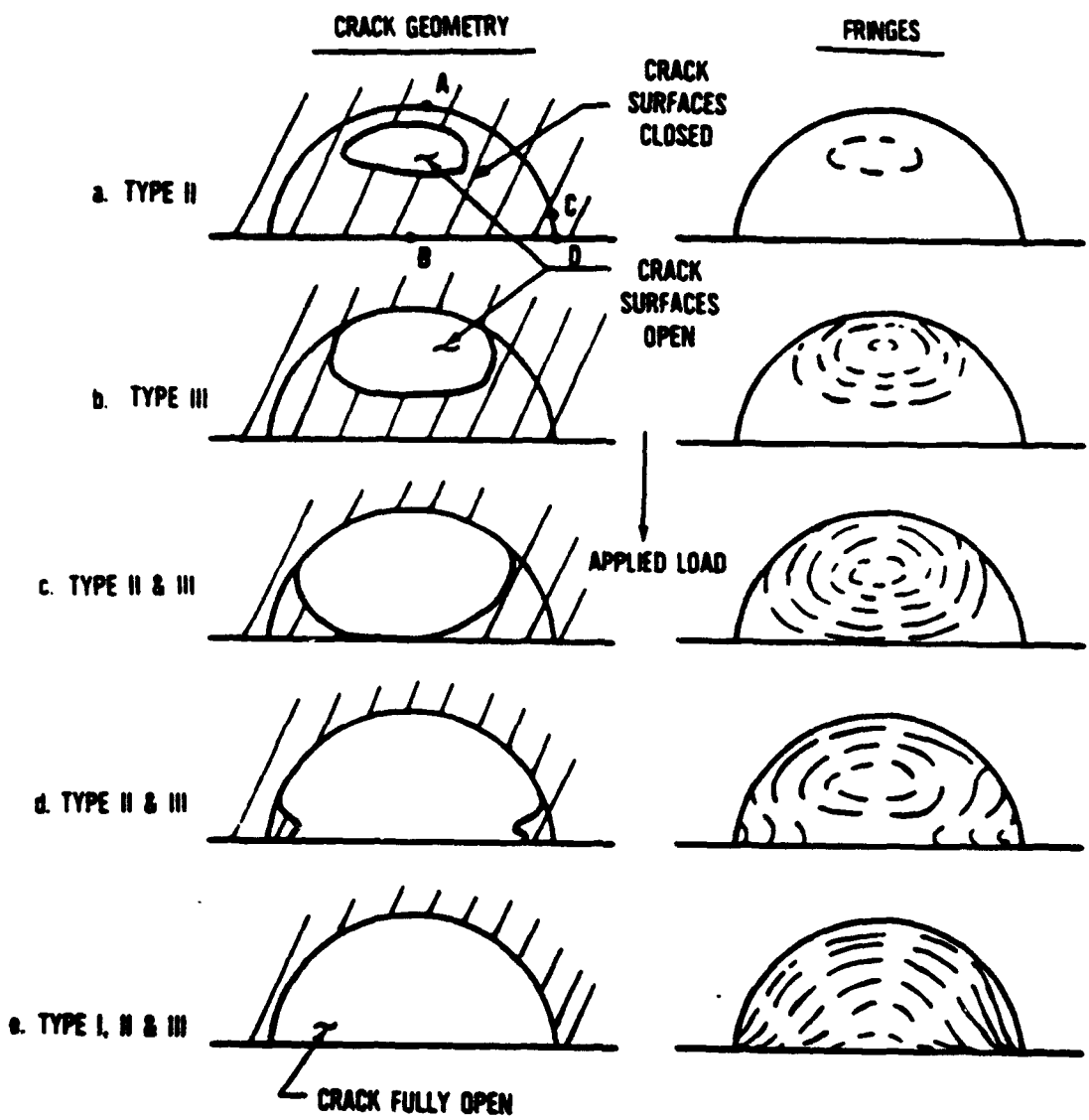


Figure 5.4 Schematic of the crack opening displacement patterns as load is applied to a type II crack from zero load at (a) to a load level where the crack is completely open at (e)

(Figure 5.4a) and applying a load, the internal crack displacement void increases in area and displacement until the crack tip separates at location A (Figure 5.4b). As load continues to increase, the void area expands to the specimen free-surface at location B (Figure 5.4c). The crack free-surface then begins to open, and the crack internal surfaces continue to separate (Figure 5.4d) until the crack tip boundary AD is completely open (Figure 5.4e).

The type III COD pattern follows the same general trend as a type II, but begins at Figure 5.4b and progresses to Figure 5.4e upon load application. It should be noted that the fringe patterns in Figures 5.4a-d show the crack maximum displacement to be internal to the crack, whereas it is at the crack free-surface in Figure 5.4e. These patterns are described in more detail using COD measurements in the next section.

Photographic examples of the fringe order patterns are shown in Figures 5.5a and 5.5b (reference Figures 4.4a-d). Note the crack tip at location A is open. Figure 5.5a is an interferometric photograph of a type III crack with zero applied load ($a = 0.195$ inch $c = 0.300$ inch). Figure 5.5b shows a type II crack with an applied load level sufficient to completely open the crack surfaces ($a = 0.168$ inch $c = 0.249$ inch). The dark interference fringe patterns can be seen in each photo.

Figure 5.5b fringe orders shows a fully open crack with the maximum displacement internal to the crack surfaces (i.e., COD at the free-surface is less than the internal displacement, reference Figure 5.4d). The mating surfaces at location C are noted to be the last portion of the crack to open. Location C ranged from 12 to 15 degrees from the crack free-surface (angel ϕ , Figure 5.1). This condition is speculated to be caused by an apparent transition from a state of plane stress to one of plane strain.

A three-dimensional elastic-plastic finite element analysis of a surface crack by Trantina, deLorenze and Wilkening (43) clearly shows a plane stress/strain transition zone at $\phi = 15$ degrees. This effect was not observed in the elastic analysis, but was prevalent in the elastic-plastic predictions. The paper describes this variation of K along the crack boundary as "...a combination of increased K due to plasticity effects and a loss of plane strain

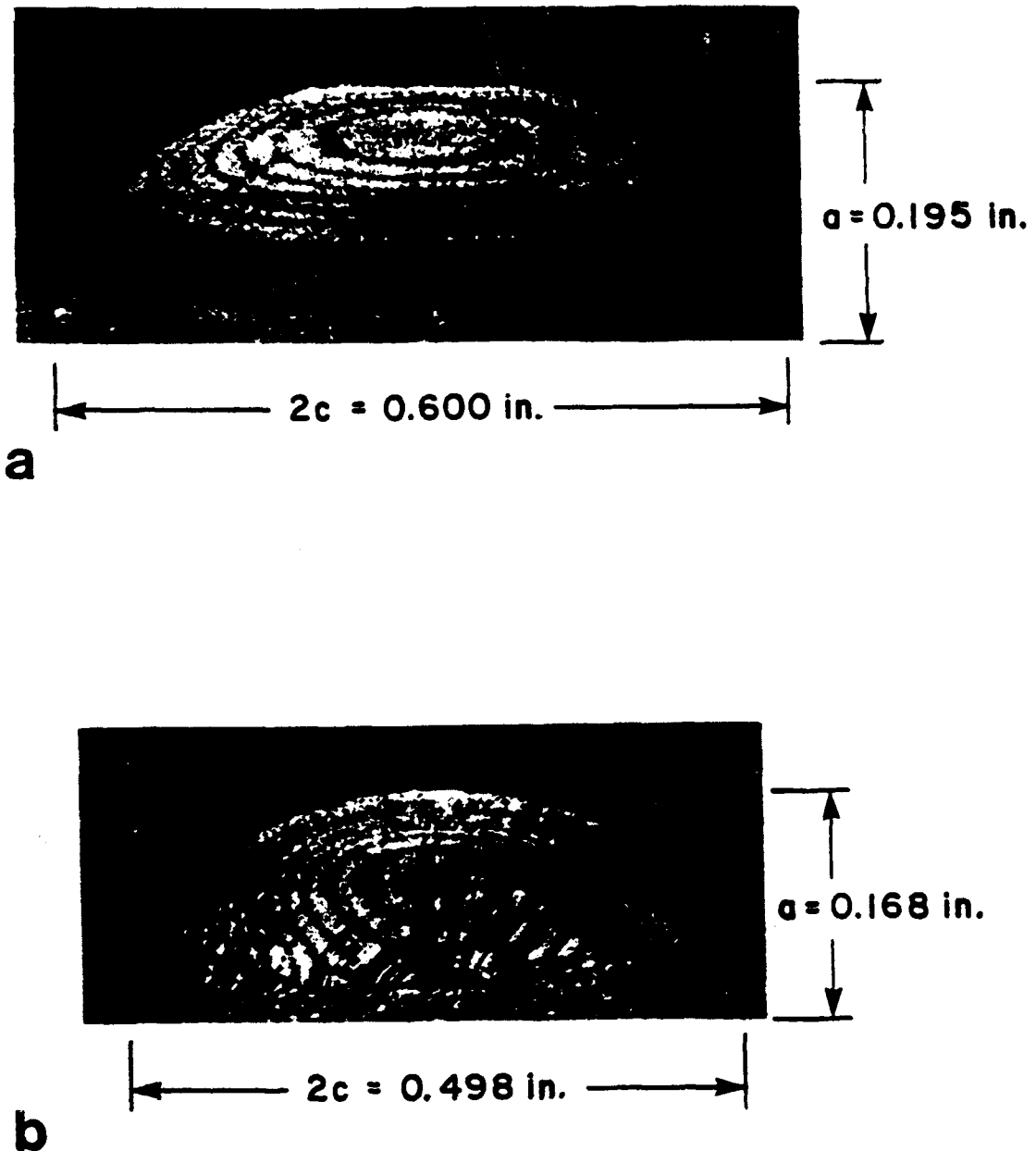


Figure 5.5 Interference photograph of the crack surface displacement at (a) near zero load showing the internal void formation for a type III crack (ref. Figure 5.4b), and (b) for a fully-open crack in the closure load region showing the minimum displacement at location C, $\phi=12$ to 15 degrees (ref. Figure 5.4d)

constraint at the free surface." Their analysis showed a rapid decrease in the plane strain constraint $\sigma_1/(\sigma_2 + \sigma_3)$ at $\phi = 15$ degrees, causing "...increased yielding at the free surface and a decrease in effective K. The region below the free surface carries a larger portion of the load and thus a peak in the K variation with ϕ develops at about 15 ϕ ." The effects of more plasticity induced from a higher strain hardening exponent or higher strain level were found to reduce the plane strain constraint at the free surface and decrease the K effectivity for $\phi < 15$ degrees.

COD Variation with Crack Size

Fatigue crack size is a dominant factor in categorizing the three crack types, and their corresponding crack opening displacement (COD) patterns. The question of crack size when the void forms a type II crack, and then a type III crack, was covered by data presented in Table 5.1. The question of void changes with increasing crack size and applied load is presented in this section. First, data are presented to track void growth patterns at zero load. Second, data to track the void changes with an applied load are presented.

Organization of this information can be described best by taking a cross-sectional slice between locations A and B (Figure 5.1, $\phi = 90$ degrees) to visualize the crack opening displacement profile as a function of applied load -- shown in Figure 5.6. The type II crack data are from the constant ΔK_d test ($a = 0.12$ and $c = 0.17$ inch), and represent half the COD profile sketch shown in Figure 5.3b. The two diamonds located along the abscissa represent a zero fringe order, or zero displacement. The dotted line connecting the two measured zero fringe order points is a projected estimate of the crack surface profile.

Note that for low load levels the void maximum displacement is located internal to the crack surfaces, and is closer to the crack tip (location A) than the crack free-surface (location B). With an applied load, the void maximum displacement moves away from the

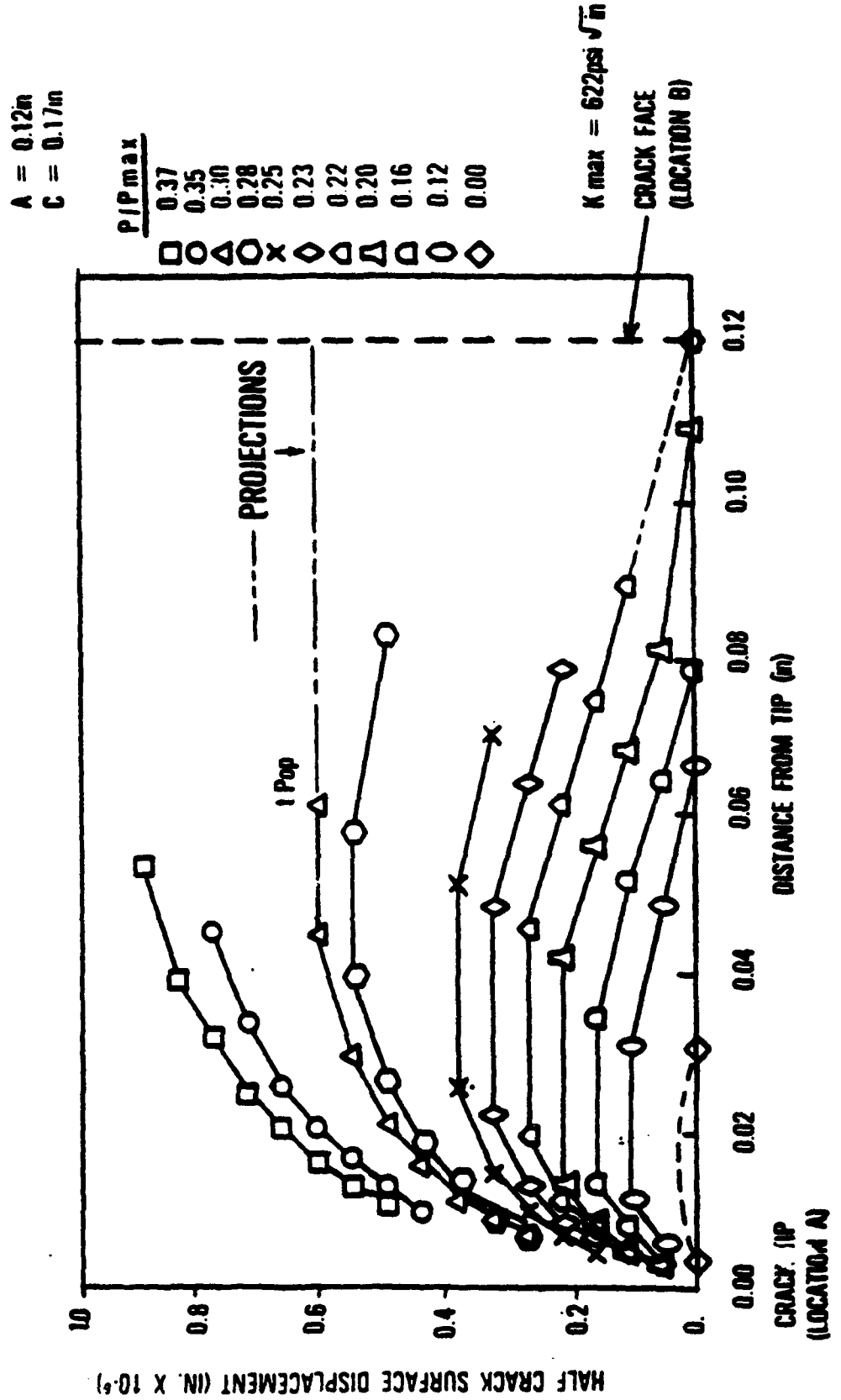


Figure 5.6 Surface flaw crack opening displacement pattern for half the crack displacement for various loads in the closure load region of the constant ΔK_d eff test ($\beta=90$ degrees)

location A crack tip and toward the crack free-surface at location B. The applied load level where the void maximum displacement transitions from being internal, to being at the crack free-surface, is defined as tP_{op} (K value of $187 \text{ psi}^{\ast} \text{in}^{1/2}$ in Figure 5.6).

To track the crack internal void displacement and movement with crack size and applied load, three variables have been established. These variables are schematically illustrated in Figures 5.7a and 5.7b such that:

- (1) δ defines the crack maximum fringe order (h , ref eqn. 4.1) measured for a given applied load.
- (2) Δ_1 and Δ_2 define the measured distances from the crack tip (along a line between locations A and B) to the fringe orders which encompass the void maximum displacement. That is, the displacement δ , and Δ_1 and Δ_2 distances from the crack tip, locate the COD maximum point for a given applied load.

These definitions are used in Tables 5.3 and 5.4 to describe void COD patterns due to crack size and applied load. Table 5.3 presents COD patterns under zero load for representative crack sizes.

Table 5.3: Constant ΔK_d Test Effects on the Void Maximum Displacement Location with Zero Load

Crack Size <u>a</u>	<u>c</u>	Applied Moment (in-lb)	Fringe Order		δ Void (fringe order)
			Distance from <u>Crack Tip (in)</u>	<u>Δ_1</u>	
0.09	0.15	0	--	--	1
0.14	0.20	0	0.010	0.034	1
0.20	0.30	0	0.033	0.056	6
0.28	0.50	0	0.085	0.098	14
0.30	0.55	0	0.080	0.113	15

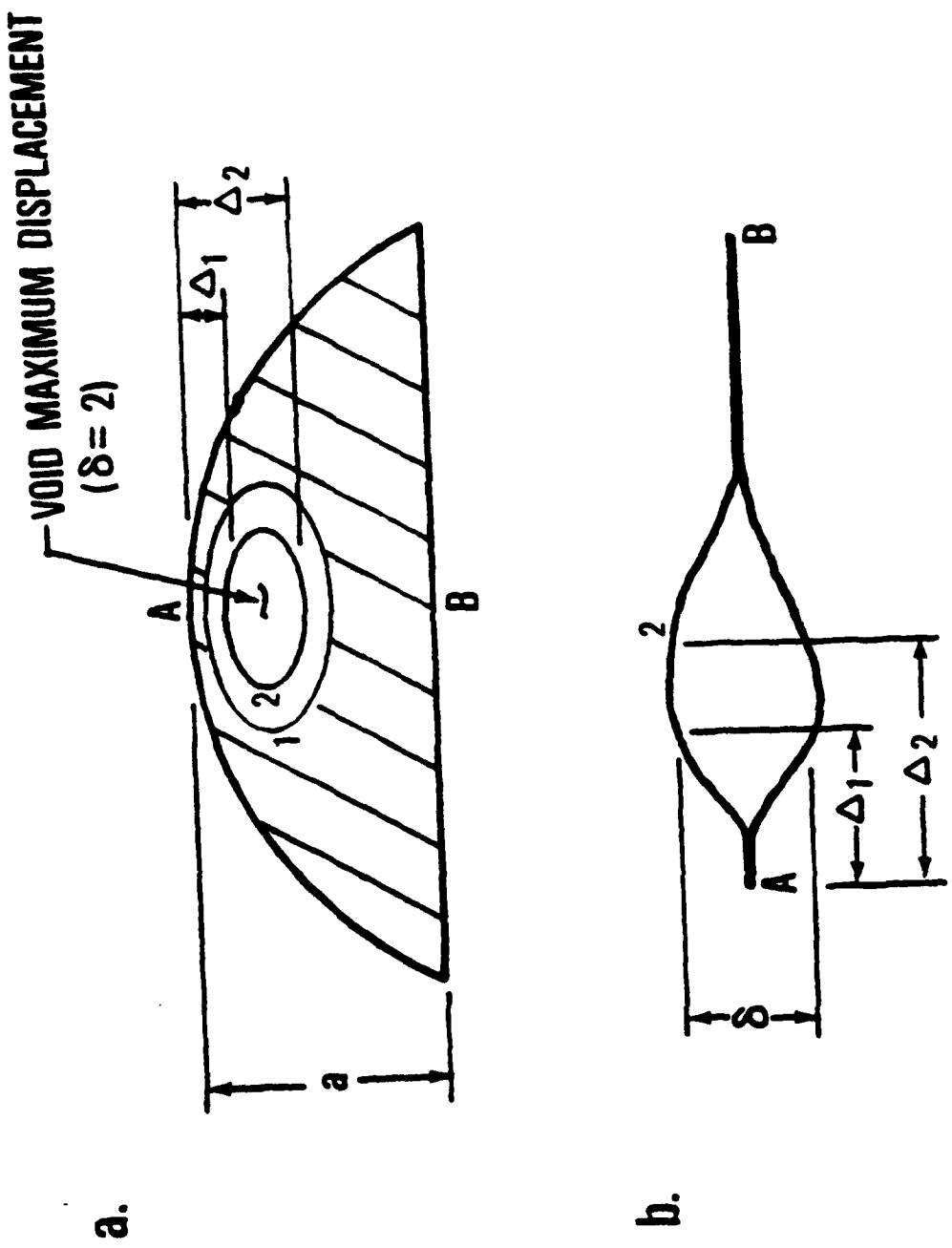


Figure 5.7 Schematics of the COD pattern for defining the "void" displacement δ , and Δ_1 & Δ_2 distances from the crack tip

A plot of the Table 5.3 data is presented in Figure 5.8 to show relative change in void displacement with increasing crack size. Again, measurements are made at zero load, and the Δ_1 and Δ_2 distances from the crack tip bound the void maximum displacement point. Note that the void maximum displacement point increases in height and moves away from the crack tip and toward the crack free-surface as the crack increases in size. The crack tip location is also plotted to show relative effects with crack growth.

Table 5.4 presents the same type of data as Table 5.3, but for several values of applied load. The void maximum displacement data from Table 5.4 are plotted for two crack sizes in Figure 5.9 to show general trends in void movement with applied load. Note in Figure 5.9 that the void position is plotted as a function of the crack tip instead of from the crack free-surface as in Figure 5.8.

COD WITH ZERO LOAD

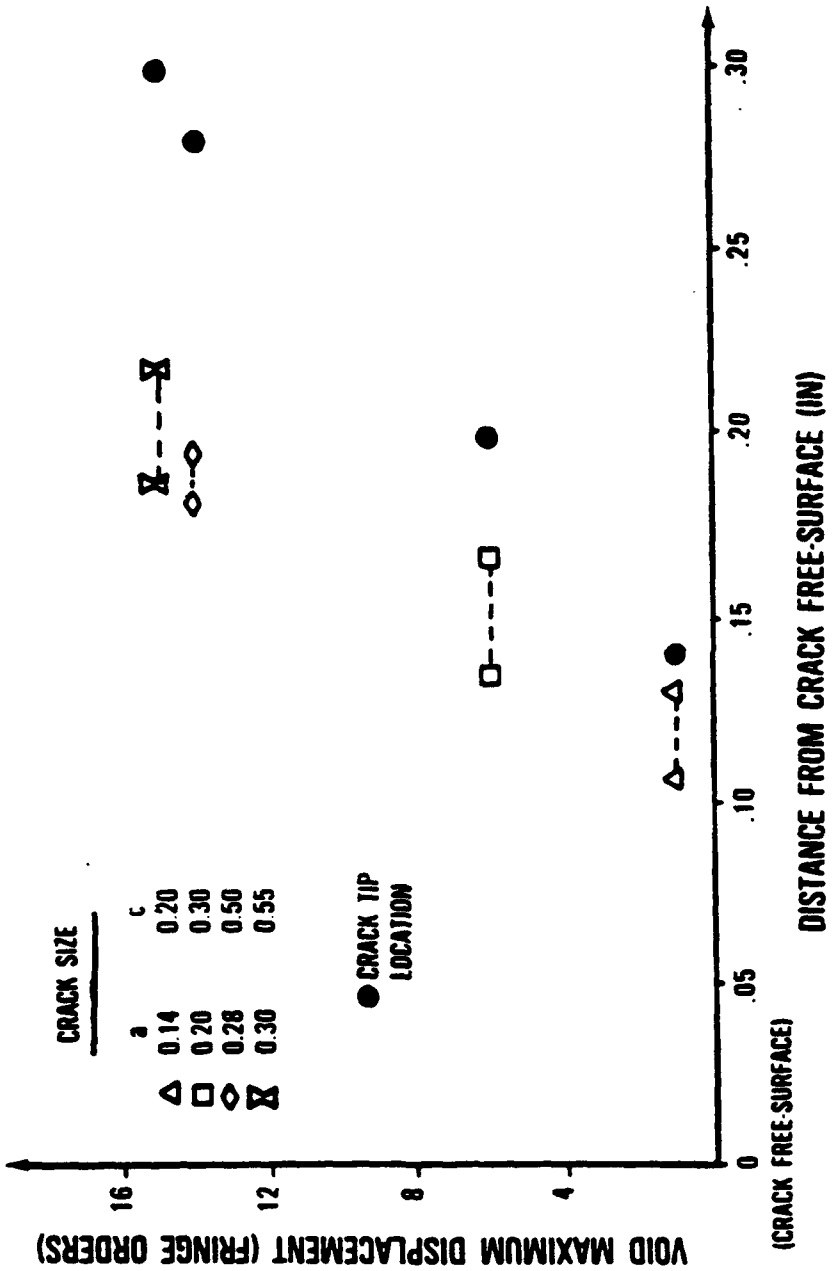


Figure 5.8 Location of the void maximum displacement for various crack size under zero load

Table 5.4: Void Maximum Displacement Location for a Constant ΔK_d Test Effects with an Applied Load

<u>a</u>	<u>c</u>	Applied Moment (in-lb)	Fringe Order		δ – Void Max Displacement (fringe order)
			Distance from <u>Crack Tip (in)</u>	Δ_1	
0.09	0.15	72	0.017	0.030	2
0.09	0.15	88	0.020	0.027	3
0.09	0.15	102	0.023	0.039	4
0.09	0.15	132	0.041	0.048	8
0.09	0.15	163	0.038	0.048	10
0.14	0.20	18	0.016	0.023	2
0.14	0.20	88	0.023	0.050	6
0.14	0.20	102	0.038	0.049	9
0.14	0.20	132	0.038	0.094	13
0.20	0.30	18	0.034	0.057	7
0.20	0.30	51	0.045	0.059	10
0.20	0.30	88	0.045	0.082	16
0.20	0.30	102	0.058	0.082	19
0.20	0.30	32	0.082	0.105	24
0.30	0.55	18	0.084	0.115	17
0.30	0.55	51	0.104	0.116	23
0.30	0.55	72	0.113	0.142	28
0.30	0.55	88	0.119	0.153	33

COD WITH APPLIED LOADS

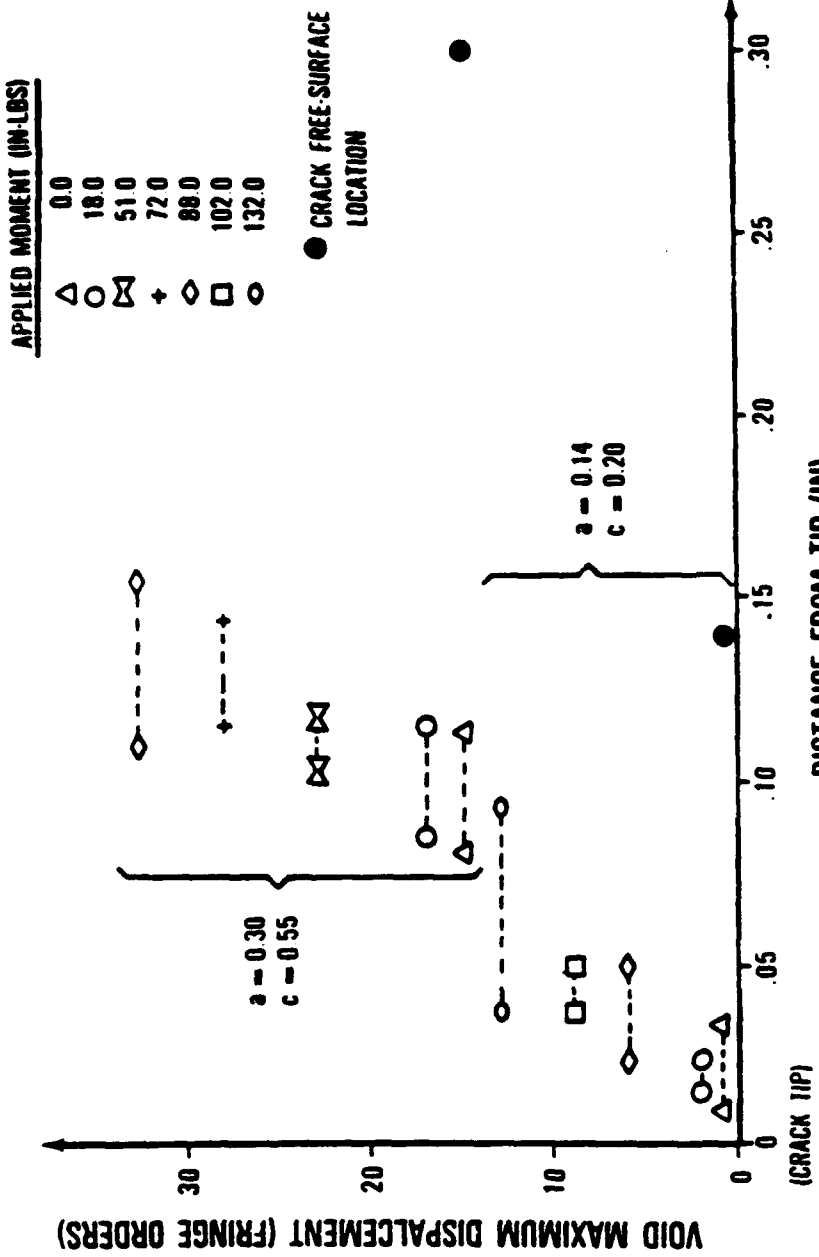


Figure 5.9 Changes in void maximum displacement for two crack sizes and at several applied moments

Three primary observations can be made about the void maximum displacement point from these data:

- (1) The void maximum displacement location is closer to the crack tip (location A) for smaller cracks.
- (2) The void height is lower for smaller cracks than for larger cracks at an equivalent applied load.
- (3) As load is applied to the specimen, the void height increases, and moves away from the crack tip and toward the crack free-surface -- eventually opening .

COD Variation with Load History

The previous section described the void movement with increased crack size and with an applied load for the constant ΔK_d test. This section will expand this data set to include experimental results from the other tests. The same definitions of δ , Δ_1 and Δ_2 will be used in tables 5.5 through 5.7 to cover the constant ΔK_a , constant load and block loading tests.

Table 5.5: Void Maximum Displacement Location for a Constant ΔK_a Test Effects with an Applied Load

Crack Size		Applied Moment (in-lb)	Fringe Order		δ - Void Max Displacement (fringe order)
a	c		Distance from Crack Tip (in)	Δ_1	
0.10	0.12	24	0.019	0.031	2
0.10	0.12	36	0.011	0.047	2
0.10	0.12	57	0.013	0.058	3
0.10	0.12	73	0.021	0.065	5
0.10	0.12	90	0.033	0.082	7
0.13	0.15	0	0.012	0.045	2
0.13	0.15	24	0.017	0.045	3
0.13	0.15	36	0.029	0.036	4
0.13	0.15	57	0.028	0.050	6
0.13	0.15	90	0.058	0.088	11
0.14	0.20	23	0.022	0.060	5
0.14	0.20	36	0.026	0.059	6
0.14	0.20	57	0.044	0.059	10
0.14	0.20	73	0.051	0.077	13
0.19	0.30	0	0.040	0.089	6
0.19	0.30	23	0.052	0.091	9
0.19	0.30	57	0.072	0.098	17
0.19	0.30	73	0.079	0.119	21
0.19	0.30	81	0.084	0.150	23
0.20	0.32	0	0.050	0.091	7
0.20	0.32	23	0.064	0.093	10
0.20	0.32	57	0.083	0.107	19
0.20	0.32	81	0.092	0.116	24
0.20	0.32	98	0.107	0.122	30

**Table 5.6: Void Maximum Displacement Location for a Constant Load Test with an
Applied Load**

Crack Size <u>a</u>	<u>c</u>	Applied Moment (in-lb)	Fringe Order		δ – Void Max Displacement (fringe order)
			Distance from <u>Crack Tip (in)</u>	Δ_1	
0.08	0.10	132	0.007	0.035	1
0.08	0.10	138	0.018	0.026	2
0.08	0.10	154	0.022	0.047	3
0.08	0.10	162	0.029	0.047	4
0.09	0.12	100	0.007	0.031	1
0.09	0.12	114	0.012	0.024	2
0.09	0.12	132	0.016	0.027	3
0.09	0.12	138	0.015	0.036	3
0.09	0.12	154	0.022	0.033	5
0.09	0.12	163	0.028	0.035	6
0.09	0.12	195	0.036	0.067	9
0.10	0.15	100	0.018	0.027	3
0.10	0.15	114	0.012	0.042	3
0.10	0.15	132	0.021	0.036	5
0.10	0.15	138	0.015	0.050	5
0.10	0.15	154	0.020	0.050	7
0.10	0.15	163	0.029	0.049	9
0.10	0.15	195	0.051	0.082	14
0.12	0.17	46	0.016	0.042	1
0.12	0.17	100	0.021	0.031	5
0.12	0.17	114	0.026	0.035	6
0.12	0.17	132	0.021	0.047	7
0.12	0.17	138	0.027	0.046	8
0.12	0.17	163	0.032	0.055	11
0.12	0.17	195	0.052	0.088	17
0.14	0.20	46	0.019	0.039	3
0.14	0.20	82	0.023	0.042	5

**Table 5.7: Void Maximum Displacement Location for a Block Loading Test with an
Applied Load**

<u>a</u>	<u>c</u>	Applied Moment (in-lb)	Fringe Order		δ - Void Max Displacement (fringe order)
			Distance from <u>Crack Tip (in)</u>	Δ_1	
0.25	0.35	0	0.060	0.105	8
0.25	0.35	23	0.073	0.110	11
0.25	0.35	32	0.081	0.107	12
0.25	0.35	47	0.085	0.100	16
0.25	0.35	57	0.088	0.099	19
0.25	0.35	73	0.101	0.128	23
0.25	0.35	81	0.110	0.120	25
0.25	0.35	98	0.111	0.159	28

To compare the void displacement patterns for all tests, it is desirable to select a common crack aspect ratio (a/c) and a/t value. This point is shown in Figure 5.10 where a/c versus a/t is plotted for all four tests. The common point selected from this Figure was $a/c = 0.69$ and $a/t = 0.19$. Comparison of the void displacement patterns are shown in Figure 5.11 with applied load for a common crack size. The reference line segment is drawn for the constant ΔK_d data, and is found to fit the other data sets quite well.

It can be seen from this plot that the void movement toward the crack free-surface with applied load (as discussed in the last section, ref. Figure 5.9) is consistent for various load histories. However, the applied moment required to achieve a given displacement (shown in parentheses) varies with load history. That is, to achieve a void maximum displacement of 13 fringe orders requires an applied moment of 132 in-lb. for the constant ΔK_d test, but only 73 in-lb. for the constant ΔK_a test. These differences are also seen in

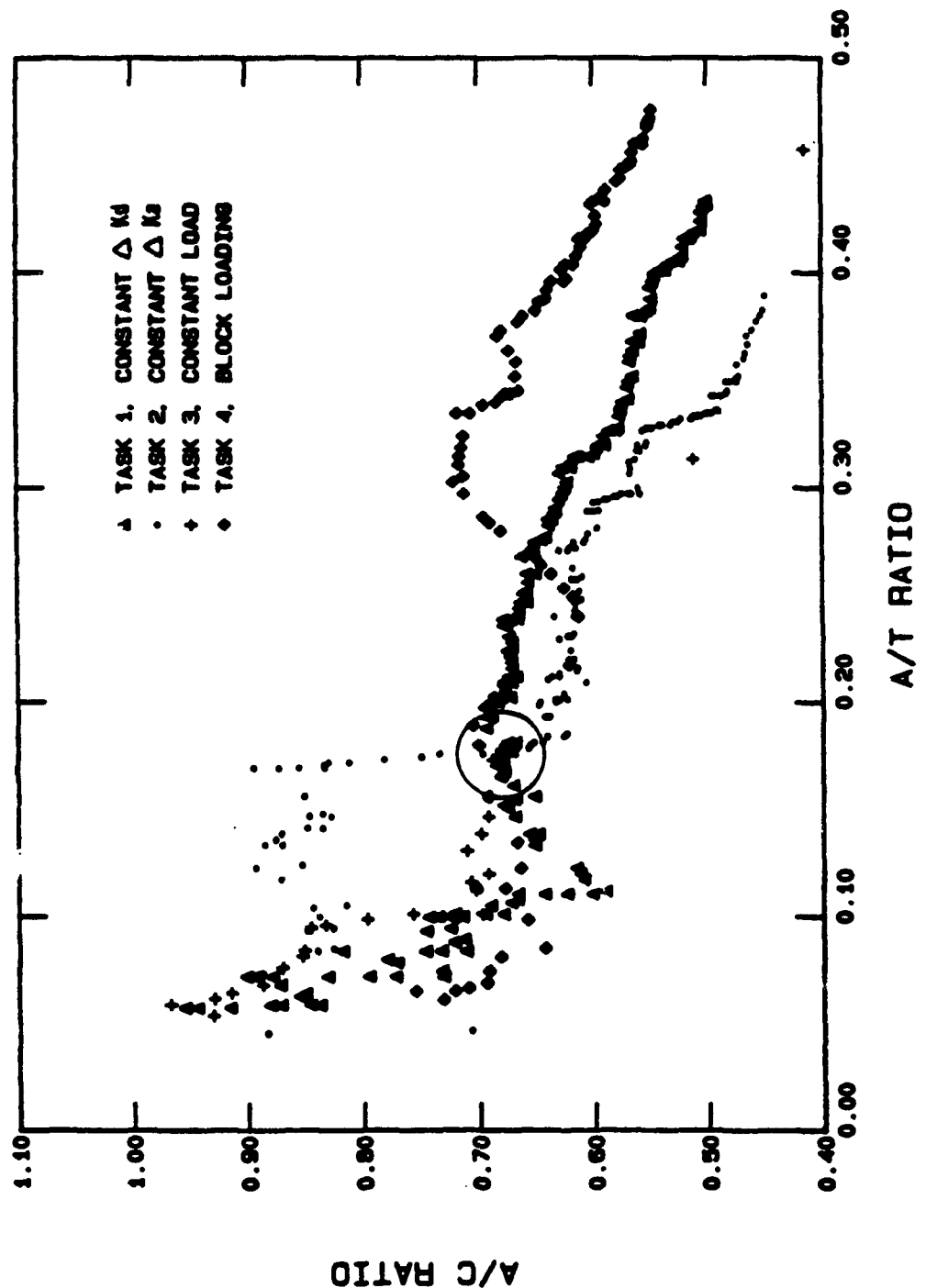


Figure 5.10 Measured crack aspect ratio (a/c) versus a/t size of four tests. The circle identifies a common crack size used to compare COD and closure loads

COD FOR DIFFERENT LOAD HISTORIES

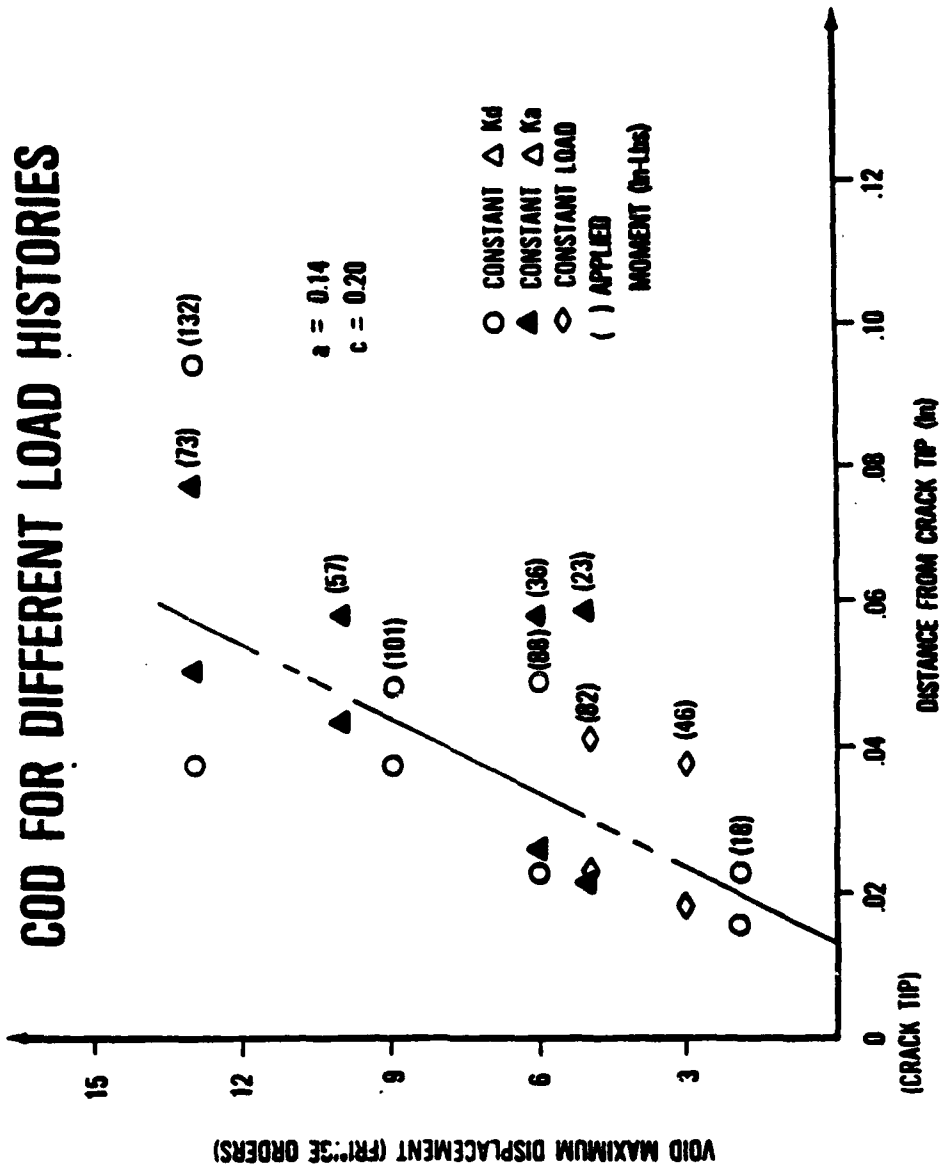


Figure 5.11 Void maximum displacement pattern at several load levels for three load histories at a common crack size. Numbers in parentheses represent applied moments.

Figure 5.12, where the void maximum displacement is plotted as a function of applied load. Here, the constant load test is shown to require a higher applied load to achieve a given level of COD than either a constant ΔK^d or ΔK_a test. Also, a constant ΔK_d test requires a higher applied load to achieve a given displacement than does a constant ΔK_a test. These differences are a clear indication of load history effects on closure load, and will be discussed in the next section on "Closure/Opening Loads."

In all tests, three primary observations of the void COD pattern were noted:

- (1) Under zero load, the void maximum displacement is a direct function of crack size
- (2) Under zero load, the void maximum displacement location relative to the crack tip (location A) is a direct function of crack size
- (3) With applied load, the void maximum displacement increases, and moves away from the crack tip and toward the crack free-surface (location B).

Crack Compliance

Using the crack opening displacement profile data from Figure 5.6, load versus displacement plots (typically used to define closure load when measurements are made at the crack free-surface) can be constructed for different distances from the crack tip. These load-displacement plots are presented in Figure 5.13 for points along a line between location A and B, $\phi = 90$ degrees. The inverse slope of the load versus displacement graph is defined as the compliance at a particular point, and represents the crack opening displacement per unit load.

For a linear-elastic body, compliance at a point is independent of load level, and a load-displacement curve would, therefore, be linear. Any deviation from linearity in a linear-elastic body, such as those due to closure, could be attributed to changes in the

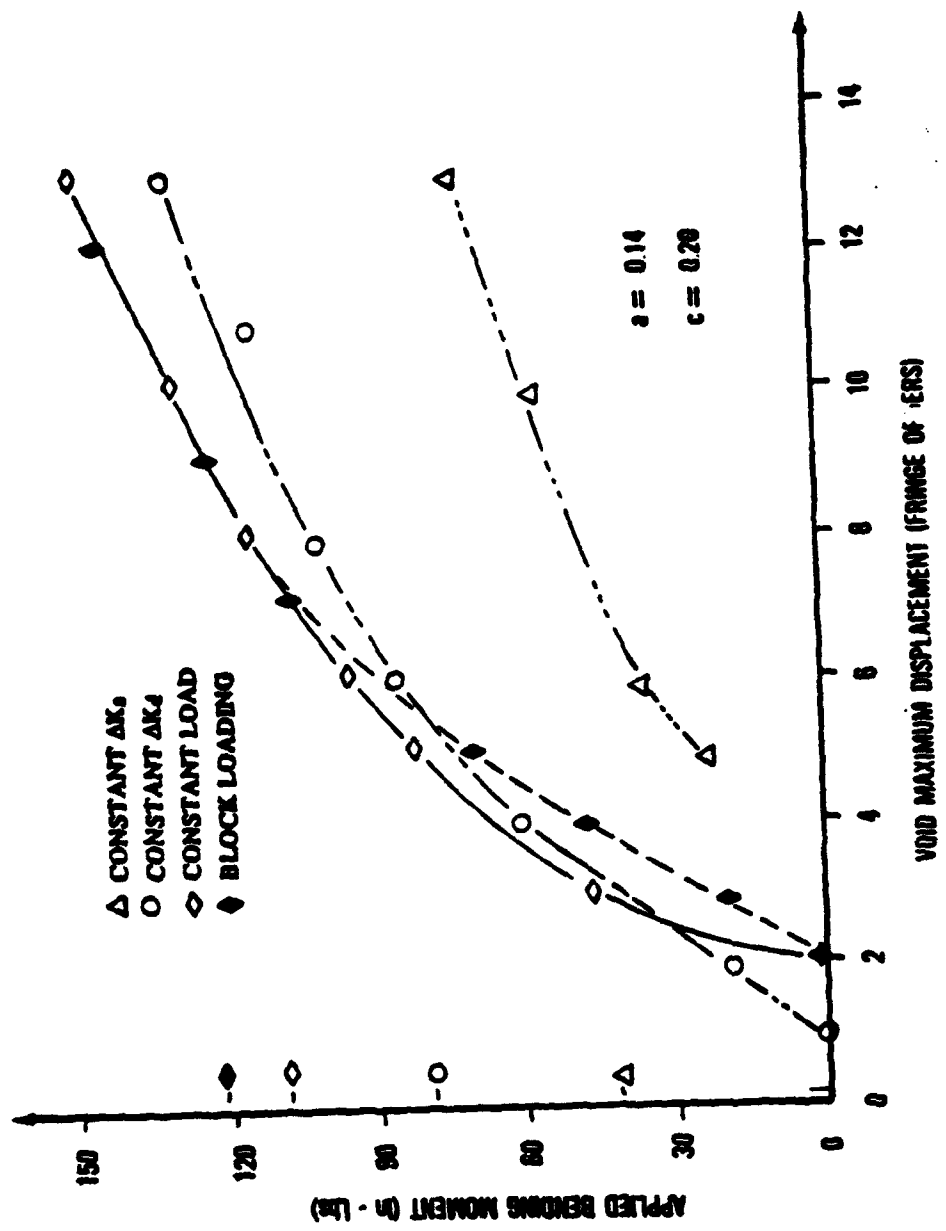


Figure 5.12 Load versus displacement comparison of the four load histories (constant ΔK_a , ΔK_d , load and block loading) at a common crack size

CRACK DISPLACEMENT MEASUREMENTS

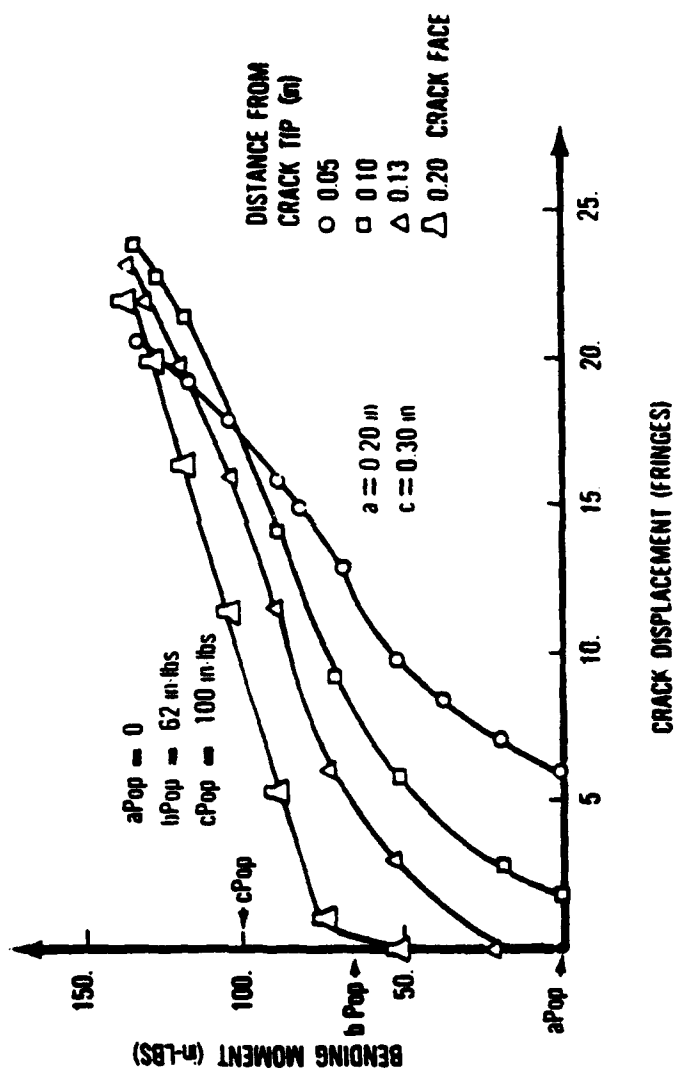


Figure 5.13 Load versus displacement plot to compare the COD patterns measured at various distances from the crack tip along the $\downarrow=90$ degree line.

geometry of the body. This nonlinearity is seen in Figure 5.13, where compliance changes until the load is increased above a certain value. This nonlinear behavior in the load-displacement plot is due to changes in crack shape during the loading cycle. The compliance nonlinearity, caused by changes in crack geometry, also indicates that the stress intensity factor at any given point along the crack boundary is also nonlinear with applied load (44).

Besides the nonlinearity of the load-displacement profile, compliance is also noted to be dependent on measurement location. This is seen in Figure 5.13 where the compliance, or the inverse slope of the load-displacement trace, is approximately 4 times greater at the crack free-surface (0.2 in from the crack tip) than at a distance of 0.05 in from the crack tip for loads greater than 80 in-lb. As the crack grows in size due to fatigue cycling, compliance is shown to increase at the crack free-surface (Figure 5.14). This pattern follows typical trends for thru-thickness cracks which increase in flexibility or decrease in rigidity with increasing crack size (12,27).

Closure/Opening Loads

The experimental investigation identified three primary closure loads which are considered important for the understanding of fatigue crack growth. How these closure loads correlate with the three crack types described above forms the basis for relating the geometric crack opening displacement (COD) patterns with the residual induced closure mechanisms. This section will discuss these relationships by defining three unique closure/opening loads measurements, and then relating them to the three COD types, crack size and fatigue load history.

CRACK DISPLACEMENT MEASUREMENTS

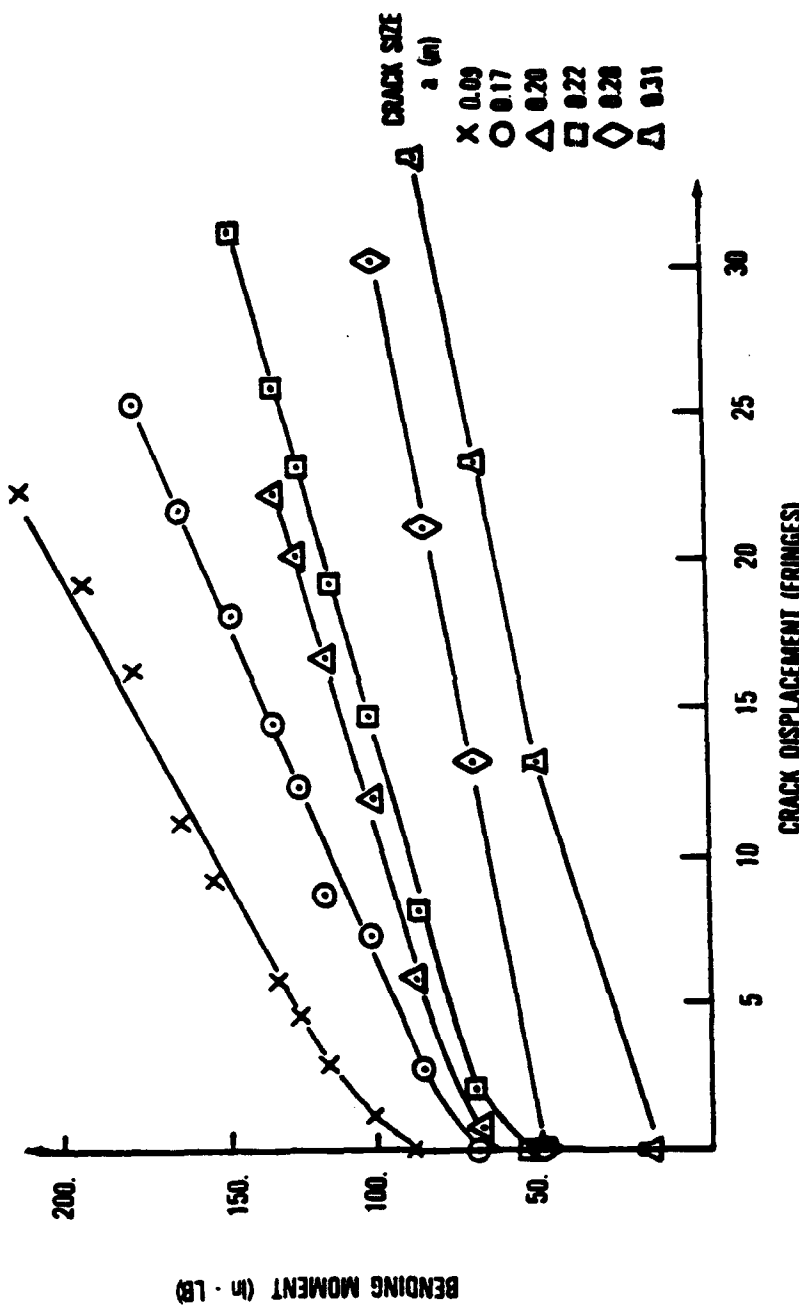


Figure 5.14 Load versus displacement plot at the crack face (location B,
 $\angle = 90$ degrees) as a function of crack size.

Closure Load Definitions

The identification of three distinct closure loads raises several questions concerning their relationship to the standard definition of closure load (defined from a load versus displacement plots as described in Chapter IV). In reality, the potential for having more than one closure load for the same crack size is not hypothetical. For example, the load-displacement measurements described in Figure 5.13 identified the influence of measurement location on closure load. As can be seen, several closure load values can also be generated using the standard definition of closure if different measurement locations are used. This sensitivity to measurement location has been discussed by several investigators using clip gages, back face strain and interferometry techniques (11,12,24). These considerations will be evaluated more fully in the next chapter when the definitions of ΔK_{eff} are considered.

Figure 5.15 is used to define the three primary closure loads (aP_{op} , bP_{op} and cP_{op}) of this investigation. The aP_{op} , bP_{op} and cP_{op} closure loads are defined here as the loads needed to open the crack surfaces (P_{op}) at the A, B and C locations, respectively. Location C is the last portion of the crack surface to completely open under an applied load, and is typically located 12 to 15 degrees into the specimen thickness from the crack free-surface. Figure 5.15 also illustrates typical interference fringe order patterns, or lines of constant displacement, where the maximum displacement (highest fringe order) is internal to the crack surfaces. The dotted line represents a section slice between locations A and B, and is used to illustrate COD profiles as shown in Figure 5.16.

Correlation of the bP_{op} and cP_{op} closure load measurements with the geometric COD profiles is shown in Figure 5.16. This information was collected independently, with the closure load measurements being made directly from the fatigue machine load cell readings, the COD profiles generated using 35 mm negatives and a digitizing board (described in Chapter IV). This information is combined in Figure 5.16 by projecting the COD profile at the same P/P_{max} ratio as the bP_{op}/P_{max} closure load ratio of 0.22. The

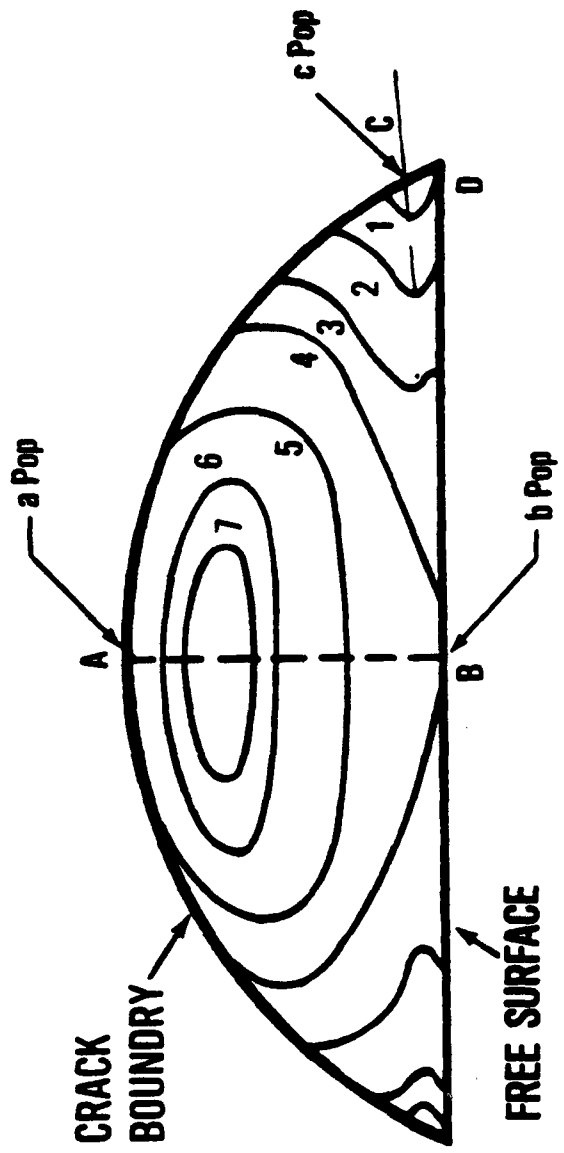


Figure 5.15 Typical crack opening displacement fringe pattern with applied load. The three closure/opening loads are defined as a_{Pop} , b_{Pop} , and c_{Pop} at locations A, B and C.

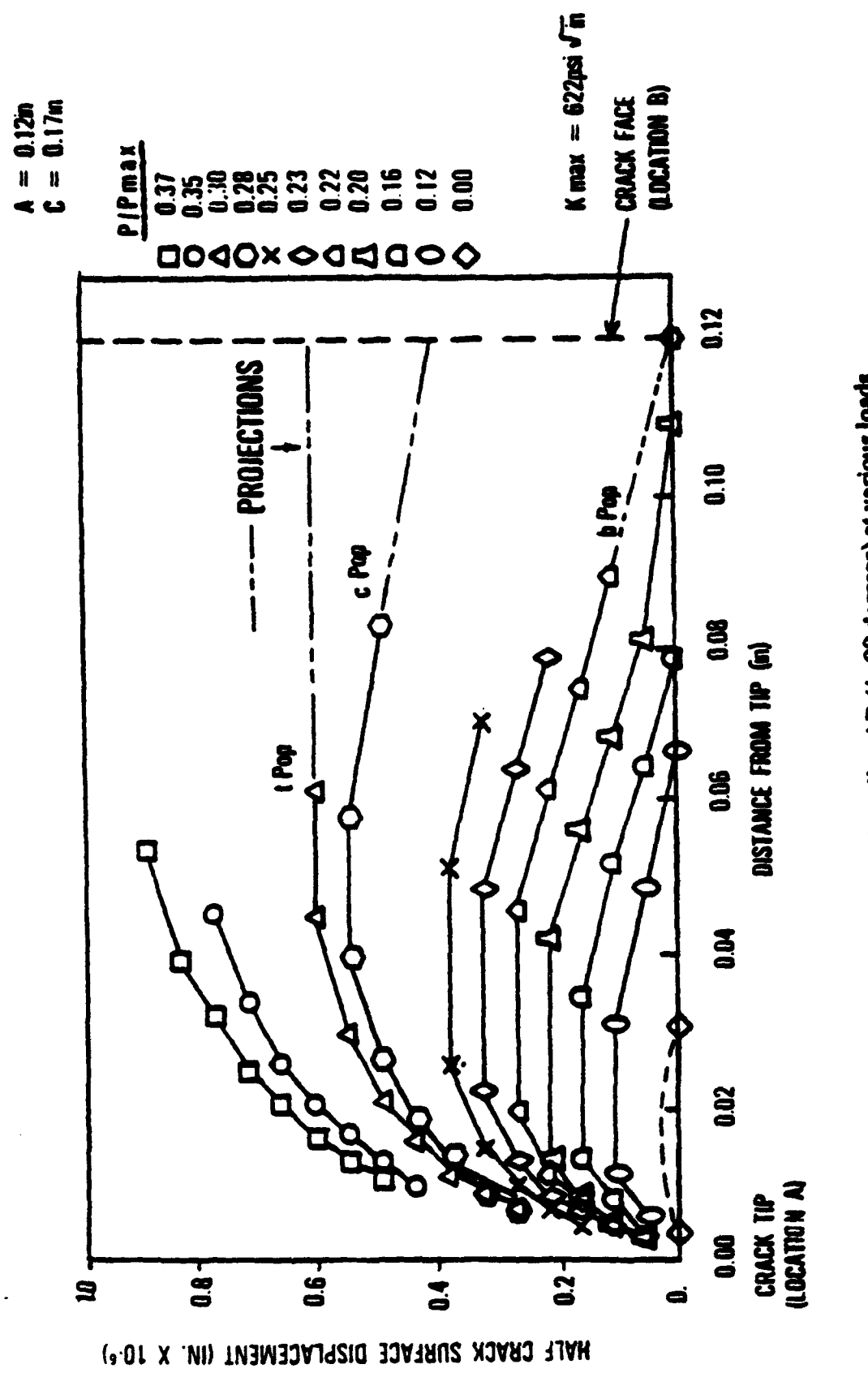


Figure 5.16 COD profiles along line AB ($\theta=90$ degrees) at various loads.
to correlate closure loads with opening patterns.

profile projection at this load level is noted to intersect at the crack face (free-surface), thus correlating the definition of the bP_{op} -- the load level which begins to open the crack free-surface. Thus, very good agreement is noted between the COD profiles and the bP_{op} closure load measurement. Projection of the crack profile at the $cP_{op}/P_{max} = 0.28$ load level corresponds to the crack free-surface at location B being open approximately $8.6E-5$ inches. The tP_{op} transition load is defined as the level needed to move the void maximum displacement from the crack interior to the crack free-surface. For a load ratio of $P/P_{max} = 0.30$, the crack maximum displacement is approximately $12.8E-5$ inches at location B. For loads above tP_{op} , the COD is no longer in the closure load region, and follows a classical linear-elastic pattern.

Figure 5.17 schematically illustrates the relationships between the three closure loads (aP_{op} , bP_{op} and cP_{op}) and the three crack opening displacement types (types I, II and III). For a type I crack (Figure 5.17a), the crack surfaces are closed under zero load. As load is applied the crack remains closed until a load level of bP_{op} is reached and the crack begins to open at the crack free-surface (location B). With increased load, the crack opens symmetrically inward and is fully open at locations A and C at the same load level ($aP_{op} = cP_{op}$). Since the maximum displacement is always at the crack free-surface, $tP_{op} = bP_{op}$, and $cP_{op} = aP_{op} >> bP_{op} >> 0$.

For a type II crack, a void formation has developed internal to the crack surfaces as shown for zero load in Figure 5.17b. The crack boundary and free-surface is closed (locations A, B and C) under zero load. With load application, location A opens at a load level of aP_{op} . At the bP_{op} load level, the crack free-surface begins to open at location B and is completely open between A and B ($\phi = 90$ degrees); however, the crack tip is closed at location C. At the cP_{op} load level, the crack surfaces are completely open with the maximum displacement along the $\phi = 90$ degree line. For a type II crack, $tP_{op} >> cP_{op} >> bP_{op} >> aP_{op}$.

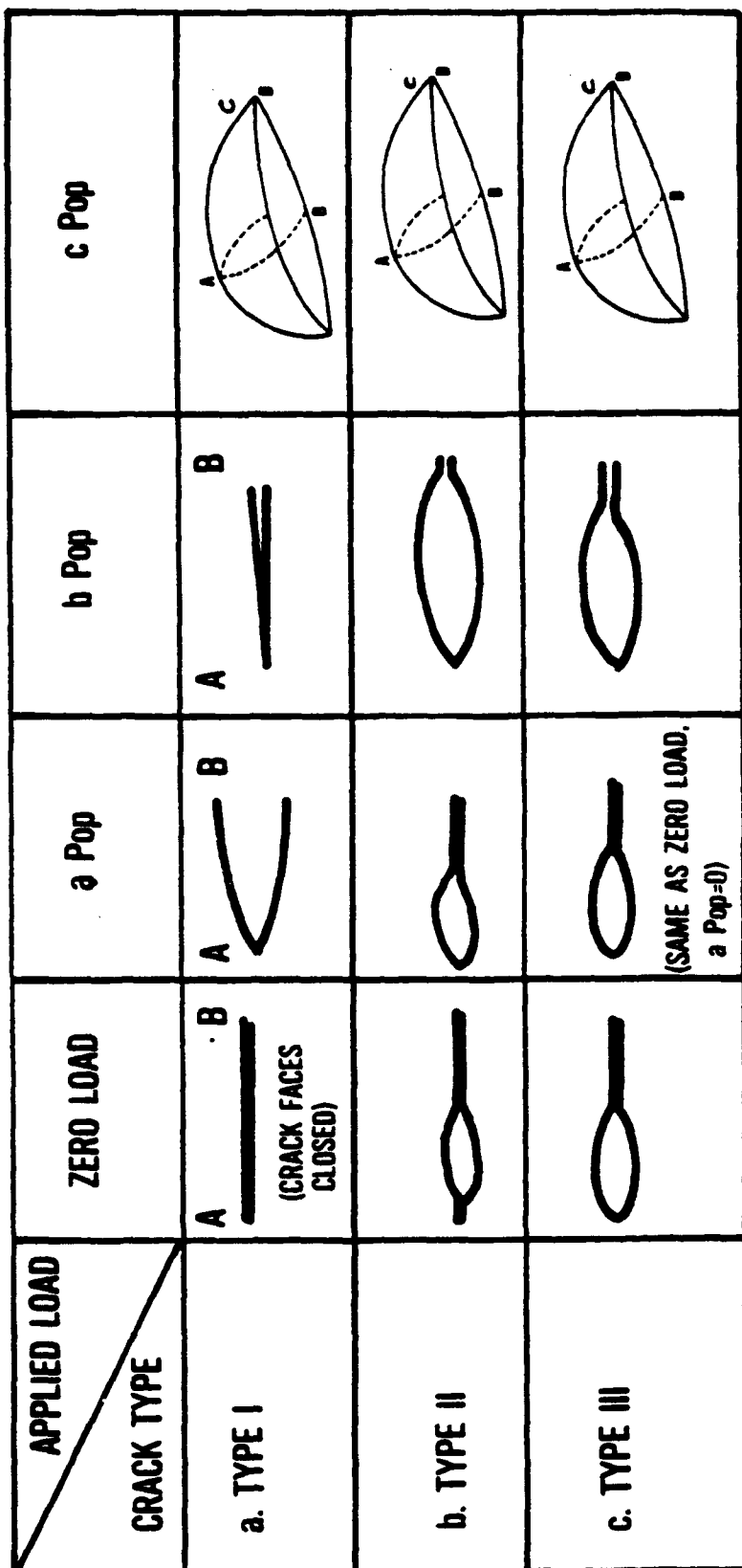


Figure 5.17 Schematic COD profiles between locations A & B ($\angle = 90$ degrees) for the three crack types at zero load, and the three closure load levels (aPop, bPop & cPop)

For a type III crack, location A is always open while locations B and C are closed under zero load. Therefore, the aP_{op} load level is zero for a type III crack. Location B begins to open at the bP_{op} load level, and at cP_{op} the crack is completely open. That is, $aP_{op}=0$ and $tP_{op} >> cP_{op} >> bP_{op}$.

Closure Load Variations with Crack Size

Closure load variations with crack growth are found to be directly related to crack size. This is seen in Figure 5.18, where the three visually observed closure load absolute values are plotted as a function of crack size for the constant ΔK_d test. The inverse relationship of decreasing closure load with increasing crack size is evident in this Figure. For a type I crack, aP_{op} and cP_{op} are at approximately the same load level, which is greater than bP_{op} . With crack growth, a type II crack is developed due to the formation of a void close to the location A crack tip. This void formation causes the crack tip at location A to open before the crack free-surface at location B. Although aP_{op} is initially larger than bP_{op} , the void formation causes aP_{op} to decrease at a faster rate than bP_{op} with respect to crack growth. With continued crack growth, the void becomes sufficiently large to physically open the crack tip at location A, forming a type III crack.

Crack sizes (a/t) where transition occurs between a type I, II and III crack were determined from visual observations and analysis of the 35 mm film. When this information is plotted independently on Figure 5.18 (Reference. Table 5.1), and dashed lines extended from the a/t transition points through the experimental data sets, definite changes in slope are observed in the bP_{op} and cP_{op} data sets at the transition between type II to type III crack. The aP_{op} closure loads follow a continually decreasing trend with increasing crack size, and is zero for a type III crack.

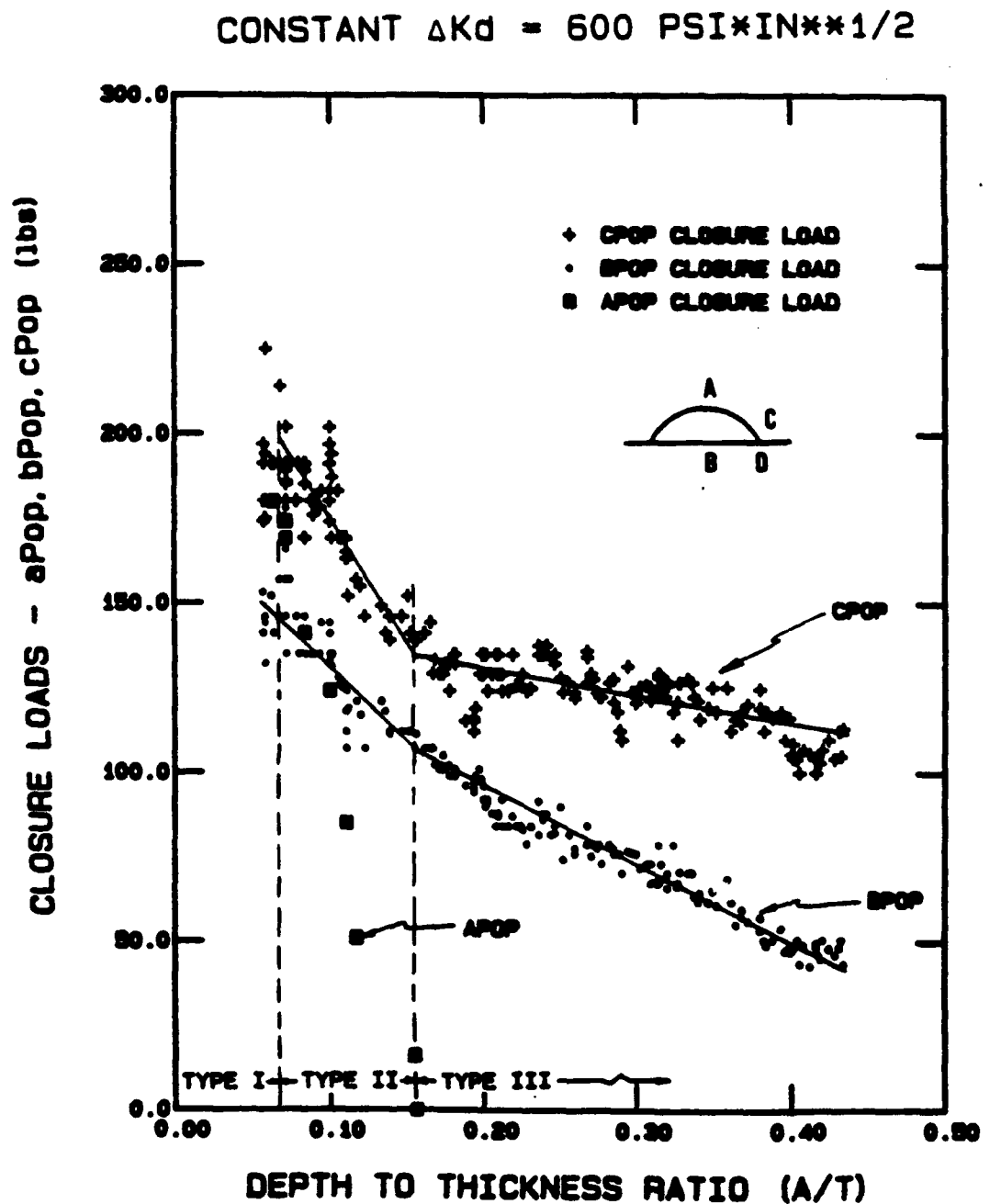


Figure 5.18 Closure load (aPop, bPop & cPop) variation with crack size (a/t) from the constant ΔK_d test

Figure 5.19 presents the closure load ratio (P_{op}/P_{max}) as a function of crack size for aP_{op} , bP_{op} and cP_{op} . The cP_{op} closure ratio (cP_{op}/P_{max}) is seen to increase to an average value of 0.29 during the formation of type I and II cracks. With the formation of a type III crack ($a/t = 0.156$), cP_{op}/P_{max} gradually increases and levels-out at around 0.36. These values of closure ratio correspond to the general range of published values summarized by Schijve (45) for mild steel, titanium 6-4 and aluminum 7475-T73. Schijve also reported the results of Minakawa and McEvily (46) which showed K_{op}/K_{max} (equivalent to P_{op}/P_{max}) increasing with decreasing ΔK (load shedding). This trend is consistent with the cP_{op}/P_{max} trend in Figure 5.19 after the formation of a type III crack.

The bP_{op} closure ratio (bP_{op}/P_{max}) is relatively constant at a level of 0.21 for a type I and II crack in Figure 5.19. With the formation of a type III crack, bP_{op}/P_{max} begins to decrease, reaching a value of about 0.15 at the test maximum crack size.

This significant reduction in closure load is attributed to the large void formation with increasing crack size.

Closure Load Variations with Load History

The closure load data presented in this section compares the constant ΔK_d , constant load and block loading test results with the constant ΔK_d data from above. The closure load absolute values ($aPop$, $bPop$ and $cPop$) are presented for the three tests in Figure 5.20 through 5.22. Comparisons of all four tests are made in Figure 5.23 through 5.28.

Figures 5.20 through 5.22 appear to show the same general trend in closure load as seen for both $aPop$ and $cPop$ discussed above for the constant ΔK_d test (Figure 5.18). In Figure 5.21, bP_{op} appears to show a different trend in the type I crack size region since it increases before decreasing with crack growth. Although different, the trend is considered consistent and representative of the crack geometry stabilizing in the types I and II transition regions. This trend of closure load increasing and then decreasing was also observed in

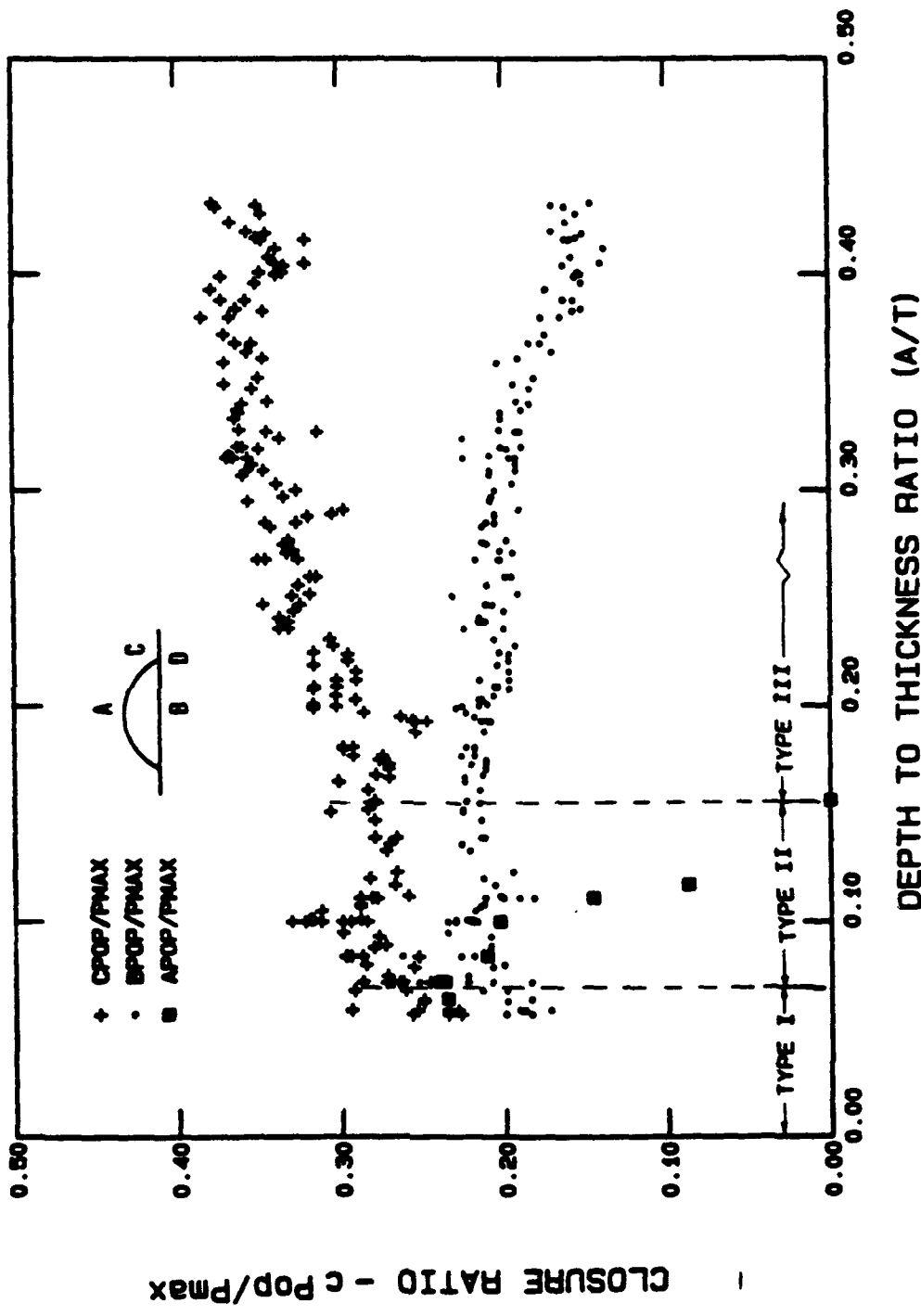


Figure 5.19 Closure to maximum load ratios plotted as a function of crack size (a/t) from the constant ΔK_d test

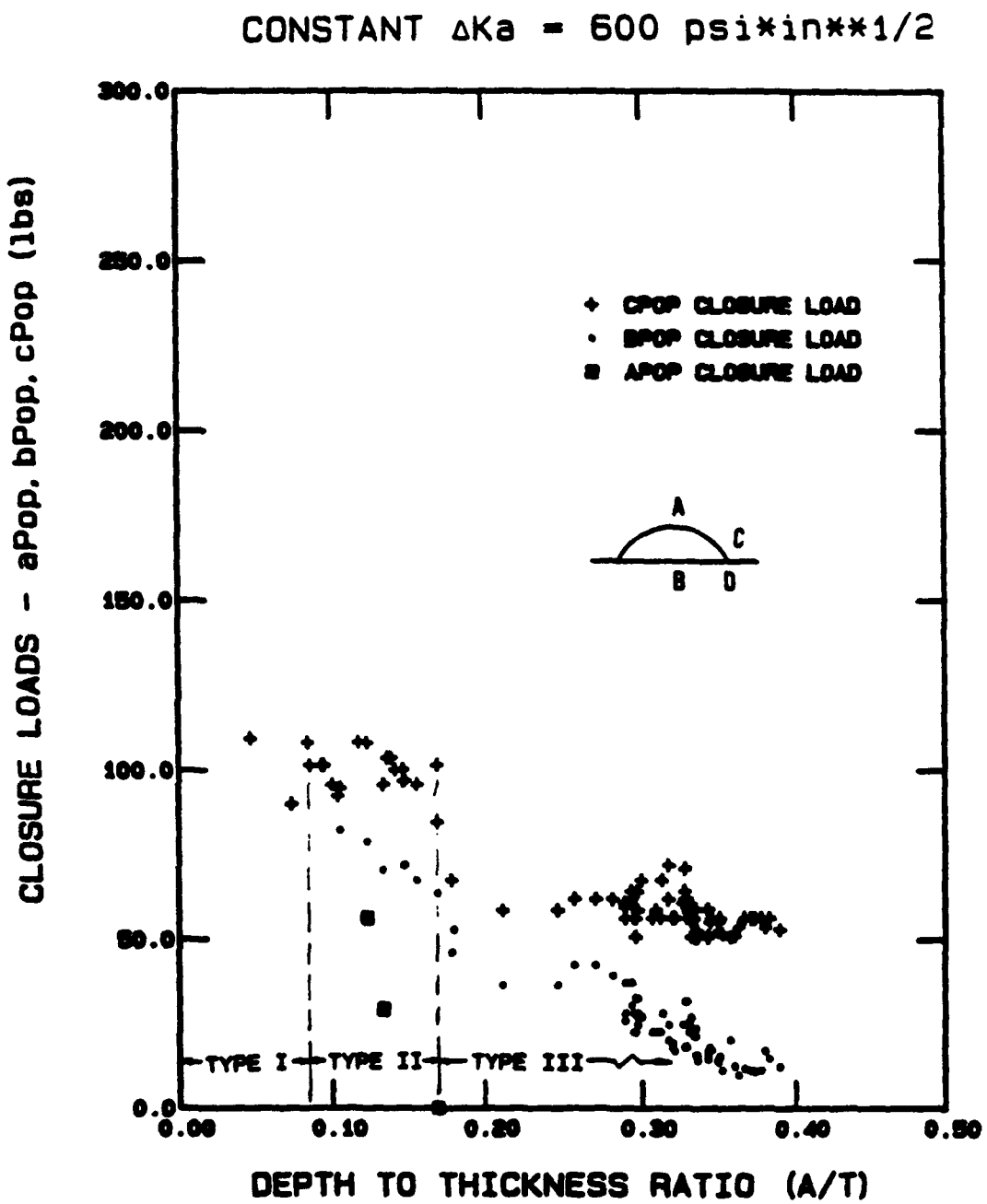


Figure 5.20 Closure load (aPop, bPop & cPop) as function of crack size (a/t) from the constant ΔK_a test

CONSTANT LOAD

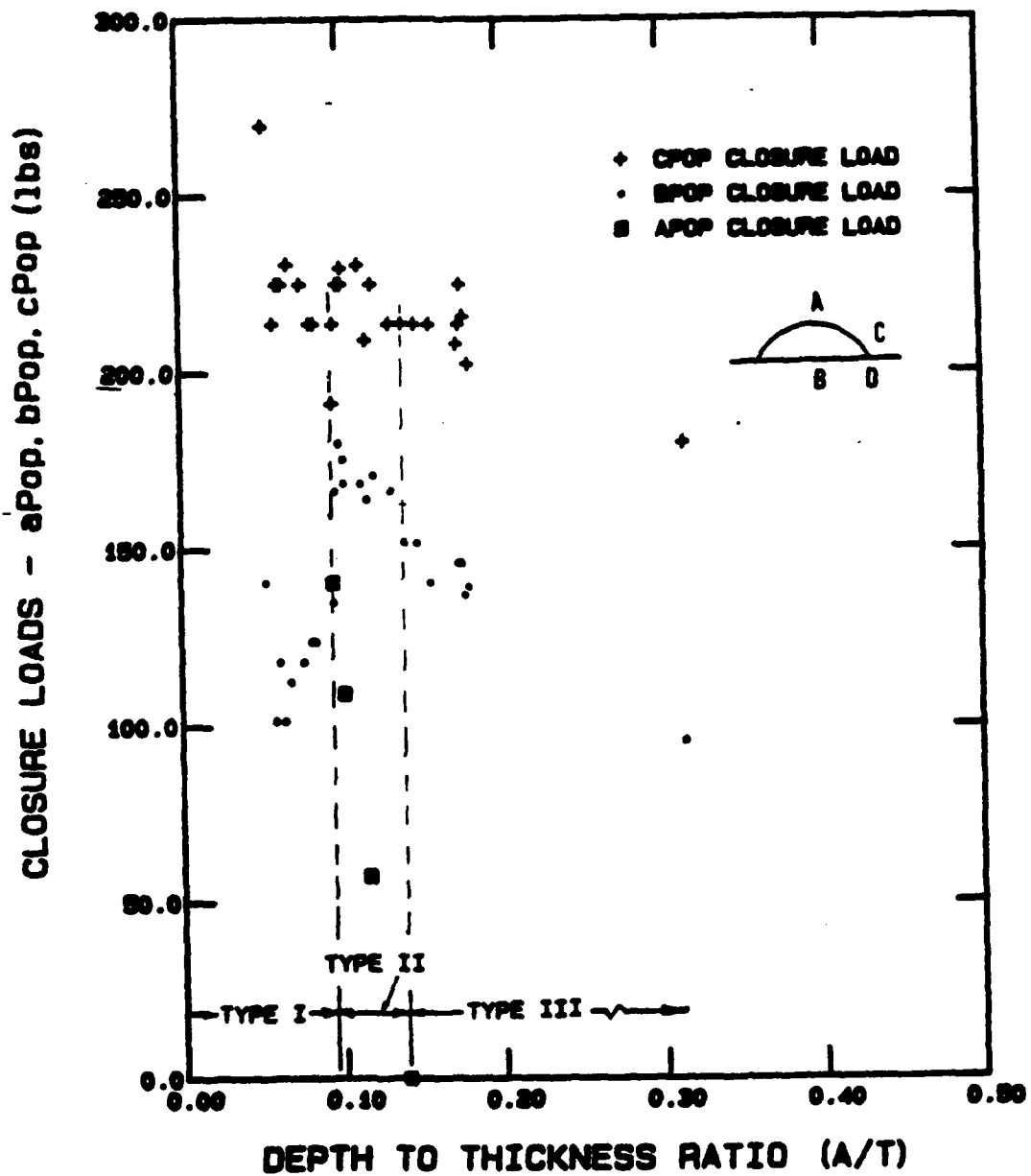


Figure 5.21 Closure load (aPop, bPop & cPop) as function of crack size (a/t) from the constant load test

BLOCK LOADING

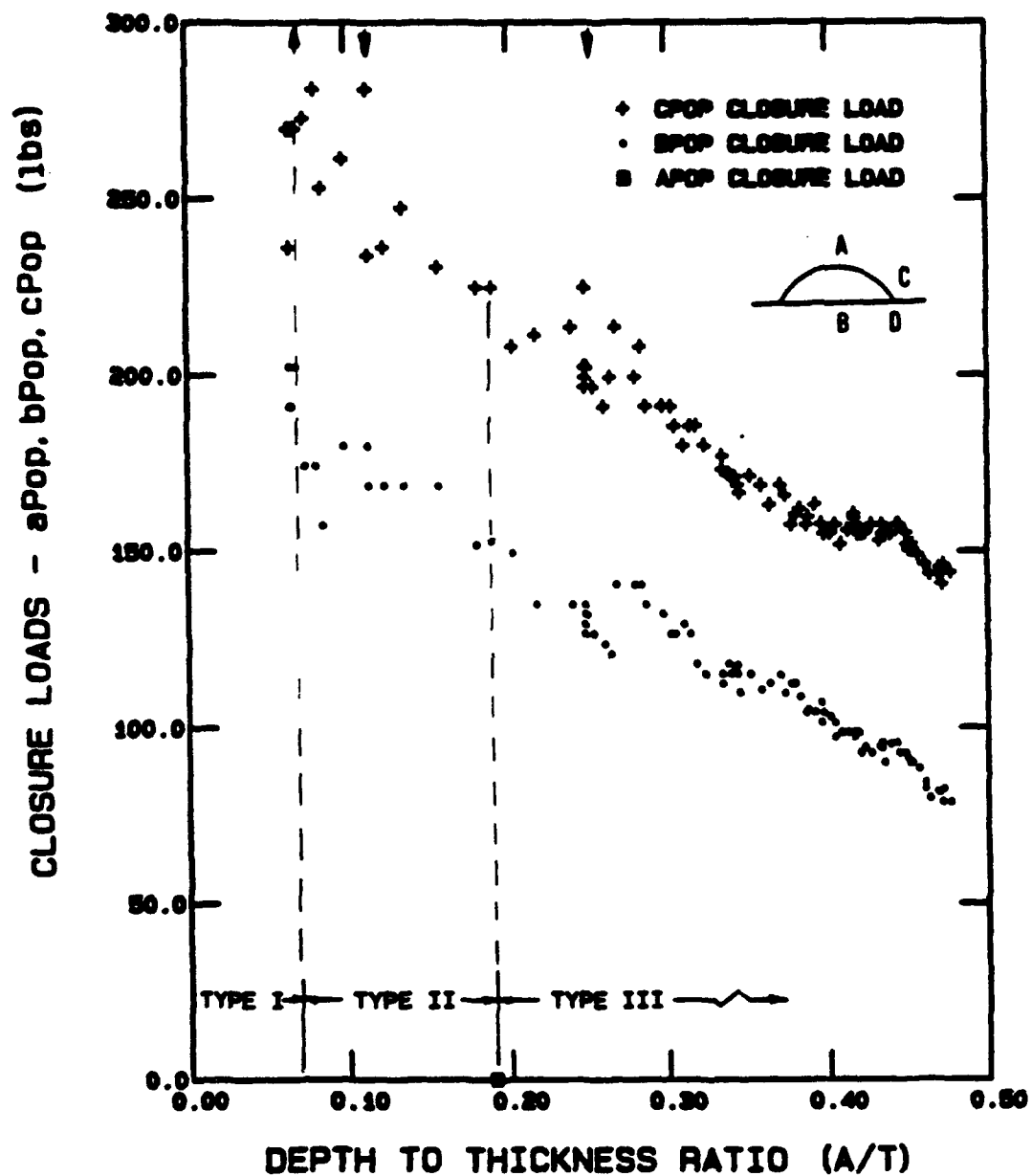


Figure 5.22 Closure load (aPop, bPop & cPop) as function of crack size (a/t) from the block loading test

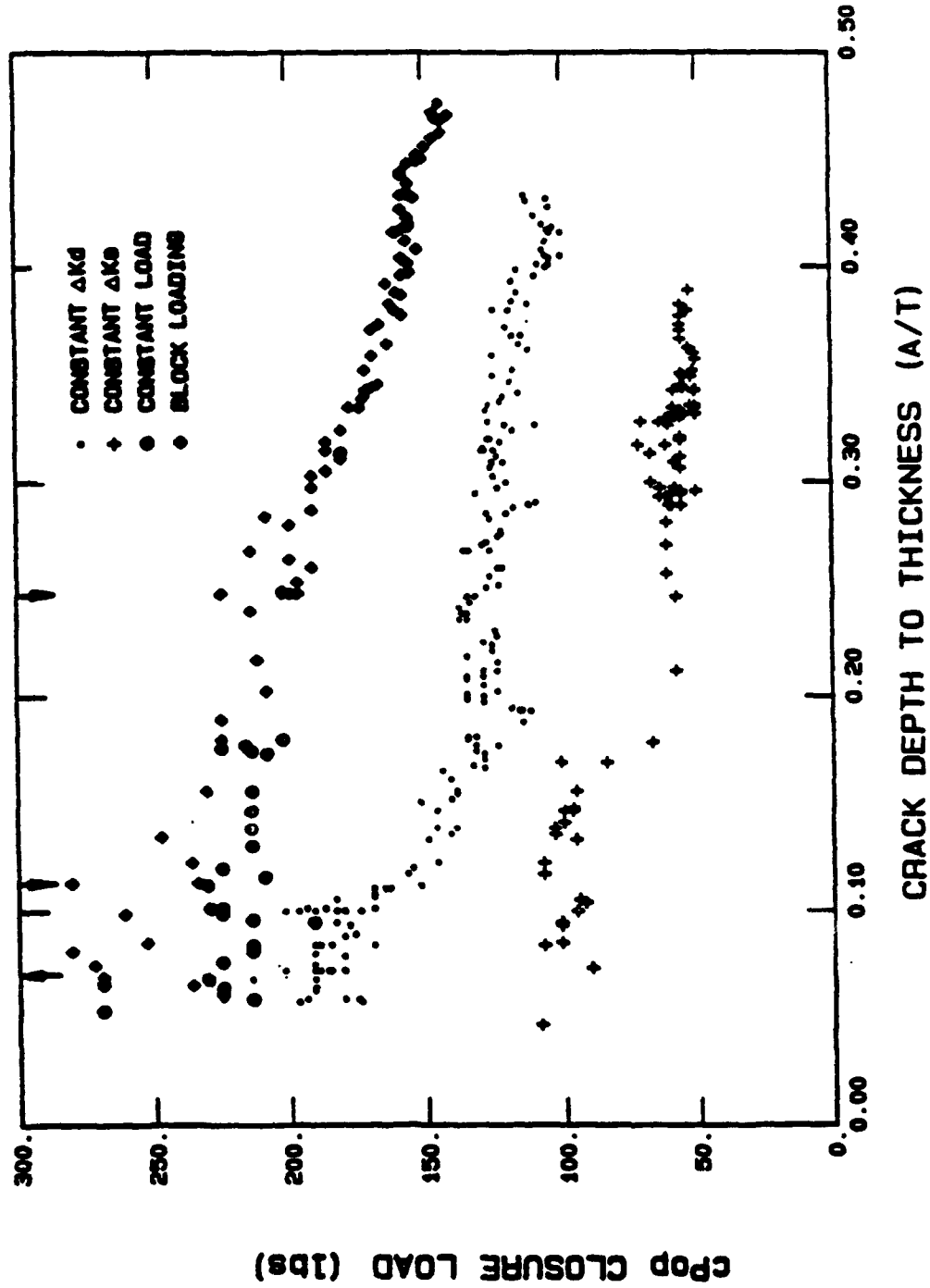


Figure 5.23 Comparison of the CPoP closure loads for all four tests as a function of crack size (A/T)

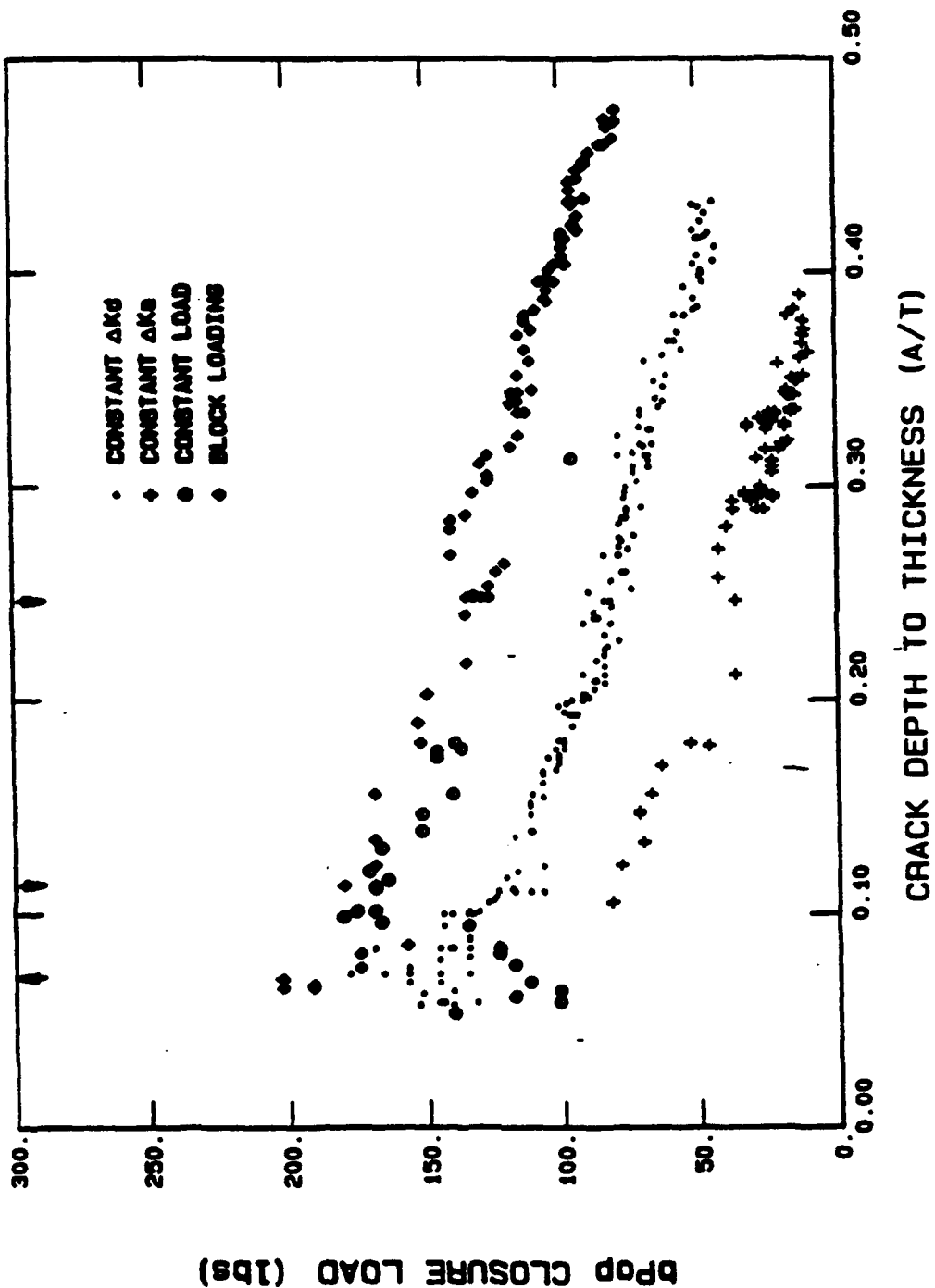


Figure 5.24 Comparison of the bPop closure load for all four tests as a function of crack size (a/t)

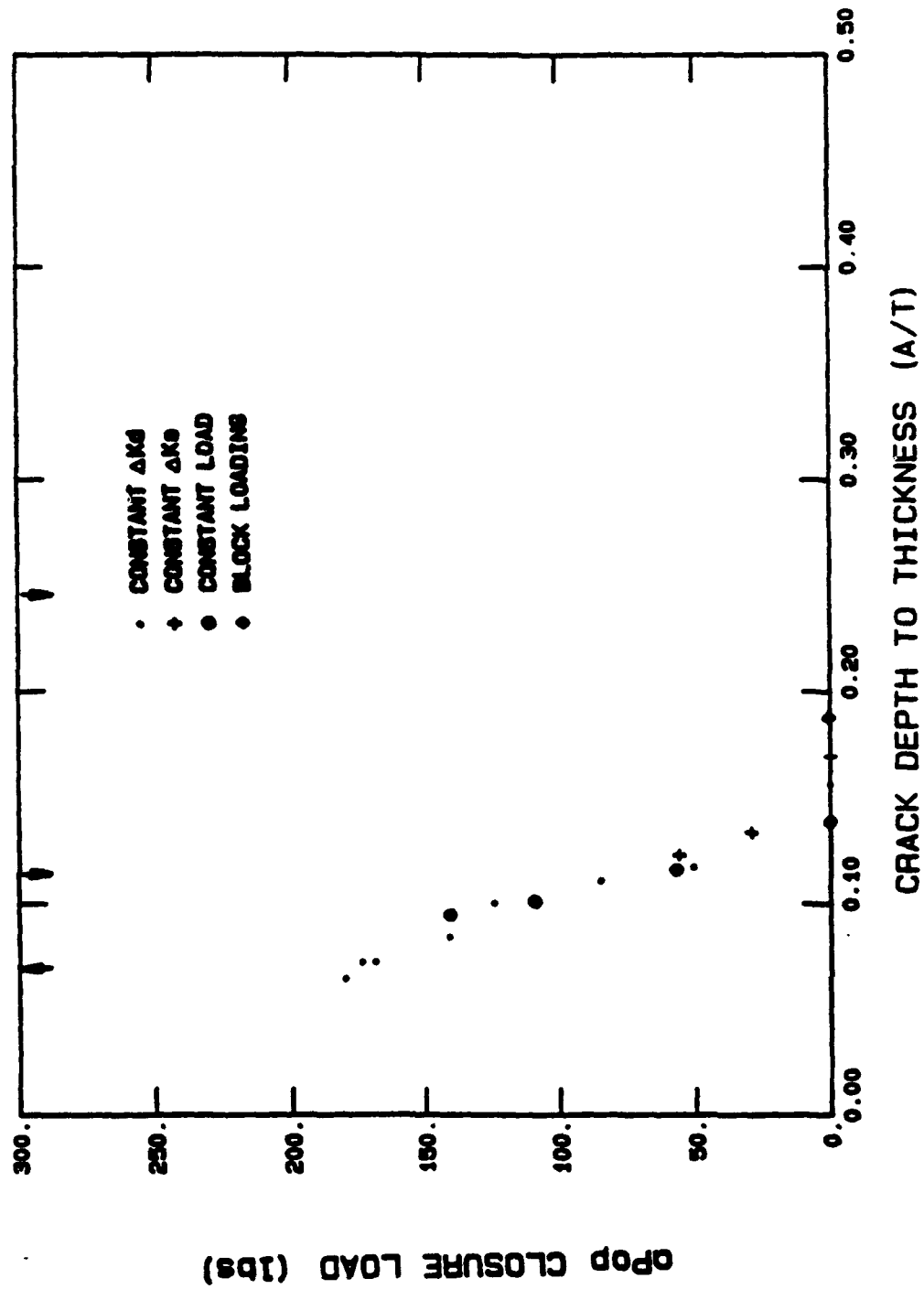


Figure 5.25 Comparison of the a_{Pop} closure load for all four tests as a function of crack size (A/t)

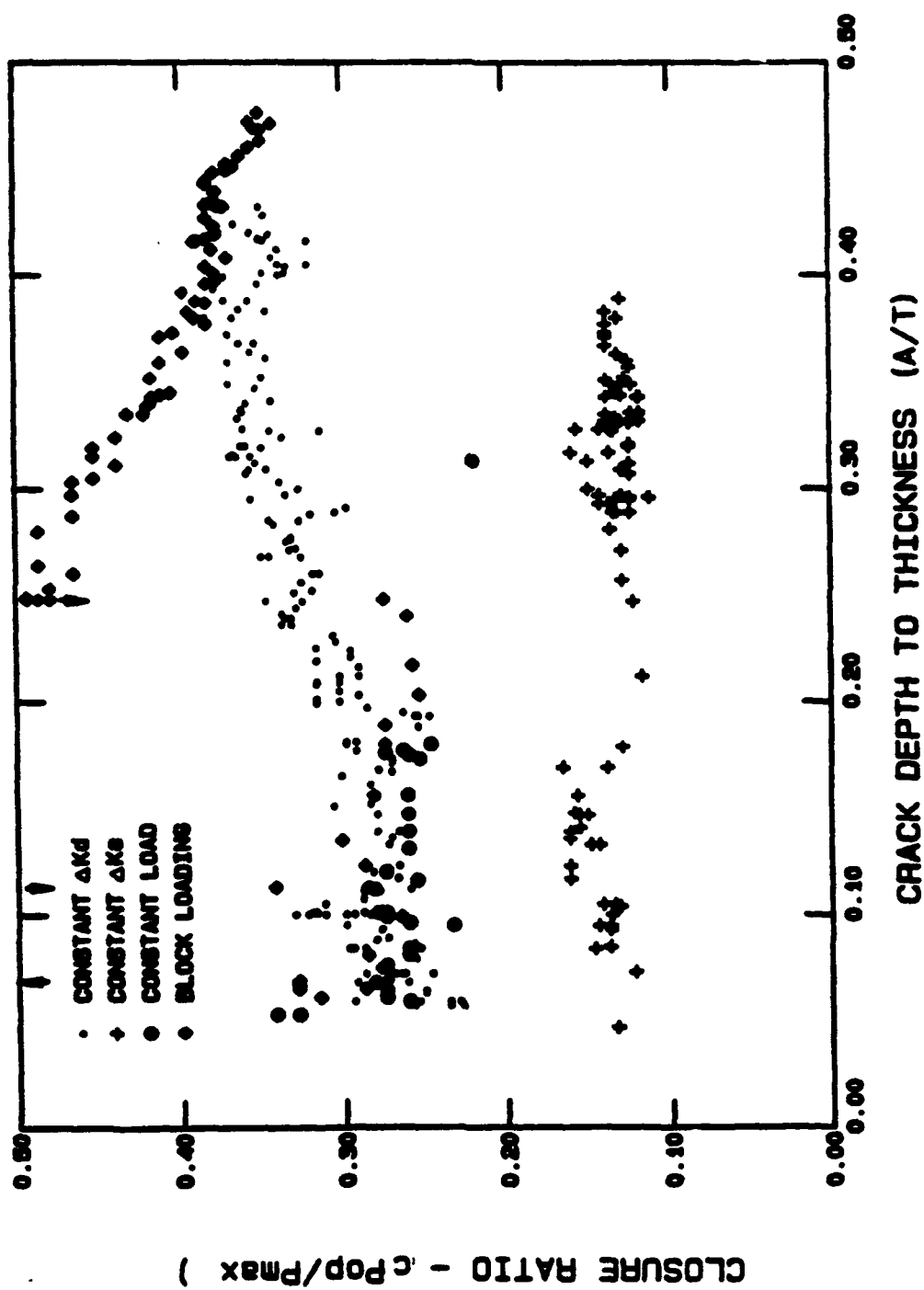


Figure 5.26 Comparison of the c_{Pop}/P_{max} closure ratio as a function of crack size

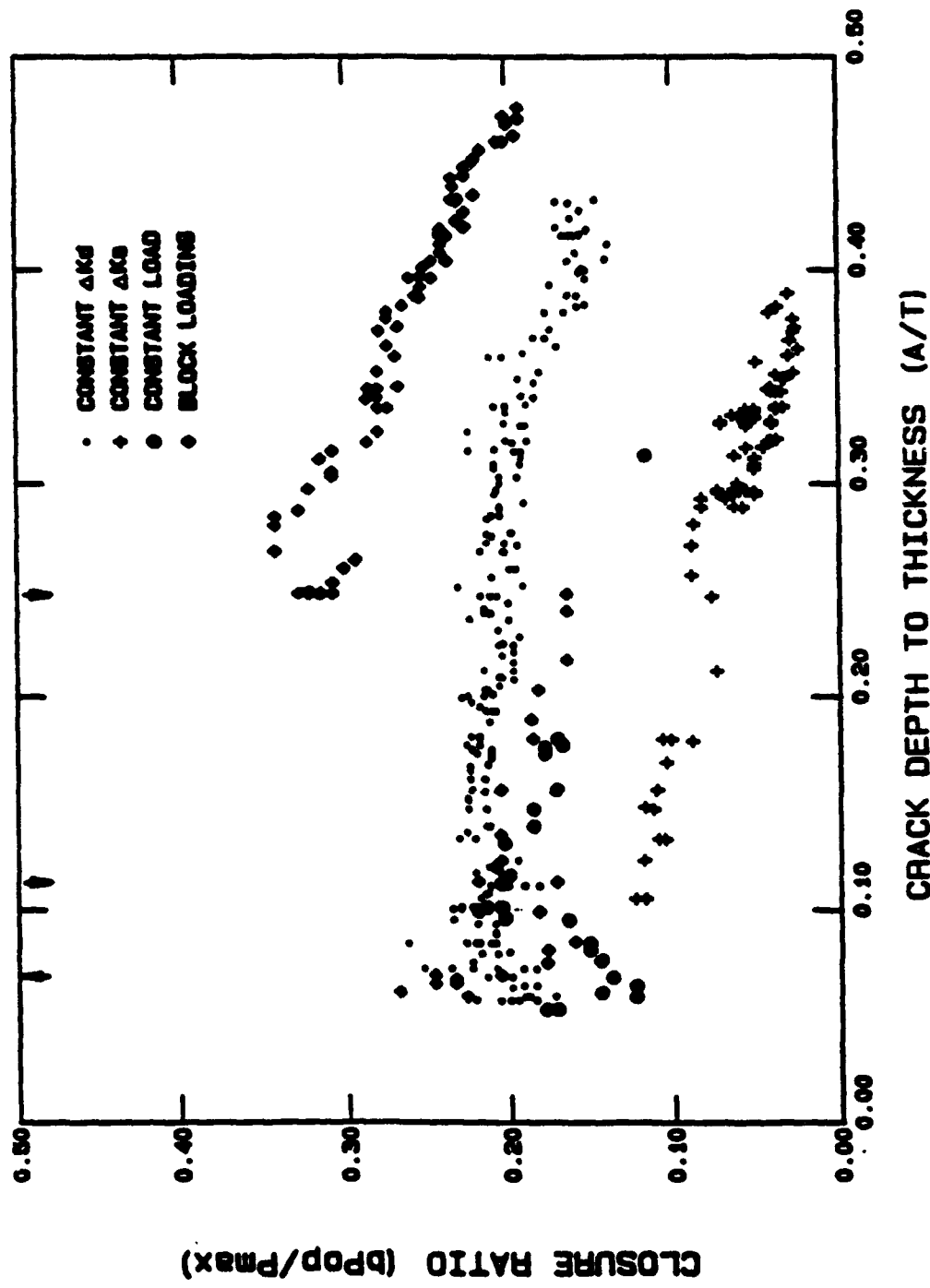


Figure 5.27 Comparison of the bP_0P/P_{max} closure ratio as a function of crack size

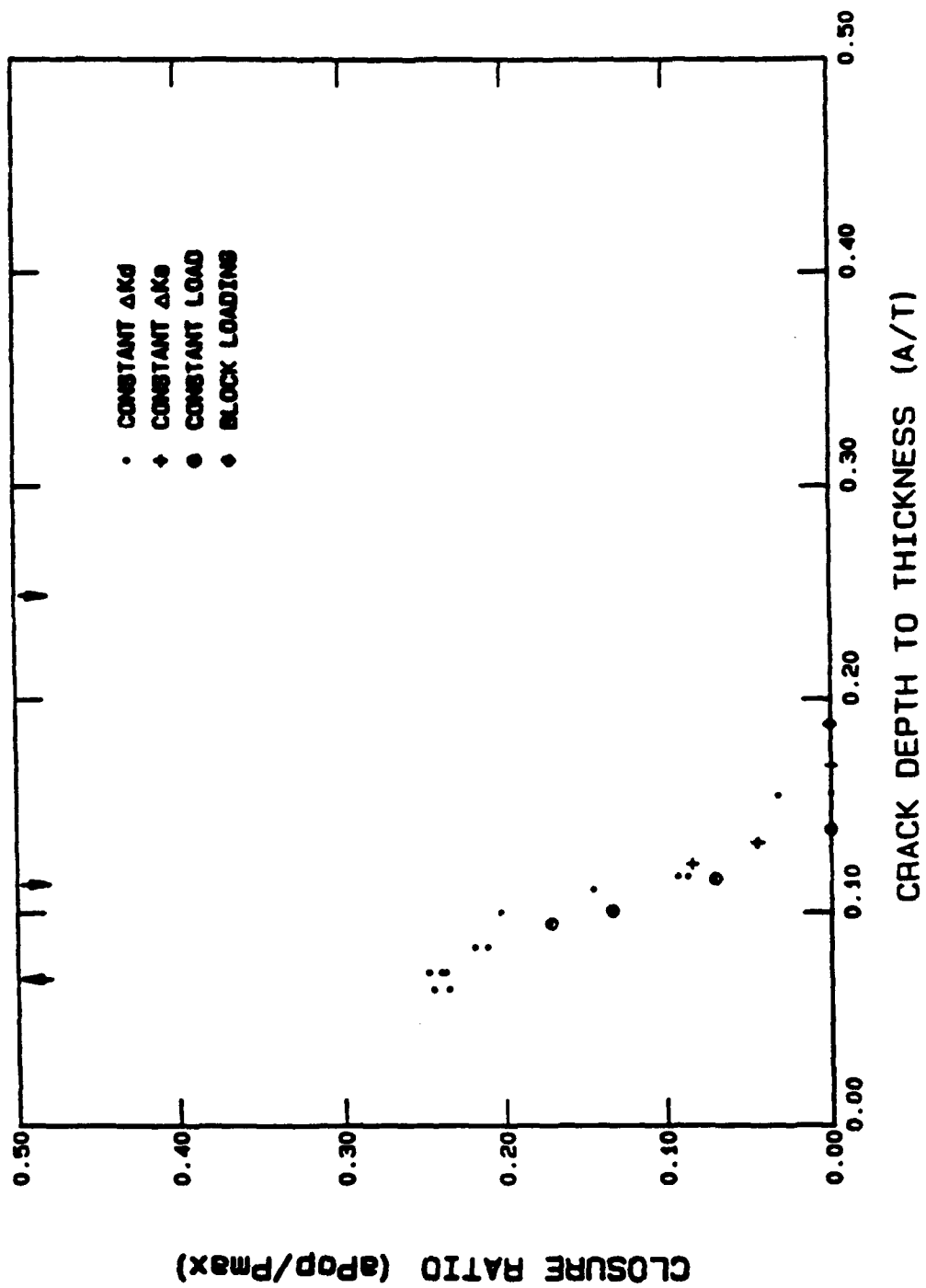


Figure 5.28 Comparison of the a_{Pop}/P_{max} closure ratio as a function of crack size

Ray's (25) data. However, when Ray repeated the same test, the closure load was found to continually decrease with crack size. Also, bP_{op} measurements made in this investigation during precracking (presented in Appendix E) ranged from 146 to 176 lb., which is equivalent to the bP_{op} levels shown in Figure 5.21. Once a type II crack is formed, the bP_{op} trend follows the same decreasing pattern with crack growth as the other tests.

The block loading data in Figure 5.22 identifies the applied load transition points at the top of the plot (Figure 4.12). The first arrow indicated an increase in applied load from a delta moment of 644 in-lb. to 773 in-lb. The next two arrows represent a reduction in applied load from 773 in-lb to 644 in-lb and then to 322 in-lb for the remainder of the test. These load transition point arrows are also presented on all of the block loading plots for reference.

Absolute closure load values (aP_{op} , bP_{op} and cP_{op}) for all four tests are compared in Figures 5.23 through 5.25. Each of the Figures present characteristic information concerning the closure load mechanism as discussed in items A through D below.

A. Overall observations from Figures 5.23 through 5.25 are:

1. Closure load absolute values decrease with increasing crack size.
2. bP_{op} and cP_{op} load levels are higher for the constant load and block loading tests than for the constant stress intensity factor tests.
3. aP_{op} trends (Figure 5.25) follow the same slope of decreasing closure load with increasing crack length for all four tests. Therefore, aP_{op} is inversely proportional to crack size.

B. Comparing trends from the constant ΔK_d test with the constant ΔK_a tests:

1. bP_{op} and cP_{op} are higher for the constant ΔK_d tests than for the constant ΔK_a tests.
2. aP_{op} , bP_{op} and cP_{op} are inversely proportional to crack size.

C. Comparing the constant load test (continually increasing ΔK) with the constant ΔK_d test:

1. The constant load test closure loads are consistently higher than the constant ΔK_d levels. This is anticipated (as discussed in the approach) since the plastic zone size is continually increasing while the constant ΔK_d plastic zone remains constant after precracking.
2. aP_{op} and bP_{op} closure loads follow the same slope once a type II crack is formed.

D. Comparing the constant load test with the block loading test:

1. cP_{op} for the block loading test are only slightly higher than the constant load test during the types I and II crack formation. Once a type III crack is formed, the closure loads are the same.
2. cP_{op} is relatively constant for the constant load test until a type III crack is formed. For the block loading test, abrupt increases in applied load cause cP_{op} to increase, and decreases in applied load cause cP_{op} to decreased.
3. bP_{op} is only slightly larger in the block loading test than in the constant load test once a type II crack is formed. The bP_{op} versus a/t slopes are consistent for both tests.

Comparisons of the closure load ratios (P_{op}/P_{max}) for all four tests are shown in Figures 5.26 through 5.28. In Figure 5.26, three of the four tests (constant ΔK_C , load and block loading) are seen to have average closure load ratio values of approximately 0.29 for $0.0 \ll a/t \ll 0.20$ (during transition between a type I and II crack). The constant ΔK_a test is at a level of approximately 0.14.

Closure load ratios for the constant ΔK_d test are noted to increase from a level of about 0.29 before the formation of a type III crack, to a level of 0.35 after a type III crack is formed. A ratio of 0.35 is also a level at which the block loading test stabilizes.

Although the 20% load change at $a/t = 0.07$ and 0.11 during the block loading test caused minor changes in cP_{op}/P_{max} , these changes were noted to quickly return to a stable level of about 0.29 with crack growth. However, with a major P_{max} load reduction of 50% at $a/t = 0.25$, an abrupt change in cP_{op}/P_{max} occurs, and does not return to the original level for the remainder of the test. This is similar to results observed by Ashbaugh (47) when testing thru-thickness compact tension specimens of Inconel 718 material. He observed that with a 60% reduction in load level for an $R = 0.1$, the crack was required to grow twice its length in order to return to the original closure load ratio.

Although the constant ΔK_a test is noted to vary around the crack type transition points, it is relatively constant for the complete test. The constant load test is initially at a level of approximately 0.29, and reduces to a level of 0.22 with crack growth.

Table 5.8 is a comparison of closure loads at a common crack size ($a = 0.14$, $c = 0.20$). Note the trend of closure load absolute values being highest for the block loading test and lowest for the constant ΔK_a test. The closure load ratios are at the same relative level except for the constant ΔK_a test.

Table 5.8: Closure Load Values at a Common Crack Size ($a = 0.14$, $c = 0.20$)

Test	$\frac{cP_{cr}}{P_{max}}$	$\frac{bP_{cr}}{P_{max}}$	$\frac{cP_{cr}}{P_{max}}$	$\frac{bP_{cr}}{P_{max}}$
Block Loading	225	152	0.27	0.19
Constant Load	202	139	0.25	0.17
Constant ΔK^d	115	96	0.25	0.21
Constant ΔK^a	67	53	0.13	0.09

VI. EFFECTIVE STRESS INTENSITY FACTOR DEFINITIONS

The widely accepted definition of effective stress intensity factor (ΔK_{eff}) proposed by Elber (1) is based on the use of an effective load range ($P_{max} - P_{cl}$) instead of an applied load range ($P_{max} - P_{min}$) for predicting fatigue crack growth (reference Chapter 2, "Plasticity-Induced Closure"). Although this basic definition is readily accepted, defining the closure load and the corresponding stress intensity factor (K_{cl}) is a problem which has plagued the fracture mechanics community for over 15 years. For example, numerous papers have been written on closure load measurement problems ranging from instrumentation type to measurement location (3,25,26). Interpretation of the crack internal surfaces opening before the external free-surface for thru-thickness cracks (19,20,21) is another problem area. These considerations are all relevant for surface flaws, which also have the additional complication of a three-dimensional crack boundary.

An approach for organizing the experimental results presented in Chapter V is essential before a definition of ΔK_{eff} can be proposed for surface flaws. That rationale is presented in this chapter, and forms the basis for data correlation relating to various definitions of ΔK_{eff} which follow in the next two chapters. The primary variables associated with these definitions can be grouped into four major areas of influence:

1. The closure load range ($P_{max} - P_{cl}$, where P_{cl} is one of the three measured closure loads aP_{op} , bP_{op} or cP_{op}).
2. The location at which K is being calculated (i.e., crack tip location A or C).
3. The crack opening displacement (COD) associated with a particular crack tip location and crack size (i.e., crack types I, II and III).
4. The stress intensity factor solution used to calculate K .

Organizing the above four areas into a useful format requires a concise set of definitions. The first two areas can be characterized by a matrix format of closure load and crack tip locations. This format is summarized below, and will be used extensively throughout the remainder of this report. The closure load range is denoted by superscripts, the crack tip locations by subscripts, and ΔK and ΔK_{eff} are defined as follows:

Applied Stress Intensity Factor (K):

$$\Delta K_a = \text{applied } \Delta K \text{ at location A due to } (P_{max} - P_{min})$$

$$\Delta K_c = \text{applied } \Delta K \text{ at location C due to } (P_{max} - P_{min})$$

Effective Stress Intensity Factor (ΔK_{eff}):

$$\Delta K_{a\ eff}^a = \text{effective } \Delta K \text{ at location A due to } (P_{max} - aP_{op})$$

$$\Delta K_{a\ eff}^b = \text{effective } \Delta K \text{ at location A due to } (P_{max} - bP_{op})$$

$$\Delta K_{a\ eff}^c = \text{effective } \Delta K \text{ at location A due to } (P_{max} - cP_{op})$$

$$\Delta K_{c\ eff}^c = \text{effective } \Delta K \text{ at location C due to } (P_{max} - cP_{op})$$

or

$$\Delta K_{j\ eff}^i = \text{effective } \Delta K \text{ at location j due to } (P_{max} - iP_{op})$$

where $i = a, b, c$ to define the closure load, and $j = a$ or c to define the crack tip location A or C, respectively.

Organizing the third area from above (COD influences) requires a comprehensive evaluation of the individual crack types, and their relationship to crack size, closure load and crack tip location. These relationships form the basis for defining ΔK_{eff} , and address key questions such as:

1. How do the three crack types (I, II and III) influence the stress intensity factor around the crack tip boundary?
2. Which of the closure loads (a_{Pop} , b_{Pop} or c_{Pop}) should be used to define K_{cl} ?
3. How are the crack tip locations, crack types and various closure load measurements used to define ΔK_{eff} ?

The fourth area for consideration (K-solutions) will be discussed in each of the following sections.

Effective Stress Intensity Factor for a Type I Crack

A type I crack opening displacement (COD) pattern was described in Chapter V ("Typical COD Profiles") as being classical in that the complete crack boundary opens at the same load level. That is, with load application the crack initially opens at the crack free-surface (b_{Pop} , reference Figure 5.15), and continues to open inwardly from the free-surface until the internal surfaces and crack tip boundary are completely open (such that $b_{Pop} \ll a_{Pop} = c_{Pop}$, reference Figures 5.2 and 5.3).

Because of the type I crack opening pattern, classical fracture mechanics K-solutions, such as Newman-Raju (5), can be used to predict ΔK_{eff} as proposed by Elber (1, eqn. 2.7). That is:

$$\Delta K_{eff} = U \Delta K = \frac{P_{max} - P_{cl}}{P_{max} - P_{min}} \Delta K \quad (6.1)$$

$$= K_{max} - K_{cl}$$

Since the closure load (P_{cl}) needed to open a type I crack tip boundary is approximately equal at locations A and C (that is, $aP_{op} = cP_{op}$), the effective load range is calculated using either aP_{op} or cP_{op} . These two values of ΔK_{eff} are shown in Figure 6.1, where the ordinate represents either K_a or K_c , and the abscissa an applied load. Then:

$$\Delta K_{a\ eff}^a = \frac{P_{max} - aP_{op}}{P_{max} - P_{min}} \Delta K_a \quad (6.2)$$

$$\Delta K_{c\ eff}^c = \frac{P_{max} - cP_{op}}{P_{max} - P_{min}} \Delta K_c \quad (6.3)$$

The solid line (region 3) defines fully-open COD patterns where K-solutions are available for calculating ΔK_{eff} . A double dashed line extends from the solid line to the zero load to identify available fully-open K-solutions. The heavier dashed line (extended horizontally from the solid line) reflects a hypothesized constant K-level associated with the crack tip boundary being completely closed. This conclusion is based on the observation that at cP_{op} and lower loads the crack tip is closed, and represents two possible solutions either the K-level remains constant, or the K-level is instantaneously zero as load is reduced below cP_{op} . To choose the later would require K to be a discontinuous function, and therefore the choice of a constant K-level was made.

For loads between bP_{op} and cP_{op} (region 2), the crack tip is closed while the crack internal surfaces are open. For loads between zero and bP_{op} (region 1), both surfaces are closed. For both region (1) and (2), the K-level is considered to be constant since the crack tip is closed.

Load regions (1), (2), and (3) are identified on this plot to illustrate their expected relationship to the classical definition of closure on a load versus displacement plot,

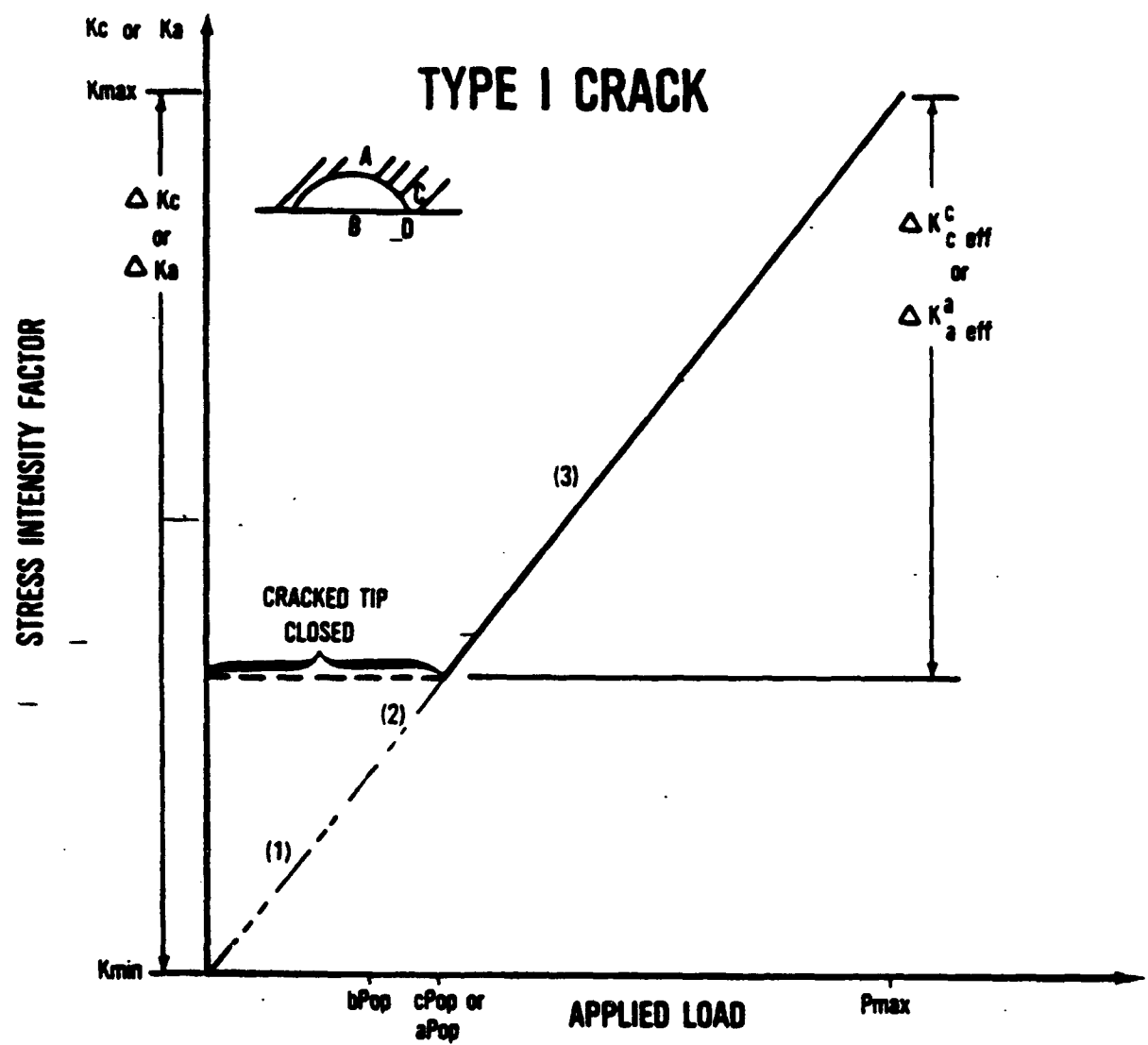


Figure 6.1 Schematic representation of K as a function of applied load for a type I crack at location A or C

where displacement is measured at the crack middle free-surface (Figure 6.2). This load-displacement format is similar to data presented in Figure 5.13.

For the R ratio of 0.035 used in investigation, bP_{op} , is always greater than P_{min} . Therefore, for an applied load less than cP_{op} the crack tip boundary is always closed. If a higher R ratio were used, such that P_{min} were greater than cP_{op} , P_{cl} would be defined as P_{min} instead of cP_{op} .

Effective Stress Intensity Factor for a Type II Cracks

A type II crack is distinguished by the formation of a "void" internal to the crack surfaces while the crack tip boundary is closed under zero load (reference Chapter V, "Typical COD Profiles," Figures 5.2 and 5.3). This "void" formation complicates the definition of K around the crack tip boundary because the load required to open the crack tip at location A (aP_{op}) is different from the load required to open location C (cP_{op}). Therefore, for applied loads between aP_{op} and cP_{op} , the crack tip is open at location A while it is closed at location C. This forms a crack tip boundary which is "partially-open" and "partially-closed" (as opposed to "fully-open"), for which there are no K-solutions known to be available.

The crack opening displacement (COD) process for a type II crack is shown schematically in Figure 6.3, where K_a is plotted as a function of applied load. The opening process is separated into four regions such that region (1) is between a load of zero and aP_{op} , region (2) between aP_{op} and bP_{op} , region (3) between bP_{op} and cP_{op} , and region (4) between cP_{op} and P_{max} . The hypothesized partially-open K-level experienced by the crack tip in the closure load region (1-3) is identified on the plot by the heavy dashed line. The solid line (region 4) represents available "fully-open" K-

TYPE I CRACK SCHEMATIC

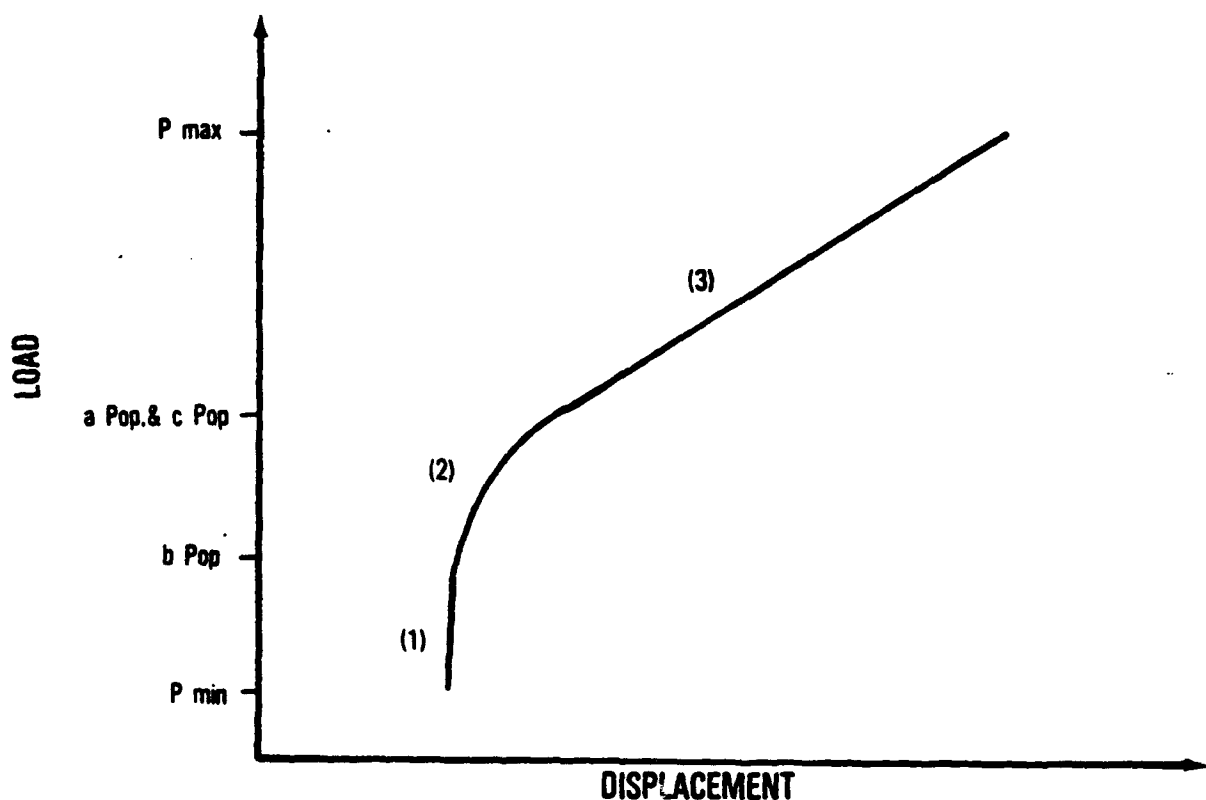


Figure 6.2 Schematic of load versus displacement at the crack free-surface to relate closure load regions (1,2,3) to figure 6.1 for a type I crack

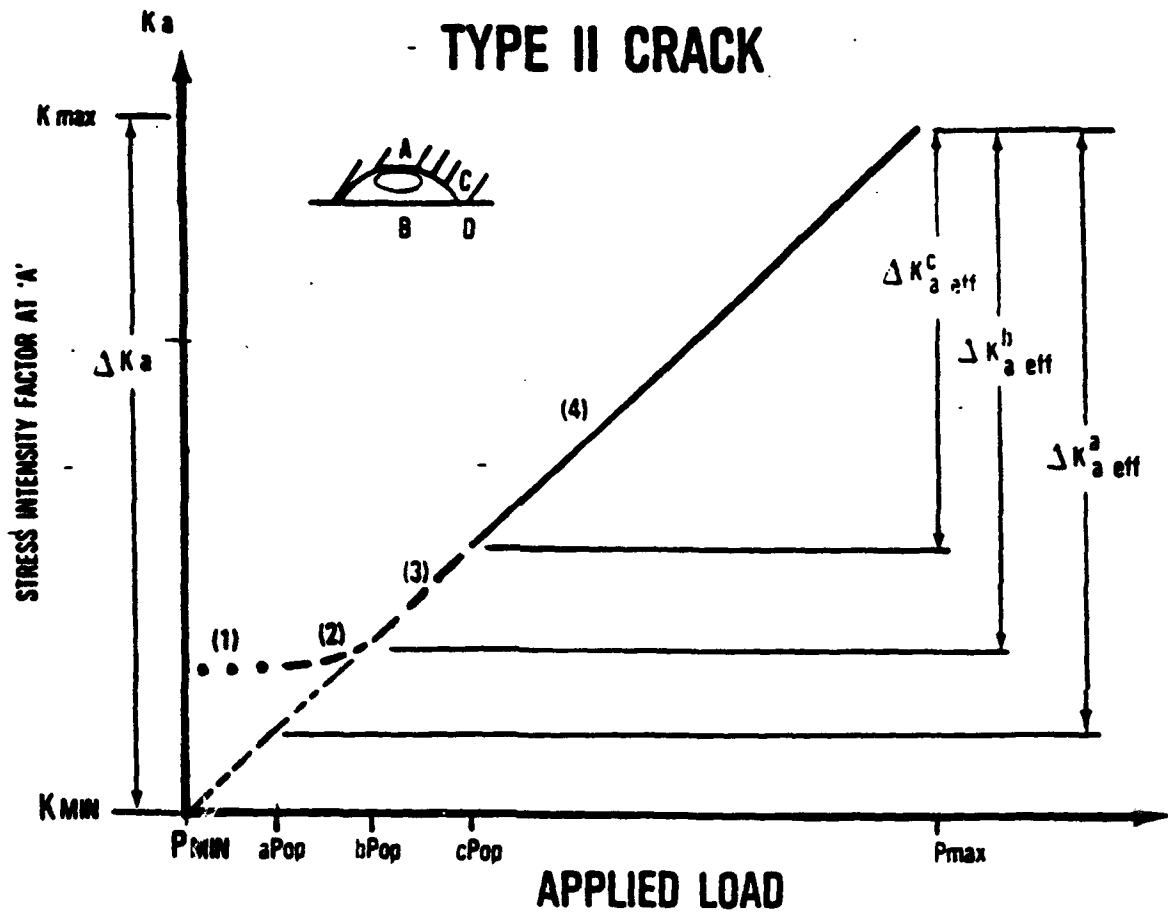


Figure 6.3 Schematic representation of K as a function of applied load for a type II crack at location A ($\phi=90$ degrees). Three potential ΔK_a eff definitions are represented

solutions when the crack is completely open for loads greater than cP_{op} . Each of these COD regions is described in the following paragraphs.

In region 1 of Figure 6.3, the crack tip boundary is closed at zero load. Upon load application, the internal void increases in size and initially opens the crack tip at location A at a load level of aP_{op} . Since the crack tip is closed below aP_{op} , there is little change in crack tip geometry and K_a remains relatively constant. The projected K_a levels are depicted by a heavy dashed line since K-solutions are not directly available for this crack tip geometry.

As load is increased above aP_{op} , the void increases in size until the crack free-surface (location B) at the bP_{op} load level. Below bP_{op} the crack free-surface is closed while the crack tip boundary is open between locations A and C, and results in the specimen geometry being relatively stiff. Therefore, changes in K_a with increased load are expected to be very small, as well as being nonlinear because of the continual change in crack geometry between aP_{op} and bP_{op} (region 2). As load is increased above bP_{op} , changes in K_a are expected to be much greater with applied load since the geometry is more compliant due to the crack free-surface being open. Between bP_{op} and cP_{op} (region 3), the crack surfaces and tip boundary continues to open until the cP_{op} load is reached and the crack is fully-open. Between cP_{op} and P_{max} (region 4), K_a (solid line) is linear with applied load since the crack is fully-open and the geometry remains constant. That is, the slope of the linear portion of the K_a versus applied load curve is proportional to the geometry factor corresponding to a fully-open surface flaw, and K_a can be defined using available K-solutions such as $K = P^*F(a,a/c,\phi)$; where $F(a,a/c,\phi)$ is the boundary correction factors corresponding to a fully-open surface flaw of depth "a", aspect ratio "a/c" and location angle ϕ .

In summary, changes in actual K_a are nonlinear with respect to applied load between zero and cP_{op} because of the continually changing crack geometry with increasing load. K_a is hypothesized to increase from a constant value between a load of

zero and aP_{op} (region 1), and to continue along a nonlinear path (regions 2 and 3) until it reaches the cP_{op} load. It then becomes linear (region 4) up to and including the maximum applied load.

The relationship of actual K_a experienced by the crack tip at location A (discussed above) and calculated ΔK_a eff can be seen in Figure 6.3. Here, three separate ΔK_a eff definitions are presented by using available fully-open K-solutions and measured closure loads (aP_{op} , bP_{op} and cP_{op}), such that:

$$\Delta K_a^a \text{ eff} = \frac{P_{max} - aP_{op}}{P_{max} - P_{min}} \Delta K_a \quad (6.4)$$

$$\Delta K_a^b \text{ eff} = \frac{P_{max} - bP_{op}}{P_{max} - P_{min}} \Delta K_a \quad (6.5)$$

$$\Delta K_a^c \text{ eff} = \frac{P_{max} - cP_{op}}{P_{max} - P_{min}} \Delta K_a \quad (6.6)$$

where ΔK_a is defined from the fully-open K-solution (solid line), and the double-dashed line extended to the ordinate and abscissa (for $K_{min} = 0$). Here, ΔK_a^a eff and ΔK_a^b eff is projected to bound the actual ΔK_a value (shown by heavy dashed line), and it would appear that the best P_{cl} value to define the actual ΔK_a is between aP_{op} and bP_{op} when using available K-solutions. On the other hand, not having accurate K-solutions to represent the actual crack geometry leaves this selection open for further evaluation (Chapter VII). Note that all three of the ΔK_a^i eff definitions provide values which are less than the applied ΔK_a valued defined by $K_{max} - K_{min}$.

Extending this evaluation to the classical definition of closure load on a load-displacement plot can be seen schematically in Figure 6.4. In this format, selection of the

TYPE II SCHEMATIC

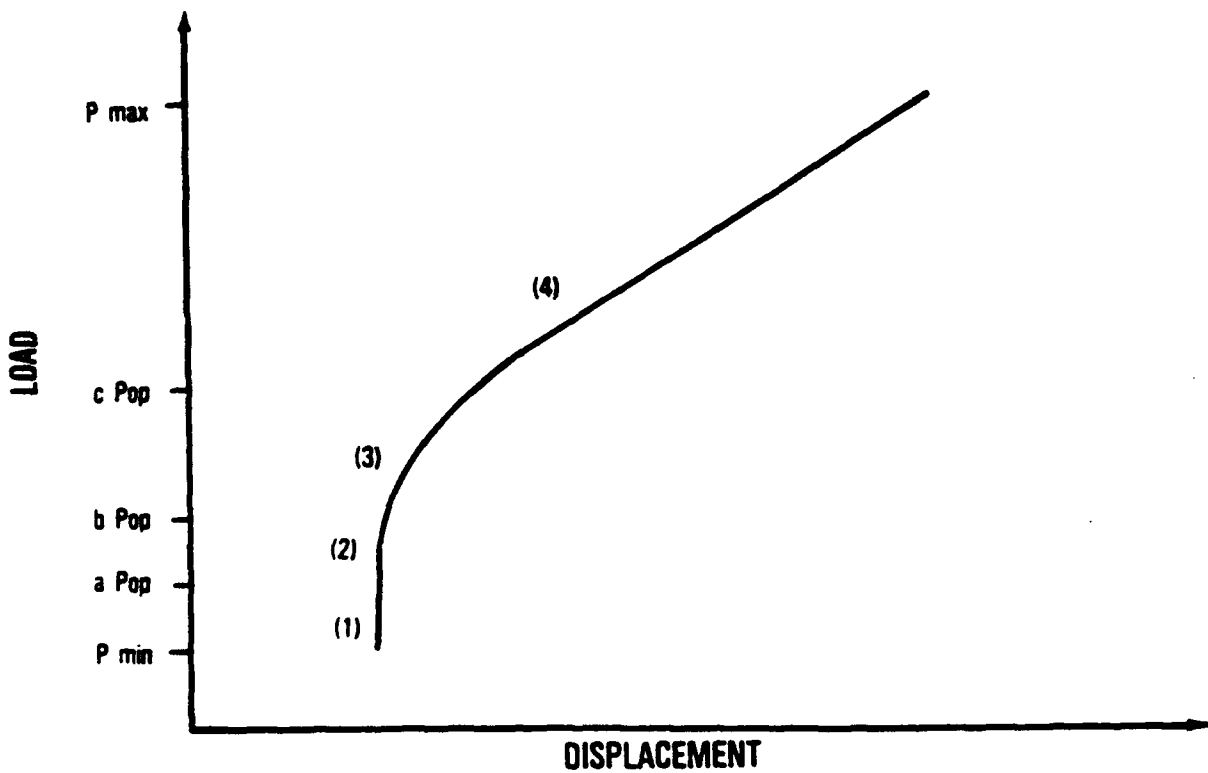


Figure 6.4 Schematic of load versus displacement at the crack free-surface to relate closure load regions (1,2,3,4) to Figure 6.3 for a type II crack

aP_{op} to bP_{op} closure load range to calculate actual K_a also corresponds to a primary definition of closure load for thru-thickness cracks. It should be noted that although the slope changes in region (2) and (3) may be minor and difficult to detect by conventional instrumentation (clip gauges, back face strain, etc), they represent definite changes in crack geometry which were described in Chapter V (Figure 5.13).

In comparison, $\Delta K_c \text{ eff}$ at location C (Figure 6.5) is much simpler to evaluate than $\Delta K_a \text{ eff}$. Here, the crack is closed at location C until the cP_{op} load level is reached (defined as the last portion of the crack surfaces to open). Thereafter, the crack is fully-open and $\Delta K_c^C \text{ eff}$ is calculated from available formulae using an effective load range of $P_{max} - cP_{op}$. The COD representation on a load versus displacement plot is shown in Figure 6.4 as region (4). This analysis is valid for all three crack types.

Effective Stress Intensity Factor for a Type III Crack

The difference between a type II and type III crack is associated with the "void" displacement having reached a sufficient size to geometrically open the crack tip boundary at location A at zero load. That is, the crack tip at location A is open at zero load ($aP_{op} = 0$), while other locations around the crack tip boundary are closed (reference Figures 5.2 and 5.3).

The process of defining K_a and $\Delta K_a \text{ eff}$ for a type III crack at location A is shown schematically in Figure 6.6 where K_a is plotted as a function of applied load. It should be noted that for a type III crack, K_a is not zero at zero load since the crack tip is open, but is a variable which is directly proportional to crack size. That is, with increased crack growth the void size increases (area and displacement), causing a larger displacement at location A and more of the crack tip boundary between location A and C to open. The crack tip boundary length which is open at zero load has been measured to

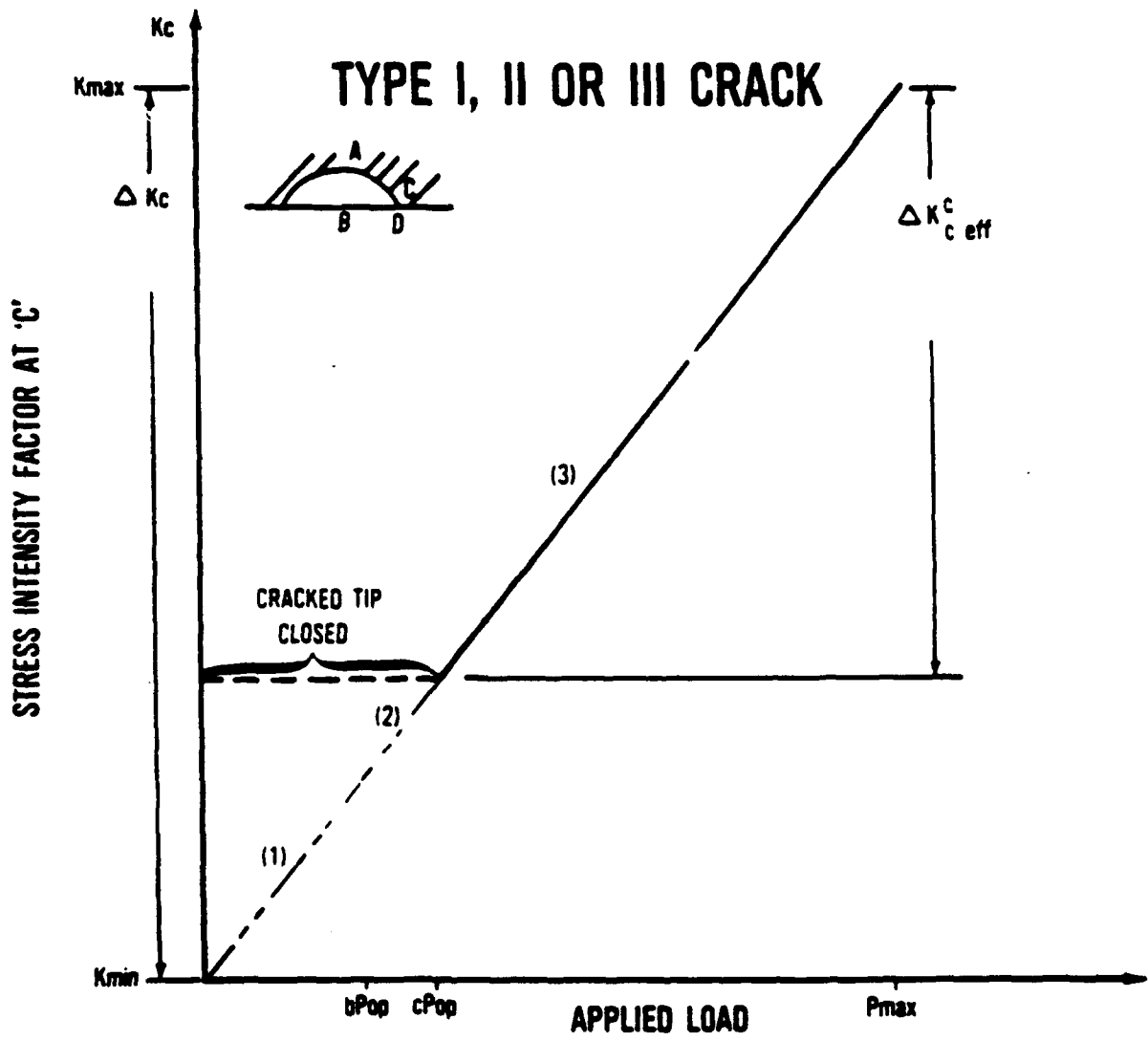


Figure 6.5 Schematic representation of K as a function of applied load at location C ($\theta=12$ degrees) for three crack types

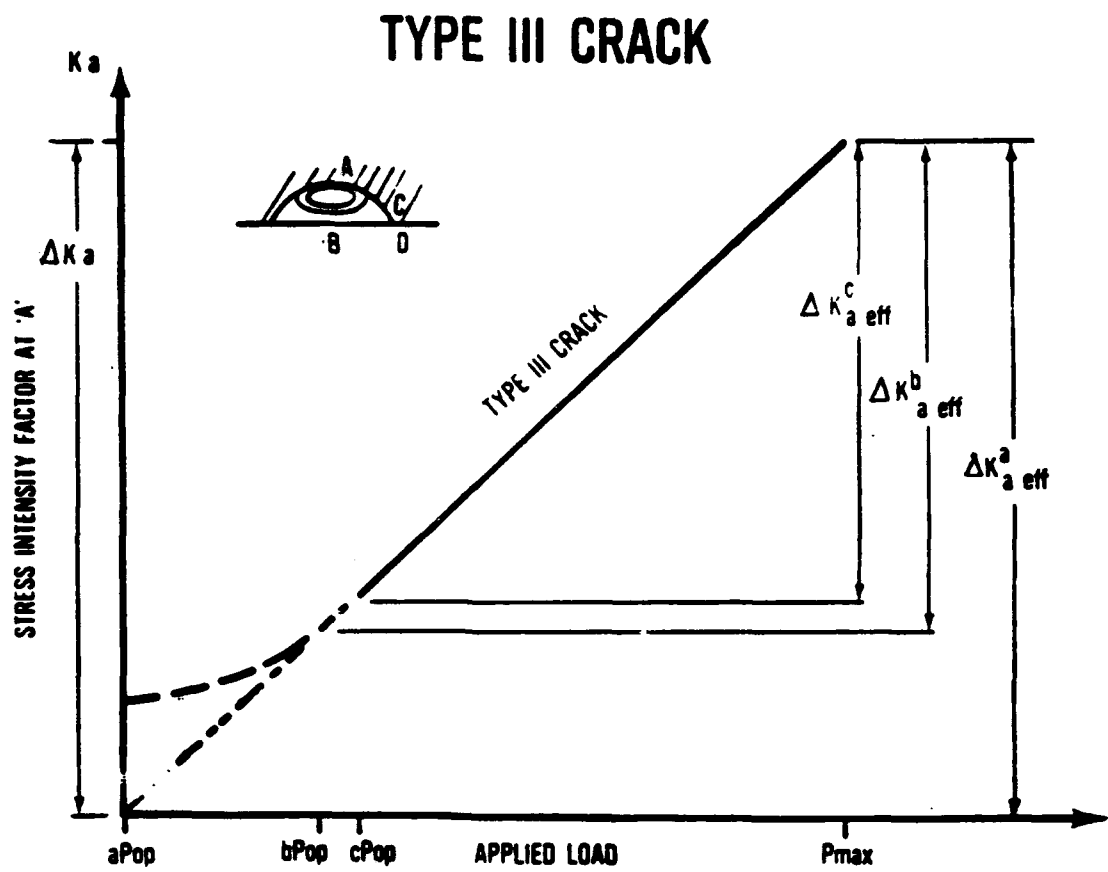


Figure 6.6 Schematic representation of K as a function of applied load for a type III crack at location A ($\phi=90$ degrees). Three potential $\Delta K_{a\ eff}$ definitions are represented

range from 17% for $a/t = 0.208$ to 65% for $a/t = 0.260$ (reference Chapter V, "Typical COD Profiles").

For load levels between zero and bP_{Op} , the crack free-surface is closed, the resultant specimen geometry is relatively stiff, and changes to K_a with increased load are expected to be small and nonlinear. As load is increased above bP_{Op} , the crack geometry is more compliant since the crack free-surface is open, and the K_a rate of change with applied load is expected to be much greater. This process is identified as a nonlinear heavy dashed line between aP_{Op} and cP_{Op} in Figure 6.6 since K-solutions for a type III partially-open crack (with an internal void formation) are not known to exist -- thus precluding K_a from be determined directly.

For loads above cP_{Op} , K_a increases linearly with load since the crack is fully-open and the geometry remains constant. These K_a values can be defined using available K-solutions such as $K = P^*F(a,a/c,\phi)$, and is represented by a linear solid line between cP_{Op} and the maximum applied load. The correlation of closure load regions on a load versus displacement plot are projected to be represented by regions 2 through 4 on Figure 6.4. However, since compliance is greater for large cracks (reference Figure 5.14), regions (2) and (3) will not be as distinct as with a type II crack. This observation is consistent with measurements by Bucci (48), who presented load-displacement data for thru-thickness cracks which showed a smoothing of the nonlinear regions 2 and 3, as well as a reduction in closure load with increased crack sizes for a high strength aluminum alloy.

As can be seen in Figure 6.6, each of the three closure loads (aP_{Op} , bP_{Op} and cP_{Op}) can be used to define three distinct effective stress intensity factors at location A (ΔK_a^{eff} , $\Delta K_a^{b,eff}$, $\Delta K_a^{c,eff}$). Again, only estimates of actual ΔK_a can be determined using available fully- open K-solutions and measured load ranges. From the Figure 6.6 schematic it would appear that the actual ΔK_a is best defined between the aP_{Op} and bP_{Op} closure loads. As with a type II crack, this evaluation is difficult to substantiate using

fully-open K-solutions when the crack is partially-open (part of the crack tip is closed while other parts are closed).

Note that ΔK_a^b and ΔK_a^c values are less than the classical applied ΔK_a defined by $K_{max} - K_{min}$. ΔK_a^a is either greater than applied ΔK_a for P_{min} loads greater than zero, or equal to ΔK_a when $P_{min} = 0$.

Again, the definition of ΔK_c^i for a type III crack is much simpler than ΔK_a^i as depicted in Figure 6.5. Here, the crack is closed at location C until the cPop load level is reached and the crack becomes fully-open. Then, K_c is calculated using available formulae, and ΔK_c^c is a function of the effective load range ($P_{max} - cP_{op}$).

Closure Load Considerations

It is apparent from the previous discussion that the void formation (reference Figure 5.4) is not modeled by available K-solutions. Although it is not apparent this represents a calculation problem at the crack free-surface (reference Figure 5.1, K_c), it does present a calculation problem at location A (K_a , $\phi = 90$ degrees).

For a type I crack, the aP_{op} or cP_{op} closure loads (P_{cl}) can be used to define ΔK_{eff} using an effective load range ($P_{max} - P_{cl}$) and fully-open K-solutions at either location A or C of the crack tip boundary. For a type II crack, it is not known whether aP_{op} or bP_{op} best represents the location A effective load range. K-solutions are not known to exist for this crack geometry. For a type III crack the closure load at location A is zero, and the crack residual opening is a function of crack sizes (larger cracks have larger internal displacement, reference Figure 5.8). Again, K-solutions are not known to exist for this partially-open crack geometry. These considerations for selecting a closure load, and the need for K-solutions which match the crack geometry, are summarized in Tables 6.1 and 6.2.

**Table 6.1: Hypothesized Closure Load and K-Solution Needs to Define
 ΔK_{eff} at Crack Tip Location A**

<u>Crack Type</u>	<u>Closure Load (P_{cl}) Variable</u>	<u>K-solution</u>
I	cPop	OK
II	bPop	Needed
III	bPop	Needed

**Table 6.2: Hypothesized Closure Load and K-Solution Needs to Define
 ΔK_{eff} at Crack Tip Location C**

<u>Crack Type</u>	<u>Closure Load (P_{cl}) Variable</u>	<u>K-solution</u>
I	cPop	OK
II	cPop	OK
III	cPop	OK

It is apparent from Table 6.1 that although a need exists for partially-open crack K-solutions, available fully-open crack models represents a major portion of the crack growth process and are expected to provide good estimates of partially-open cracks. First, $\Delta K_c \text{ eff}$ (location C) can be obtained from the effective load range ($P_{max} - cP_{op}$), and existing K-solution for a fully-open crack. Second, for both type II and type III cracks, it is hypothesized that $\Delta K_a \text{ eff}$ (location A) can be approximated from the ($P_{max} - bP_{op}$) load range and available K-solutions for partially-open cracks. Since the region

between bP_{op} and cP_{op} corresponds to a crack geometry such as that shown in Figures 5.4c-d, K_a , although not known, is felt to be representative of a fully-open crack. Thus, the slope between bP_{op} and cP_{op} in Figures 6.3 and 6.6 should be similar to that of a fully-open crack; allowing the use of available K-solutions and the $(P_{max} - bP_{op})$ effective load range.

For a type II crack, the K-solution at location A (reference Figure 5.4b crack geometry), although not known, is expected to yield smaller values than for a fully-open crack because of the inherent "stiffness" of that geometry due to closure along the free-surface. That is, the slope of the curve in Figure 6.3 between aP_{op} and bP_{op} is expected to be smaller than for a fully-open crack. Selecting the $(P_{max} - aP_{op})$ load range for determining ΔK_a eff would appear to overestimate the crack tip K_a value. Thus, the use of bP_{op} for calculating ΔK_a eff appears to be a reasonable average choice instead of aP_{op} which becomes zero when transition occurs between a type II and type III crack (reference Figure 5.18).

Therefore, the definition of ΔK_{eff} depends on the crack tip boundary location (ϕ), crack depth, aspect ratio and selection of a closure load which corresponds to a given crack type. Considering the current status of K-solutions, selection of a representative closure load (P_{cl}) to define an effective load range $(P_{max} - P_{cl})$ can only be hypothesized at location A. For these cases, an average load range of $(P_{max} - bP_{op})$ is considered a reasonable choice, such that:

$$\Delta K_a^b \text{ eff} = (P_{max} - bP_{op}) F(a, a/c, \phi=90) \quad (6.7)$$

It is of interest to note that the degree of difficulty associated with the location A crack tip has also been reported by other investigators. A detailed review of surface crack K-solutions and aspect ratios for plates in bending by Mahmoud and Hosseini (41), identified major prediction errors at the location A crack tip. Their comparison of the

Newman-Raju K-solutions to photoelastic experimental results identified a 56% error for one case at location A, versus a $\pm 14\%$ error at the crack free-surface. The authors attributed this error to experimental extrapolation from a two-dimensional specimen to a three-dimensional crack. Discrepancies for surface flaws were also identified by Carter, et al. (42) when testing aluminum in tension. This study reported that "It has not been determined whether the source of error is due to fundamental different crack growth rates at surface and depth or due to inaccurate stress intensity solutions."

VII. EFFECTIVE STRESS INTENSITY FACTOR CORRELATION WITH FATIGUE CRACK GROWTH RATES

Identification of the three crack types, and their influence on crack opening displacement (COD), closure loads and effective stress intensity factor, have raised a number of questions concerning the prediction of fatigue crack growth (FCG). One of the more significant questions is based on selecting the load range which "best" defines effective stress intensity factor using fully-open K-solutions. The approach for selecting this "best" effective load range is formulated around correlating experimental FCG rate data -- as described in this chapter. The evaluation is conducted using data from Chapter V, along with the effective stress intensity factors definitions discussed in Chapter VI.

It merits re-emphasizing that this chapter will utilize available K-solutions to bound the crack growth rate prediction by evaluating various effective load ranges. In effect, not having partially-open K-solutions for a "void" geometry (as experimentally identified in this investigation) precludes selecting the optimum effective load range. Therefore, an evaluation of the "best" correlation of the data utilizing linear elastic fully-open K-solutions is presented. This condition only effects location A, not location C where the crack is fully-open above the cP_{op} closure load. The K-solution differences at location A are expected to be small as discussed in the previous chapter.

Closure Load Stress Intensity Factor

Selecting closure load ($P_{max} - P_{cl}$) which produces the least data scatter can be accomplished by evaluating the ability of several ΔK_{eff} definitions to correlate fatigue crack growth rate (FCGR) data into the specimen depth (da/dN) and the crack free-surface (dc/dN). That is, the evaluation process for selecting the most representative closure load

range to match the experimental data is based on the correlation of predicted da/dN and dc/dN versus applied ΔK and several definitions of ΔK_{eff} . The matrix of ΔK_{eff} definitions are based on the bP_{op} and cP_{op} closure load effects at locations A and C (Table 7.1). These four combinations of effective load ranges are represented by $\Delta K_{c\ eff}^c$, $\Delta K_{c\ eff}^b$, $\Delta K_{a\ eff}^c$ and $\Delta K_{a\ eff}^b$ and a cross term of $\Delta K_{a\ eff}^b$ and $\Delta K_{c\ eff}^c$. From the evaluation in Chapter VI, the logical selections for correlating da/dN data is $\Delta K_{a\ eff}^b$, and for dc/dN is $\Delta K_{c\ eff}^c$ (assuming partially-open K-solutions are available).

Table 7.1: Closure Stress Intensity Factor (K_{cl}) Variables Used to Evaluate Several ΔK_{eff} definitions

FCGR	<u>cPop Closure</u>	<u>bPop Closure</u>
<u>Direction</u>	<u>Load Effects</u>	<u>Load Effects</u>
dc/dN	$K_{c\ cl}^c$	$K_{c\ cl}^b$
da/dN	$K_{a\ cl}^c$	$K_{a\ cl}^b$

An example calculation of $\Delta K_{c\ eff}$ using K_{cl} at locations C with the cP_{op} closure load follows from equations 2.7 and 2.8. In that:

$$\Delta K_{c\ eff}^c = U_c \Delta K_c$$

where: $U_c = (P_{max} - P_{c\ cl}^c) / (P_{max} - P_{min})$

$$= (1. - cP_{op}/P_{max}) / (1. - R) \quad (7.1)$$

Then:

$$\begin{aligned}\Delta K_{c \text{ eff}}^c &= K_{\max} (1 - c P_{op} / P_{\max}) \\ &= K_{c \max} - K_{c cl}^c\end{aligned}\quad (7.2)$$

Likewise, at location A:

$$\Delta K_{a \text{ eff}}^c = K_{a \max} - K_{a cl}^c \quad (7.3)$$

The K_{cl} values defined in Table 7.1 were calculated at locations A ($K_{a cl}$) and C ($K_{c cl}$) using measured closure loads as a function of crack size. The data were then curve fitted with a second order polynomial as shown by the dotted lines in Figures 7.1 through 7.4. Figures 7.1 and 7.2 present the stress intensity factors at location C due to $c P_{op}$ and $b P_{op}$ ($K_{c cl}^c$ and $K_{c cl}^b$), respectively. Figures 7.3 and 7.4 present $K_{a cl}^c$ and $K_{a cl}^b$, respectively. The K_{cl} format was selected over percent closure load (P_{op} / P_{\max}) since it is a more continuous function -- especially for the block loading data (Figure 5.26 and 5.27).

The coefficients for these curves (k, l, m) are given in Table 7.2 through 7.5, where the general equation of K_{cl} is presented as a function of a/t such that:

$$K_{j cl}^i = k + l * (a/t) + m * (a/t)^2 \quad (7.4)$$

where $i = b$ or c for the closure load $b P_{op}$ or $c P_{op}$, respectively, and $j = a$ or c for the crack tip locations A and C, respectively.

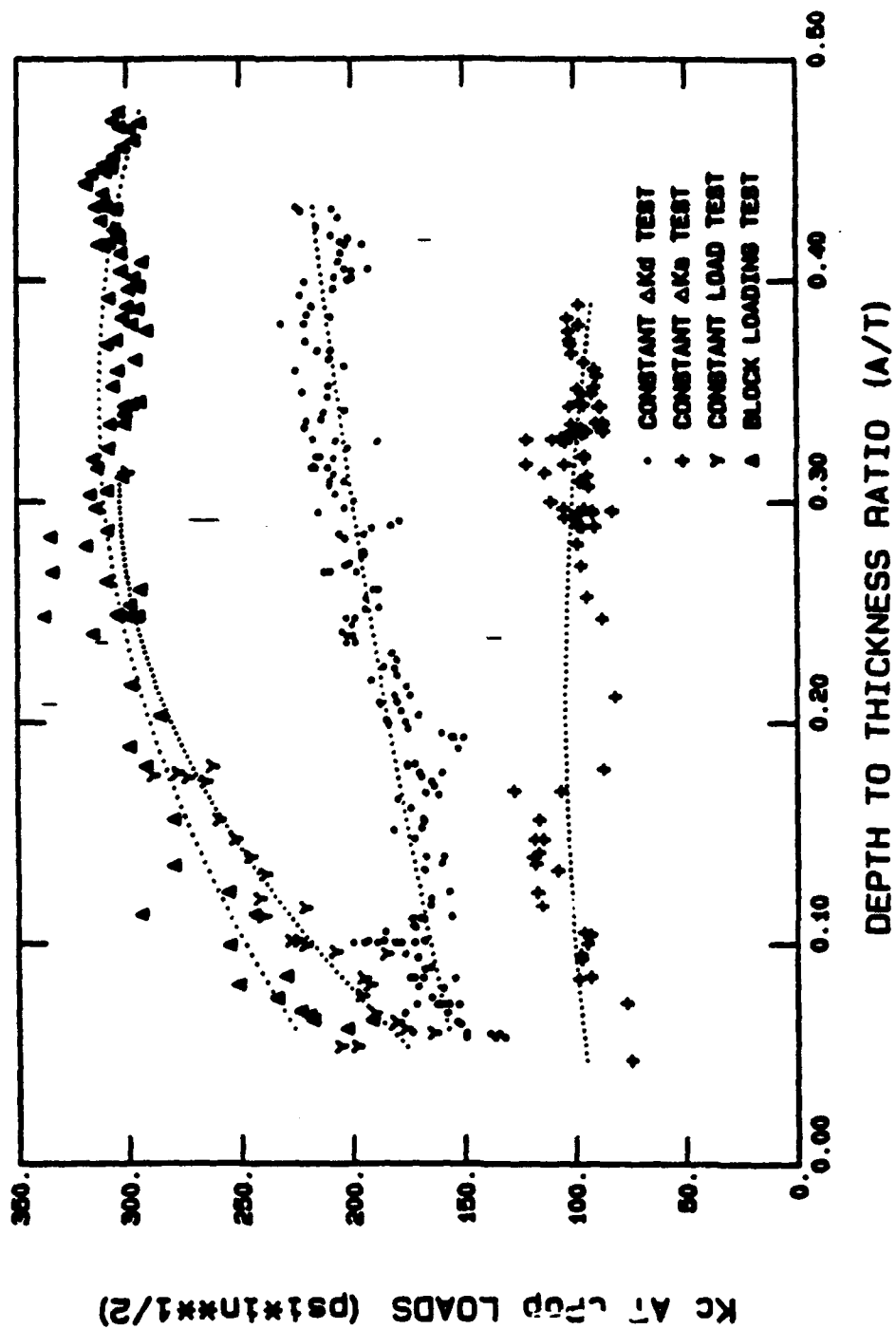


Figure 7.1 Stress intensity factors at the crack tip free-surface ($\theta=0$ degrees) due to the $cPop$ closure load level as a function of crack size (a/t) for all tests

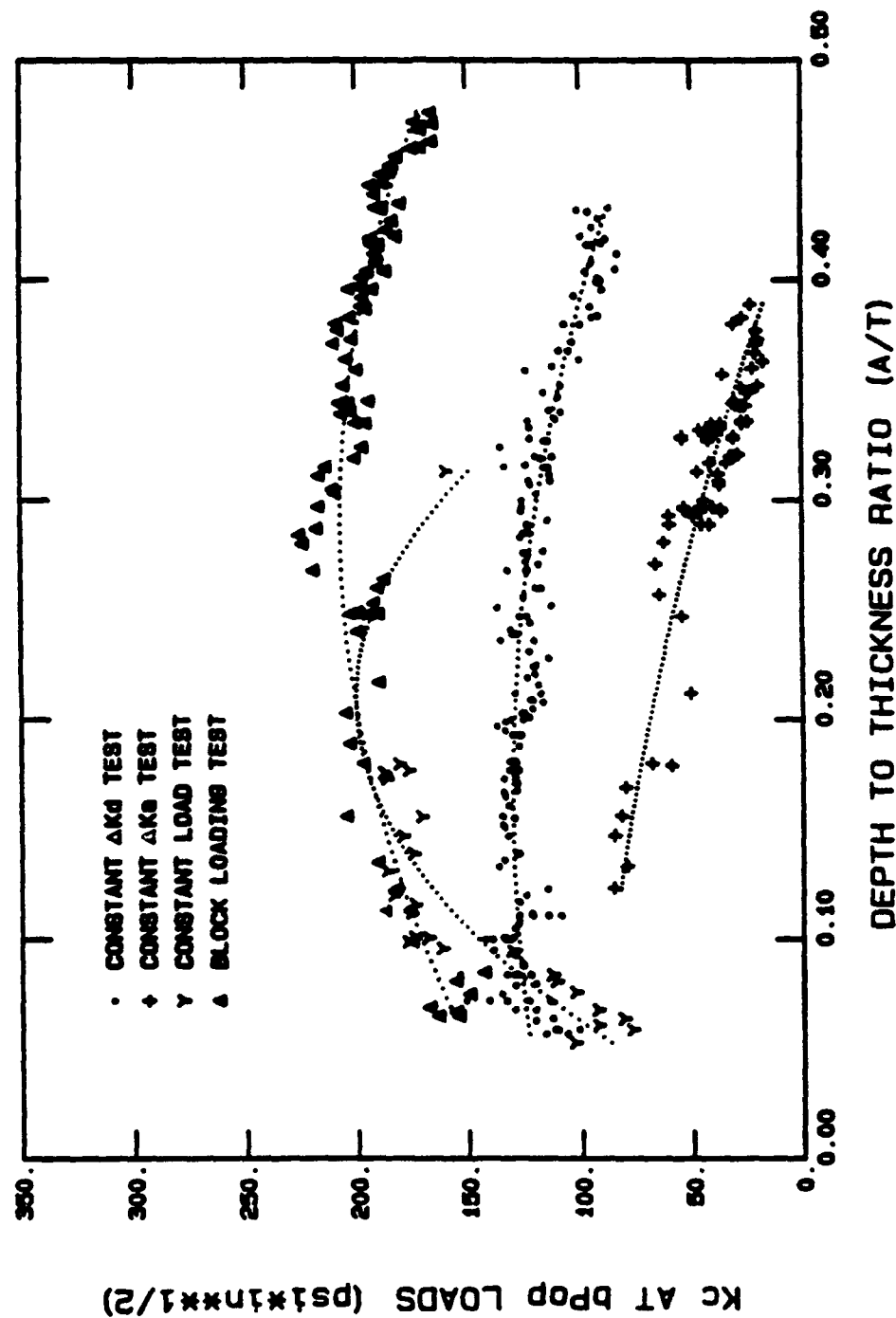


Figure 7.2 Stress intensity factors at the crack tip free-surface ($\theta=0$ degrees) due to the bPop closure load level as a function of crack size (a/t) for all tests

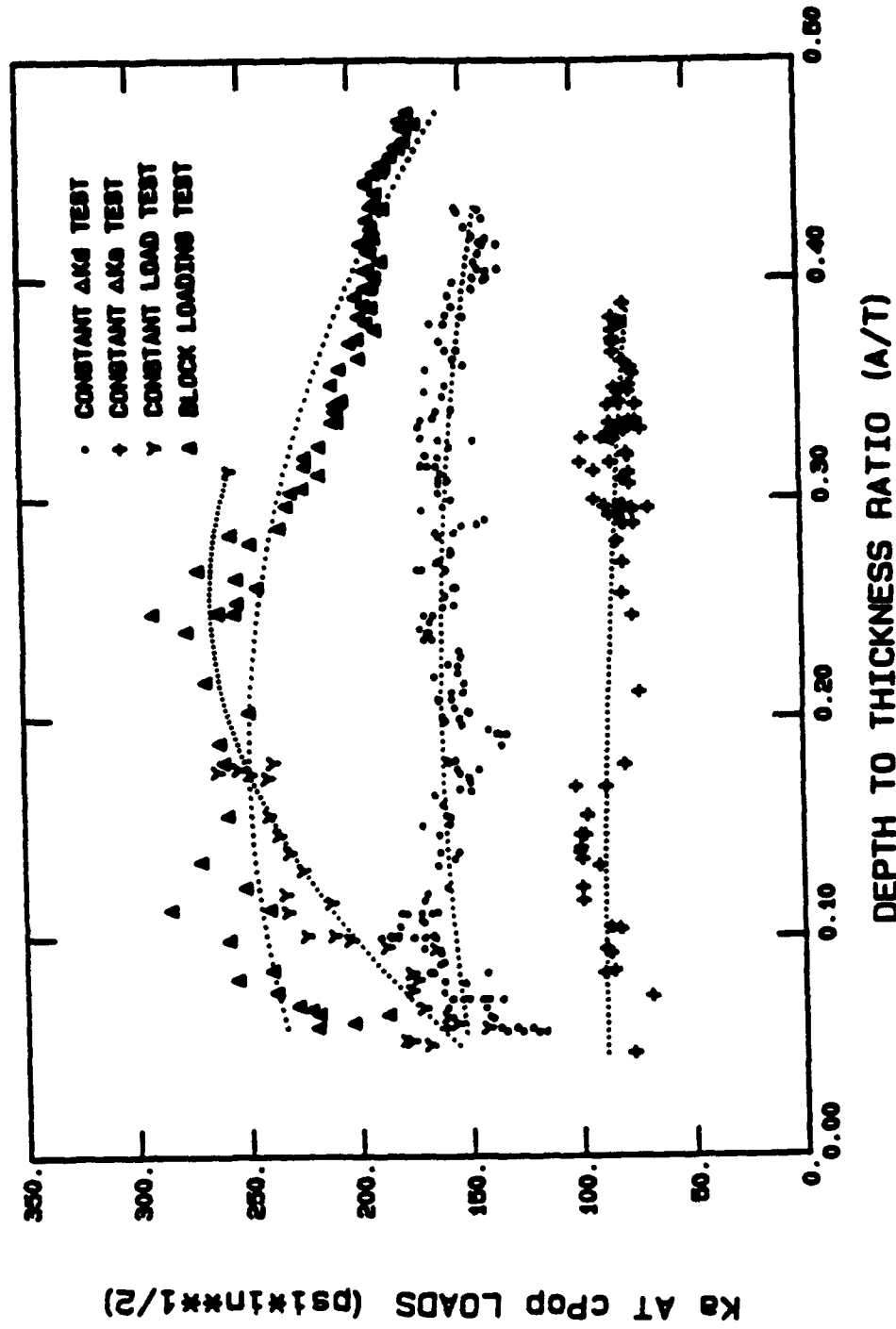


Figure 7.3 Stress intensity factors into the specimen thickness at the crack tip ($\theta=90$ degrees) due to the CPoP closure load level as a function of crack size (A/t)

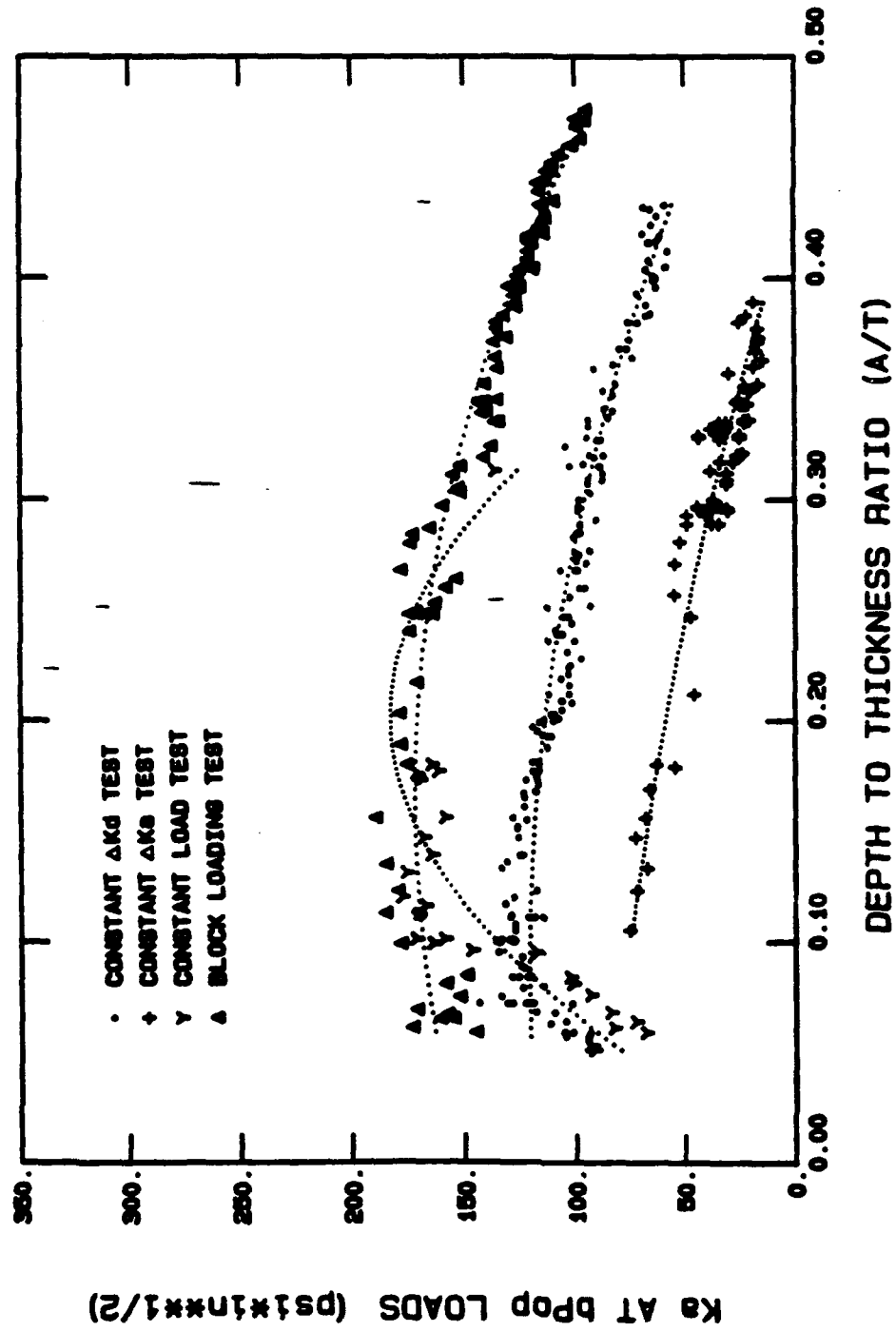


Figure 7.4 Stress intensity factors into the specimen thickness at the crack tip ($\theta=90$ degrees) due to the bPop closure load level as a function of crack size (a/t)

Table 7.2: Polynomial Coefficients for K_c^c as a Function of a/t (Figure 7.1)

<u>Test</u>	<u>k</u>	<u>l</u>	<u>m</u>
Constant ΔK_c	144	223	-124
Constant ΔK_a	89	140	-337
Constant Load	116	1227	-2008
Block Loading	183	740	-1059

Table 7.3: Polynomial Coefficients for K_c^b as a Function of a/t (Figure 7.2)

<u>Test</u>	<u>k</u>	<u>l</u>	<u>m</u>
Constant ΔK_c	115	188	-508
Constant ΔK_a	95	-51	-381
Constant Load	-3	1953	-4684
Block Loading	123	583	-1010

Table 7.4: Polynomial Coefficients for K_a^c as a Function of a/t (Figure 7.3)

<u>Test</u>	<u>k</u>	<u>l</u>	<u>m</u>
Constant ΔK_c	145	159	-371
Constant ΔK_a	89	18	-128
Constant Load	94	1351	-2657
Block Loading	216	369	-1018

Table 7.5: Polynomial Coefficients for $K^b_{a cl}$ as a Function of a/t (Figure 7.4)

<u>Test</u>	<u>k</u>	<u>l</u>	<u>m</u>
Constant ΔK_c	118	83	-526
Constant ΔK_a	86	-84	-262
Constant Load	-6	1884	-4676
Block Loading	154	243	-778

Effective Stress Intensity Factor Correlation

The fatigue crack growth rate (FCGR) data are plotted in figures 7.5 through 7.7 as a function of applied ΔK for the four tests. The FCGR data (da/dN and dc/dN) are calculated using a modified incremental polynomial smoothing routine developed by Larsen (49). The differences in data scatter between locations A and C are shown in Figures 7.5 and 7.6 for da/dN and dc/dN , respectively, while Figure 7.7 combines them on one plot. The solid line fitted through the surface flaw data has Paris Law constants of $C = 5.737 \times 10^{-22}$, and $n = 5.5945$ (reference eqn. 2.1). The dashed line is data generated by Perez (37) using thru-thickness compact tension (CT) specimens from the same sheet of PMMA as was used in this experiment. The Paris Law constants for this reference data is $C = 4.807 \times 10^{-20}$, and $n = 5.0806$. This reference line shows the surface flaw crack growth rate to be slower than the thru-thickness FCGR. It is important to note that both da/dN and dc/dN for the constant ΔK_a test are greater than the ΔK_d test. These differences reflect the influence of plastic zones on FCGR.

The ΔK_{eff} versus da/dN and dc/dN data are shown in Figures 7.8 through 7.13 for the four closure load ranges -- represented by $\Delta K^c_{c cl}$, $\Delta K^b_{c cl}$, $\Delta K^c_{a cl}$ and $\Delta K^b_{a cl}$. Closure load effects on both da/dN and dc/dN are shown separately in Figures 7.8 through

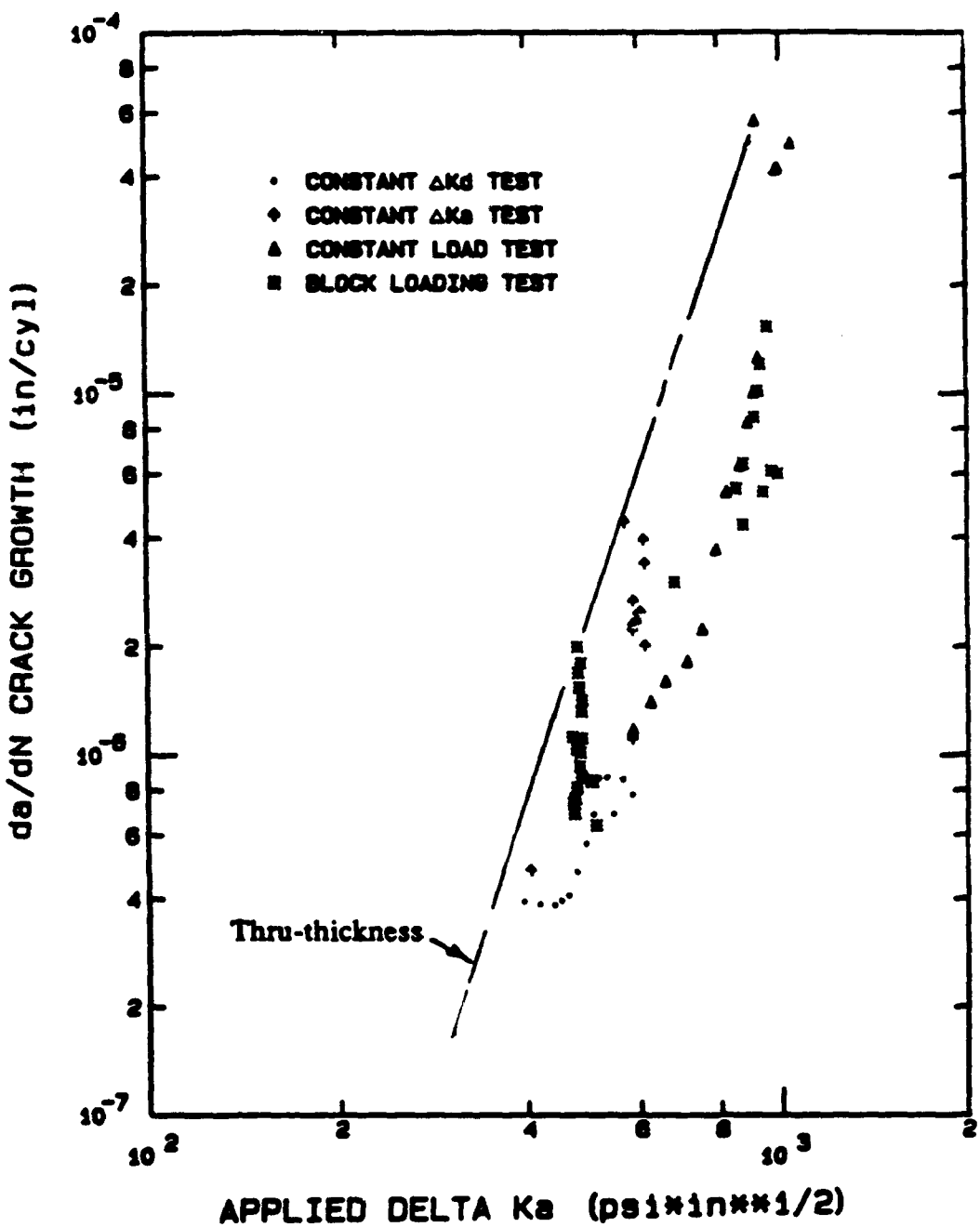


Figure 7.5 Crack growth rate at location A (da/dN) due to the nominal applied load ($K_{max} - K_{min}$) for all four test cycles

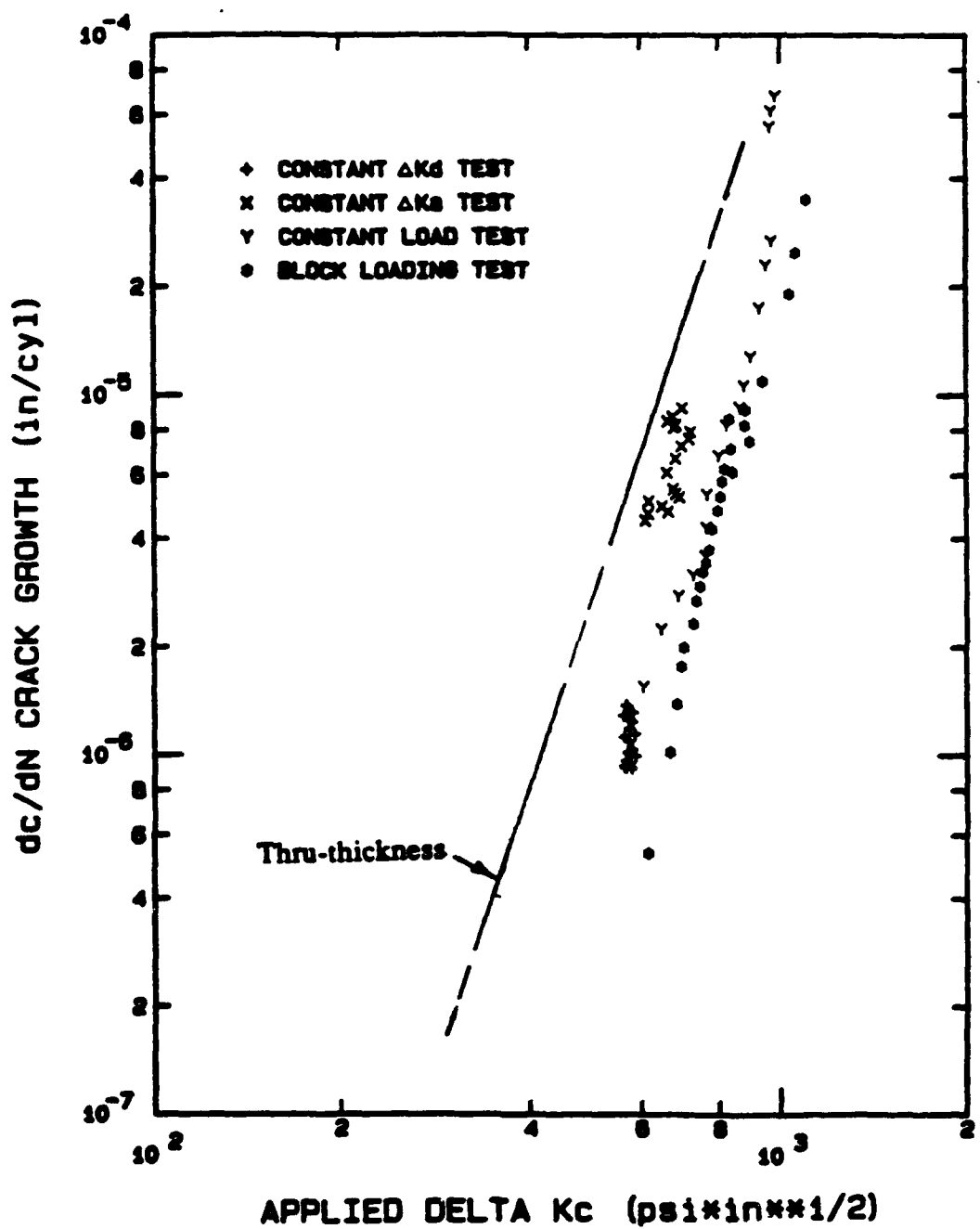


Figure 7.6 Crack growth rate at location C (dc/dN) due to the nominal applied load ($K_{max} - K_{min}$) for all four test cycles

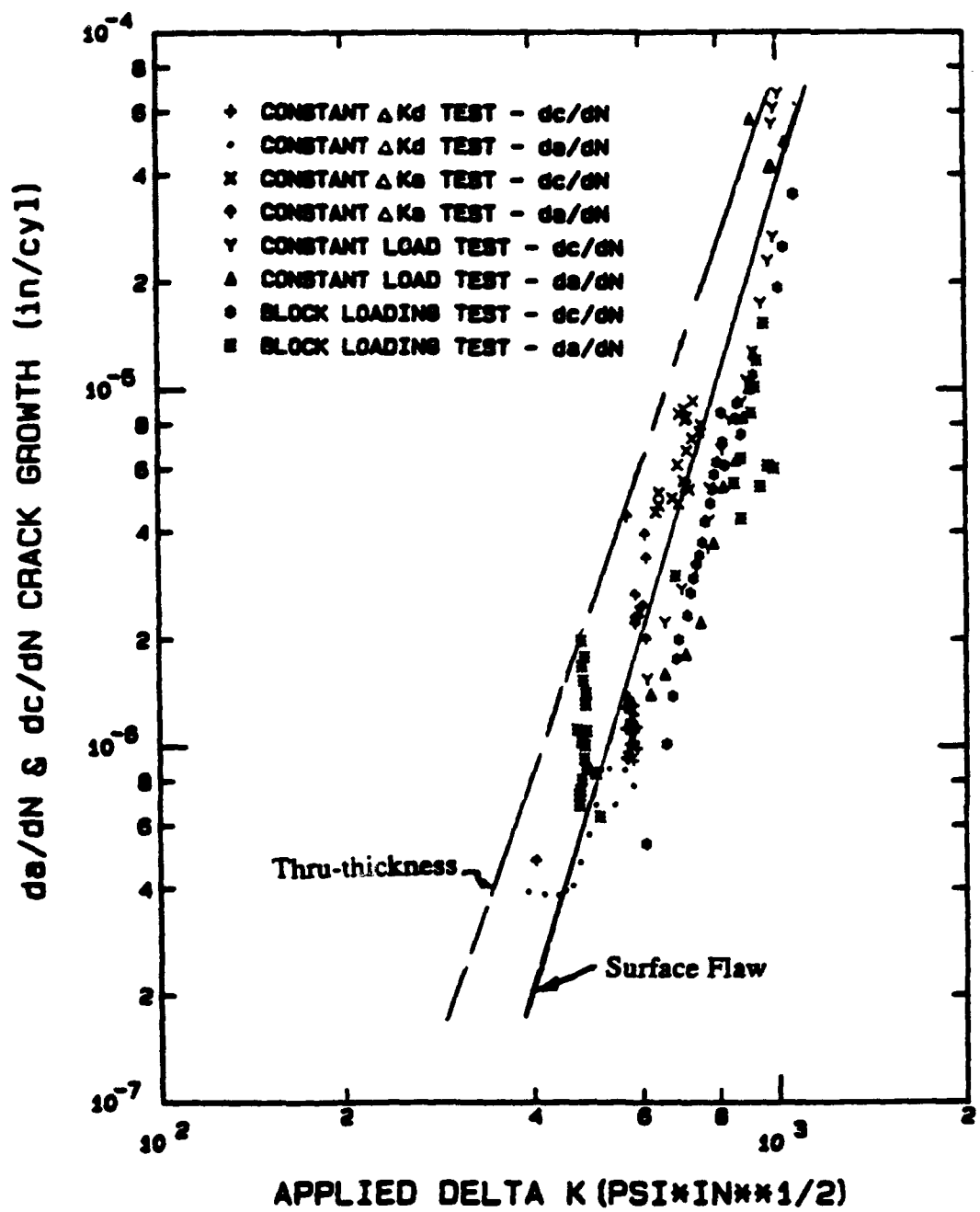


Figure 7.7 Crack growth rate at locations A (da/dN) and C (dc/dN) due to the nominal load ($K_{max} - K_{min}$) for all four test cycles

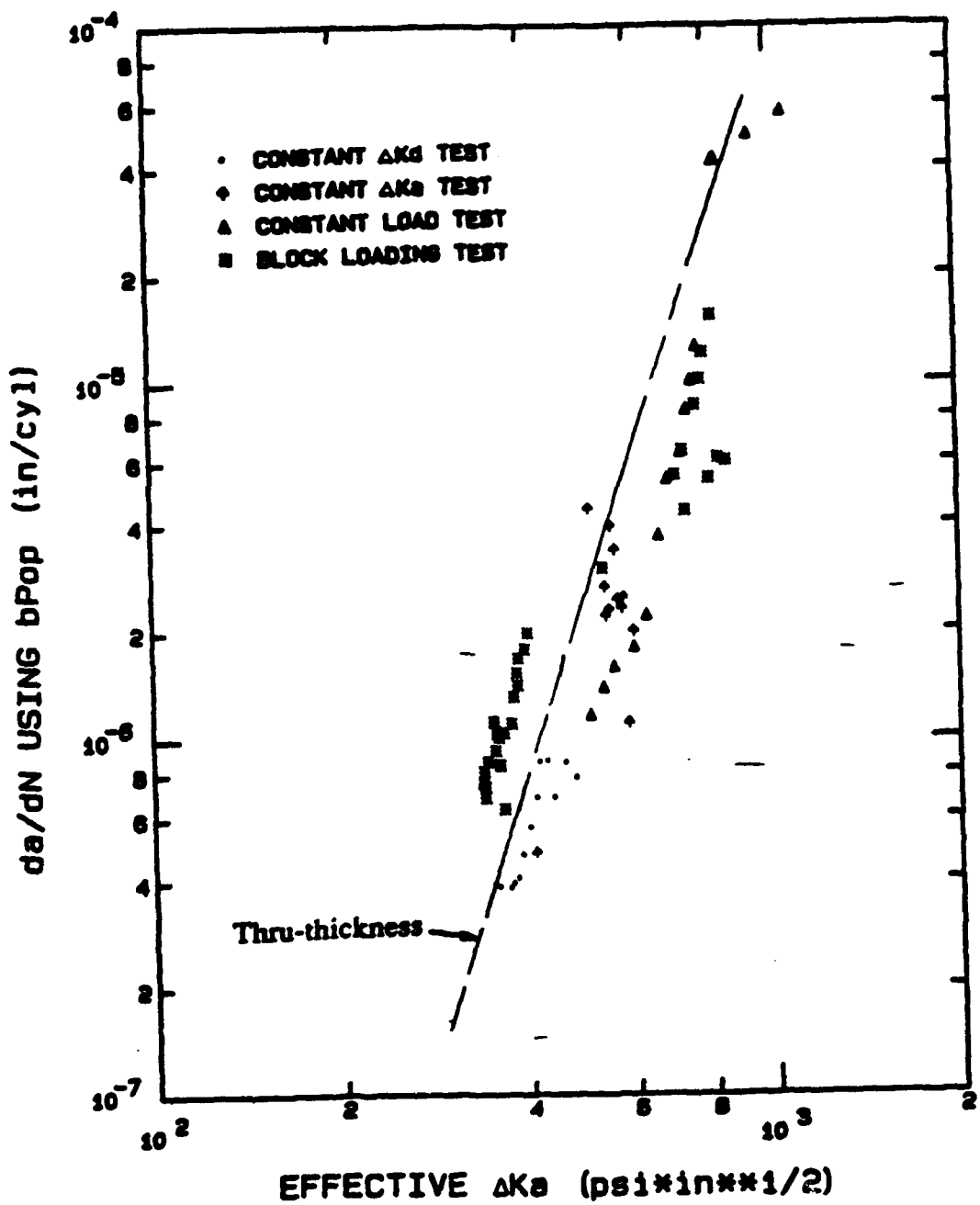


Figure 7.8 Crack growth rate at location A (da/dN) due to the effective load (ΔK_{eff} a.c) for all four test cycles

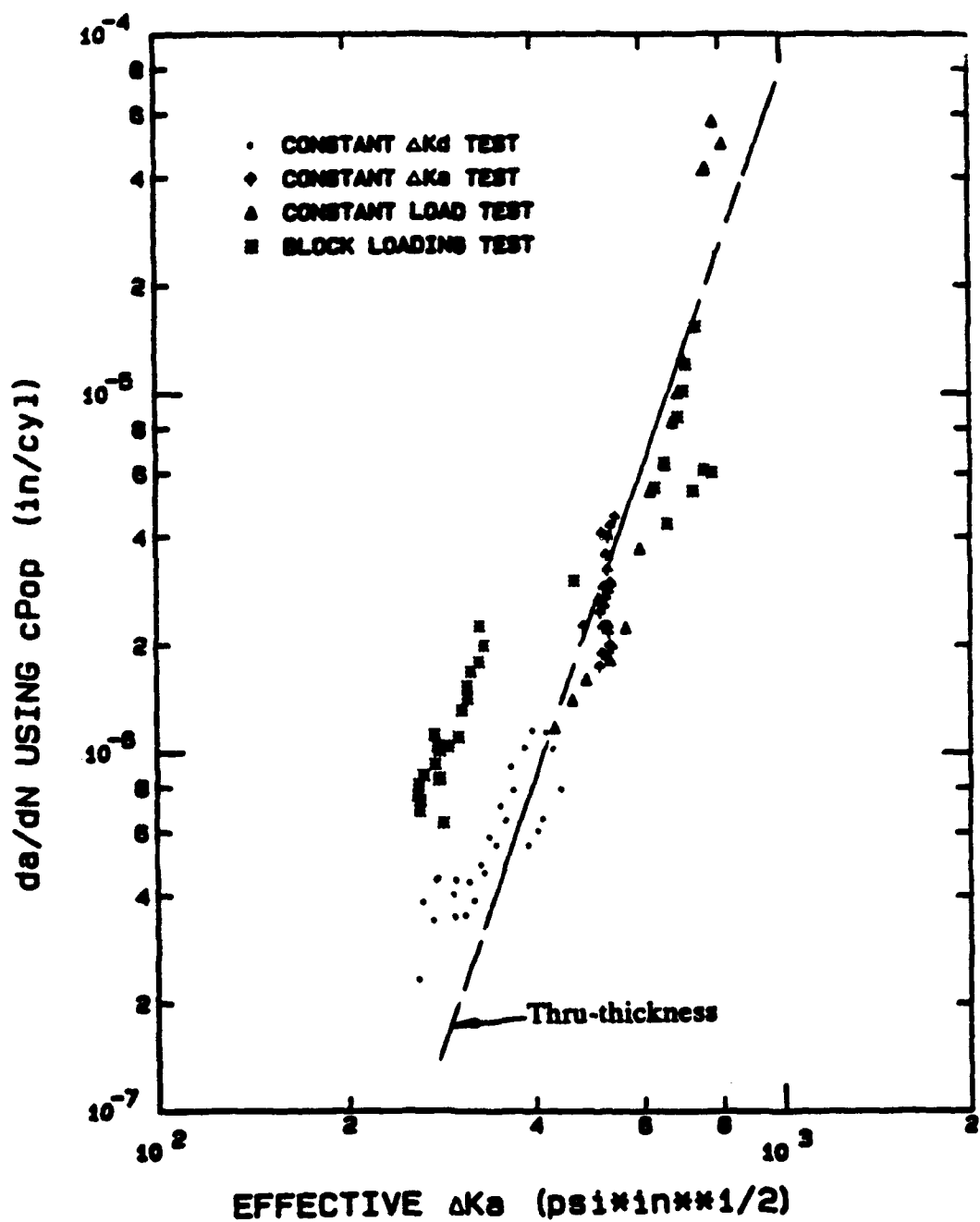


Figure 7.9 Crack growth rate at location A (da/dN) due to the effective load (ΔK_{eff}) for all four test cycles

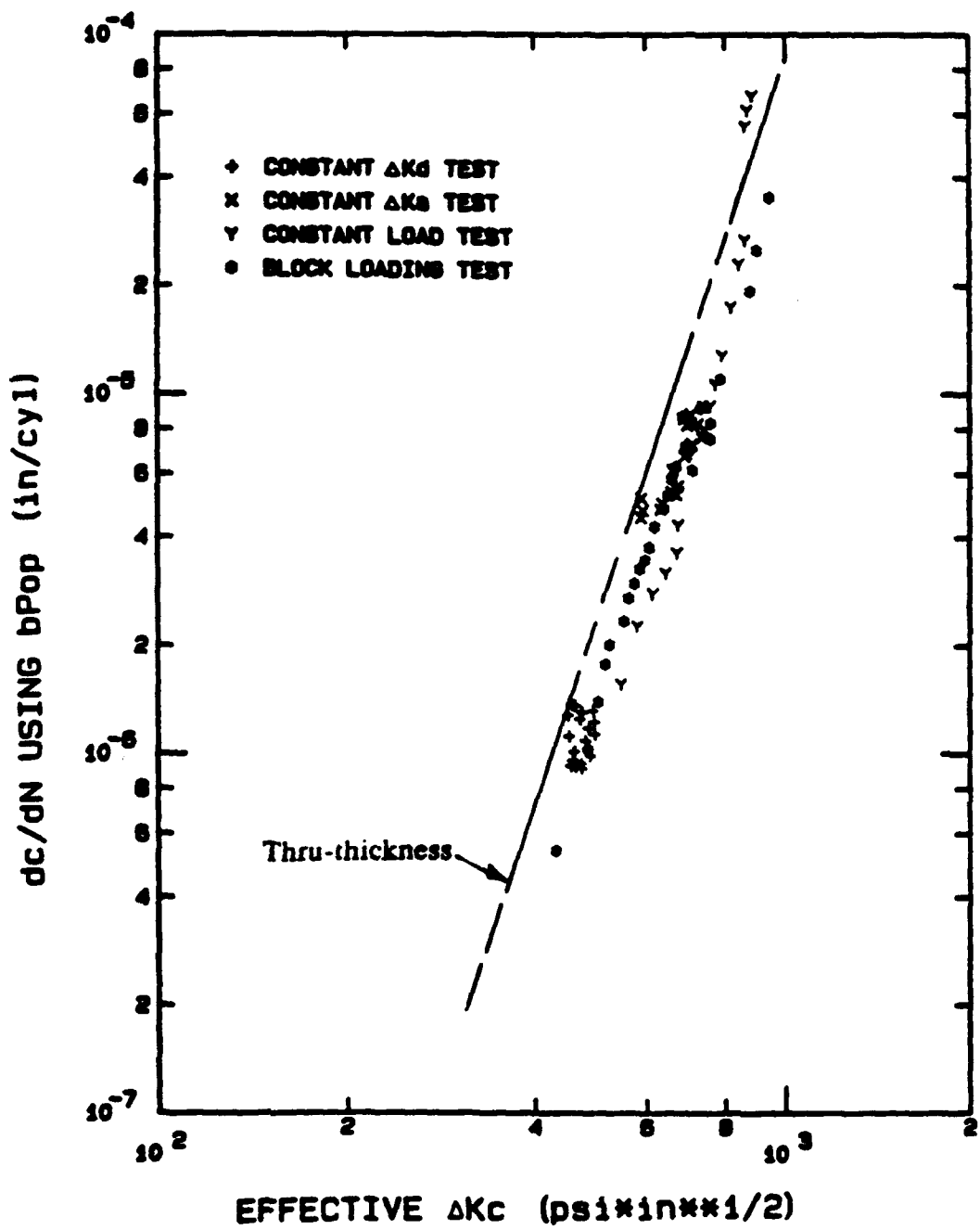


Figure 7.10 Crack growth rate at location C (dc/dN) due to the effective load (ΔK_c) for all four test cycles

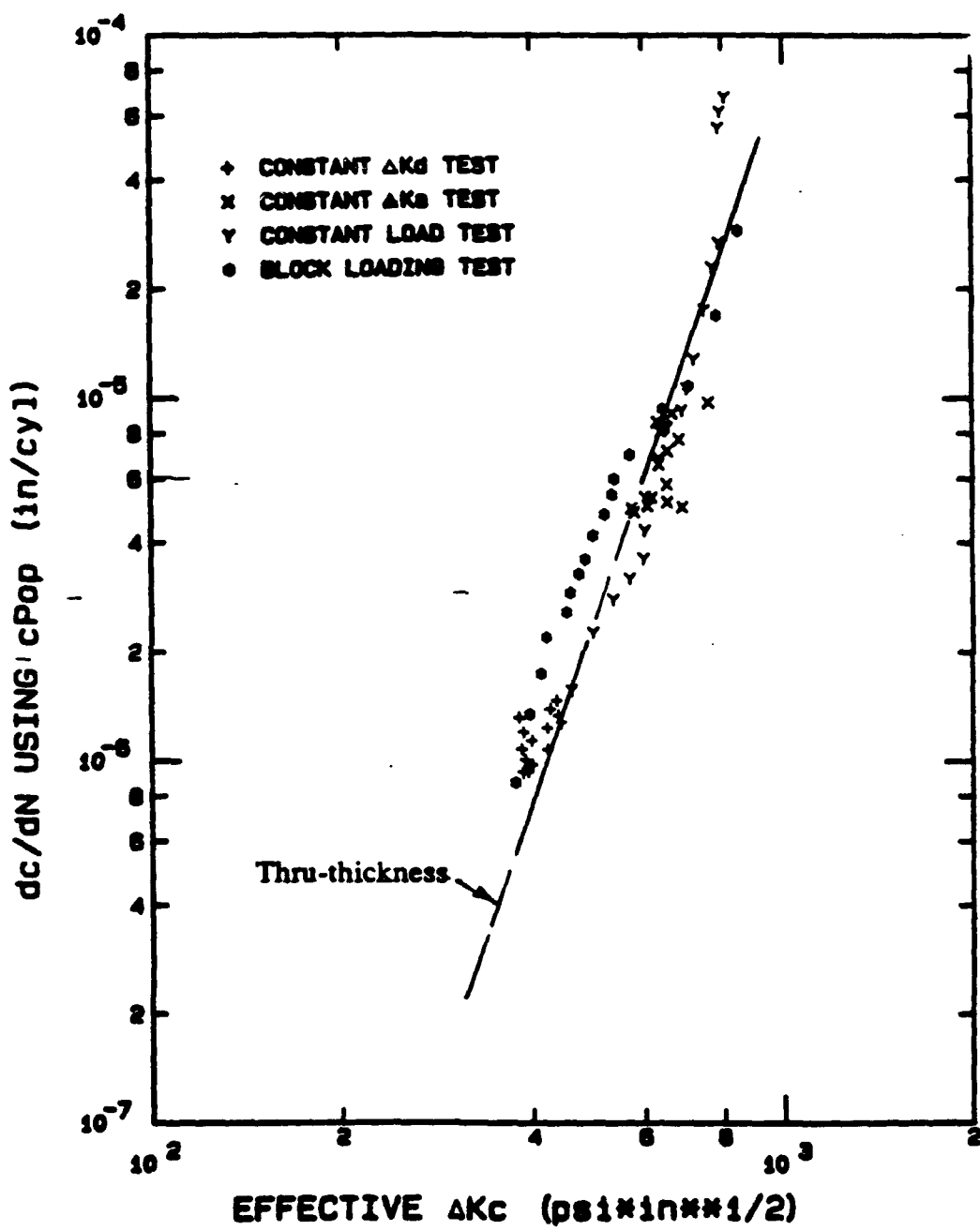


Figure 7.11 Crack growth rate at location C (dc/dN) due to the effective load (ΔK_c) for all four test cycles

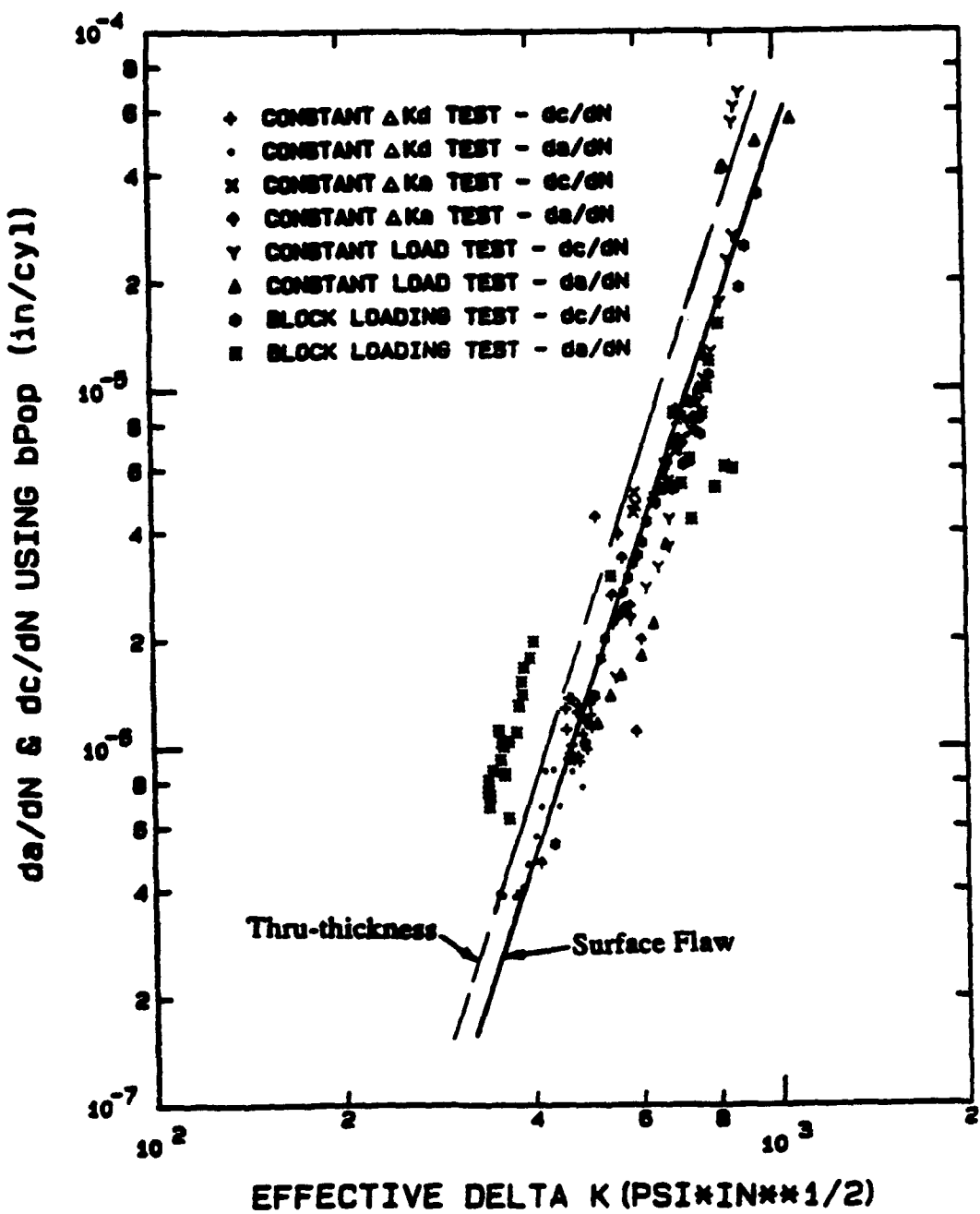


Figure 7.12 Crack growth rate at location A (da/dN) and C (dc/dN) due to the effective load (ΔK_{eff}) for all four test cycles

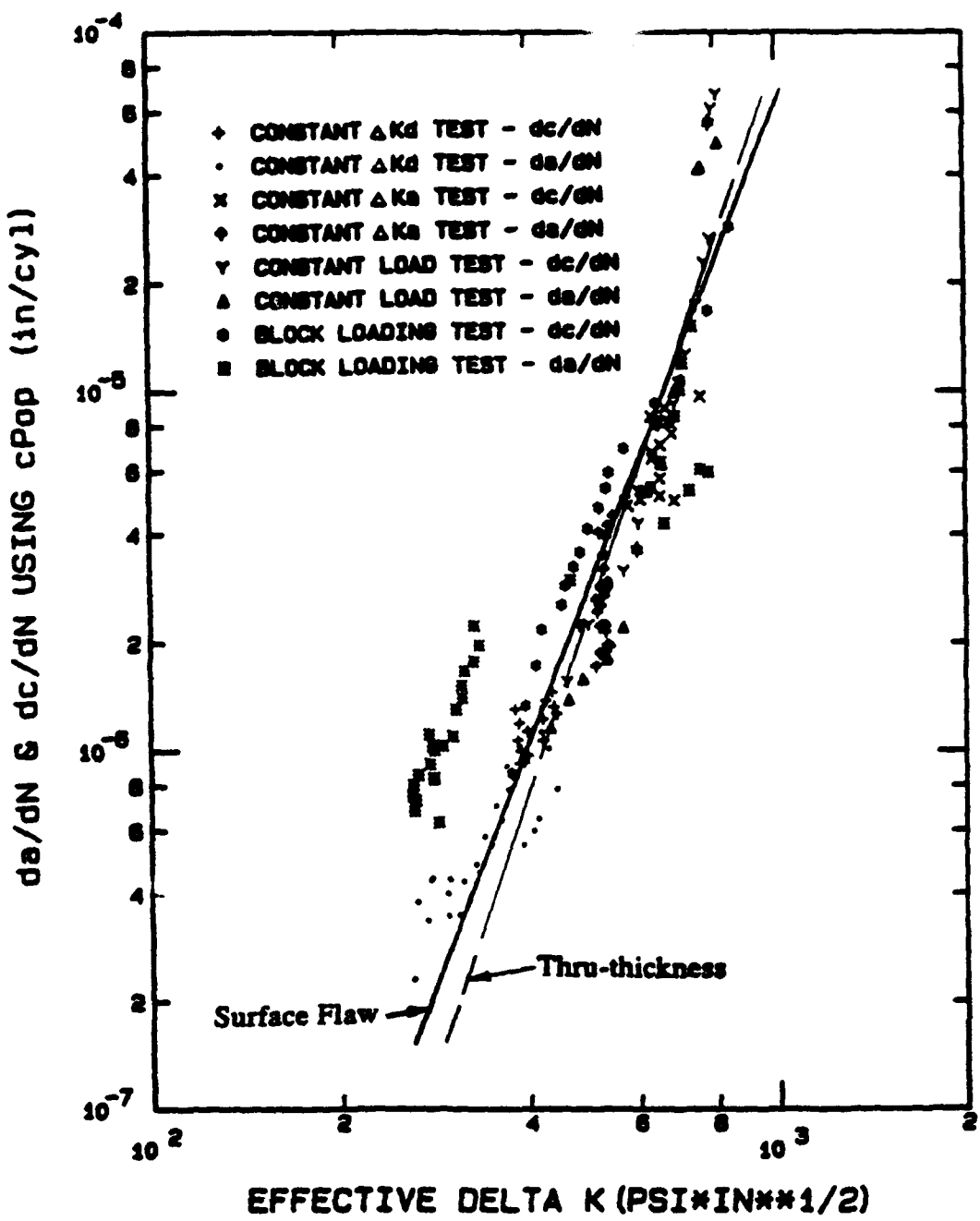


Figure 7.13 Crack growth rate at location A (da/dN) and C (dc/dN) due to the effective load (ΔK_{eff}) for all four test cycles

7.11, and then combined in Figures 7.12 and 7.13. Thru-thickness CT specimen results are also plotted on these figures for reference (dashed line) -- the reference line is for applied ΔK and is, therefore, not corrected for closure.

First, consider the effect of closure load on da/dN . The bP_{op} closure load ($\Delta K^b_{a cl}$, Figure 7.8) effects are noted to make only minor improvements when compared with applied ΔK data in Figure 7.5. The effects of cP_{op} ($\Delta K^c_{a cl}$, Figure 7.9) are found to be slightly worse than applied ΔK (Figure 7.5) -- particularly at the lower K levels where the block loading data is separated from the other data points.

In contrast to da/dN , closure load effects along the crack free-surface (dc/dN , Figures 7.10 and 7.11) are noted to show excellent correlation. The bP_{op} closure load ($\Delta K^b_{c cl}$, Figure 7.10) coalesces both the constant ΔK and the constant load test results when compared with applied ΔK data in Figure 7.6. The effects of cP_{op} ($\Delta K^c_{c cl}$, Figure 7.11) are also found to be very good, but to produce slightly more scatter than bP_{op} .

Of the four ΔK_{eff} definitions, the best correlation (least scatter) is that of the dc/dN data seen in Figure 7.10, where the use of $K^b_{c cl}$ (bP_{op} closure load, or the load required to open the middle free-surface) collapses even the block loading data. The correlation of dc/dN in Figure 7.11 using cP_{op} is also very good. The best da/dN correlation is seen in Figure 7.8 ($K^b_{a cl}$), where the bP_{op} closure load is again found to best correlate the experimental data.

Figures 7.12 and 7.13 combines the da/dN and dc/dN FCGR data using bP_{op} and cP_{op} ($K^b_{j cl}$ and $K^c_{j cl}$), respectively. From this evaluation, use of the bP_{op} is found to best correlate both the da/dN and dc/dN FCGR data (Figure 7.12). This correlation is noted to be quite good except for the da/dN block loading data.

It should be noted that correlation of the bP_{op} closure load is consistent with thru-thickness FCGR investigations which measure free-surface crack displacement using clip gauges and/or interferometry methods.

Fatigue Crack Growth Predictions

The above correlation of closure loads for collapsing FCGR data can also be evaluated by using analytical models to compare experimental measurements with predictions of cycles and crack aspect ratio for a given crack length. Although the approach is not as direct as was presented in the previous section because of computational influences, sample calculations are presented in this section for reference. These comparisons are made using four different Paris Law constants (C and n) -- two cases using applied ΔK ("uncorrected" constants), and three cases using "corrected" constants derived from ΔK_{eff} definitions described in the previous section. Since the closure load corrected constants are derived from this investigation and are not independent, the calculations are presented as an example of how this approach is applied.

The analytical program developed for this effort calculates crack stress intensity factors in the "a" and "c" directions (K_a and K_c) using the Newman-Raju boundary correction factors at $\phi = 90$ and 0 degrees, respectively. As discussed in Chapter VI, although K -solutions for ΔK_a in the closure load region are not known to be available for types II and III cracks, the use of effective load ranges and existing K -solutions are expected to produce reasonable results. The model uses either the applied stress intensity factor range of ($\Delta K = K_{\max} - K_{\min}$), or effective stress intensity factor range of ($\Delta K_{\text{eff}} = K_{\max} - K_c$). The formulation is an expansion of the Paris Law relationship of crack growth rate, such that along the specimen free-surface:

$$\frac{dc}{dN} = C_c (\Delta K_{c \text{ eff}})^n_c \quad (7.5)$$

and into the specimen thickness:

$$\frac{da}{dN} = C_a (\Delta K_{a \text{ eff}})^n_a \quad (7.6)$$

where C_C and n_C are Paris Law constants generated from FCGR data along the crack free-surface, and C_a and n_a into the crack thickness. The constants can be generated independently when da/dN and dc/dN data are available -- i.e., Figures 7.8 through 7.11. Although the analytical formulation was set-up to recognize these potential Paris Law constant differences into the specimen thickness and along the crack free-surface, this investigation used $C_a = C_C$ and $n_a = n_C$ since they were approximately equal (Figures 7.12 and 7.13). This assumption is typically made for surface flaws in metals even though non-homogenous condition are known to exist. For example, Hodulak (50) suggested that for metal plates in tension, the material resistance is greater at the surfaces than at the plate mid-thickness.

The FCG calculation approach is based on an iterative crack growth model described in (51) and (52), and follows from the relationship of:

$$\Delta N = \Delta a / (da/dN) \quad (7.7)$$

By assuming a " Δa " value and knowing da/dN from an applicable crack growth model such as the Paris Law or Walker relationships, ΔN can be calculated to match the assumed Δa increment. K_a and K_C are then calculated for the new crack size, and the iterative process repeated until a desired crack size is reached. An error term is built into the routine to ensure only small increments of ΔN are calculated even when the crack rate is high. This error function was established to maintain efficient computational speed and accuracy.

The fatigue crack growth (FCG) prediction code was validated using thru-thickness specimen data generated in conjunction with an ASTM "Round Robin" (53) evaluation task group E24.06.01 on corner cracked holes. During the "Round Robin" evaluation, predictions were made by representative industry, academia, and government organizations. The error range of prediction to experimental results is as follows:

0.68 << Life ratio (N_p/N_e) >> 1.18

0.84 << Crack shape ratio ($(a/c)_p/(a/c)_e$) >> 1.19

where N_p/N_e is the ratio of predicted ("p") to experimental ("e") cycles. Likewise, for the crack shape ratio $(a/c)_p/(a/c)_e$, Table 7.6 compares predictions made by the code developed for this investigation with the "Round Robin" experimental results. These results are all well within "Round Robin" prediction ranges shown above.

Table 7.6: Comparison of fatigue crack growth predictions using a "Round Robin" experimental data set and the Newman-Raju K-solutions

<u>R</u>	<u>S_{max} (ksi)</u>	<u>N_r/N_e</u>	<u>(a/c)_r/(a/c)_e</u>
0.1	15	0.91	0.89
0.1	20	0.85	0.94
0.3	15	1.00	1.02

The fatigue crack growth (FCG) computational program was then used to predict crack growth patterns and cycles to achieve a given crack length for this investigation. Calculations were made using five different combinations of Paris Law constants (C and n) and closure load. The two uncorrected constants came from thru-thickness data (37), and surface flaw data developed in this investigation (Figure 7.7). Two of the corrected constants were developed from Figures 7.12 and 7.13 using b_{Pop} and c_{Pop}, respectively; that is, one calculation used ΔK_a^b eff and ΔK_c^b eff, and the other ΔK_a^c eff and ΔK_c^c eff. The final calculation used b_{Pop} for the da/dN and c_{Pop} for the dc/dN calculations, or ΔK_a^b

eff and $\Delta K_c^c \text{ eff}$ -- as discussed in Chapter VI. The constant ΔK_d test results were used for these sample calculations after eliminating precracking effects.

The predicted crack growth patterns (a/c and a/t) and cycles to achieve a given crack length are compared to experimental results in Table 7.7. Here, the cycle prediction improvements of using ΔK_{eff} (where K_{cl} varies with crack size, ref. Figures 7.1 through 7.4) versus an applied ΔK are apparent. However, crack growth pattern results are not as apparent, as shown in Figure 7.14. Several of the calculations are equivalent: (1) the two calculations using the nominal applied ΔK for thru-thickness and surface flaws, and (2) the two calculations using bP_{op} ($\Delta K_a^b \text{ eff}$ and $\Delta K_c^b \text{ eff}$) or cP_{op} ($\Delta K_a^c \text{ eff}$ and $\Delta K_c^c \text{ eff}$) for both da/dN and dc/dN . Although all of the combinations are quite good, using bP_{op} for da/dN ($\Delta K_a^b \text{ eff}$) and cP_{op} for dc/dN ($\Delta K_c^c \text{ eff}$) provided the best overall match. In general, all of the analytical results using effective load range provide a better match with experimental data than the nominal applied load range.

Table 7.7: Comparison of Experimental and Predicted Fatigue Crack Growth Patterns and Cycles Using Uncorrected and Corrected Paris Law Constants

<u>Condition</u>	<u>a/t</u>	<u>(a/c)_r/(a/c)_e</u>	<u>N_r/N_e</u>
<u>Applied Load (ΔK)</u>			
Thru-Thickness	0.1	1.10	0.16
	0.2	1.00	0.24
	0.4	0.87	0.23
Surface Flaw	0.1	1.09	0.53
	0.2	0.99	0.77
	0.4	0.84	0.77
<u>Effective Load Range (ΔK_{eff}) for Surface Flaws</u>			
bPop	0.1	1.09	0.70
(K^b_a eff & K^b_c eff)	0.2	1.01	0.97
	0.4	0.91	0.89
cPop	0.1	1.09	0.50
(K^c_a eff & K^c_c eff)	0.2	1.01	0.79
	0.4	0.92	0.95
bPop/cPop	0.1	1.02	0.56
(K^b_a eff & K^c_c eff)	0.2	0.97	0.82
	0.4	0.98	0.87
<u>Experimental Results:</u>			
	<u>a/t</u>	<u>(a/c)_e</u>	<u>N_e(cycles)</u>
	0.1	0.72	57,000
	0.2	0.68	140,000
	0.4	0.54	480,000

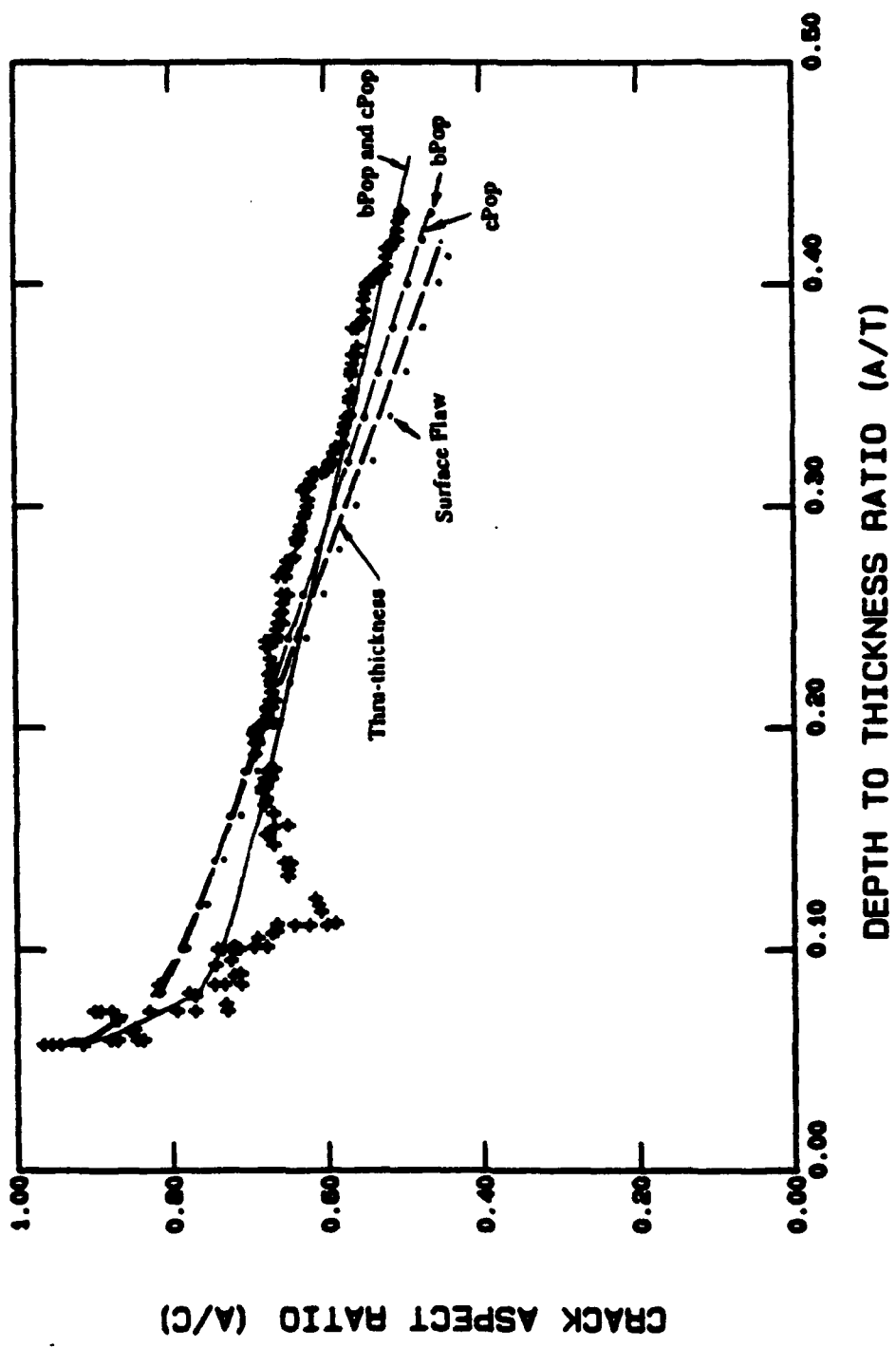


Figure 7.14 Comparisons of predicted and experimental crack growth patterns for the constant ΔK_d test

The results presented in Figure 7.14 would indicate that the fully-open K-solutions are sufficiently accurate to provide good crack growth pattern predictions for various combinations of Paris Law constants when using detailed closure load measurements. The questions then arise as to how good the predictions are if only Paris Law constants are available, and one assumes a constant (not a function of crack length) closure load ratio (P_{cl}/P_{max}). Results of this approach are shown in Table 7.8, where applied ΔK Paris Law constants are shifted 20% and 30% for thru-thickness (37) and surface flaw (Figure 7.7) tests data. Two combinations of constant closure load ratio are evaluated: (1) 30% for both da/dN and dc/dN , and (2) 20% for da/dN and 30% for dc/dN (Figure 5.19).

Table 7.8: Comparison of Experimental and Predicted Fatigue Crack Growth Using an Assumed Constant P_{cl}/P_{max} Value for Surface Flaws

<u>Condition</u>	<u>a/t</u>	<u>$(a/c)_n/(a/c)_e$</u>	<u>N_n/N_e</u>
$P_{cl}/P_{max} = 0.3$	0.1	1.07	0.42
	0.2	0.98	0.68
	0.4	0.87	0.89
$P_{cl}/P_{max} = 0.2/0.3$	0.1	1.09	0.52
	0.2	0.99	0.76
	0.4	0.84	0.77

It is, therefore, observed from these calculations that:

- (1) Existing crack growth pattern predictions are quite accurate.

(2) Cyclic predictions using an assumed constant closure load are reasonable,
but not as accurate as using measured variable closure load data --

Table 7.7.

(3) The best approach for predicting FCG of surface flaws in bending when
only fully-open K-solutions and closure load data is not available is to: (1)
use Paris Law constants generated from thru-thickness specimens data and
assume a constant closure load ratio which is based on the general material
class being analyzed.

VIII. CRACK OPENING DISPLACEMENT PREDICTIONS USING WEIGHT FUNCTIONS

One of the few analytical solutions available for predicting surface flaw crack opening displacement (COD) was developed by Mattheck, Morawietz and Munz (54). Their approach is based on a weight function method developed by Petroski and Achenbach (55) to calculate COD of thru-thickness cracks. The linear-elastic model was developed for applied loads, and does not reflect closure load effects. Therefore, the predicted elastic displacement is a function of the applied stress intensity factor.

The weight function mathematical formulation was originally introduced by Bueckner (56,57) in 1970 to calculate stress intensity factor for complex loads. The formulation uses superposition to calculate the stress intensity factor (K_{new}) for a new stress distribution (σ_{new}) when the mode I stress intensity factor (K) and elastic displacement are known for a symmetrically loaded body. The weight function formula is given as:

$$K_{\text{new}} = (H/K_I) \int_0^a \sigma_{\text{new}}(x) [\partial u_I(a,x) / \partial a] dx \quad (8.1)$$

where x is the distance from the crack free-surface into the crack depth (Figure 5.1), $H = E/(1 - \nu^2)$ for plane strain or E for plane stress conditions. K_I and u_I are known reference stress intensity factor and displacement, respectively, for a simple symmetrical loading. The weight function relationship has been used successfully by a number of investigators such as; Rice (58), Grandt (59-63), Paris (64), and Labbens (65,66).

The uniqueness of the Petroski and Achenbach weight function approach for predicting COD is their formulation of a reference crack displacement function u_I . The proposed displacement is:

$$u_r(a,x) = [\sigma_0 / \sqrt{2} H] [4F(a) \sqrt{a} \sqrt{(a-x)} + G(a) (a-x)^{3/2} / \sqrt{a}] \quad (8.2)$$

where $F(a)$ is a known boundary correction factor, and $G(a)$ is unknown. Given a reference stress (σ_r) and stress intensity factor (K_r) for a reference displacement, equation 8.1 becomes:

$$K_r^2 = H \int_0^a \sigma_r(x) [\partial u_r(a,x) / \partial a] dx \quad (8.3)$$

Since $u_r(a,x)=0$ when $x=a$, the partial derivative can be moved outside the integral, and the integral expression reduced to:

$$\int_0^a K_r^2 da = H \int_0^a \sigma_r(x) u_r(a,x) dx \quad (8.4)$$

Next, the reference stress intensity factor takes the familiar form of:

$$K_r = \sigma_0 \sqrt{\pi a} F(a) \quad (8.5)$$

and solving for the unknown $G(a)$ term by substituting equation 8.2 into equation 8.4. Then, for a constant uniform stress field σ_0 :

$$\begin{aligned} \int_0^a K_r^2 da &= \pi \sigma_0^2 \int_0^a F^2(a) da \\ &= [\sigma_0 / \sqrt{2}] [4F(a) \sqrt{a} \int_0^a \sigma_r(x) \sqrt{(a-x)} dx \\ &\quad + G(a) / \sqrt{a} \int_0^a \sigma_r(x) (a-x)^{3/2} dx] \end{aligned} \quad (8.6)$$

Letting:

$$\begin{aligned} I_1(a) &= \pi \sigma_0 \sqrt{2} \int_0^a a F^2(a) da \\ I_2(a) &= \int_0^a \sigma_r(x) \sqrt{(a-x)} dx \\ I_3(a) &= \int_0^a \sigma_r(x) (a-x)^{3/2} dx \end{aligned} \quad (8.7)$$

and solving for G(a):

$$G(a) = [I_1(a) - 4F(a)\sqrt{a} I_2(a)] \sqrt{a} / I_3(a) \quad (8.8)$$

Next, a standard formulation can be derived for the integrals in equation 8.7 for various load distributions. For a constant reference load where $\sigma_r = \sigma_0$ (tension):

$$I_2(a) = \sigma_0 \int_0^a \sqrt{(a-x)} dx = 2/3 \sigma_0 a^{3/2}$$

$$I_3(a) = \sigma_0 \int_0^a (a-x)^{3/2} dx = 2/5 \sigma_0 a^{5/2} \quad (8.9)$$

Using a general stress distribution equation presented by Yagawa (67) to represent pure bending in a plate:

$$\begin{aligned} \sigma_r(x) &= \sum_{i=0}^n (1 - x/b)^i \\ &= \sigma_0 + \sigma_1 (1 - x/b) \end{aligned} \quad (8.10)$$

where b is the plate half width. Then:

$$\begin{aligned} I_2(a) &= \int_0^a [\sigma_0 + \sigma_1 (1 - x/b)] (a-x) dx \\ &= 2/3 a^{3/2} [\sigma_0 + \sigma_1 (1 - 2/5 a/b)] \end{aligned}$$

$$\begin{aligned} I_3(a) &= \int_0^a [\sigma_0 + \sigma_1 (1 - x/b)] (a-x)^{3/2} dx \\ &= 2/5 a^{5/2} [\sigma_0 + \sigma_1 (1 - 2/7 a/b)] \end{aligned} \quad (8.11)$$

Then, using equation 8.8 to calculate G(a), the crack opening displacement (COD) can be determined from equation 8.2.

The above Petroski and Achenbach crack opening displacement formulation for thru-cracks was expanded by Mattheck, et al. to three-dimensional surface cracks under symmetrical loading. The surface flaw solution is separated into three regions of analysis; $u_r(x,y=0)$, $u_r(x=0,y)$ and $u_r(x,y)$. The first region ($x,y=0$) was solved by Petroski and

Achenbach as described above. The second region ($x=0, y$) uses the Griffith crack relationship of:

$$u_r(x=0, y) = u_r^{\max} [1 - (y/c)^2]^{1/2} \quad (8.12)$$

where $u_r^{\max} = u_r(x=0, y=0)$ from equation 8.2. Thus, the first two crack regions displacement are described for $(x, y=0)$ and $(x=0, -c < y < +c)$.

For the complete crack area (x, y) , the crack depth profile can be defined in a similar manner as the crack free-surface where:

$$a^* = a [1 - (y/c)^2]^{1/2} \quad (8.13)$$

$$\begin{aligned} u_r(x, y) = & [\sigma_0 / (\sqrt{2} H)] [4F_0(a^*) \sqrt{a^*} \sqrt{a^* - x} \\ & + G_0(a^*) (a^* - x)^{3/2} / \sqrt{a^*}] \end{aligned} \quad (8.14)$$

To match the surface displacement profile, the unknown $G_0(a^*)$ is defined as:

$$G_0(a^*) = [-2H u_r^{\max} / (a \sigma_0)] - 4 F_0(a^*) \quad (8.15)$$

The above formulation is a very useful approach for predicting three-dimensional surface flaw COD because of its flexibility to utilize sophisticated stress intensity factor solutions and complex stress fields. The paper by Mattheck, et al. presented a closed form solution for tension (eqn. 8.10) using simple K-solution developed by Dufresne (54).

This investigation developed a closed form solution for a plate in bending (eqn. 8.11), and utilized the more complex Newman-Raju K-solutions. In addition, a numerical computation program was developed (Appendix A) to calculate surface flaw COD of more complex stress distributions using an eight order Newton-Cotes integral formulation and the Newman-Raju K-solutions. The program closed form solutions for tension and bending, and

the numerical integration routines, were validated by comparing the calculations to published results (54,68,69).

COD Predictions Versus Measurements

Comparisons between experimental data and weight function (WF) COD predictions are presented in this section. Perez (70) made comparisons between numerous displacement models, and thus, this section will concentrate on the Petroski-Achenbach formulation. The predictions are made at a Poisson ratio of 0.4, and average elastic modulus of 4.E5 psi (71).

Figure 8.1 is a plot of experimental and predicted COD profiles into the crack depth (Figure 5.15, between locations A and B) at three applied load levels -- bP_{op} , tP_{op} and tP_{op}^+ . In this figure, "r" is the distance from the crack tip and "a" the crack depth. The bP_{op} load level (22% of P_{max}) is in the closure load region, and is the load required to open the crack free-surface at location B. The tP_{op} load level (30% of P_{max}) is defined as the transition load where the "void" maximum displacement is at the crack free-surface (location B). Loads greater than tP_{op} are considered to be in the COD elastic region, and loads less than tP_{op} are in the closure load region. The third load level (38% of P_{max}) is within the elastic load range, and is designated as tP_{op}^+ in Figure 8.1.

At the crack free-surface ($r/a=1.0$) in Figure 8.1, the WF model is found to underpredict the displacement at the tP_{op}^+ load level, match it quite favorable at tP_{op} , and poorly predict displacement at bP_{op} . At the bP_{op} load level, the crack free-surface is just beginning to open while the elastic model predicts a displacement of 0.9E-4 inches. Note that the displacement points at the crack free-surface are extrapolations of measured data (Figure 5.16).

The predicted displacement profiles show a favorable agreement near the crack tip ($r/a < 0.05$) for all three load levels. At the lower bP_{op} load level, the elliptical profile

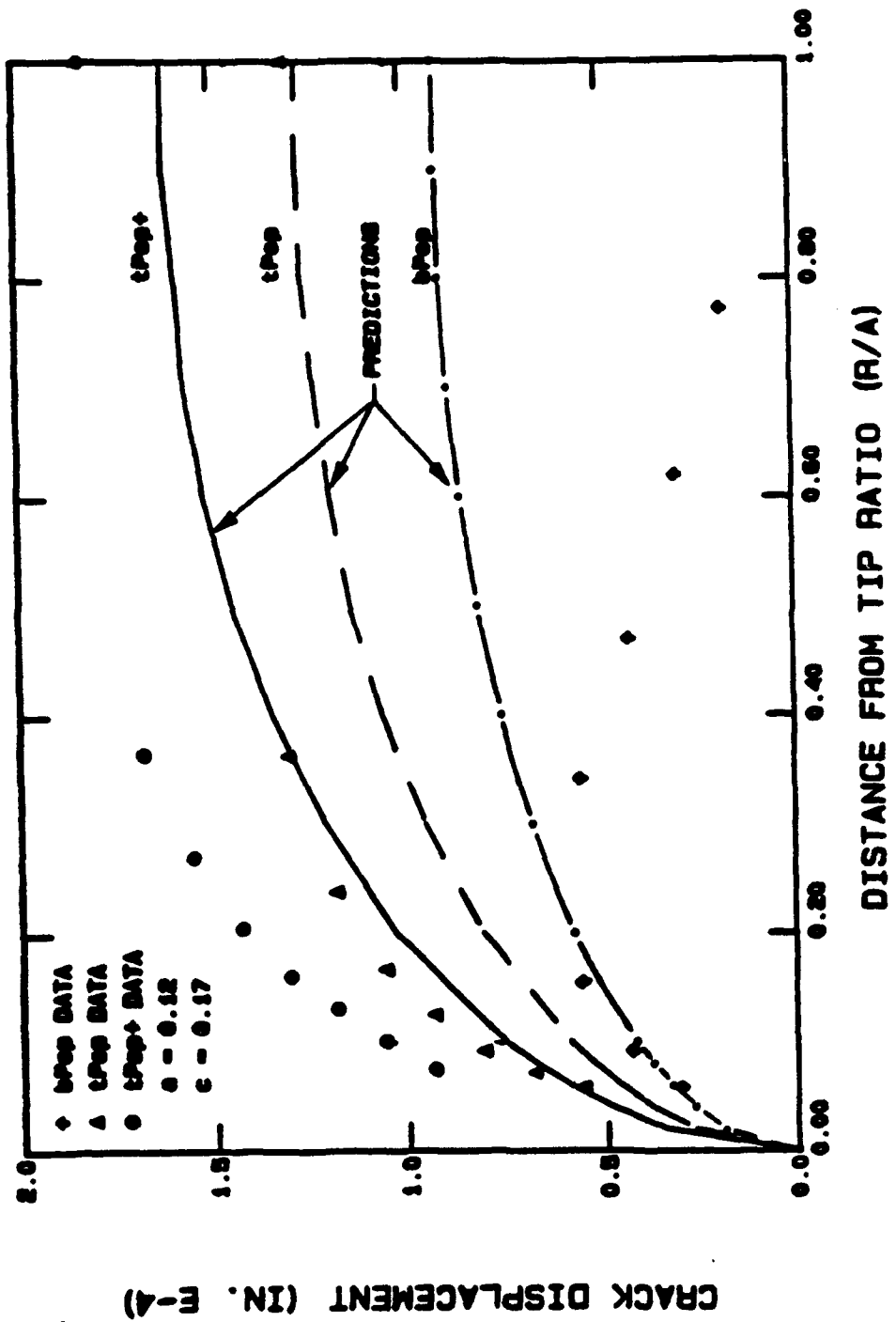


Figure 8.1 Comparison of experimental and analytical predictions of crack opening displacement profiles at three load levels. The crack tip into the specimen depth is at $r/a=0$, and the crack free-surface at $r/a=1$.

proposed by the Griffith formulation (eqn. 8.13) follows the experimental data for $r/a < 0.2$, but then deviated due to inelastic closure at the crack free-surface. At tP_{Op} , the predicted displacement matches the experimental data at the crack free-surface, but does not match the profile for $0.05 < r/a > 0.8$. At tP_{Op+} , the predicted displacement profile only matches the experimental measurements near the crack tip ($r/a \approx 0.0$).

The prediction sensitivity to modulus of elasticity, which ranges from 3.5E5 to 4.9E5 psi for PMMA (69), can be calculated directly since displacement is inversely proportional to modulus. For this modulus range, maximum displacement ranges from 1.46E-4 to 1.04E-4 at the tP_{Op} load level. This range is not sufficient to account for differences between predicted and experimental data. The maximum displacement is directly proportional to applied load, and is not effected by Poissons ratio. Variations in Poissons ratio were found to have minor influences on displacement profile distribution, but not of sufficient effect to match the experimental data.

The data in Figure 8.1 can also be presented in a load versus displacement format as shown in Figure 8.2 at the crack free-surface (location B). Here the predicted elastic displacement emanates from the origin and passes through the tP_{Op} data point. In the closure load region ($P/P_{max} < 0.3$), linear elastic fracture mechanic (LEFM) predictions are not expected to match experimental data, and significantly overpredict the displacement. In the elastic COD region ($F_{max} > 0.3$), the extrapolated experimental displacement is found to be greater than predicted at the crack free-surface. Even though the crack free-surface is extrapolated data, the measured displacement internal to the crack at $r/a = 0.4$ is noted to have a greater displacement than predicted at the crack free-surface. (Figure 8.1). At P_{max} , these differences represent a factor of 3 error between experimental and prediction displacement at the free-surface.

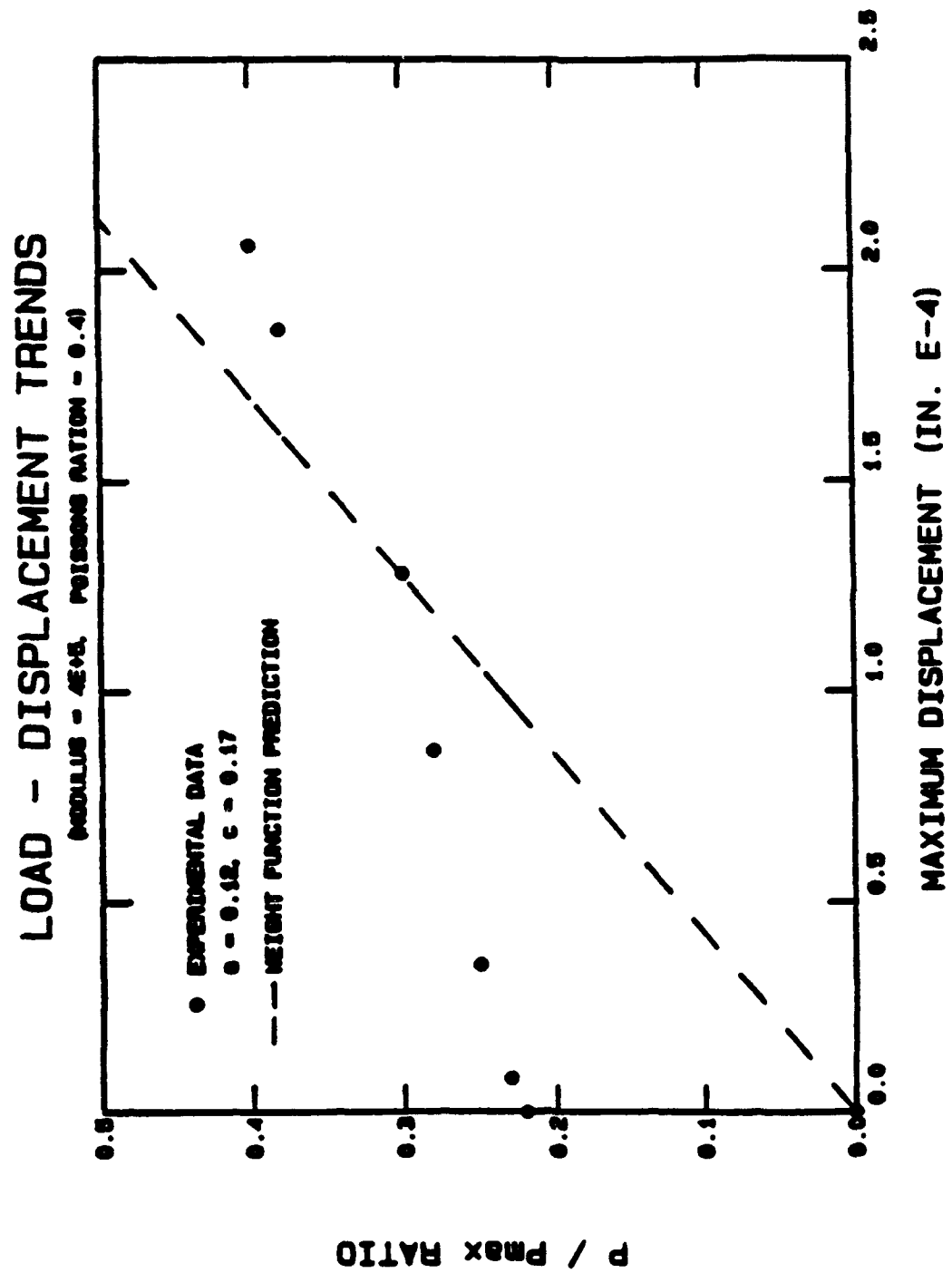


Figure 8.2 Comparison of experimental and analytical predictions on a load-displacement plot for the same crack size as Figure 8.1.

Displacement Profile Model Modifications

Differences between experimental data and elastic predictions can be attributed to inelastic effects not accounted for in the model particularly in the closure load region. Other modeling limitations are generated from the assumed elliptical profile distribution not matching the experimental displacement profile shape. This can be seen in Figure 8.1. One possible approach is to modify the shape factors associated with the Petroski-Achenbach relationship (eqn. 8.3).

Since the weight function model is elastic, improvements to the displacement profile should be evaluated in the elastic region ($P/P_{max} > 0.3$, Figure 8.2. Near the crack tip, the shape factor term proposed by Paris and Sih (72):

$$u(a,x) = 4K/H [(a-x)/\sqrt{2}] \quad (8.16)$$

appears to match the experimental data. However, the predicted amplitude is low by a factor of approximately 1.4 at $r/a = 0.1$. This could be improved by using a model other than the current elliptical profile for $r/a > 0.05$.

In addition, the "G(a)" term shape factor could be modified to reflect experimental results. As stated in the Petroski-Achenbach publication concerning the higher order terms in $(a-x)$, "The choice of subsequent terms is largely a matter of judgment, the limitation being that only one unknown function can be determined from eqn. (8.4)."

IX. SUMMARY, CONCLUSIONS AND RECOMMENDATIONS

Summary and Conclusions

The objective of this investigation was to determine the effect of fatigue crack closure on the growth of surface flaws in bending. A transparent polymethylmethacrylate (PMMA) specimen and a Newton interferometry system were used to map the crack opening displacement (COD) patterns for various crack sizes. Crack closure/opening load measurements were made concurrent with the COD interference measurements.

Interference fringe order photographs were made at crack growth increments (Δc) of approximately 0.05 inch for surface crack lengths "c" between 0.02 and 0.60 inch long. These measurements were duplicated for four different load cycles -- two constant stress intensity factor (ΔK) tests (generated by measuring "a" and "c" crack lengths and load shedding), a constant load and a block loading test. COD interference photos were digitized using a photo enlarger and digitizing table. Fatigue crack growth rate correlations were made for various definitions of effective stress intensity factor (ΔK_{eff}). Fatigue crack growth predictions are compared to experimental cycles and aspect ratios using ΔK and ΔK_{eff} values. COD measurements were compared to analytical predictions using a weight function approach for surface flaws.

The experimentally measured crack opening displacement (COD) profiles and visual observations identified three patterns which directly influence closure load level and crack tip stress intensity factor in the nonlinear closure region. These three distinct patterns are referred to as crack types I, II and III in this investigation. The COD patterns (i.e. crack types) were found to be a function of crack length (a/t), but not load history. Crack types II

and III COD patterns are distinguishable by a "void" area which separates the crack interior surfaces, while the crack free-surface is closed under zero load. As a load is applied to the specimen, these two crack types begin to initially open at the interior crack tip, and then open outward toward the crack free-surface. At the crack free-surface, its middle begins to open first, and then continues to open until the full surface crack is open. The last portion of the crack to open is not at the free-surface, but along the crack internal surfaces, 12 to 15 degrees from the crack free-surface. This surface flaw crack tip opening pattern, which occurs in the closure load region, is referred to as a "partially-open" condition since the crack tip boundary is open at certain locations while it is closed at others.

Closure load measurements were made at three distinct locations on the crack surface. These three locations correspond to closure load measurements when (1) the crack surface is completely open, (2) opening at the crack middle free-surface, and (3) opening at the deepest portion of the crack tip boundary. The closure load ratios (P_{cl}/P_{max}), and inherent closure load stress intensity factors (K_{cl}), were found to be a function of both crack size and load history. Qualitatively, the measured crack closure ratios compared favorably to published experimental and finite element analytical results.

As the cracks grow in size due to fatigue cycling, the "void" area also increases in size, causing a decrease in closure/opening load level and an increase in crack displacement at zero load. These "void" crack opening displacement patterns had a direct impact on crack tip boundary in the closure load region. There are no known K-solutions for this type of "partially-open" crack tip boundary. Available K-solutions used in this investigation are referred to as "fully-open" as opposed to "partially-open" geometric COD patterns which were measured.

It is hypothesized from the COD patterns and crack growth rate data that available "fully-open" K-solutions over predict the actual ΔK_a value (ΔK values into the crack depth) when the minimum applied load is in the closure load region. This difference is hypothesized to be caused by available K-solutions not modeling the "partially-open" crack

tip boundary developed by the "void" formation internal to the crack surfaces. This is considered a conservative discrepancy in that ΔK_a "actual" is less than available "fully-open" K-solutions predict. This leads to higher predicted crack growth rates and fewer cycles to failure. The error associated with not having a "partially-open" K-solution appears to vary with the number of cycles to achieve a given crack length. That is, for shorter a/t values, the error is estimated to be a factor of 2. However, for larger a/t values the error is less since the crack COD pattern better represents a "fully-open" condition, and the error is estimated to be a factor of 1.2.

The correlation of fatigue crack growth rates with several definitions of ΔK_{eff} (using closure load measurements and available "fully-open" K-solutions) found the crack middle free-surface closure load measurement (bP_{op}) produced the least scatter when compared with experimental results. Complete opening of the crack surfaces (cP_{op}) also produced good correlation. An analytical evaluation of fatigue crack growth using several ΔK_{eff} definitions found that (1) crack growth pattern (a/c and a/t) results are quite accurate whether closure load corrections are used or not, and (2) fatigue cycle predictions are improved when using closure corrections. These results indicate that reasonably accurate crack growth predictions can be made using "fully-open" K-solutions. When measured closure load data are not available, fatigue crack growth predictions which assume a constant closure load, and are representative of the material being considered, are shown to provide reasonably good results. The best match of crack growth pattern and cycles predictions and experimental measurements occurs when a bimodal analysis was used. That is, when two different closure loads were used in the calculation -- one for crack growth into the specimen depth (bP_{op} with da/dN), and a different one along the crack free-surface (cP_{op} with dc/dN).

Evaluation of the elastic weight function approach for predicting COD for surface flaws found the prediction to underestimate the data. A primary cause for this error is associated with the linear elastic model not matching the nonlinear COD pattern in the

closure load region. Additional error occurs from the assumed elliptical COD profile, which does not match experimental data taken at loads above the closure load level.

Recommendations

The following recommendations are offered as suggestions for further research:

1. There is a need to develop "partially-open" K-solutions for surface flaw and thru-thickness cracks in the closure load region. These solutions are required for the complete crack tip boundary, and would allow the use of K-solutions which match geometric COD profiles experienced by the crack tip -- versus "fully-open" K-solutions currently in use.
2. Develop a crack opening displacement model which matches the "void" formation in the closure load region.
3. Conduct an experimental program which measures crack opening displacement (COD) in the elastic load region in order to improve the COD prediction models. These data would provide the elastic displacement profile shape factors -- as opposed to the inelastic closure load region described in #2 above. The use of a higher frequency monochromatic light source than was used in this investigation is required to generate the increased fringe order resolution at the higher load levels. For example, by reducing the number of fringe orders by half (for a typical crack size which begins to open in the elastic region) requires a wavelength of approximately 12,000 Å, versus the 6328 Å laser light source used in this investigation. Since a light source is not known to be available at this high frequency, light filtering techniques would appear to be the most reasonable approach for this type investigation.
4. A need exists to experimentally evaluate plasticity induced closure effects on the plane strain constraint [$\sigma_1 / (\sigma_2 + \sigma_3)$] near the crack free-surface. Trantina, et al. (43) identifies plasticity as a primary factor for defining plane stress and strain plastic zones size influences on the plane strain constraint. Using a 3-D elastic-plastic finite element analysis of surface flaws, the authors showed a rapid loss in constraint for $\phi < 15$ degrees which was not identified using elastic solutions. These plane stress/strain effects were also noted in this

investigation, where the last portion of the crack tip boundary to open was at $12 < \phi < 15$ degrees. However, these effects were not observed by Ray (73), and merit further evaluation.

LIST OF REFERENCES

1. Elber, W., "Fatigue Crack Closure Under Cyclic Tension," Engineering Fracture Mechanics, Vol 2, 1970, pp. 37-45.
2. Paris, P.C., "Twenty Years of Reflection on Questions Involving Fatigue Crack Growth Part I: Historical Observations and Perspectives," EMAS Publications Ltd., Warley, U.K., 1981, pp. 3-10.
3. Banerjee, S., "Review of Crack Closure," U.S. Air Force Materials Laboratory Report, AFWAL-TR-84-4031, 1984.
4. Suresh, S. and Ritchie, R.O., "Near-Threshold Fatigue Crack Propagation on the Role of Crack Closure," Fatigue Crack Growth Threshold: Concepts, D.L.Davidson and S. Suresh, Ed, TMS-AIME, Warrendale, PA., 1984, pp. 227-261.
5. Newman, J.C. and Raju, I.S., "An Empirical Stress-Intensity Factor Equation for the Surface Crack," Engineering Fracture Mechanics, 15(1-2), 1981, pp. 185-192.
6. Orange, T. W., "Fracture Testing with Surface Crack Specimens," Jr. of Testing and Evaluation, JTEVA, 3(5), 1975, pp. 335-342.
7. Irwin, G. R., "Plastic Zone Near a Crack and Fracture Toughness," Proc 7th Sagamore Conf., 1960, pp. IV-63.
8. Dugdale, D. S., "Yielding of Steel Sheets Containing Slits," J. Mech. Phys. Sol., 8, 1960, pp. 100-108.
9. Banks, T. M. and Garlick, A., "The Form of Crack Tip Plastic Zones," Engineering Fracture Mechanics, 19(3), 1984, pp. 571-581.
10. Fuchs, H.O. and Stephens, R.I., Metal Fatigue In Engineering, John Wiley and Sons, New York, 1980.
11. Elber, W., "The Significance of Fatigue Crack Closure," Damage Tolerance in Aircraft Structures, ASTM STP 486, 1971, pp. 230-242.
12. Sharpe, W.N., Jr. and Grandt, A.F., Jr., "A Laser Interferometric Technique for Crack Surface Displacement Measurements," Proceedings of the 20th International Instrumentation Symposium of the Instrument Society of America, Albuquerque, N.M., May 1974.

13. Sharpe, W.N., Jr. and Grandt, A.F., Jr., "A Preliminary Study of Fatigue Crack Retardation Using Laser Interferometry to Measure Crack Surface Displacement," Mechanics of Crack Growth, ASTM STP 590, American Society of Testing and Materials, pp.302-330 (1976).
14. Larsen, J.M., Jira, J.R. and Weerasooriya, T., "Crack Opening Displacement Measurements on Small Cracks in Fatigue," Proceedings of the 18th National Symposium on Fracture Mechanics, Boulder, CO, June 1985.
15. Private communication with J. Jira, Air Force Materials Laboratory (AFWAL/MLLN), Wright-Patterson Air Force Base, Ohio, 1987.
16. Packman, P.F., "The Role of Interferometry in Fracture Studies," Experimental Techniques in Fracture Mechanics, A. S. Kobayashi, Ed, SASE Publication, 1975.
17. Murty, M.V.R.K. Newton, Fizeau, Hardinger Interferometers. Optical Shop Testing, D. Malacara, Ed, John Wiley and Sons, New York, 1978.
18. Fleck, N. A., Smith, I. F. C. and Smith, R. A., "Closure Behavior of Surface Cracks," Fatigue of Engineering Materials, Vol 6(3), 1983, pp. 225-239.
19. Pitoniak, F. J., "Experimental Study of Fatigue Crack Propagation and Retardation using Polymethacrylate," U.S. Air Force Materials Laboratory Report, AFML-TR-72-35, 1972.
20. Pitoniak, F.J., Grandt, A.F., Jr., Montulli, L.T. and Packman, P.F., "Fatigue Crack Retardation and Closure in Polymethylmethacrylate," Engineering Fracture Mechanics, Vol 6, 1974, pp. 663-670.
21. Pelloux, R.M., Faral, M. and McGee, W.M., "Fractographic Measurements of Crack-Tip Closure," Fracture Mechanics: Twelfth Conference, ASTM STP 700, American Society of Testing and Materials, 1980, pp. 35-48.
22. Newman, J. C., "Finite Element Analysis of Fatigue Crack Propagation Including the Effects of Crack Closure," Ph.D. Thesis, Virginia Polytechnic Institute and State University, 1974.
23. Fleck, N.A., "Finite Element Analysis of Plasticity- Induced Crack Closure Under Plane Strain Conditions," Engineering Fracture Mechanics, Vol 25, No. 4, 1986, pp. 441-449.
24. Newman, J.C., Jr., "A Finite Element Analysis of Fatigue Crack Closure," Mechanics of Crack Growth, ASTM STP 590, 1976, pp. 291-301.

25. Ray, S.K. and Grandt,A.F., Jr., "Comparison of Methods for Measuring Fatigue Crack Closure in a Thick Specimen," Accepted for publication in ASTM STP devoted to the International Symposium on Fatigue Crack Closure, Charleston, S.C., May 1986.
26. Ray, S.K. and Grandt, A.F., Jr., "Fatigue Crack Closure of Surface Flaws Loaded in Pure Bending," Experimental Mechanics (In Press).
27. Broek, D., Elementary Engineering Fracture Mechanics. Martinus Nijhoff Publishers. Third Edition, 1982, pp. 183.
28. Irwin, G.R., "Plastic Zone Near a Crack and Fracture Toughness," Proc. 7th Sagamore Conf., 1960, p. IV-63.
29. Hahn, G.T. and Rosenfield, A.R., "Experimental Determination of Plastic Constraint Ahead of a Sharp Crack Under Plane-Strain Conditions," ASM Trans., 59, 1966, pp. 909-919.
30. Grandt, A.F., Jr. and Sinclair, G.M., "Stress Intensity Factor for Surface Cracks in Bending," Stress Analysis and Growth of Cracks, ASTM STP 513, 1972, pp. 37-58.
31. Radon, J.C., "Fatigue Crack Growth in Polymers," International Journal of Fracture, Vol 16, No. 6, 1980, pp. 533-552.
32. Hertzberg, R. W. and Manson, J. A., Fatigue of Engineering Plastics, Academic Press, New York, 1980.
33. Hertzberg, R. W., Manson, J. A. and Wu, W. C., "Structure of Polymers and Fatigue Crack Propagation," ASTM STP 536, 1973, pp. 391-403.
34. Aterno, R. and Ostberg, G., "Measurements of the Temperature Rise Ahead of a Fatigue Crack," Int. J. Fract. Mech., 7(1), 1971, pp. 122-124.
35. Margolis, R. D., Dunlap, R. W. and Markovitz, H., "Fracture Toughness Testing of Glassy Plastics," ASTM STP 601, 1976, pp. 391-408.
36. Jolles, M., McGowen, J.J. and Smith, C.W., "Experimental Determination of Side Boundary Effects on Stress Intensity Factors in Surface Flaws," Journal of Engineering Materials, Vol 97, No. 1, 1975, pp.45-51.
37. Perez, R., "Initiation, Growth and Coalescence of Fatigue Cracks," M.S. Thesis, School of Aeronautics and Astronautics, Purdue University, August 1983.
38. Private communication with Mr. Ed Harper, Scientific Research Laboratory, Air Force Materials Laboratory (AFWAL/MLLM), Wright-Patterson Air Force Base, Ohio, 1984.
39. ASTM Standards E647.

40. Corn, D., "A Study of Crack Techniques for Obtaining Partial Thickness Cracks of Pre-Selected Depth and Shapes," Engineering Fracture Mechanics, Vol 3, No. 1, 1971, pp. 45-52.
41. Mahmoud, M.A. and Hosseini, A., "Assessment of Stress Intensity Factor and Aspect Ratio Variability of Surface Cracks in Bending Plates," Engineering Fracture Mechanics, Vol 24, No. 2, 1986, pp. 207-221.
42. Carter, D.W., Canda, W.R. and Bling, J.A., "Surface Flaw Crack Growth in Plates of Finite Thickness," US Air Force Academy Report AFWAL-TR-86-4034, January, 1987.
43. Trantina, G.G., deLorenzi, H.G. and Wilkening, W.W., "Three-Dimensional Elastic-Plastic Finite Element Analysis of Small Surface Cracks," Engineering Fracture Mechanics, Vol 18, No. 5, 1983, pp. 925-938.
44. Troha, W.A., Nicholas, T. and Grandt, A.F., Jr., "Three-Dimensional Aspects of Fatigue Crack Closure in Surface Flaws in a Transparent Material," Accepted for Publication in ASTM STP devoted to the International Symposium on Fatigue Crack Closure, Charleston, SC, May 1986.
45. Schijve, J., "Fatigue Crack Closure, Observations and Technical Significance," Delft University of Technology Report LR-485, April 1986.
46. Minakawa, K. and McEvily, A.J., in Fatigue Thresholds, Fundamentals and Engineering Applications, Vol. I, pp. 373-390, EMAS 1982.
47. Ashbaugh, N. E. and Ahrens, G. R., "Evaluation of Crack Closure," Presentation at the AIAA Mini-Symposium, Wright-Patterson AFB, Ohio, March 1984.
48. Bucci, R.J., "Effect of Residual Stress on Fatigue Crack Growth Rate Measurement," Fracture Mechanics: Thirteenth Conference, ASTM STP 743, 1981, pp. 28-47.
49. Larsen, J.M., "An Automated Photomicroscopic System for Monitoring the Growth of Small Fatigue Cracks," Fracture Mechanics: Seventeenth Volume, ASTM STP 905, 1986, pp. 226-238.
50. Hodulak, et al., "Growth of Part-Thru Cracks," Fracture Mechanics, ASTM STP 677, 1979, pp. 399-410.
51. Grandt, A.F., Jr., Harter, J.A. and Tritsch, D.E., "Semielliptical Cracks Along Holes in Plates and Lugs," AFWAL-TR-83-3043, AFWAL Flight Dynamics Laboratory, Wright-Patterson AFB, Ohio, May 1983.

52. Grandt, A.F., Jr., Perez, R. and Tritsch, D.E., "Cyclic Growth and Coalescence of Multiple Fatigue Cracks," *Advances in Fracture Research, Sixth International Conference on Fracture, ICF6*, New Delhi, India, Vol 3, pp. 1571-1578, December 1984.

53. Rudd, J.C. and Chang, J.C., "Round Robin Life Prediction for Corner Cracks in Holes," *ASTM Task Group E24.06.01*, 1983.

54. Mattheck, C., Morawietz, P., Munz, D., "Stress Intensity Factor at the Surface and at the Deepest Point of a Semi-Elliptical Surface Crack in Plates Under Stress Gradients," *Int. J. Fracture*, 23, 1983, pp. 201-212.

55. Petroski, H. J. and Achenbach, J. D., "Computation of the Weight Function from a Stress Intensity Factor," *Engineering Fracture Mechanics*, 10, 1978, pp. 257-266.

56. Bueckner, H. F. "A Novel Principle for the Computation of Stress Intensity Factors," *Z. angeu. Math. Mech.*, 50, 1970, pp. 529-546.

57. Bueckner, H. F., "Weight Functions for the Notched Bar," *Z. angeu. Math. Mech.*, 51, 1971, pp. 97-109.

58. Rice, J. R., "Some Remarks on Elastic Crack-tip Stress Fields," *Int. J. Solids and Struct.*, 8(6), 1972, pp. 751-758.

59. Grandt, A. F., Jr., "Stress Intensity Factors for some Through-Cracked Fastener Holes," *Int. J. Fracture*, 11(2), 1975, pp. 283-294.

60. Grandt, A. F., Jr., "Two-dimensional Stress Intensity Factor Solutions for Radially Cracked Rings," U.S. Air Force Materials Laboratory, AFML-TR-75-121, 1975.

61. Grandt, A. F., Jr. and Kullgren, T. E., "Stress Intensity Factors for Corner Cracked Holes Under General Loading Conditions," *J. Engr. Matl and Tech.*, 103, 1981, pp. 171.

62. Grandt, A. F., Jr., "Crack Face Pressure Loading of Semielliptical Cracks Located Along the Bore of a Hole," *Engineering Fracture Mechanics*, 14(4), 1981, pp. 843-852.

63. Bar-Tikva, D., Grandt, A. F., Jr. and Palazotto, A. N., "An Experimental Weight Function for Stress-Intensity- Factor Calibrations," *Experimental Mechanics*, 21(10), 1981, pp. 371-378.

64. Paris, P. C., McMeeking, R. M. and Tada, H., "The Weight Function Method for Determining Stress Intensity Factors," *ASTM STP 601*, 1976, pp. 471-489.

65. Labbens, R. C., Heliot, J. and Pellissier-Tanon, A., "Weight Functions for Three-Dimensional Symmetrical Crack Problems," *ASTM STP 601*, 1976, pp. 448-470.

66. Labbens, R., Pellissier-Tanon, A. and Heliot, J., "Practical Methods for Calculating Stress-Intensity Factors Through Weight Functions," ASTM STP 590, 1976, pp.368-384.
67. Yagawa, G., Ichimiya, M. and Ando, Y., "Theoretical and Experimental Analysis of Semi-Elliptical Surface Cracks Subjected to Thermal Shock," ASTM STP 677, 1979, pp. 381-398.
68. Mattheck, C., Munz, D. and Stamm, H., "Stress Intensity Factor for Semi-Elliptical Surface Cracks Loaded by Stress Gradients," Engineering Fracture Mechanics, 18(3), 1983, pp. 633-641.
69. Niu, X. and Glinka, G., "On the 'Limitations of the Petroski-Achenbach Crack Opening Displacement Approximation for the Calculation of Weight Functions' - Do They Really Exist?," Engr. Fracture Mechanics Vol 25, No. 5, pp 701-706, 1987.
70. Perez, R., "Stress Intensity Factors for Fatigue Cracks at Holes Under Cyclic Stress Gradients," Ph. D. Thesis, School of Aeronautics and Astronautics, Purdue University, May 1986.
71. Hertzberg, R.W., Deformation and Fracture Mechanics of Experimental Materials, John Wiley and Sons, New York, 2nd Edition, 1983.
72. Paris, P.C. and Sih, G.C., "Stress Analysis of Cracks," Fracture Toughness Testing and Its Application, ASTM STP 381, 1965, pp. 30-81.
73. Ray, S.K., "A Three-Dimensional Investigation of Steady State Fatigue Crack Closure Behavior for Through-Thickness and Part- Through Flaws," Ph.D. Thesis, Purdue University, W. Lafayette, Indiana, August 1987.

Appendix A Constant ΔK_a Test Data

A complete listing of the experimental data is presented in this appendix for the constant K_a test. The data sheet column variables are follows: the applied delta bending moment ($M_{max} - M_{min}$, in-lbs.), "a" and "c" crack lengths, a/c, a/t, accumulated fatigue cycles, ΔK_c , K_c max, plastic zone size at location C, ΔK_a , K_a max, plastic zone size at location A, cP_{op} , bP_{op} and aP_{op} applied load (lb). Negative one (-1.0) is a designator to indicate that closure load data were not recorded at that crack size. Blank lines between the data separate categories of precracking, type I, type II and type III cracks.

SPECIMEN 2-11 CONSTANT AA = 600 SIGNING 1/2 AT 0 DEGREES

Appendix B Constant ΔK_d Test Data

A complete listing of the experimental data is presented in this appendix for the constant K_d test. The data sheet column variables are as follows: the applied delta bending moment ($M_{max} - M_{min}$, in-lbs.), "a" and "c" crack lengths, a/c, a/t, accumulated fatigue cycles, ΔK_c , K_c max, plastic zone size at location C, ΔK_a , K_a max, plastic zone size at location A, cP_{op} , bP_{op} and aP_{op} applied load (lb.). Negative one (-1.0) is an indication that closure load data were not recorded at that crack size. Blank lines in the data separate categories of precracking, type I, type II and type III cracks.

SPECIMIN J-14 CONSTANT AC + 600 PS161M061/2 AT 0 DEGREES

DEBLNT	A	C	ADG	ADT	CTL	BELKIC	MANNIC	KPC	HELMIA	MANNIA	RPA	CPDP	BPDP	APDP		
781.	0.020	0.0242	0.0247	101000.0	633.5	656.4	0.280E-02	652.7	676.4	0.911E-03	-1.0	-1.0	-1.0	-1.0		
781.	0.022	0.0295	0.0293	101300.0	663.4	687.5	0.307E-02	679.4	700.0	0.107E-02	-1.0	-1.0	-1.0	-1.0		
793.	0.022	0.0295	0.0293	101300.0	537.4	557.1	0.292E-02	550.9	570.8	0.704E-03	-1.0	-1.0	-1.0	-1.0		
793.	0.024	0.0320	0.0320	102000.0	540.6	581.0	0.219E-02	571.9	592.4	0.40E-03	-1.0	-1.0	-1.0	-1.0		
793.	0.024	0.0345	0.0345	103000.0	584.0	605.2	0.238E-02	580.0	609.4	0.804E-03	245.1	-1.0	245.1	-1.0		
793.	0.024	0.0355	0.0347	103500.0	583.1	604.2	0.237E-02	599.2	621.0	0.335E-03	194.9	140.1	194.9	140.1		
793.	0.030	0.0345	0.0322	0.0339	104000.0	426.1	448.8	0.273E-02	465.1	427.0	0.511E-03	214.1	112.0	214.1	112.0	
795.	0.032	0.0365	0.0374	0.0427	104500.0	446.0	469.4	0.291E-02	488.3	422.1	0.494E-03	252.9	121.0	252.9	121.0	
644.	0.032	0.0345	0.0345	0.0427	104500.0	523.2	542.2	0.191E-02	560.0	509.7	0.554E-03	252.9	121.0	252.9	121.0	
644.	0.032	0.0370	0.0365	0.0427	104600.0	523.1	542.4	0.191E-02	491.4	501.2	0.611E-03	174.0	153.1	174.0	153.1	
644.	0.033	0.0370	0.0370	0.0439	108000.0	530.1	549.4	0.194E-02	496.1	501.9	0.359E-03	211.1	138.9	211.1	138.9	
644.	0.035	0.0385	0.0391	0.0446	110000.0	545.4	565.4	0.208E-02	497.6	515.9	0.374E-03	194.0	152.0	194.0	152.0	
644.	0.036	0.0400	0.0397	0.0479	112000.0	552.0	572.9	0.213E-02	506.9	522.3	0.398E-03	174.0	145.9	174.0	145.9	
644.	0.038	0.0420	0.0420	0.0497	114000.0	567.7	588.3	0.223E-02	516.9	535.4	0.421E-03	191.1	154.9	191.1	154.9	
644.	0.040	0.0440	0.0440	0.0533	114000.0	581.5	602.4	0.234E-02	527.2	544.3	0.444E-03	191.1	154.9	191.1	154.9	
644.	0.043	0.0443	0.0443	0.0552	117000.0	599.7	621.7	0.251E-02	525.4	544.4	0.442E-03	201.9	149.1	201.9	149.1	
600.	0.043	0.0445	0.0445	0.0553	117000.0	557.3	579.4	0.210E-02	489.5	507.2	0.357E-03	201.9	149.1	201.9	149.1	
600.	0.043	0.0445	0.0445	0.0553	119000.0	559.0	579.3	0.218E-02	489.4	507.1	0.357E-03	185.0	149.1	185.0	149.1	
600.	0.043	0.0450	0.0450	0.0573	119000.0	339.1	359.7	0.218E-02	492.7	510.4	0.352E-03	191.1	141.0	191.1	141.0	
600.	0.043	0.0450	0.0454	0.0573	120000.0	339.4	359.7	0.218E-02	492.7	510.4	0.352E-03	186.1	141.0	186.1	141.0	
400.	0.043	0.0455	0.0440	0.0573	121000.0	339.8	350.1	0.219E-02	495.9	511.9	0.372E-03	174.0	141.0	174.0	141.0	
400.	0.043	0.0469	0.0454	0.0573	123000.0	346.8	361.1	0.219E-02	504.4	522.7	0.392E-03	153.1	-1.0	153.1	-1.0	
600.	0.044	0.0500	0.0492	0.0582	125000.0	366.0	386.0	0.223E-02	520.4	537.2	0.410E-03	174.0	141.0	174.0	141.0	
600.	0.044	0.0505	0.0571	0.0587	127000.0	366.2	386.8	0.225E-02	523.2	542.1	0.434E-03	132.0	-1.0	132.0	-1.0	
600.	0.044	0.0520	0.0548	0.0587	129000.0	368.5	389.2	0.225E-02	531.3	550.4	0.454E-03	145.9	-1.0	145.9	-1.0	
600.	0.044	0.0525	0.0527	0.0587	130000.0	361.4	389.2	0.246E-02	534.0	553.4	0.463E-03	145.9	-1.0	145.9	-1.0	
600.	0.047	0.0530	0.0530	0.0627	132000.0	364.4	407.9	0.246E-02	543.0	562.7	0.484E-03	191.1	152.0	191.1	152.0	
600.	0.048	0.0563	0.0563	0.0651	0.0649	133000.0	597.7	614.2	0.235E-02	549.5	569.4	0.702E-03	191.1	141.0	191.1	141.0
575.	0.048	0.0563	0.0563	0.0646	133000.0	367.1	388.5	0.235E-02	526.4	535.7	0.443E-03	191.1	141.0	191.1	141.0	
400.	0.043	0.0455	0.0440	0.0573	121000.0	339.8	350.1	0.219E-02	495.9	511.9	0.372E-03	174.0	-1.0	174.0	-1.0	
600.	0.043	0.0469	0.0454	0.0573	123000.0	346.8	361.1	0.219E-02	504.4	522.7	0.392E-03	153.1	-1.0	153.1	-1.0	
600.	0.044	0.0500	0.0492	0.0582	125000.0	366.0	386.0	0.223E-02	520.4	537.2	0.410E-03	174.0	-1.0	174.0	-1.0	
600.	0.044	0.0505	0.0571	0.0587	127000.0	366.2	386.8	0.225E-02	523.2	542.1	0.434E-03	134.9	-1.0	134.9	-1.0	
600.	0.044	0.0520	0.0548	0.0587	129000.0	368.5	389.2	0.225E-02	531.3	550.4	0.454E-03	145.9	-1.0	145.9	-1.0	
600.	0.044	0.0525	0.0527	0.0587	130000.0	361.4	389.2	0.246E-02	534.0	553.4	0.463E-03	145.9	-1.0	145.9	-1.0	
600.	0.047	0.0530	0.0530	0.0627	132000.0	364.4	407.9	0.246E-02	543.0	562.7	0.484E-03	191.1	152.0	191.1	152.0	
575.	0.048	0.0563	0.0563	0.0646	133000.0	367.1	388.5	0.235E-02	526.4	535.7	0.443E-03	191.1	141.0	191.1	141.0	
575.	0.051	0.0535	0.0535	0.0651	0.0651	133000.0	374.5	395.3	0.230E-02	513.2	531.0	0.446E-03	160.1	-1.0	160.1	-1.0
575.	0.051	0.0535	0.0535	0.0651	0.0651	133000.0	374.5	395.3	0.230E-02	513.2	531.0	0.446E-03	160.1	-1.0	160.1	-1.0
575.	0.051	0.0535	0.0535	0.0651	0.0651	133000.0	374.5	395.3	0.230E-02	513.2	531.0	0.446E-03	160.1	-1.0	160.1	-1.0
551.	0.054	0.0605	0.0605	0.0724	0.0724	137000.0	374.5	395.3	0.230E-02	513.2	531.0	0.446E-03	160.1	-1.0	160.1	-1.0
551.	0.054	0.0605	0.0605	0.0724	0.0724	138000.0	374.5	395.3	0.230E-02	513.2	531.0	0.446E-03	160.1	-1.0	160.1	-1.0
551.	0.054	0.0605	0.0605	0.0724	0.0724	140000.0	375.1	396.0	0.231E-02	520.0	538.9	0.447E-03	160.1	-1.0	160.1	-1.0
551.	0.054	0.0605	0.0605	0.0724	0.0724	142000.0	375.8	396.7	0.231E-02	525.5	534.9	0.447E-03	201.9	-1.0	201.9	-1.0
551.	0.054	0.0605	0.0605	0.0724	0.0724	144000.0	376.5	397.4	0.231E-02	527.5	547.5	0.447E-03	191.1	-1.0	191.1	-1.0
551.	0.054	0.0605	0.0605	0.0724	0.0724	146000.0	377.3	398.1	0.231E-02	535.3	555.4	0.447E-03	191.1	-1.0	191.1	-1.0
551.	0.054	0.0605	0.0605	0.0724	0.0724	148000.0	378.0	398.8	0.231E-02	537.0	557.4	0.447E-03	191.1	-1.0	191.1	-1.0
551.	0.054	0.0605	0.0605	0.0724	0.0724	150000.0	378.8	399.5	0.231E-02	537.0	557.4	0.447E-03	191.1	-1.0	191.1	-1.0
551.	0.054	0.0605	0.0605	0.0724	0.0724	151000.0	379.5	400.2	0.231E-02	537.0	557.4	0.447E-03	191.1	-1.0	191.1	-1.0
525.	0.059	0.0745	0.0745	0.0772	0.0772	151000.0	379.5	400.2	0.222E-02	548.0	567.9	0.448E-03	180.1	-1.0	180.1	-1.0
525.	0.059	0.0745	0.0745	0.0772	0.0772	151000.0	379.5	400.2	0.222E-02	548.0	567.9	0.448E-03	180.1	-1.0	180.1	-1.0
525.	0.059	0.0745	0.0745	0.0772	0.0772	151000.0	379.5	400.2	0.222E-02	548.0	567.9	0.448E-03	180.1	-1.0	180.1	-1.0
525.	0.059	0.0745	0.0745	0.0772	0.0772	151000.0	379.5	400.2	0.222E-02	548.0	567.9	0.448E-03	180.1	-1.0	180.1	-1.0
525.	0.059	0.0745	0.0745	0.0772	0.0772	151000.0	379.5	400.2	0.222E-02	548.0	567.9	0.448E-03	180.1	-1.0	180.1	-1.0
525.	0.059	0.0745	0.0745	0.0772	0.0772	151000.0	379.5	400.2	0.222E-02	548.0	567.9	0.448E-03	180.1	-1.0	180.1	-1.0
525.	0.059	0.0745	0.0745	0.0772	0.0772	151000.0	379.5	400.2	0.222E-02	548.0	567.9	0.448E-03	180.1	-1.0	180.1	-1.0
525.	0.059	0.0745	0.0745	0.0772	0.0772	151000.0	379.5	400.2	0.222E-02	548.0	567.9	0.448E-03	180.1	-1.0	180.1	-1.0
525.	0.059	0.0745	0.0745	0.0772	0.0772	151000.0	379.5	400.2	0.222E-02	548.0	567.9	0.448E-03	180.1	-1.0	180.1	-1.0
525.	0.059	0.0745	0.0745	0.0772	0.0772	151000.0	379.5	400.2	0.222E-02	548.0	567.9	0.448E-03	180.1	-1.0	180.1	-1.0
525.	0.059	0.0745	0.0745	0.0772	0.0772	151000.0	379.5	400.2	0.222E-02	548.0	567.9	0.448E-03	180.1	-1.0	180.1	-1.0
525.	0.059	0.0745	0.0745	0.0772	0.0772	151000.0	379.5	400.2	0.222E-02	548.0	567.9	0.448E-03	180.1	-1.0	180.1	-1.0
525.	0.059	0.0745	0.0745													

355.	0.134	0.2013	0.474	0.242000.0	567.0	307.4	0.224E-02	134.9	513.4	512.4	0.414E-02		
355.	0.134	0.2013	0.4662	0.1813	244000.0	567.0	307.4	0.223E-02	134.9	513.4	512.4	0.413E-02	
355.	0.141	0.2033	0.4691	0.1800	244000.0	577.1	400.1	0.235E-02	115.1	511.4	511.4	0.412E-02	
355.	0.145	0.2059	0.4730	0.1934	248000.0	586.8	408.1	0.235E-02	115.1	511.4	511.4	0.412E-02	
355.	0.145	0.2160	0.4768	0.1934	249000.0	586.8	408.1	0.236E-02	115.1	511.4	511.4	0.412E-02	
355.	0.145	0.2160	0.4791	0.1924	250000.0	586.7	408.0	0.236E-02	115.1	511.4	511.4	0.412E-02	
355.	0.145	0.2163	0.4891	0.1924	250000.0	586.7	408.0	0.236E-02	115.1	511.4	511.4	0.412E-02	
355.	0.144	0.2113	0.4792	0.1944	251000.0	586.5	407.8	0.235E-02	116.0	511.2	511.2	0.412E-02	
355.	0.148	0.2130	0.4749	0.1974	252000.0	592.5	414.0	0.235E-02	127.0	517.1	515.9	0.412E-02	
355.	0.149	0.2150	0.4897	0.1984	254000.0	586.9	409.2	0.235E-02	129.0	504.9	504.9	0.412E-02	
355.	0.150	0.2175	0.4897	0.2000	254000.0	582.3	402.3	0.231E-02	129.0	508.6	508.6	0.412E-02	
355.	0.150	0.2193	0.4833	0.2000	258000.0	562.1	392.3	0.220E-02	129.0	510.9	510.9	0.412E-02	
355.	0.151	0.2210	0.4832	0.2014	240000.0	583.7	404.3	0.222E-02	118.0	511.4	511.4	0.412E-02	
355.	0.152	0.2235	0.4860	0.2026	242000.0	585.4	405.9	0.223E-02	117.0	511.4	511.4	0.412E-02	
355.	0.152	0.2262	0.4723	0.2026	244000.0	585.2	405.7	0.223E-02	124.1	514.1	514.1	0.412E-02	
355.	0.154	0.2273	0.4749	0.2054	244000.0	589.5	409.5	0.224E-02	124.1	515.7	515.7	0.412E-02	
355.	0.154	0.2154	0.4737	0.2054	248000.0	587.3	403.1	0.224E-02	124.1	514.9	514.9	0.412E-02	
355.	0.155	0.2157	0.2315	0.4753	0.2080	248000.0	574.1	394.9	0.224E-02	124.1	514.9	514.9	0.412E-02
355.	0.155	0.2157	0.2340	0.4769	0.2094	272000.0	573.4	394.7	0.220E-02	124.1	514.9	514.9	0.412E-02
355.	0.155	0.2159	0.2346	0.4737	0.2120	274000.0	577.3	398.3	0.213E-02	124.1	514.9	514.9	0.412E-02
355.	0.157	0.2159	0.2383	0.4664	0.2120	276000.0	582.3	403.1	0.227E-02	124.1	503.9	503.9	0.412E-02
355.	0.157	0.2157	0.2315	0.4753	0.2160	278000.0	581.6	407.4	0.229E-02	124.1	504.9	504.9	0.412E-02
355.	0.157	0.2157	0.2340	0.4769	0.2160	279000.0	581.6	407.4	0.229E-02	124.1	504.9	504.9	0.412E-02
355.	0.157	0.2159	0.2346	0.4737	0.2120	274000.0	577.3	398.3	0.213E-02	124.1	504.9	504.9	0.412E-02
355.	0.159	0.2159	0.2383	0.4664	0.2120	276000.0	582.3	403.1	0.227E-02	124.1	503.9	503.9	0.412E-02
355.	0.159	0.2159	0.2443	0.4753	0.2160	286000.0	581.6	407.4	0.229E-02	124.1	502.5	502.5	0.412E-02
355.	0.164	0.2164	0.4722	0.2213	292000.0	589.1	416.3	0.224E-02	125.0	503.4	503.4	0.412E-02	
320.	0.143	0.1524	0.2479	0.2240	284000.0	544.1	384.7	0.218E-02	125.0	502.4	502.4	0.412E-02	
320.	0.149	0.1524	0.2476	0.2253	287000.0	567.5	500.1	0.218E-02	125.0	502.4	502.4	0.412E-02	
320.	0.171	0.2550	0.4705	0.2280	291000.0	579.4	591.3	0.227E-02	125.0	502.7	502.7	0.412E-02	
320.	0.173	0.2570	0.4732	0.2307	293000.0	579.4	591.7	0.230E-02	125.0	502.5	502.5	0.412E-02	
320.	0.177	0.2610	0.4769	0.2359	297000.0	586.1	401.2	0.235E-02	125.0	502.5	502.5	0.412E-02	
320.	0.177	0.2620	0.4753	0.2359	299000.0	586.1	401.1	0.235E-02	125.0	502.5	502.5	0.412E-02	
320.	0.179	0.2649	0.4780	0.2317	301000.0	583.3	401.5	0.237E-02	125.0	502.4	502.4	0.412E-02	
320.	0.179	0.2649	0.4770	0.2387	303000.0	581.1	401.3	0.237E-02	125.0	502.4	502.4	0.412E-02	
320.	0.181	0.2223	0.4663	0.2113	309000.0	586.0	407.2	0.240E-02	125.0	500.3	500.3	0.412E-02	
320.	0.183	0.2753	0.4641	0.2437	312000.0	587.0	410.3	0.222E-02	125.0	502.4	502.4	0.412E-02	
320.	0.183	0.2770	0.4632	0.2447	315000.0	592.1	411.4	0.245E-02	125.0	502.4	502.4	0.412E-02	
365.	0.183	0.2793	0.4631	0.2447	315000.0	584.3	584.9	0.222E-02	125.0	502.4	502.4	0.412E-02	
365.	0.183	0.2793	0.4577	0.2447	315000.0	584.2	584.7	0.222E-02	125.0	502.4	502.4	0.412E-02	
365.	0.183	0.2813	0.4572	0.2447	315000.0	588.4	589.3	0.222E-02	125.0	502.4	502.4	0.412E-02	
365.	0.188	0.2844	0.4653	0.2387	304000.0	584.0	407.2	0.227E-02	125.0	502.4	502.4	0.412E-02	
365.	0.188	0.2875	0.4653	0.2321	327000.0	579.0	409.7	0.227E-02	125.0	502.4	502.4	0.412E-02	
365.	0.192	0.293	0.4634	0.2340	332000.0	574.3	595.1	0.230E-02	125.0	502.4	502.4	0.412E-02	
365.	0.193	0.293	0.4577	0.2460	337000.0	578.4	599.4	0.234E-02	125.0	502.4	502.4	0.412E-02	
365.	0.193	0.3060	0.4591	0.2460	345000.0	587.2	601.4	0.240E-02	125.0	502.4	502.4	0.412E-02	
365.	0.201	0.3013	0.4623	0.2480	347000.0	586.9	600.2	0.240E-02	125.0	502.4	502.4	0.412E-02	
365.	0.201	0.3060	0.4524	0.2324	349000.0	586.2	597.7	0.240E-02	125.0	502.4	502.4	0.412E-02	
365.	0.203	0.3103	0.4538	0.2340	352000.0	587.7	611.1	0.243E-02	125.0	502.4	502.4	0.412E-02	
365.	0.204	0.3130	0.4516	0.2370	354000.0	591.1	612.3	0.244E-02	125.0	502.4	502.4	0.412E-02	
290.	0.204	0.3130	0.4516	0.2370	354000.0	562.1	562.5	0.220E-02	125.0	502.4	502.4	0.412E-02	
290.	0.204	0.3165	0.4598	0.2374	359000.0	564.4	565.1	0.222E-02	125.0	502.4	502.4	0.412E-02	
290.	0.207	0.3210	0.4549	0.2374	364000.0	565.9	566.2	0.223E-02	125.0	502.4	502.4	0.412E-02	
290.	0.209	0.3243	0.4649	0.2374	377000.0	567.4	568.4	0.224E-02	125.0	502.4	502.4	0.412E-02	
290.	0.212	0.3236	0.4585	0.2374	375000.0	572.2	573.4	0.226E-02	125.0	502.4	502.4	0.412E-02	
290.	0.214	0.3350	0.4596	0.2374	389000.0	575.0	576.2	0.227E-02	125.0	502.4	502.4	0.412E-02	
290.	0.214	0.3370	0.4592	0.2374	392000.0	576.8	578.0	0.228E-02	125.0	502.4	502.4	0.412E-02	

245.	0.304	0.5204	0.4080	4.250000.0	500.9	602.0	0.235E-02	607.1	421.9
245.	0.309	0.5735	0.5204	0.4120	4.180000.0	584.2	605.4	0.230E-02	405.6
245.	0.312	0.6005	0.5195	0.4160	4.350000.0	507.3	608.4	0.241E-02	404.4
245.	0.312	0.6005	0.5194	0.4160	4.350000.0	543.4	583.6	0.221E-02	388.0
250.	0.312	0.6070	0.5140	0.4160	4.600000.0	563.0	583.4	0.221E-02	390.4
250.	0.312	0.6105	0.5127	0.4171	4.550000.0	564.0	584.5	0.222E-02	390.4
250.	0.313	0.6105	0.5114	0.4187	4.500000.0	565.0	585.5	0.223E-02	370.5
250.	0.314	0.6140	0.5114	0.4187	4.500000.0	565.0	585.5	0.223E-02	370.5
250.	0.315	0.6235	0.5052	0.4200	4.550000.0	545.7	586.2	0.223E-02	372.7
250.	0.316	0.6360	0.5047	0.4200	4.600000.0	548.8	589.4	0.224E-02	391.5
250.	0.321	0.6360	0.5047	0.4200	4.650000.0	571.9	592.7	0.224E-02	390.0
2.5.	0.323	0.6431	0.5024	0.4307	4.700000.0	574.0	594.0	0.210E-02	389.7
2.5.	0.324	0.6495	0.4998	0.4219	4.750000.0	575.9	595.4	0.208E-02	371.0
2.5.	0.325	0.6500	0.4998	0.4333	4.755000.0	576.0	596.0	0.211E-02	390.0

Appendix C Constant Load Test Data

A complete listing of the experimental data is presented in this appendix for the constant load test. The data sheet column variables are as follows: the applied delta bending moment ($M_{max} - M_{min}$, in-lb.), "a" and "c" crack lengths, a/c, a/t, accumulated fatigue cycles, ΔK_c , $K_c \text{ max}$, plastic zone size at location C, ΔK_a , $K_a \text{ max}$, plastic zone size at location A, cP_{op} , bP_{op} and aP_{op} applied load (lb.). Negative one (-1.0) indicates that closure load data were not recorded at that crack size. Blank lines in the data separate categories of precracking, type I, type II and type III cracks.

SPECIMEN J-15 (UNCONSTANT LOAD TEST)												
TEST NUMBER	A	B	C	INFLUENT MOMENTS = 644 IN-LBS) AT 0 DEGREES								APR
				DELTA CYL	DELTA HANNIC	RPC	DELKJA	HANNIA	RPA	CPOP	PPOP	
1487.	0.020	0.0190	1.0524	0.0267	17200.0	973.0	1009.2	0.442E-02	941.9	0.193E-02	272.7	272.7
981.	0.020	0.0210	1.0524	0.0267	17200.0	442.4	465.7	0.298E-02	555.4	0.737E-03	272.7	272.7
981.	0.022	0.0210	1.0474	0.0293	18000.0	471.0	496.1	0.315E-02	586.7	601.9	0.744E-03	281.0
795.	0.022	0.0210	1.0474	0.0293	18000.0	544.4	544.2	0.277E-02	476.4	487.7	0.539E-03	281.0
795.	0.022	0.0220	1.0499	0.0293	19000.0	514.4	554.0	0.199E-02	473.9	499.2	0.129E-03	369.0
795.	0.022	0.0230	1.0545	0.0293	20000.0	536.3	555.8	0.201E-02	495.2	502.8	0.327E-03	247.1
795.	0.023	0.0230	1.0545	0.0307	21000.0	564.3	564.2	0.208E-02	482.8	500.3	0.322E-03	249.0
795.	0.023	0.0230	1.0545	0.0307	22000.0	546.2	546.2	0.208E-02	492.8	500.3	0.322E-03	292.3
795.	0.023	0.0230	1.0545	0.0307	23000.0	546.3	564.2	0.208E-02	482.8	500.3	0.322E-03	281.0
795.	0.023	0.0240	1.0583	0.0307	25000.0	546.0	567.9	0.209E-02	494.7	512.4	0.349E-03	369.1
795.	0.023	0.0240	1.0583	0.0307	34000.0	548.0	567.9	0.209E-02	494.7	512.4	0.349E-03	281.0
981.	0.024	0.0240	1.0600	0.0320	35000.0	488.3	713.2	0.310E-02	607.4	429.4	0.639E-03	281.0
981.	0.024	0.0245	1.0729	0.0320	36000.0	687.3	714.3	0.311E-02	614.7	637.9	0.679E-03	281.0
981.	0.024	0.0245	1.0729	0.0320	37000.0	691.4	718.5	0.315E-02	641.0	685.0	0.802E-02	281.0
981.	0.024	0.0250	1.0771	0.0320	37000.0	758.5	786.0	0.491E-02	693.4	719.3	0.112E-02	281.0
981.	0.024	0.0250	1.0771	0.0320	37500.0	633.0	633.0	0.299E-02	542.4	562.4	0.735E-03	267.1
795.	0.033	0.0330	1.0600	0.0440	40000.0	656.0	674.4	0.295E-02	567.6	588.2	0.799E-03	369.1
644.	0.033	0.0330	1.0600	0.0440	40000.0	527.1	546.2	0.194E-02	459.7	476.4	0.491E-03	369.1
644.	0.034	0.0335	1.0744	0.0440	42000.0	536.4	536.4	0.223E-02	473.1	496.4	0.371E-03	292.3
644.	0.034	0.0335	1.0744	0.0440	43000.0	546.9	565.4	0.223E-02	473.1	496.4	0.371E-03	369.1
644.	0.034	0.0340	1.0744	0.0440	45000.0	561.7	582.2	0.226E-02	474.3	491.3	0.323E-03	286.4
644.	0.034	0.0340	1.0744	0.0440	52000.0	561.9	582.2	0.226E-02	474.3	491.3	0.323E-03	292.3
644.	0.037	0.0350	1.0571	0.0440	55000.0	547.0	569.6	0.224E-02	480.0	497.4	0.334E-03	292.3
644.	0.037	0.0360	1.0627	0.0473	58000.0	562.9	583.3	0.221E-02	481.7	497.2	0.349E-03	292.3
644.	0.038	0.0360	1.0627	0.0473	61000.0	565.2	585.7	0.223E-02	496.1	514.1	0.372E-03	281.0
644.	0.040	0.0410	0.9790	0.0473	64000.0	579.2	586.3	0.216E-02	506.7	525.1	0.397E-03	281.0
644.	0.040	0.0430	0.9392	0.0533	67000.0	581.0	492.1	0.213E-02	520.5	539.4	0.410E-03	269.0
644.	0.044	0.0455	0.9470	0.0587	70000.0	604.4	628.4	0.237E-02	530.1	547.3	0.433E-03	253.4
644.	0.044	0.0455	0.9473	0.0587	73000.0	621.1	643.7	0.249E-02	532.2	567.2	0.299E-03	224.0
644.	0.048	0.0495	0.9293	0.0513	75000.0	634.4	637.4	0.201E-02	567.6	587.4	0.749E-03	224.0
644.	0.051	0.0575	0.9870	0.0640	78000.0	653.0	677.5	0.298E-02	590.8	612.3	0.812E-03	236.4
644.	0.057	0.0655	0.9870	0.0740	81000.0	689.4	714.6	0.332E-02	623.8	646.5	0.939E-03	246.0
644.	0.061	0.0715	0.9853	0.0813	83000.0	712.3	728.2	0.354E-02	647.2	672.3	0.779E-03	212.3
644.	0.063	0.0740	0.9854	0.0840	86000.0	723.3	749.5	0.355E-02	655.7	679.7	0.100E-02	213.7
644.	0.074	0.1005	0.7542	0.0913	87000.0	745.2	792.9	0.408E-02	688.2	713.2	0.119E-02	191.1
644.	0.074	0.1090	0.4972	0.1013	94000.0	787.2	815.7	0.432E-02	774.3	802.3	0.139E-02	175.4
644.	0.084	0.1195	0.7029	0.1120	96000.0	825.5	855.4	0.473E-02	798.0	827.8	0.148E-02	166.1
644.	0.087	0.1230	0.7073	0.1140	96500.0	837.4	861.7	0.492E-02	804.0	825.3	0.151E-02	166.1
644.	0.090	0.1300	0.6923	0.1200	97500.0	831.9	862.8	0.504E-02	823.1	832.9	0.158E-02	170.9
644.	0.098	0.1380	0.7101	0.1307	95500.0	807.4	819.0	0.556E-02	835.9	846.3	0.162E-02	213.4

Appendix D Block Loading Test Data

A complete listing of the experimental data is presented in this appendix for the block loading test. The data sheet column variables are as follows: the applied delta bending moment ($M_{max} - M_{min}$, in-lb.), "a" and "c" crack lengths, a/c, a/t, accumulated fatigue cycles, ΔK_c , $K_c \text{ max}$, plastic zone size at location C, ΔK_a , $K_a \text{ max}$, plastic zone size at location A, cP_{op} , bP_{op} and aP_{op} applied load (lb.). Negative one (-1.0) indicates that closure load data were not recorded at that crack size. Blank lines in the data separate categories of precracking, type I, type II and type III cracks.

STLCLN. : 3-14 VARIABLE LOAD TEST AT 0 DEGREES

DELTAN	A	E	ADC	ADC	CIL	DELNIC	HANNIC	KFC	DELKIN	HAKKA	HFA	CFOP	BFUF	AFUF		
981.	0.020	0.0419	0.0267	12930.0	398.0	420.5	0.250E-02	765.4	793.1	0.136E-02	-1.0	-1.0	-1.0	-1.0		
981.	0.033	0.0530	0.0440	13750.0	796.0	825.7	0.443E-02	913.0	913.0	0.180E-02	210.9	210.9	210.9	210.9		
795.	0.033	0.0530	0.0440	13750.0	445.7	449.1	0.291E-02	714.0	739.9	0.119E-02	310.7	310.7	310.7	310.7		
795.	0.036	0.0550	0.0480	14490.0	449.0	477.0	701.5	0.320E-02	727.2	753.4	0.123E-02	309.1	309.1	309.1	309.1	
645.	0.034	0.0550	0.04545	14490.0	548.3	548.2	0.210E-02	589.0	610.4	0.867E-03	369.4	369.4	369.4	369.4		
644.	0.034	0.0550	0.04545	0.0480	15880.0	545.3	545.1	0.207E-02	401.6	423.4	0.842E-03	314.7	314.7	314.7	314.7	
644.	0.034	0.0550	0.04207	0.0480	17000.0	551.2	572.2	0.213E-02	510.3	632.3	0.844E-03	281.0	281.0	281.0	281.0	
644.	0.037	0.0480	0.04167	0.0493	17000.0	568.4	589.3	0.226E-02	415.4	437.9	0.881E-03	297.3	297.3	297.3	297.3	
644.	0.039	0.0410	0.04393	0.0520	19000.0	568.4	589.3	0.226E-02	420.1	420.1	0.944E-03	281.0	281.0	281.0	281.0	
644.	0.042	0.0420	0.04597	0.0597	21000.0	607.7	629.7	0.259E-02	620.1	642.4	0.944E-03	281.0	281.0	281.0	281.0	
644.	0.044	0.0430	0.0413	0.0613	23000.0	621.7	644.2	0.276E-02	623.0	646.4	0.965E-03	250.5	250.5	250.5	250.5	
644.	0.047	0.0450	0.0453	0.07302	0.0613	642.0	664.2	0.276E-02	623.0	646.4	0.965E-03	220.3	220.3	220.3	220.3	
644.	0.049	0.0480	0.07204	0.07992	0.0667	29000.0	646.4	663.4	0.286E-02	644.1	667.4	0.965E-03	247.3	247.3	247.3	247.3
644.	0.050	0.0705	0.07992	0.07992	29000.0	649.4	669.4	0.291E-02	654.1	677.0	0.995E-03	247.3	247.3	247.3	247.3	
644.	0.0750	0.0750	0.0493	0.0493	31000.0	457.5	481.1	0.301E-02	471.2	495.4	0.105E-02	269.8	269.8	269.8	269.8	
773.	0.052	0.0750	0.0493	0.0493	31133	31600.0	789.0	817.4	0.434E-02	805.0	835.0	0.151E-02	269.8	269.8	269.8	269.8
773.	0.054	0.0810	0.04914	0.0747	32000.0	817.2	844.9	0.444E-02	831.1	841.3	0.161E-02	272.7	272.7	272.7	272.7	
773.	0.061	0.0895	0.04816	0.0813	33000.0	850.3	881.2	0.504E-02	864.8	894.2	0.174E-02	281.0	281.0	281.0	281.0	
773.	0.064	0.0995	0.04432	0.08533	34000.0	845.8	897.2	0.523E-02	902.7	935.4	0.189E-02	252.9	252.9	252.9	252.9	
773.	0.074	0.1125	0.04578	0.0987	35000.0	929.3	943.0	0.402E-02	944.1	978.4	0.202E-02	261.2	261.2	261.2	261.2	
773.	0.085	0.1210	0.07025	0.1133	35500.0	994.0	1032.5	0.493E-02	963.0	998.0	0.216E-02	261.0	261.0	261.0	261.0	
644.	0.085	0.1210	0.07025	0.1133	35500.0	830.0	860.1	0.481E-02	802.3	831.4	0.193E-02	261.0	261.0	261.0	261.0	
644.	0.085	0.1295	0.04773	0.1133	34500.0	828.2	858.3	0.479E-02	815.4	845.4	0.153E-02	232.0	232.0	232.0	232.0	
644.	0.092	0.1385	0.04443	0.1227	35500.0	858.5	889.4	0.514E-02	844.3	874.9	0.144E-02	236.1	236.1	236.1	236.1	
644.	0.101	0.1515	0.04467	0.1347	40000.0	897.1	929.4	0.541E-02	868.1	899.4	0.175E-02	247.3	247.3	247.3	247.3	
644.	0.117	0.1690	0.1546	0.1546	42000.0	943.0	971.9	0.647E-02	890.2	922.3	0.184E-02	230.4	230.4	230.4	230.4	
644.	0.135	0.1930	0.04995	0.1995	44000.0	1029.0	1067.1	0.740E-02	917.5	950.0	0.194E-02	224.0	224.0	224.0	224.0	
644.	0.2015	0.2015	0.7047	0.1893	44500.0	1054.5	1092.6	0.774E-02	924.1	957.4	0.199E-02	224.0	224.0	224.0	224.0	
644.	0.152	0.2425	0.2173	44500.0	1118.3	1158.0	0.825E-02	948.3	982.7	0.208E-02	149.5	149.5	149.5	149.5		
644.	0.163	0.2425	0.4218	0.2173	44500.0	1118.3	1158.0	0.872E-02	1005.3	1041.0	0.235E-02	211.3	211.3	211.3	211.3	
644.	0.180	0.2940	0.4122	0.2460	47000.0	1171.4	1214.1	0.958E-02	1025.0	1063.0	0.245E-02	213.4	213.4	213.4	213.4	
644.	0.184	0.3025	0.41225	0.4149	0.2480	47100.0	1190.4	1233.0	0.989E-02	1027.2	1064.5	0.245E-02	224.0	224.0	224.0	224.0
644.	0.184	0.3025	0.41225	0.4149	0.2480	595.5	617.1	0.247E-02	513.0	532.4	0.414E-02	224.0	224.0	224.0	224.0	
322.	0.184	0.3025	0.41225	0.4149	0.2480	48100.0	595.5	617.1	0.247E-02	513.0	532.4	0.414E-02	224.0	224.0	224.0	224.0
322.	0.184	0.3025	0.41225	0.4149	0.2480	50000.0	595.5	617.1	0.247E-02	513.0	532.4	0.414E-02	224.0	224.0	224.0	224.0
322.	0.184	0.3025	0.41225	0.4149	0.2480	52000.0	595.5	617.1	0.247E-02	513.0	532.4	0.414E-02	224.0	224.0	224.0	224.0
322.	0.186	0.3025	0.41225	0.4149	0.2480	54000.0	595.5	617.1	0.247E-02	513.0	532.4	0.414E-02	224.0	224.0	224.0	224.0
322.	0.186	0.3025	0.41225	0.4149	0.2480	56000.0	595.5	617.1	0.247E-02	513.0	532.4	0.414E-02	224.0	224.0	224.0	224.0
322.	0.187	0.3019	0.41172	0.2493	40000.0	597.1	618.0	0.249E-02	513.1	531.7	0.414E-02	202.3	202.3	202.3	202.3	
322.	0.190	0.3040	0.4250	0.2333	45000.0	402.2	424.0	0.253E-02	510.0	529.3	0.467E-02	194.7	194.7	194.7	194.7	
322.	0.193	0.3043	0.4342	0.2460	70000.0	410.3	432.4	0.246E-02	507.3	525.0	0.599E-02	191.1	191.1	191.1	191.1	
322.	0.198	0.3070	0.4436	0.2440	75000.0	415.1	437.4	0.244E-02	504.4	522.7	0.597E-02	191.4	191.4	191.4	191.4	
322.	0.201	0.3090	0.4505	0.2480	80000.0	419.7	442.2	0.248E-02	502.4	520.0	0.587E-02	213.4	213.4	213.4	213.4	
322.	0.210	0.3090	0.4794	0.2860	85000.0	433.4	454.4	0.280E-02	491.7	509.4	0.562E-02	197.4	197.4	197.4	197.4	
322.	0.213	0.3093	0.4893	0.2840	90000.0	437.8	456.0	0.284E-02	487.9	505.4	0.558E-02	198.0	198.0	198.0	198.0	
322.	0.215	0.3095	0.4947	0.2847	95000.0	440.4	463.9	0.284E-02	485.0	503.4	0.547E-02	191.1	191.1	191.1	191.1	
322.	0.223	0.3135	0.7113	0.2973	100000.0	451.7	473.3	0.294E-02	478.7	496.1	0.533E-02	132.2	132.2	132.2	132.2	

322.	0.345	0.4210	0.5554	0.44600	222000.0	0.468E-02	485.0	502.4	0.397E-03
322.	0.347	0.4235	0.5548	0.4627	223000.0	0.471E-02	483.4	501.2	0.394E-03
322.	0.351	0.4365	0.5515	0.4160	224000.0	0.477E-02	481.7	499.2	0.340E-03
322.	0.352	0.4385	0.5513	0.493	224500.0	0.479E-02	480.9	498.3	0.386E-03
322.	0.353	0.4415	0.5503	0.707	225000.0	0.480E-02	480.5	497.9	0.337E-03
322.	0.354	0.4445	0.5493	0.4220	225500.0	0.482E-02	480.1	497.5	0.336E-03
322.	0.357	0.4510	0.5364	0.7760	226000.0	0.487E-02	477.4	495.0	0.330E-03
322.	0.357	0.4510	0.5364	0.7760	226000.0	0.487E-02	477.4	495.0	0.330E-03

Appendix E Precracking Load Cycle Determination

An iterative computer code was generated to define the precracking load cycle needed to meet the ASTM recommendations for thru-thickness cracks, plus additional criteria established for this investigation of surface flaws. The computational procedure iterates backward from the desired stress intensity factor level where the experiment test is to begin using plastic zone size as the major load-shedding criteria. That is, given a desired beginning stress intensity factor, and other test variables discussed in Chapter IV, the program calculates backwards to define an appropriate beginning load and load-shedding cycle. The largest load-shedding step-size of 20% (recommended by ASTM) is initially assumed, and then reduced as required to meet all other criteria. The iterative procedure continues until a solution is reached, or it is determined there is no solution within the bounds of the established criteria.

The two fundamental criteria established by the ASTM-E647 (39) committee to define a specimen precracking load cycle are:

1. Load reduction levels should be no greater than 20% of the applied load.
2. The crack growth before load-shedding should be at least three times the plastic zone size established by the prior load level.

In addition, a third criterion was established for this investigation to ensure the plastic zone size was decreasing with load-shedding steps. That is, the stress intensity factor after each load-shedding step shall be less than the prior stress intensity level.

These three criteria were programmed into the computer code as follows:

- Step #1: a load-shed factor (LSF) is defined to ensure load-shedding is less than 20% of the applied load. That is:

$$LSF = 0.8 * M/M' \quad (B1)$$

where M is the new applied moment to the specimen, and M' the applied moment before load-shedding. Once a surface crack length of size "c" is assumed, and a desired initial stress intensity factor defined, the program predicts the load level required to fatigue the crack to a size 6 times the plastic zone diameter. That is, for a desired final K value (where K is the value when the fatigue crack growth experimental test begins after precracking), and an assumed crack length "c" (typically defined as a measurable value which is consistent with available instrumentation accuracy), the program calculates the load-shedding steps by reducing the LSF and checking to ensure the constraints are satisfied. In effect, the procedure is a backward-marching iterative approach for meeting the required criteria.

- Step #2: the program utilizes the Irwin plastic zone size prediction for plane stress to meet the ASTM crack growth criteria of at least 3 times the plastic zone size. That is:

$$r_p = (K / \sigma_{ys})^2 / \pi \quad (B.1)$$

The crack growth length (Δc) along the surface is defined as:

$$\Delta c = c - c' \quad (B.2)$$

Letting the crack stress intensity factor be K' (where the prime mark represents the K value before load-shedding):

$$3r'_p = 3(K'/\sigma_{ys})^2 / \pi$$

$$K' = \sigma'_b H' \pi a' / Q' B'(a', c', \phi) \quad (B.3)$$

where $\phi = 0$ degrees and σ'_b is the bending stress such that:

$$\sigma'_b = 6M'/bt^2 = 6P' \Delta L / 4bt^2 \quad (B.4)$$

To meet criterion #3, a restriction was set on the iteration procedure to ensure the plastic zone size after load-shedding was smaller than the plastic zone size before load-shedding. The equations to develop this criteria are:

$$c' = c - 3 * K'^2 / \pi \sigma_{ys}^2 \quad (B.5)$$

$$c' = c - 3a'M'^2 (6H'B'/\sigma_{ys}bt^2)^2/Q' \quad (B.6)$$

$$c/(1+3*36(M'H'B')^2 (a'/c')/(Q'bt^2\sigma_{ys})^2) \quad (B.7)$$

or using the LSF value:

$$c' = c/(1+3(a'/c')/Q'^*(6H'B'/(σ_{ys}bt^2)^2(M/LSF)^2)) \quad (B.8)$$

The plane strain plastic zone size was also checked by using the Irwin relationship of:

$$r_p = (K / \sigma_{ys})^2 / (3 * \pi) \quad (B.9)$$

$$c' = (c - K'^2 / \pi \sigma_{ys}^2) \quad (B.10)$$

$$= c/(1+(6H'B'M')^2/Q'(bt^2\sigma_{ys})^2) \quad (B.11)$$

Or:

$$K = K' * LSF \quad (B.12)$$

To initiate the precracking analysis, it was necessary to assume an a/c value. This value was established by reviewing surface flaw experimental data on PMMA and metals (from published literature) to determine crack growth aspect ratio patterns. The review indicated that for crack where "c" < 0.1 in, the crack aspect ratio (a/c) was in the range of 0.82 < a/c < 1.0. A sensitivity study to define the range of K for this range of a/c was then conducted, showing there was little difference between a value of K for a/c between 0.9 and 0.8. Therefore, an average value of 0.85 was selected for the load-shedding iterative calculations.

For the research described in this report, the beginning stress intensity factor was set at 600 psi^{*}in^{1/2} (659 KPa*M^{1/2}) for all specimen tests. The crack growth prediction was initiated by assuming an LSF of 20%, and an a/c value of 0.85. The ASTM crack growth recommendation of 3 times the plastic zone size for thru-thickness cracks was initially set at 6 to provide a safety factor for surface flaws. However, if the program could not converge using a factor of 6, the crack growth requirement was reduced by increments of one plastic zone diameter until a factor of 3 plastic zone diameter was reached. If the program was unable to converge by meeting all the above criteria, a statement was generated indicating that a precracking load cycle could not be generated for the established criteria.